

Proceeding of JSPS-CAS Core University Program (CUP) Seminar on Modeling of Theory and Simulation of Fusion Plasmas

August 30 - September 2, 2010 Beijing, CHINA

Edited by

LI Ding, KISHIMOTO Yasuaki, GAO Zhe and TOMITA Yukihiro

Abstract

The JSPS-CAS Core University Program (CUP) seminar on "Modeling of Theory and Simulation of Fusion Plasmas" was held in Peking University, Beijing, China, from August 30 through September 2, 2010. This seminar was organized in the framework of the CUP in the field of plasma and nuclear fusion.

This year is the final year of the CUP on Fusion and Plasma. One special talk and 26 oral talks were presented in the seminar including 11 Japanese attendees. This seminar included timely and very interesting reviews and discussions of: (1) progress in theory, simulation and integrated modeling of fusion plasmas; (2) newly experimental results closed related with present theoretical interest; (3) present status of collaboration research activities and new ideas for post-CUP collaboration. The meeting consisted of 26 oral presentations, which covered the following topical areas: (1) Turbulence and transport; (2) MHD equilibrium and stability; (3) Peripheral plasma behaviors. Several future collaboration researches were proposed in this seminar.

Key words: turbulent transport, plasma turbulence, geodesic acoustic mode, zonal flow, tearing mode, chaotic magnetic field, SOL/divertor plasma, MHD simulation, integrate modeling, particle simulation, Monte Carlo simulation, molecular dynamics simulations, dust particle

Organization:

Representatives:

LI Ding (李 定)

Chairperson, Chinese Academy of Science, China

KISHIMOTO Yasuaki (岸本泰明)

Chairperson, Kyoto University, Japan

Program Committee:

GAO Zhe (高 喆)

Chair, Tsinghua University, China

TOMITA Yukihiro (冨田幸博)

Co-chair, National Institute for Fusion Science, Japan

NAKAJIMA Noriyoshi (中島徳嘉)

National Institute for Fusion Science, Japan

LI Jiquan (李 继全)

Kyoto University, Japan

WANG Xiaogang (王 晓钢)

Peking University, China

Local Organization Committee:

WANG Xiaogang (王 晓钢)

Chair, Peking University, China

XIAO Chijie (肖 池阶)

Peking University, China

LIU Liwei (刘力玮)

Secretary, Peking University, China

Preface

The JSPS-CAS Core University Program (CUP) seminar on "Modeling of Theory and Simulation of Fusion Plasmas" was held in Peking University, Beijing, China, from August 30 through September 2, 2010. This seminar was organized in the framework of the CUP in the field of plasma and nuclear fusion.

The plasma researches using the theories and computer simulations are one of the most powerful and important methods for realizing a nuclear fusion reactor. A lot of collaboration researches under CUP have been carried out along the aims in the categories of 30A: "Study on Theoretical Analysis of MHD and Micro-instabilities in Plasmas", 30B: "Study on Transport Theory • Code Development of Numerical Analysis and Confinement Improved Mode in Torus Plasmas" and 30D: "Modeling of edge and divertor plasma and control of impurities and recycling particles."

This year is the final year of the CUP on Fusion and Plasma. One special talk and 26 oral talks were presented in the seminar including 11 Japanese attendees. This seminar included timely and very interesting reviews and discussions of: (1) progress in theory, simulation and integrated modeling of fusion plasmas; (2) newly experimental results closed related with present theoretical interest; (3) present status of collaboration research activities and new ideas for post-CUP collaboration. The meeting consisted of 26 oral presentations, which covered the following topical areas: (1) Turbulence and transport; (2) MHD equilibrium and stability; (3) Peripheral plasma behaviors. Several future collaboration researches were proposed in this seminar.

This seminar was completed with fruitful discussions and great success and fruitful, clarifying remarkable progresses through the collaboration researches under CUP. The organizing and program committees express the gratitude for all participants for their supports and corporation to this seminar.

LI Ding, KISHIMOTO Yasuaki, GAO Zhe and TOMITA Yukihiro

Contents

Preface

Contents

Photo of Participants

1. Analytical theory of the geodesic acoustic mode: plasma shaping effects in small and large orbit drift width limit	1
GAO Zhe (Tsinghua University)	
2. Wave-number spectral characteristics of drift wave micro-turbulence with large-scale structures	10
LI Jiquan (Kyoto University)	
3. Zonal flow modes in a tokamak plasma with dominantly poloidal mean flows	19
ZHOU Deng (ASIPP)	
4. Magnetic islands caused by microturbulence	28
ISHIZAWA Akihiro (NIFS)	
5. Significant features of low frequency zonal flow and geodesic acoustic mode in the edge plasma of HL-2A tokamak	38
ZHAO Kaijun (SWIP)	
6. Heavy Ion Beam Probe Measurement in Turbulence Diagnostic Simulator	48
KASUYA Naohiro (NIFS)	
7. Global and Kinetic MHD Simulation by the Gpic-MHD Code	56
NAITOU Hiroshi (Yamaguchi University)	
8. Full Particle Simulation of a Tokamak Plasma with Open-field SOL-Divertor Region	67
TAKIZUKA Tomonori (JAEA)	
9. Edge Impurity Transport Study in Stochastic Layer of LHD and Scrape-off Layer of HL-2A	80
KOBAYASHI Masahiro (NIFS)	

10. Modelling of Edge Plasma on JT-60U Tokamak by Using SOLPS5.0 code	88
CHEN Yiping (ASIPP)	
11. Monte Carlo simulation of carbon redeposition on LHD first wall	95
KAWAMURA Gakushi (NIFS)	
12. Second stable regime of internal kink modes excited by barely passing energetic ions in tokamak plasmas	100
HE Hongda (SWIP)	
13. Integrated Modeling of Tokamak Plasmas by TASK Code	112
FUKUYAMA Atsushi (Kyoto University)	
14. Simulation of ECR startup and comparison to experimental observations in SUNIST	120
TAN Yi (Tsinghua University)	
15. Monte Carlo study of the H/C ratio of impurities depositing on the bottom of the toroidal gaps between divertor tiles	130
DAI Shuyu (Dalian University of Technology)	
16. The simulation of erosion and deposition behavior on EAST	139
XU Qian (ASIPP)	
17. Theoretical modeling of hydrogen retention and recycling in plasma-facing graphite	144
LIU Shengguang (Dalian University of Technology)	
18. Atomic Modeling of Interactions between Hydrogen and Tungsten ...	154
YANG Zhongshi (ASIPP)	
19. Dust Charging and Dynamics in Tokamaks	158
TOMITA Yukihiro (NIFS)	
Agenda	164
List of Participants	168

China-Japan CUP seminar on
“Modeling of Theory and Simulation of Fusion Plasmas”

August 30-September 2, 2010 Beijing, China



Analytical theory of the geodesic acoustic mode: plasma shaping effects in small and large orbit drift width limit

GAO Zhe

Department of Engineering Physics, Tsinghua University, Beijing 100084

ABSTRACT: The analytical theories of the geodesic acoustic mode (GAM) are reviewed in the small and large orbit drift width limit respectively. Different physics pictures in these two limits are displayed. These analytical methods are applied to investigate the plasma shaping effect on the frequency and collisionless damping rate of the GAM.

Keywords: geodesic acoustic mode, plasma shaping, orbit drift width, analytical theory

PACS: 52.35.FP, 52.30.Gz, 52.25.Fi, 52.55.Fa

1. Introduction

In scientific research activities, the analytical theory is playing very unique and important roles, such as to provide a clear physics picture, to verify and/or benchmark numerical simulations, to explain and/or promote experiment observations, and so on. The geodesic acoustic mode (GAM) [1] is a coherent oscillating mode with toroidal and poloidal symmetric electrostatic potential in toroidal plasmas. It is driven by drift wave turbulence, and thus moderates turbulent transport. The frequency and damping rate indicate the fundamental characters of the GAM, which is closely related to its generation, evolution, and impact. The formulae of the frequency and damping rate of the GAM have been given for low beta tokamak plasmas with circular cross section and infinite large aspect ratio.[2-5] However, most of present and planned tokamak devices have the strongly shaped geometry and finite aspect ratio (usually not larger than 3). The dependence of the GAM frequency on the elongation was investigated experimentally in ASDEX-Upgrade and a scaling law was given.[6] Simulations [7-8] also show the similar effect of elongation on the frequency, but cannot give a quantitative comparison due to lack of an analytical formula. Recent simulation [9] also gave the dependence the GAM frequency and damping rate on the inverse aspect ratio, which needs to be verified by the analytical theory as well. Following the Winsor et al's original fluid procedure and employing the Solov'ev type analytical equilibrium or the Culham equilibrium, some analytical efforts [10, 11] were performed. However, due to different definitions of plasma shape parameters in the equilibrium model to conventional-used shaped parameters, some additional treatments, for example, the profile assumption or the average operation should be made. Moreover, it is noted the fluid model cannot investigate the damping mechanism. Therefore, analytical formulae for the GAM frequency and damping rate are still urgent for shaped plasmas.

The drift kinetic theory was introduced to investigate the GAM by Novakovskii.[12] The frequency with a different numerical coefficient to the fluid theory is derived but the collisionless damping is not considered. Instead the collisional damping rate is given. Watari et al [2] also used the drift kinetic equation to get a clear formula of the collisionless damping rate of the GAM for the first time. However, the finite wavelength effect (or finite orbit drift width effect, finite ODW) cannot be included due to the limitation of drift kinetic equation. Moreover, in the mathematic treatment, the plasmas response is decomposed to sine and cosine functions, which is not convenient to be applied in future gyrokinetic theory. The gyrokinetic equation is employed to study the GAM by Sugama and Watanabe. [3] The enhanced damping by the finite orbit width effect is firstly investigated. However, this effect is included only to the second order, then the residual damping at high q is not found, which was examined in numerical simulation [8] firstly and could be successfully explained by the high order harmonic resonance to transit motions presented in our previous works.[4,5] In Refs. 3-5, the Bessel function expansion method is used to solve the gyrokinetic equation, which make the analytical treatment possible especially in small ODW limit. Recently, another new method based on the large ODW expansion is developed by Zonca and Chen [13] and clearly presented by Qiu et al.[14]. In this theory, the resonant and non-resonant responses are divided and for different response, the gyrokinetic equation itself is expanded by different ordering. Using this method, the residual damping at high safety factor could be analytically derived, [14] which is consistent to the result from the simulation and our previous theory based on high harmonic resonance. These two analytical approaches are effective in the small and large ODW limit, respectively, and they could be used to investigate the plasma shaping effect on the GAM as well.

The paper is organized as follows. In section 2, the gyrokinetic model of the GAM is introduced and two analytical approaches developed previously are reviewed. The emphasis is focusing on the different physics pictures in these two limits. In section 3, these two analytical methods are applied in the study of plasma shaping effect and the formulae of the GAM frequency and damping rate is given as functions of shape parameters. The summary is given in section 4.

2. Analytical methods of the gyrokinetic model of the GAM

2.1 The gyrokinetic model of the GAM

The gyrokinetic model of the GAM was presented in previous publication [3-5] for many times. However, it is still briefly given here for the completeness. Firstly, We consider a toroidally axisymmetric plasma with a flux surface (R_s, Z_s) , then the magnetic field $\mathbf{B} = \mathbf{B}_p + \mathbf{B}_t$ can be expressed by typical equilibrium model. An zonal potential, $\phi = \sum_{\omega, k} \hat{\phi}(\theta) \exp(ikx|\nabla r| - i\omega t)$ is introduced, where $|\nabla r|$ is the inverse Jacobian from the axisymmetric coordinates to the natural coordinates attached a given flux surface and x is a

normal distance from the flux surface. The flux surface average of the potential $\langle\phi\rangle$ is toroidally and poloidally symmetric and the poloidal variation of the potential $\phi - \langle\phi\rangle$ is assumed much smaller than $\langle\phi\rangle$. Then, the ion response can be written as

$$\hat{f} = -qF_0\hat{\phi}/T + \hat{h}J_0(\delta) \quad , \quad (1)$$

and the nonadiabatic part satisfies the linear gyrokinetic equation,

$$\left(1 - \frac{\omega_d}{\omega} + \frac{i\omega_t}{\omega}\partial_\theta\right)\hat{h} = \frac{e\hat{\phi}}{T}J_0(\delta)F_0. \quad (2)$$

Here, F_0 is a Maxwellian distribution, $T = mv_t^2/2$, J_0 is a zero order Bessel function, $\delta = k\rho_t(v_\perp B_0/v_t B)$, where $\rho_t = v_t/\Omega_0$ is the gyroradius at the magnetic axis B_0 , and $\omega_t = v_\parallel B_p/[(dl/d\theta)B]$ and $\omega_d = k|\nabla r|\hat{\mathbf{x}} \cdot \mathbf{b} \times (\mu\nabla B + mv_\parallel^2\mathbf{b} \cdot \nabla\mathbf{b})/m\Omega$ are the transit frequency and magnetic drift frequency, respectively, where v_\parallel is the parallel velocity, μ is the magnetic momentum and $dl/d\theta$ is the differential of poloidal arc length with respect to poloidal angle. In fact, Eq. (2) is also valid for electrons, However, due to small gyroradius and the fast parallel motion of electrons, the electron response could be given by the Boltzmann relation

$$\hat{f}_e = eF_{0e}(\hat{\phi} - \langle\hat{\phi}\rangle)/T_e. \quad (3)$$

Then, the quasi-neutrality condition

$$D \equiv \frac{en_0}{T_e}(\hat{\phi} - \langle\hat{\phi}\rangle) + \frac{en_0\hat{\phi}}{T_i} - \frac{2\pi}{m^2} \int dE d\mu \frac{B}{|v_\parallel|} \hat{h}J_0(\delta) = 0, \quad (4)$$

gives the dispersion relation of the GAM.

Obviously, the key issue is how to solve the gyrokinetic equation, Eq. (2). Two analytical approaches developed previously are introduced below.

2.2 The analytical solution in the small orbit drift width limit

Let us examine Eq. (2). It is a one-order linear non-homogeneous differential equation. We can write the solution of Eq. (2) directly, as follows

$$h = \exp\left[i\int\left(\frac{\omega}{\omega_t} - \frac{\omega_d}{\omega_t}\right)d\theta\right] \int d\theta \frac{-iqF_0\hat{\phi}}{T} \frac{\omega}{\omega_t} J_0(\delta) \exp\left[-i\int\left(\frac{\omega}{\omega_t} - \frac{\omega_d}{\omega_t}\right)d\theta\right] \quad (5)$$

where the periodic boundary condition is automatically satisfied. It is noted that all of $\omega_t, \omega_d, \delta$ and $\hat{\phi}$ are trigonometric functions of θ . If we have the expressions of these quantities, we can obtain the θ integral of $(\omega - \omega_d)/\omega_t$ as trigonometric functions as well, where some assumptions of weak shape deformation may be used for the analytical treatment. Then, using the Bessel function expansion $e^{ia\cos\theta} = \sum i^n J_n(a)\exp(in\theta)$, the expression of h can be analytical obtained. For clarity, the case of infinite larger aspect ratio and circular cross section is presented here. At this case, the $\omega_t = v_\parallel/qR$ and $\delta = k\rho_t v_\perp/v_t$ are independent to

θ and the $\omega_d = \omega_{d0} \sin \theta$ has a simple $\sin \theta$ dependence, then Eq. (5) can be simplified to

$$h = \frac{qF_0}{T} \sum_{m,n,l=-\infty}^{+\infty} \hat{\phi}_l i^{m-n} e^{i(m-n+l)\theta} J_0^2(\delta) \frac{\omega J_m J_n}{\omega + (n-l)\omega_l}. \quad (6)$$

Here, $J_{m,n} = J_{m,n}(\omega_d/\omega_l)$. It is noted $\omega_d/\omega_l \sim k\rho_l q$, where $\rho_l q$ is the ODW of passing ion in toroidal geometry. Then the ion response is analytically solved as a sum of different harmonic resonance to the parallel transit motion multiplied by corresponding order Bessel function of finite ODW. Substituting the solution of h into Eq. (4), the dispersion relation of the GAM with arbitrary order finite ODW effects could be obtained, which is shown in Ref. [5] in details. This theory, in principle, does not restrict the limit of small orbit shift width, since we can expand to enough order to satisfy the convergence for large orbit shift width. However, only for small orbit shift width, only a few terms need to be retained and then the analytical formulae can be reached without the assistant of numerical methods.

2.3 The analytical solution in the large orbit drift width limit

In this subsection, we may review another analytical approach to solve Eq. (2), which is clearly presented by Qiu et al [14] and only a slight improvement. The idea is to avoid solving the different equation using the perturbation method. Since for resonant and non-resonant ions, the orderings are different. Therefore, the ion response is divided into the parts from non-resonant ions and that from resonant ions, $\hat{h} = \hat{h}^{nr} + \hat{h}^{res}$. For non-resonant ions, the assumption of $\omega_l/\omega \sim 1/q \ll 1$ is used to decrease the order of the differential term in Eq. (2) and the assumption of $\omega_d/\omega \sim k\rho_{ii} \ll 1$ is used to separating the contribution from different harmonics of the potential. Without loss the generality, putting these two terms into the same order, Eq. (2) is expanded as follows:

$$\hat{h}_0^{nr} = \frac{e\hat{\phi}_0}{T} J_0(\delta) F_0, \quad (7a)$$

$$\hat{h}_{l+1}^{nr} - \left(\frac{\omega_d}{\omega} - \frac{i\omega_l}{\omega} \partial_\theta \right) \hat{h}_l^{nr} = \frac{e\hat{\phi}_l}{T} J_0(\delta) F_0 \quad l = 0, 1, 2... \quad (7b)$$

Then the \hat{h}^{nr} can be solved from this hierarchy. Substituting the solution into Eq. (4), the real part of dielectric constant, $\langle D \rangle_r$, are obtained, and, at the mean time, the harmonic components of the potential are obtained as well. Now we need to calculate the contribution from the resonant ions. For the case of large ODW with $\omega_d \gg \omega_l$, then we still drop the differential term out of the lowest order equation. However, the order $\omega \sim \omega_d$ should be satisfied for the resonant ions. Then, Eq. (2) is expanded as

$$\left(1 - \frac{\omega_d}{\omega} \right) \hat{h}_0^{res} = \frac{e\hat{\phi}_0}{T} J_0(\delta) F_0, \quad (8a)$$

$$\left(1 - \frac{\omega_d}{\omega} \right) \hat{h}_{l+1}^{res} + \frac{i\omega_l}{\omega} \partial_\theta \hat{h}_l^{res} = 0, \quad l = 0, 1, 2... \quad (8b)$$

Here, the procedure is slightly different to that in Ref. [14], where the potential term is divided by ordering and assigned to different order equations of resonant ions. However, since the potential has been obtained when we solve the non-resonant response, we can place the whole potential term in the RHS of Eq. (8a). The \hat{h}^r can be solved directly. By a rather complex Landau-type integral, the imaginary part of dielectric constant $\langle D \rangle_i$ is obtained. Finally, under the weak damping assumption, the real frequency and the damping rate of GAM can be obtained by letting $\langle D \rangle_r = 0$ and $\gamma \partial_\omega \langle D \rangle_r + \langle D \rangle_i = 0$.

2.4 Physics pictures in these two limits

Let us compare these two analytical methods above. For the method shown in subsection 2.2, the gyrokinetic equation is directly solved; therefore, the method is valid for wide parameters, although the pure analytical formulae can be obtained only in the small ODW limit, otherwise the assistance of numerical calculation are required. The accompanying disadvantage of this method is rather complicated calculation in two-fold integral operation, especially for the strong or complex poloidal dependence of the ω_i, ω_d and δ . On the contrary, for the method shown in subsection 2.3, the gyrokinetic equation is expanded perturbatively. The simplification of the equation brings the relatively simple and direct mathematics without integral operation. However, this method is only valid for large ODW. Since the radial wavelength of the GAM is shown to be several ion gyroradius, the large ODW usually means the large safety factor.

It is interesting to consider the damping mechanism which is involved in the mathematics and seems to be different in these two approaches. In the first treatment, the damping comes from harmonic resonance to the parallel transit motion and the lower order is dominant at small ODW; while, in the large ODW limit, the damping comes from the magnetic drift resonance. This transition may be explained by the schematic drawing in Figure 1. When the ODW is quite smaller than the wavelength of the GAM [Fig. 1(a)], the period of the ion parallel transit motion (in the cross section, shown as a circular motion around the flux surface) should be complete in phase with the period of the GAM potential. It is the first order transit resonance. When the ODW is finite [Fig. 1(b)], accompanying with the parallel transit, the ion drifts from the original flux surface. However, the potential oscillates spatially around the flux surface with a certain wavelength. Then, harmonic resonances become effective. The weight of different harmonics is the order of Bessel function. This picture is quite similar to that of cyclotron damping. When the ODW is very large comparing to the GAM wavelength [Fig. 1(c)], high order resonance to parallel transit are dominant. We can consider this issue in another view. The resonant parallel velocity $v_{||res}/v_{ti} \sim q/N$ approaches to zero, so resonant particles always feel the magnetic drift motion in the vertical direction rather than the parallel motion. The resonance occurs at the condition $\omega_G \sim \mathbf{k}_r \cdot \mathbf{v}_d$, which is the Landau mechanism in the perpendicular direction. Therefore, the effect of very high harmonic resonances is equivalent to that of the magnetic drift resonance.

3. Application in the study of plasma shaping effect

3.1 The equilibrium model

Since the radial wavelength of the GAM is much shorter than the scale length of macroscopic equilibrium profiles, it can be thought that the leading order dynamics of the GAM is dominated in the vicinity of the flux surface. Therefore, the Miller's local equilibrium model [15] is employed. Considering a flux surface $R_s = R_0(r) + r \cos \theta$, $Z_s = \kappa(r)r \sin \theta$, where such parameters as the elongation κ , the inverse aspect ratio $\varepsilon = r/R_0$, the Shafranov shift gradient $\Delta' = \partial_r R_0$ and the radial derivative of elongation $s_\kappa = (r/\kappa)\partial_r \kappa$ are included, the toroidal and poloidal fields in the flux surface can be described as $B_t = B_0 R_0 / R_s$ and

$$B_p = B_0 \frac{\varepsilon}{q} \frac{dl/d\theta}{J_s R_s / R_0} \frac{1}{2\pi} \oint d\theta \frac{J_s / r}{R_s / R_0},$$

where $J_s = (\partial R_s / \partial r)(\partial Z_s / \partial \theta) - (\partial Z_s / \partial r)(\partial R_s / \partial \theta)$ and $dl/d\theta = \sqrt{(dR_s/d\theta)^2 + (dZ_s/d\theta)^2}$, q is the safety factor and B_0 is the field at the magnetic axis. Then, we can write the expressions of ω_t, ω_d and δ . In the analytical work, we assume the plasma shape is not far from the elliptic nest surface with infinite aspect ratio. It implies that these three ε, Δ' and s_κ , are small. Also, we assume $1/q$ is also small and these small have the same order $\varepsilon, \Delta', s_\kappa, 1/q \sim O(\varepsilon)$. This assumption is valid for most present tokamak plasmas. Then, the quantities ω_t, ω_D and δ are expressed with functions of θ and shape parameters as follows,

$$\frac{\omega_d}{\omega} = \frac{\hat{k}}{\hat{\omega}} \left(\frac{\hat{v}_\perp^2}{2} + \hat{v}_\parallel^2 \right) \frac{\sin \theta}{\kappa (1 + \Delta' \cos \theta + s_\kappa \sin^2 \theta)} + O(\varepsilon^3), \quad (9)$$

$$\frac{\omega_t}{\omega} = \frac{\hat{v}_\parallel}{q \hat{\omega}} \frac{1 + s_\kappa / 2 + \varepsilon^2 / 2 - \varepsilon \Delta' / 2}{1 + \Delta' \cos \theta + s_\kappa \sin^2 \theta} + O(\varepsilon^3), \quad (10)$$

$$\delta = \hat{k} \hat{v}_\perp \frac{(1 + \varepsilon \cos \theta) \sqrt{\sin^2 \theta + \kappa^2 \cos^2 \theta}}{\kappa (1 + \Delta' \cos \theta + s_\kappa \sin^2 \theta)} + O(\varepsilon^3), \quad (11)$$

where the normalizations $\hat{k} = k \rho_{ii}$, $\hat{\omega} = \omega R_0 / v_{ti}$, $\hat{v}_{\parallel, \perp} = v_{\parallel, \perp} / v_{ti}$ are used. Substituting these expressions into the procedure displayed in subsection 2.2 and 2.3, the GAM frequency and collisionless damping rate are obtained and the shaping effect can be investigated, which is outlined in the following subsection

3.2 Plasma shaping effects

Firstly, we give the frequency and damping rate of the GAM from the theory in the small ODW limit as follows.

$$\frac{\omega}{v_{ii}/R_0} = \sqrt{\left(\frac{7}{4} + \tau\right) \left(\frac{2}{\kappa^2 + 1}\right) \left(1 - \frac{s_\kappa}{2} \frac{7 + 2\tau}{7 + 4\tau}\right)} \quad (12)$$

$$\left[1 - \varepsilon^2 \frac{9\kappa^2 + 3}{8\kappa^2 + 8} - \Delta'^2 \frac{\kappa^2}{4\kappa^2 + 4} + \varepsilon \Delta' \frac{4\kappa^2 + 1}{4\kappa^2 + 4} + \frac{(23 + 16\tau + 4\tau^2)(\kappa^2 + 1)}{2(7 + 4\tau)^2 q^2}\right]$$

$$\frac{\gamma}{v_{ii}/R_0} = -\frac{i2\sqrt{\pi}(R\omega_{GAM}/v_{ii})^6}{(7 + 4\tau)} \left(1 + \frac{s_\kappa}{2} \frac{7 + 2\tau}{7 + 4\tau}\right) \left[\exp(-\omega_{GAM}^2) - G(s_\kappa, \varepsilon, \Delta') \exp\left(-\frac{\omega_{GAM}^2}{4}\right)\right] \quad (13)$$

It is noted that the s_κ^2 term is dropped in Eqs. (12)-(13) since the lower order s_κ term exists. Another thing is the $G(s_\kappa, \varepsilon, \Delta')$ is the function of $s_\kappa, \varepsilon^2, \varepsilon\Delta', \Delta'^2$, but the effect of these shape parameters on the damping rate cannot be correctly given by this function. The reason is that these shaping parameters induces the trigonometric functions of $n\theta$. It implies harmonic transit resonance involved and, therefore, the damping of the GAM is influenced. However, the harmonics damping term $\exp(-\omega^2/n^2)$ increases quick with n , which means the damping rate converges much slower than the frequency does. In this case, we must retain enough orders to ensure the convergence of the damping rate, but it implies the result is given by numerical calculation rather than the analytical derivation.

The GAM frequency and damping rate from the method in the large ODW is as follows,

$$\frac{\omega}{v_{ii}/R_0} = \sqrt{\left(\frac{7}{4} + \tau\right) \left(\frac{2}{\kappa^2 + 1}\right)} \quad (14)$$

$$\left[1 - s_\kappa \frac{\kappa^2}{4\kappa^2 + 4} - \varepsilon^2 \frac{9\kappa^2 + 3}{8\kappa^2 + 8} - \Delta'^2 \frac{\kappa^2}{4\kappa^2 + 4} + \varepsilon \Delta' \frac{4\kappa^2 + 1}{4\kappa^2 + 4} + \frac{(23 + 16\tau + 4\tau^2)(\kappa^2 + 1)}{2(7 + 4\tau)^2 q^2}\right]$$

$$\frac{\gamma}{v_{ii}/R_0} = -\frac{4\kappa^2 \sqrt{7/4 + \tau}}{\hat{k}^2 (\kappa^2 + 1)^{3/2}} \left(1 + \frac{2\kappa^2 + 5}{4\kappa^2 + 4} s_\kappa - \frac{27\kappa^2 + 9}{8\kappa^2 + 8} \varepsilon^2 - \frac{7\kappa^2 + 4}{4\kappa^2 + 4} \Delta'^2 + \frac{9\kappa^2}{4\kappa^2 + 4} \varepsilon \Delta'\right) \quad (15)$$

$$\times \exp\left[-\frac{\sqrt{7/4 + \tau}}{\hat{k}} \sqrt{\frac{2\kappa^2}{\kappa^2 + 1}} \left(1 + \frac{3\kappa^2 + 4}{4\kappa^2 + 4} s_\kappa - \frac{9\kappa^2 + 3}{8\kappa^2 + 8} \varepsilon^2 - \frac{3\kappa^2 + 2}{4\kappa^2 + 4} \Delta'^2 + \frac{4\kappa^2 + 1}{4\kappa^2 + 4} \varepsilon \Delta'\right)\right].$$

It is clear that, the GAM frequencies from two methods, Eqs. (12) and (14), are almost the same. When the elongation increases, the GAM frequency decrease with the dependence of $\sqrt{2/(\kappa^2 + 1)}$. The radial derivative of elongation, s_κ , slight decreases the frequency although the coefficient is slightly different. However, if assuming the linear radial variation of the elongation, i.e. $s_\kappa = (\kappa - 1)/\kappa$, both of two formulae show that the effect of s_κ will decrease the real frequency by about 5-10% for usual elongation $1 < \kappa < 2$. The inverse aspect ratio ε also reduces the GAM frequency slightly and parabolically and this effect is enhanced by the elongation. The Shafranov shift gradient has the similar effect as the inverse aspect ratio. Considering the relation of the Shafranov shift gradient to the inverse aspect ratio, we may conclude that the effect of ε is enhanced with the inclusion of the Shafranov shift gradient.

Comparing to the real frequency, the damping rates from two methods, Eqs. (13) and (15), are quite different. For the elongation, Eq. (13) shows that, as the elongation increases, the damping rate increase dramatically due to the decrease in the real frequency in the exponential term; while Eq. (15) shows that the damping rate is weakened relatively mildly when the elongation increases. This difference comes from different dominant resonant mechanism. In the small ODW limit, the dominant damping mechanism is the first order transit resonance $\omega \sim \omega_t$, where the parallel transit motion is not influence by the elongation deformation. On the contrary, in the large ODW limit, the dominant damping mechanism is the resonance $\omega \sim \omega_d$. Although the ω decreases with an increasing elongation with the dependence of $\sqrt{2/(\kappa^2 + 1)}$, the ω_d also decrease with the dependence $1/\kappa$, more rapid than the decrease of ω . Therefore, fewer particles are involved in the resonance when κ increases and finally the damping is weakened. This behavior is displayed at large ODW, or, more directly, at high q . If we want to observe this behavior using the theory in subsection 2.2, the series expansion to enough high order is needed and then the numerical calculation should be performed, which is the similar case in studying the residual damping at high q . One most important thing is the effects of $s_\kappa, \varepsilon, \Delta'$ on the damping rate are obtained in the large ODW limit, which is hardly obtained from the expansion in small ODW due to the slow convergence. It is show that the damping rate increases parabolically with ε and the increase is strongly influenced by the radial wavenumber \hat{k} . The long wavelength mode, low \hat{k} , is easy to be damped by increasing ε .

4. Summary

The analytical methods of the gyrokinetic theory of GAM are reviewed in the small and large ODW limit respectively. One method is to write the plasma response to the zonal potential as the sum of different harmonic resonance to the parallel transit motion multiplied by corresponding order Bessel function of finite ODW by directly solving the differential equation. Then, the expression of the GAM frequency and damping rate can be analytically obtained in the small ODW limit. On the contrary, the other method is directly convert the differential gyrokinetic equation to a series of equation hierarchy by perturbation method in the large ODW limit. Then the plasma response is easily solved and the dispersion relation is obtained. Especially, different resonance mechanisms in these two limits are displayed, from low order harmonic transit resonance at small ODW to high order harmonic resonance, or equivalently, to the magnetic drift resonance, at large ODW. These two analytical methods are applied to investigate the plasma shaping effect on the frequency and collisionless damping rate of the GAM.

Acknowledgments: This work is supported by the NSFC, under Grant No. 10990214, the Major State Basic Research Development Program of China, under Grant Nos. 2009GB105002 and 2008GB717804, and the JSPS-CAS Core University Program in ‘Plasma and Nuclear Fusion’

References:

- [1] N. Winsor, J. L. Johnson and J. M. Dawson, Phys. Fluids **11**, 2448(1968).
 [2] T. Watari, Y. Hamada, A. Fujisawa, K. Toi and K. Itoh, Phys. Plasmas **12**, 062304 (2005).
 [3] H. Sugama and T.-H. Watanabe, Phys. Plasmas **13**, 012501 (2006).
 [4] Z. Gao, K. Itoh, H. Sanuki and J. Q. Dong, Phys. Plasmas **13**, 100702(2006).
 [5] Z. Gao, K. Itoh, H. Sanuki and J. Q. Dong, Phys. Plasmas **15**, 072502 (2008).
 [6] G. D. Conway, C. Troster, B. Scott, K Hallatschek and the ASDEX Upgrade Team, Plasma Phy. Control. Fusion **50**, 055009 (2008).
 [7] L. Villard, P. Angelino, A. Bottino, R. Hatzky, S. Jolliet, B. F. McMillan, O. Sauter, and T. M. Tran, Proceedings of Joint Varenna-Lausanne international workshop on theory of fusion plasmas, Varenna, 2006, edited by O. Sauter and P. Ecublens (AIP, NY, 2006), AIP Conference Proceedings, Vol. 871, p.424.
 [8] A. Kendl and B. D. Scott, Phys. Plasma **13**, 012504 (2006).
 [9] X. Q. Xu, Z. Xiong, Z. Gao, W. M Nevins, and G. R. Mckee, Phys. Rev. Lett. **100**, 215001 (2008).
 [10] B. R. Shi, J. Q. Li and J. Q. Dong Chin. Phys. Lett. **22**, 1179 (2005).
 [11] P. Angelino, X. Garbet, L. Villard, A. Bottino, S. Jolliet, Ph. Ghendrih, V. Grandgirard, B. F. McMillan, Y. Sarazin, G. Dif-Pradalier, and T. M. Tran Phys. Plasmas **15** 062306 (2008).
 [12] S.V. Novakovskii, C.S. Liu, R.Z. Sagdeev and M.N. Rosenbluth, Phys. Plasmas **4**, 4272 (1997).
 [13] F. Zonca and L. Chen, EPL **83**, 35001 (2008)
 [14] Z. Y. Qiu, L. Chen and F. Zonca, Plasma Physics Control. Fusion **51**, 012001(2009).
 [15] R. L. Miller, M. S. Chu, J. M. Greene, Y. R. Lin-Liu and R. E. Waltz, Phys. Plasmas **5**, 973 (1998).

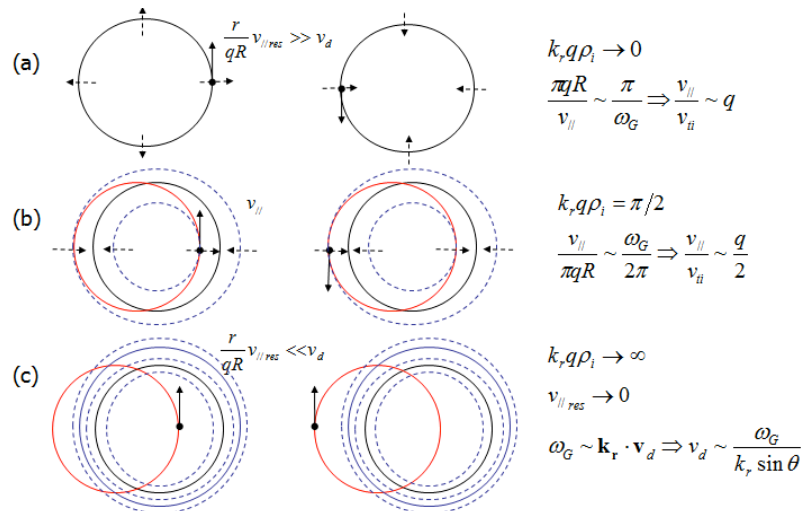


Figure 1. The damping mechanism of the GAM at different orbit-drift-widths.(the black, red and blue circles indicate the magnetic flux surface, the orbit drift surface, and the equipotential surface, respectively.)

Wave-number spectral characteristics of drift wave micro-turbulence with large-scale structures

Jiquan Li and Y. Kishimoto

Graduate School of Energy Science, Kyoto University, 611-0011 Gokasho, Uji, Japan
e-mail contact of main author: lijq@energy.kyoto-u.ac.jp

Abstract

Wave-number spectral characteristics of drift wave micro-turbulence with large-scale structures (LSSs) including zonal flows (ZFs) and Kelvin-Holmheltz (KH) mode are investigated based on 3-dimensional gyrofluid simulations in slab geometry. The focus is on the property of the wave-number spectral scaling law of the ambient turbulence under the back reaction of the self-generated LSSs. The comparison of the spectral scaling laws between ion/electron temperature gradient (ITG/ETG) driven turbulence is presented. It is shown that the spectral scaling of the ITG turbulence with robust ZFs are fitted well by an exponential-law function $\langle \phi^2/2 \rangle_E \propto e^{-\lambda k_x}$ in k_x and a power-law one $\langle \phi^2/2 \rangle_P \propto k_y^{-\beta}$ in k_y . However, the ETG turbulence is characterized by a mixing Kolmogorov-like power-law and exponential-law $\langle \phi^2/2 \rangle \propto e^{-\lambda k_{x,y}} k_{x,y}^{-3} / (1 + k_{x,y}^2)^2$ scaling for both k_x and k_y spectra due to the ZFs and KH mode dynamics. Here λ and β are the slope index factors. The underlying physical mechanism is understood as the spectral scattering caused by the back-reaction of the LSSs onto the ambient turbulence. These findings may provide helpful guideline to diagnose the plasma fluctuations and the flow structures in experiments.

Keywords: Spectral scaling law, zonal flows, micro-turbulence, gyrofluid simulation

PACS numbers: 52.35.Kt, 52.35.Ra, 52.65.Tt

1. Introduction

Experimental measurement of plasma flows and turbulence is of essential importance in transport and confinement study ^[1,2]. Recently the diagnoses of the edge fluctuations and flows including the zonal flows(ZFs) and geodesic acoustic mode(GAM) in tokamak and stellarator plasmas have been extensively carried out to characterize the structure formation such as the internal transport barriers (ITBs) and to understand the suppression mechanism of the turbulent transport by sheared mean flows and ZFs ^[3,4]. Plasma fluctuations are of wide spatio-temporal scale, which is conventionally described by wave-number and frequency spectra. Various linear and nonlinear instabilities and coherent large-scale structures (LSSs) such as the ZFs, streamers and the generalized Kelvin-Holmholtz (GKH) modes are categorized by the spectral characteristics ^[5]. The spectral analysis is extensively applied to investigate the nonlinear interaction processes through the basic three-wave coupling. Furthermore, the turbulence spectra are some of the measurable quantities in experiments, which are generally diagnosed and analyzed to characterize the fluctuation and the coherent structures.

Specifically, the drift wave turbulence is likely one of the most common fluctuations in tokamak plasmas, which has a big family including all modes originated from plasma gradients as well as the magnetic field inhomogeneity ^[6]. In past years, the ion temperature gradient (ITG) driven drift wave turbulence has attracted much attention ^[7]. A key physical mechanism involved is ascribed to the suppression of the turbulent fluctuation and ion heat transport by the ZFs ^[3]. Similarly, the electron temperature gradient (ETG) driven turbulence is expected hopefully to produce large electron transport ^[5]. Furthermore the trapped electron mode (TEM) is also proposed to be responsible to the electron transport recently. Theoretically speaking, the ZF is robust in drift wave turbulence so that the relevant problem is frequently referred to as drift wave-ZF turbulence ^[3]. The ZF is generated nonlinearly through three-wave triad couplings of higher- k components in ambient turbulence and may be saturated by the excitation of a long wavelength KH mode ^[5,8,9]. These LSSs have been extensively testified by employing the bispectral analysis in experiments and simulations ^[1,2]. Meanwhile, their back reaction onto the ambient turbulence may be also generally considered as the result of the nonlinear mode coupling to dissipation range at smaller scales. The demonstration of such processes in experiments requires the detailed measurement of the drift wave turbulence at wide scale. Furthermore it is also necessary to identify the type of the ambient turbulence such as the ITG or TEM in experiments.

Usually the drift wave turbulence is vaguely assumed to generate the ZFs as *a priori* in tokamak plasmas based on theoretical argument ^[1-4]. The statistical dispersion relation of the

fluctuations with the Doppler frequency shift effect due to the radial electric field produced $\bar{E} \times \bar{B}$ shear flows is generally analyzed in experiments ^[10]. In fact the turbulence should be characterized by the nonlinear spectral scaling of the frequency and wave-number since highly complex nonlinearities make it significantly different from the linear theory. A fluid example is the well-known Kolmogorov power-law scaling of turbulent flows ^[11]. A typical counterpart in strong plasma turbulence is estimated roughly by Hasegawa and Mima (HM) based on three-wave interaction ^[12], which shows some deviation from the usual Kolmogorov power-law featured by a factor $k^{1.8}/(1+k^2)^{2.2}$. Recently a theoretical derivation based on Hasegawa-Wakatani (HW) turbulence model ^[13] predicts a wave-number spectrum featured by $e^{-\lambda k} k^{-3}/(1+k^2)^2$, which is also compared with the experimental observation ^[14]. Here λ is determined by the growth-damping profile, which represents the dissipation and the ZF dynamics. Hence the wave-number spectral scaling is of much importance in characterizing the turbulence structure and understanding the complex nonlinear interaction between the turbulent fluctuations and flows.

In this work, we present the wave-number spectral scaling of both ITG and ETG turbulence based on gyrofluid simulations. The underlying physical mechanism behind the scaling law is analyzed considering the back-reaction of the LSSs onto the ambient turbulence. The comparison between the ITG and ETG turbulence spectra is carried out to clarify the role of the LSSs in forming the spectral scaling law of the drift wave turbulence. In Sec.II the physical model and numerical setting of 3D gyrofluid simulations are described in slab geometry. The understanding of the back reaction of the ZFs onto the ambient ITG turbulence is proposed through the feature of the spectral scaling in Sec.III. The spectral analysis of the ETG turbulence is given in Sec. IV. Finally the principal results are summarized in Sec. IV.

2. Gyrofluid model of drift wave turbulence simulations

Electrostatic ITG and ETG turbulence is of a perfect isomorphism except for different response of the adiabatic component to the ZFs. To investigate the fundamental spectral characteristics of the drift wave-ZF turbulence, the nonlinear evolution of ITG and ETG [or $\eta_{i,e}(=d \ln T_{i,e}/d \ln n)$] modes, typical drift wave fluctuations in tokamak plasmas, are simulated in sheared slab configuration for simplicity so that the simulation results can be compared with some theoretical prediction, which is usually derived from the HM or HW turbulence ^[12-14]. Here a set of modeling equations describing the ITG-ZF dynamics with adiabatic electron response is described as follows, i.e. ^[15],

$$\left(-\delta - \nabla_{\perp}^2 \right) \phi = - \left(1 + K \nabla_{\perp}^2 \right) \psi \phi - \nabla_{\parallel} v_{\parallel} + \left[\phi, \nabla_{\perp}^2 \phi \right] - \partial_x \bar{\phi} \partial_y \phi - \mu_{\perp} \nabla_{\perp}^4 \phi, \quad (1)$$

$$\partial_t v_{||} = -\nabla_{||}\phi - \nabla_{||}p - [\phi, v_{||}] + \eta_{\perp}\nabla_{\perp}^2 v_{||} \quad , \quad (2)$$

$$\partial_t p = -K\partial_y\phi - (\Gamma - 1)\sqrt{8/\pi}|k_{||}|(p - \phi) - \Gamma\nabla_{||}v_{||} - [\phi, p] + \chi_{\perp}\nabla_{\perp}^2 p \quad . \quad (3)$$

Here $\nabla_{\perp}^2 = \partial_{xx}^2 + \partial_{yy}^2$, $\nabla_{||} = ik_{||} = \partial_z + \hat{s}x\partial_y$ with magnetic shear $\hat{s} = L_n/L_s$, $L_{n,s}$ are the characteristic length of plasma density and magnetic field, respectively. $K = 1 + \eta_i$, $\Gamma = 5/3$. The term with $\partial\bar{\phi}/\partial x$ in Eq.(1) is from the correct adiabatic electron response to the self-generated ZFs in ITG turbulence. $\delta = 1$ is for ZF component and $\delta = 0$ for fluctuations^[16]. The Poisson brackets $[f, g] = \hat{z} \cdot \nabla_{\perp} f \times \nabla_{\perp} g = \partial_x f \partial_y g - \partial_x g \partial_y f$ indicate the $\vec{E} \times \vec{B}$ convective nonlinear terms. The Landau damping is represented by closure model $q_{||} = -i\sqrt{8/\pi}k_{||}T/|k_{||}|$ (Ref.17). The cross-field dissipation terms with μ_{\perp} , η_{\perp} and χ_{\perp} are included to absorb the energy at short wavelength range^[18]. \bar{x} and \bar{y} correspond to the radial and poloidal directions in a toroidal plasma, respectively. The perturbed quantities are conventionally normalized at ion-scale^[15]. The modeling equations for the ETG version are similar in form with corresponding normalization at electron-scale and the adiabatic response^[5].

The nonlinear equations (1-3) can be numerically solved by using an initial value code, in which Fourier spectral decomposition in both y and z directions and an implicit finite difference scheme for x variable are employed. The details of the code have well documented in previous publication^[5,15]. 3D simulation is bounded in domain (L_x, L_y, L_z) with reference parameters typically: $\eta_i = 2.5$, $\hat{s} = 0.4$, $\mu_{\perp} = \eta_{\perp} = \chi_{\perp} = 0.1$, $L_x = 50\rho_i \sim 200\rho_i$, $L_y = 10\pi\rho_i$, $L_z = 2\pi L_n$. The resolution and maximum wave-numbers of k_y in the simulations are $\Delta k_y = 0.2$ and $k_y^{Max} = 3.0$, respectively.

3. Spectral scaling of ITG-ZF turbulence

It is well-known that the ZF in ITG turbulence is robust so that the ambient turbulence and ion heat transport are evidently suppressed^[3]. While the suppression mechanism is usually understood through the flow shearing of the fluctuation, here we investigate the wave-number spectral characteristics under the back reaction of the ZFs to clarify the underlying interaction processes between the ZFs and turbulence. Fig.1 illustrates the k_x and k_y spectra of both the ITG-ZF turbulence and the ITG turbulence with artificially excluding the ZFs (hereafter referred to as ITG-no-ZF) for comparison. Simulations reveal several typical features^[19]. First the k_x spectrum of ITG-ZF turbulence fits well with an exponential-law function, i.e., $\langle\phi^2/2\rangle_E = Be^{-\lambda k_x}$, at short wavelength regime $k_x \geq 1.0$, while the counterpart in ITG-no-ZF turbulence is described by a Kolmogorov-like power-law function $\langle\phi^2/2\rangle_P = Ak_x^{-\alpha}/(1+k_x^2)^2$. Second the k_y spectra of both ITG-ZF and ITG-no-ZF turbulence are characterized by a pure

power-law scaling $\langle \phi^2 / 2 \rangle_P \propto k_y^{-\beta}$ with different slope index. Here (λ, α, β) are slope index factors. Furthermore, parametric scans of the k_x spectral scaling laws show better agreement with the fitting functions for the ITG-ZF turbulence with weak magnetic shear, low viscosity damping and strong drive force η_i , as shown in Fig.2 as an example of the η_i scan, in which the ZF is stronger.

The comparison of the k_x spectral characteristics in ITG-ZF and ITG-no-ZF turbulence and the comparison between k_x and k_y spectra in ITG-ZF turbulence may exhibit the back reaction mechanism of the ZFs onto the ambient turbulence since the ZF has only radial k_q spectrum. It could be understood that the ZFs may subsequently scatter the ITG spectrum from the most unstable range of $k_x \leq 1.0$ to the short wavelengths $k_x \approx 1.0 \sim 3.0$ through the nonlinear three-wave coupling with $k_{x2} = k_{x1} + k_q$. Then the k_x spectrum of the ITG-ZF turbulence is deformed at short wavelengths. The spectral scattering by the ZFs through $k_{x2} = k_{x1} + k_q$ can transfer the free energy of the ITG instability to the dissipation range. As a result, the total free energy, on one hand, is damped versus the viscosity, showing a dramatic suppression of ITG fluctuations. On the other hand, the subsequent ZF spectral scattering play a driving role in transferring the free energy to larger k_x range. Hence the k_x spectrum of the ITG turbulence could be featured by an exponential-law deformed from a Kolmogorov-like power-law under the back reaction of the ZFs.

4. Spectral scaling of ETG-ZF-KH turbulence

Generally speaking, the ZFs are relatively weak in ETG turbulence compared with those in ITG turbulence except for the weak magnetic shear case^[20]. It has been demonstrated that weak shear can enhance the ZF generation in ETG turbulence, which is saturated by the excitation of long wavelength KH mode. In this sense, the ETG turbulence is a mixture of ETG, ZFs and KH fluctuations. To understand the nonlinear interaction among them and further clarify the deformation mechanism of spectral scaling law due to the back reaction of the LSSs in k_x or k_y direction, 3D ETG simulation is performed with weak magnetic shear and larger η_e . Simulations show that after the ETG saturation, the ZF starts to grow up exponentially with small growth rate. The KH mode is then excited to saturate the ZFs when the ZF amplitude becomes higher than a threshold. The wave-number spectra at the quasi-steady state are plotted in Fig.3. A mixing Kolmogorov-like power-law and exponential-law scaling for both k_x and k_y spectra is observed in ETG-ZF-KH turbulence. It is noticed that this spectral scaling law is qualitatively in agreement with the theoretical prediction based on a Hasegawa-Wakatani turbulence model^[14]. In ETG-no-ZF turbulence, the k_x spectrum is characterized by Kolmogorov-like power-law scaling and the k_y spectrum fits with a power-law scaling. This can be understood as the back

reaction of the weaker ZFs and the KH mode in the k_x direction and the spectral scattering by the KH mode in the k_y direction.

To further manifest the back reaction interaction process, a 2D simulation with very high resolution in the y direction is performed as shown in Fig.4, in which the KH mode is slowly excited ^[21]. During the KH evolution from the creation to the saturation in ETG-ZF turbulence, the k_y spectral characteristic is changing from an approximate Kolmogorov power-law to a mixing Kolmogorov-like power-law and exponential-law scaling as shown in Fig.5. These evidences positively support the underlying mechanism behind the spectral scaling laws.

5. Summary

The wave-number spectral characteristics of the drift wave micro-turbulence at ion and electron scales have been investigated based on 3D gyrofluid simulation with an emphasis on the back reaction mechanism of the self-generated LSSs onto the ambient turbulence. It is found that the k_x spectrum of the ITG-ZF turbulence is fitted well by an exponential-law scaling, which is deformed from the usual Kolmogorov-like power-law by the back reaction of the robust ZFs through the spectral scattering. On the other hand, the ETG turbulence with ZFs and long wavelength KH fluctuation is characterized by a mixing Kolmogorov-like power-law and exponential-law scaling for both k_x and k_y spectra due to the back reaction of both the ZFs and KH mode. These observations are qualitatively in agreement with the theoretically predicted spectral scaling in drift wave turbulence based on a reduced turbulence modeling analysis and fairly match with the experimental observation of the density fluctuation spectrum in Tore Supra tokamak ^[22]. Hence, they may be likely applied to the data analyses of turbulence and flow measurement in tokamak experiments.

Acknowledgement

This work was supported by the Grant-in-Aid from JSPS (No. 19560828 and No. 21340171). It was also partially supported by the JSPS-CAS Core University program in the field of ‘Plasma and Nuclear Fusion’.

References

- 1 Fujisawa A 2003, Plasma Phys. Control. Fusion, 45: R1
- 2 Tynan G R, Fujisawa A, McKee G 2009, Plasma Phys. Control. Fusion, 51: 113001
- 3 Diamond P, Itoh S-I, Itoh K, Hahm T S 2005, Plasma Phys. Control. Fusion, 47: R35
- 4 Fujisawa A 2009, Nucl. Fusion, 49: 013001
- 5 Li Jiquan, Kishimoto Y 2004, Phys. Plasmas, 11: 1493
- 6 Horton W 1999, Rev. Mod. Phys., 71: 735
- 7 Lin Z, Hahm T S, Lee W W, et al. 1998, Science, 281: 1835
- 8 Chen L, Lin Z, White R 2000, Phys. Plasmas, 7: 3129
- 9 Smolyakov S I, Diamond P H, Malkov M 2000, Phys. Rev. Lett., 84: 491
- 10 Yu C, Brower D L, Zhao S, et al. 1992, Nucl. Fusion, 32: 1545
- 11 Frisch U 1995, Turbulence: the legacy of N. A. Kolmogorov, Cambridge University Press
- 12 Hasegawa A, Mima K 1977, Phys. Rev. Lett., 39: 205
- 13 Hasegawa A, Wakatani M 1987, Phys. Rev. Lett., 59: 1581
- 14 Gurcan O D, Garbet X, Hennequin P, et al. 2009, Phys. Rev. Lett., 102: 255002
- 15 Li Jiquan, Kishimoto Y 2003, Phys. Plasmas, 10: 683
- 16 Dorland W 1993, Ph.D. thesis, Princeton University
- 17 Hammett G W, Perkins F W 1990, Phys. Rev. Lett., 64: 3019
- 18 Horton W, Estes R D, Biskamp D 1980, Plasma Phys., 22: 663
- 19 Li Jiquan, Kishimoto Y 2010, Phys. Plasmas, 17, 072304
- 20 Li Jiquan, Kishimoto Y 2005, Phys. Plasmas, 12, 054505
- 21 Li Jiquan, Uzawa K, Lin Z, et al. 2006, Fusion Energy 2006: Proc. 21th Int. Conf. (Chengdu, 2006) (Vienna: IAEA) CD-ROM file TH/2-3
- 22 Hennequin P, Sabot R, Honore C, et al., Plasma Phys. Controlled Fusion, 46: B121

Figures and Captions

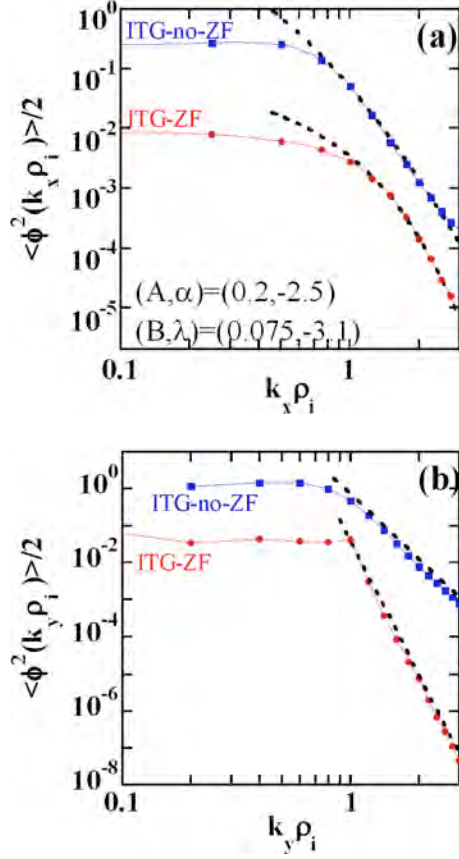


Fig.1 k_x (a) and k_y (b) spectra of both the ITG-no-ZF and the ITG-ZF turbulence. The dashed curves in (a) plot corresponding fitting functions $\langle \phi^2/2 \rangle_P = Ak_x^{-\alpha}/(1+k_x^2)^2$ and $\langle \phi^2/2 \rangle_E = Be^{-\lambda k_x}$. The dot straight lines in (b) are for reference.

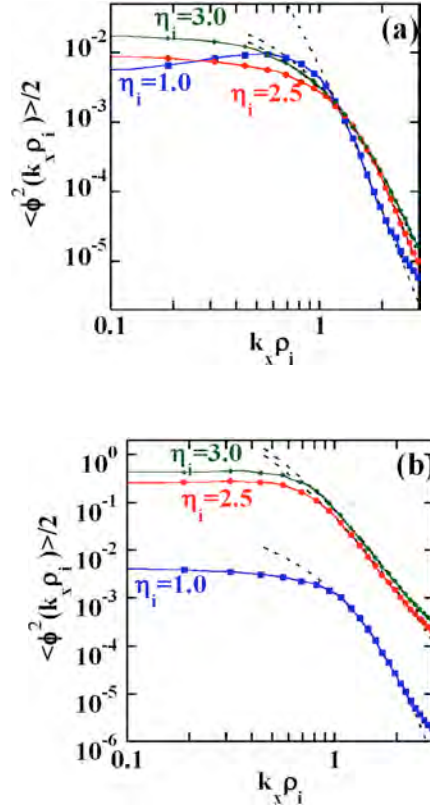


Figure 2: k_x spectra of both the ITG-ZF (a) and the ITG-no-ZF (b) turbulence for different η_i . The dashed curves plot corresponding best fitting functions $\langle \phi^2/2 \rangle_E = Be^{-\lambda k_x}$ in (a) and $\langle \phi^2/2 \rangle_P = Ak_x^{-\alpha}/(1+k_x^2)^2$ in (b). $\hat{s} = 0.2$, $\mu_{\perp} = 0.1$.

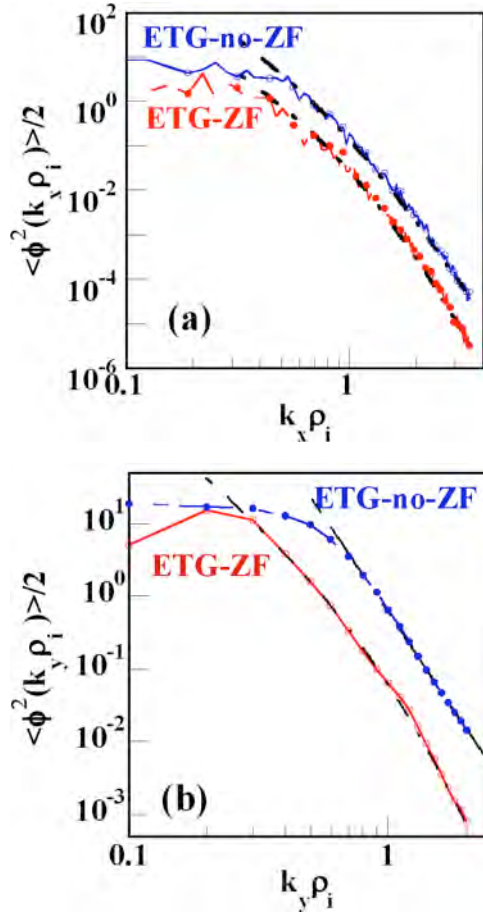


Fig.3 k_x (a) and k_y (b) spectra of both the ETG-ZF and the ETG-no-ZF turbulence. The dot-dashed curves matching with the spectra in ETG-ZF turbulence in both (a) and (b) plot corresponding best fitting functions $\langle \phi^2/2 \rangle_P = A e^{-\lambda k_{x,y}} k_{x,y}^{-\alpha} / (1 + k_{x,y}^2)^2$ and the one to the ETG-no-ZF case in (a) corresponds to the best fitting function $\langle \phi^2/2 \rangle_P = A k_x^{-\alpha} / (1 + k_x^2)^2$. The dashed straight line in (b) represents the power-law function $\langle \phi^2/2 \rangle_P \propto k_y^{-\alpha}$ for reference.

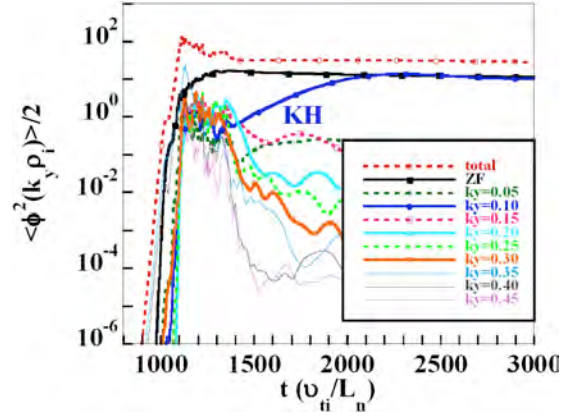


Fig.4 Time history of fluctuation energy $\langle \phi^2 \rangle / 2$ of representative k_y components in 2D ETG-ZF turbulence with high resolution. $\hat{s} = 0.1$, $\eta_i = 5.5$, $\mu_{\perp} = 1.5$, $L_x = 400 \rho_e$, $L_y = 160 \pi \rho_e$.

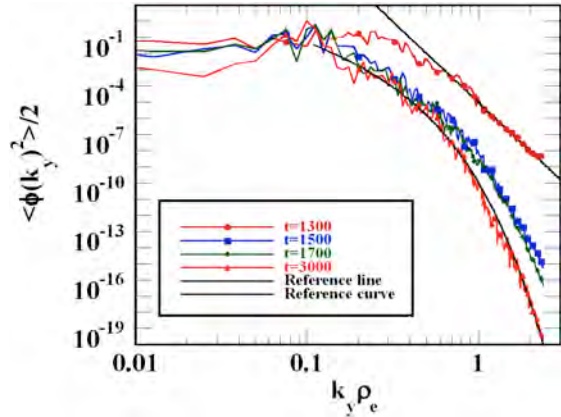


Fig.5 Time evolution of k_y spectrum in ETG-ZF turbulence of Fig.4. The change of the spectral scaling law is due to the KH creation after $t \approx 1500$.

Zonal flow modes in a tokamak plasma with dominantly poloidal mean flows

Deng Zhou , Dehui Li

Institute of Plasma Physics, Chinese Academy of Sciences, Hefei 230031, P. R. China
Centre for Magnetic Fusion Theory, Chinese Academy of Sciences, Hefei 230031, P. R. China

Abstract

The zonal flow eigenmodes in a tokamak plasma with dominantly poloidal mean flows are theoretically investigated, using different state equations. It is found that the frequencies of both the geodesic acoustic mode and the sound wave increase with respect to the poloidal Mach number. In contrast to the pure standing wave form in static plasmas, the density perturbations consist of a standing wave superimposed with a small amplitude traveling wave in the poloidally rotating plasma. A finite frequency for usual low frequency zonal flow is acquired proportional to the poloidal Mach number using the adiabatic perturbation, while for isothermal assumption of temperature, the frequency remains to be 0.

1. Introduction

Zonal flows (ZFs) have been under active investigations in the past decade, in theory and simulations as well as in experiments. ZFs are electrostatic modes which are symmetric at both poloidal and toroidal directions. They are excited and pumped by the nonlinear interaction of drift wave turbulence and they play an important role in regulating the transport of tokamak plasmas^{1,2}. In tokamak plasmas, there exist two different types of zonal oscillations, the usual low frequency zonal flow (LFZFs) with $\omega \sim 0$ and a high frequency oscillation, called geodesic acoustic modes (GAMs)³, with $\omega \sim c_s / R$, c_s the sound speed. The eigenmode analysis of ZFs in static plasmas has been carried out by many authors from different aspects³⁻⁷.

Plasma equilibrium flow or rotation seems an intrinsic phenomenon in tokamaks. The toroidal rotation can be driven by input of momentum or produced intrinsically even without momentum sources. Normally, the research is concentrated on the effect of toroidal plasma flows. Recently, ZFs induced in a toroidally rotating tokamak plasma were investigated by Wang⁸ under the electrostatic limit and separately by Wahlberg^{9,10} considering the ideal MHD electromagnetic perturbation using the Lagrangian representation¹¹. They discovered some new features of the zonal flow modes in toroidally rotating plasmas: The frequencies of the usual GAMs increase with respect to the sonic Mach number, a finite frequency of LFZFs is acquired due to the nonuniform density on flux surfaces plus the centrifuge forces, and the density perturbation takes the form of a traveling wave in rotating plasmas instead of the

standing wave form in static plasmas, etc.

It is widely believed that a poloidal plasma equilibrium flow may exist in tokamak plasmas due to strong radial electric field, Stringer spin-up effect and external momentum input, etc¹²⁻¹⁵. Hence, it is worthwhile considering the effect of a poloidal plasma flow on all kinds of plasma modes in tokamaks. Recently, Pamela *et al*¹⁶ investigated the influence of poloidal rotation on the edge localized modes.

In this work, we investigate the the zonal flow eigenmodes in a tokamak plasma with a dominantly poloidal mean flow. We consider a large aspect ratio tokamak with circular concentric magnetic surface. The poloidal Mach number $M_p = \frac{B_r u_p}{B_p c_s}$ is less than unity, where $c_s = (T/M)^{1/2}$ is sound speed. We employ the usual Euler description for perturbations. The method adopted is that given in by Wang⁸, in which no magnetic effect was included.

In Sec. 2, the equilibrium quantities are derived for a tokamak plasma with a dominantly poloidal flow. The dispersion relation of the zonal flow modes are derived and analyzed in Sec. 3. A summary is presented in Sec. 4.

2. Equilibrium Quantities for A Tokamak Plasma With A Dominantly Poloidal Mean Flow

In this section, we present the equilibrium quantities in a large aspect ratio circular cross section tokamak plasma. These quantities, which have been derived by Hassam¹², will be used in the following section in linearization of basic equations.

The axisymmetric magnetic field is written as

$$\mathbf{B} = \nabla\phi \times \nabla\psi + B_r R \nabla\phi \quad (1)$$

where ψ labels a magnetic surface, ϕ is the toroidal angle and B_r denotes the toroidal magnetic field. In the MHD limit, the general form of the flow velocity in a tokamak is written in the form^{12,17}

$$\mathbf{u} = \rho^{-1} K(\psi) \mathbf{B} + \Phi' R^2 \nabla\phi \quad (2)$$

where $\rho(\psi, \theta)$ is the mass density, $K(\psi)$ and $\Phi' = d\Phi/d\psi$ are functions of ψ . This form of the flow velocity satisfies two equations

$$\partial\rho/\partial t = \nabla \cdot \rho\mathbf{u} \quad (3a)$$

$$\mathbf{u} \times \mathbf{B} = \nabla\Phi \quad (3b)$$

Eq. (3b) means that the inertia term and the diamagnetic effect have been neglected. This is a good approximation for the MHD assumption. However, in the following Eq. (4), the inertia term and the pressure gradient term should be kept since the electric drift is ambipolar and do not contribute to current, the three terms in Eq. (4) are in the same order.

Normally, the toroidal velocity given by Eq. (2) is much higher than the poloidal velocity since $B_r \gg B_p$ unless the second term on the right hand side of Eq. (2) almost cancels the toroidal component of the first term which is the very case we are considering in the present work. Anyway, the toroidal velocity never disappears.

We consider a large aspect ratio tokamak with circular concentric flux surfaces. The

inverse aspect ratio $\varepsilon = r/R \ll 1$. We write the velocity $\mathbf{u} = u_p \hat{\theta} + u_r \hat{\phi}$, where $\hat{\theta}$ ($\hat{\phi}$) denotes the unit vector along the poloidal (toroidal) direction. We introduce the ordering $u_p \sim u_r \sim B_p c_s / B_T$, and the plasma pressure ratio $\beta \sim \varepsilon^2$. In these low beta plasmas, magnetic effect can be readily neglected.

The MHD equilibrium equation with a mass flow is given by

$$\rho \mathbf{u} \cdot \nabla \mathbf{u} = -\nabla p + \mathbf{j} \times \mathbf{B} \quad (4)$$

Scalar product of Eq. (4) with \mathbf{B} yields

$$(T / M_i) \ln \rho + u^2 / 2 - R \Phi' u_r = H(\psi) \quad (5)$$

We have assumed that the temperature is isothermal on each flux surface. Scalar product of Eq. (4) with $\nabla \phi$ yields

$$R B_T - K R u_r = I(\psi) \quad (6)$$

Multiplying Eq. (4) scalarly by $\nabla \psi$, we obtain the generalized Grad-Shafranov equation which is lengthy and is not written out. Using the introduced flux surface functions $K(\psi)$, $\Phi'(\psi)$, $I(\psi)$, $H(\psi)$ and $T(\psi)$, the Grad-Shafranov equation can be solved to give all equilibrium quantities. However, for the large aspect ratio low beta plasma we are concerned with in this paper, there is no need to solve the Grad-Shafranov equation. An analytical equilibrium calculation with poloidal flows was recently given by Ito *et al.*¹⁸

Using the ordering assumptions, we obtain from Eq. (6)

$$R B_T = I(\psi) + O(\varepsilon^3) \quad (7)$$

Substituting this equation into the toroidal velocity

$$u_r = \rho^{-1} K B_T + R \Phi' \quad (8)$$

To the leading and the next order, we obtain

$$R_0 \Phi'(\psi) + \rho_0^{-1} K(\psi) B_0 = 0 \quad (9a)$$

$$R_0 u_r + (K I / \rho_0)(\rho_1 / \rho_0) = 2 R_0 r \cos(\theta) \Phi' \quad (9b)$$

where $\rho = \rho_0(\psi) + \rho_1(\psi, \theta)$.

The leading and the next order components of Eq. (5) reads

$$c_s^2 \ln \rho_0 = H(\psi) \quad (10a)$$

$$c_s^2 (\rho_1 / \rho_0) - \Phi' R_0 u_r = 0 \quad (10b)$$

From Eqs. (9b) and (10b), we obtain

$$\rho_1 / \rho_0 = \frac{2 R_0 r \cos(\theta) \Phi'^2}{c_s^2 (1 - M_p^2)} \sim \varepsilon \quad (11)$$

where $M_p = \frac{B_T u_p}{B_p c_s}$ is the poloidal Mach number. Eq. (9a) can be written as

$R_0 \Phi'(\psi) \sim -\rho_0^{-1} K(\psi) B_0 \sim -u_p B_T / B_p$. Applying this relation into Eq. (11) leads to

$$\rho_1 / \rho_0 = \frac{2M_p^2 \varepsilon}{1 - M_p^2} \cos(\theta) \quad (12)$$

and from Eq. (10b), the toroidal velocity can be explicitly written as

$$u_T = u_{T0} - \frac{2q}{1 - M_p^2} u_p \cos(\theta) = u_{T0} - 2\hat{q}u_p \cos(\theta) \quad (13)$$

We have introduced a symbol $\hat{q} = \frac{q}{1 - M_p^2}$ for the convenience of expression in the

following section. u_{T0} is the θ -independent part of the toroidal velocity, it is actually the left hand side of Eq. (9a) and of order u_p . Contribution from this term is negligible in the following analysis.

In Eqs. (12) (13), it is obvious that a singularity appears for $M_p \sim 1$. There is a resonance occurring called sonic resonance¹². To avoid such a resonance, we only consider the cases $M_p < 1$ in the present work.

2. DERIVATION AND ANALYSIS OF DISPERSION RELATION

The basic equations to start are

$$\frac{d\rho}{dt} + \rho \nabla \cdot \mathbf{v} = 0 \quad (14a)$$

$$\rho \frac{d\mathbf{v}}{dt} = -\nabla p + \mathbf{j} \times \mathbf{B} \quad (14b)$$

$$\frac{d}{dt} (p\rho^{-\gamma}) + \frac{2}{3} \rho^{-\gamma} \nabla \cdot \mathbf{q} = 0 \quad (14c)$$

$$\mathbf{E} + \mathbf{v} \times \mathbf{B} = 0 \quad (14d)$$

In which all the symbols are well known. Considering an electrostatic perturbation of the form $\tilde{\mathbf{E}} = -\nabla \tilde{\Phi}(\psi)$, linearizing Eqs. (14) and neglecting terms of higher order in $O(\varepsilon)$, we obtain

$$\frac{\partial \tilde{\rho}}{\partial t} + \rho \nabla \cdot \tilde{\mathbf{v}} + \tilde{\mathbf{v}} \cdot \nabla \rho + \mathbf{u} \cdot \nabla \tilde{\rho} = 0 \quad (15a)$$

$$\rho \left[\frac{\partial \tilde{\mathbf{v}}}{\partial t} + \mathbf{u} \cdot \nabla \tilde{\mathbf{v}} + \tilde{\mathbf{v}} \cdot \nabla \mathbf{u} \right] = -\nabla \tilde{p} + \tilde{\mathbf{j}} \times \mathbf{B} \quad (15b)$$

$$\frac{\partial \tilde{p}}{\partial t} + \tilde{\mathbf{v}} \cdot \nabla p + \mathbf{u} \cdot \nabla \tilde{p} - c_s^2 \left(\frac{\partial \tilde{\rho}}{\partial t} + \tilde{\mathbf{v}} \cdot \nabla \rho + \mathbf{u} \cdot \nabla \tilde{\rho} \right) + \frac{2}{3} \nabla \cdot \mathbf{q} = 0 \quad (15c)$$

$$\tilde{\mathbf{v}} \times \mathbf{B} = \nabla \tilde{\Phi}(\psi) \quad (15d)$$

where a tilde denotes perturbation and symbols without a tilde denote equilibrium quantities. The perturbed velocity can be written in the form $\tilde{\mathbf{v}} = v_{\parallel}(\theta, \psi) \mathbf{b} + v_{\theta}(\psi) \hat{\theta}$ in a large aspect

ratio approximation. Taking each perturbation as the summation of the cosine and sin components, $\tilde{A} = A_s \sin(\theta) + A_c \cos(\theta)$, and assuming the time dependence of the perturbation $\sim e^{-i\omega t}$, Eqs. (15) are reduced to

$$i\Omega \hat{N}_s + M_p N_c + \frac{v_{\parallel c}}{c_s} + 2\hat{q} \frac{v_\theta}{c_s} = 0, \quad (16a)$$

$$M_p \hat{N}_s - i\Omega N_c + \frac{v_{\parallel s}}{c_s} = 0, \quad (16b)$$

$$\frac{\hat{P}_c}{c_s^2} + i\Omega \frac{v_{\parallel s}}{c_s} + M_p \frac{v_{\parallel c}}{c_s} - 2\hat{q} M_p v_\theta = 0, \quad (16c)$$

$$\frac{\hat{P}_s}{c_s^2} + M_p \frac{v_{\parallel s}}{c_s} - i\Omega \frac{v_{\parallel c}}{c_s} = 0, \quad (16d)$$

$$-q \frac{\hat{P}_s}{c_s^2} + i\Omega \frac{v_\theta}{c_s} = 0. \quad (16e)$$

$$-i\Omega \hat{N}_s - M_p N_c + i\Omega \frac{\hat{P}_s}{c_s^2} + M_p \frac{P_c}{c_s^2} + 2\tilde{q} M_p^2 \left(\frac{1}{\gamma} - 1 \right) \frac{v_\theta}{c_s} = 0 \quad (16f)$$

$$M_p \hat{N}_s - i\Omega N_c - M_p \frac{\hat{P}_s}{c_s^2} + i\Omega \frac{P_c}{c_s^2} = 0 \quad (16g)$$

We obtain Eqs (16c) and (16d) by taking the parallel component of Eq. (15b), and obtain Eq. (16e) by surface-averaging the geodesic component of Eq. (15b). We have introduced $\Omega = qR\omega/c_s$, $\hat{N} = \tilde{\rho}/\rho = N_s \sin(\theta) + N_c \cos(\theta)$, $\hat{p} = \tilde{p}/\rho$ and $c_s = (\gamma p/\rho)^{1/2}$. We have set $\nabla \cdot \mathbf{q} = 0$. For $\lambda = 5/3$, we have the usual adiabatic case of ideal gases. Setting the coefficient determinant of Eqs. (16) to be 0, we obtain the dispersion relation

$$\Omega \left(\Omega^2 - M_p^2 \right) \left[\Omega^4 - 2 \left(1 + q\hat{q} + M_p^2 \right) \Omega^2 + \left(1 - M_p^2 \right)^2 + 2q\hat{q} \left(1 + M_p^2 \right) + 4q\hat{q} M_p^2 \right] = 0. \quad (17)$$

The roots are given as

$$\Omega = 0, \quad (18a)$$

$$\Omega = \pm M_p \quad (18b)$$

$$\Omega^2 = 1 + q\hat{q} + M_p^2 \pm \sqrt{(q\hat{q})^2 + 4M_p^2 - 4q\hat{q}M_p^2}. \quad (18c)$$

The first one is the low frequency zonal flow branch with eigenfunctions $v_{\parallel c} \neq 0, v_\theta \neq 0$ and $\hat{N}_c \sim M_p$. Eq. (18b) is a new branch of LFZFs induced by the poloidal rotation, similar to the case in toroidal rotating plasmas. Eq. (18c) gives two solutions corresponding to the usual GAMs (+) and the sound wave (SWs) branch (-) observed in static plasmas. The frequencies become higher than that in static plasmas and the perturbed

densities are also modified. A cosine component of the density perturbation proportional to M_p appears in GAMs, as given by

$$\hat{N}_c = \frac{iM_p (1 + \Omega^2 - M_p^2 - 2q\bar{q})}{\Omega(1 - \Omega^2 + M_p^2)} N_s. \quad (19)$$

and a sin component in SWs by

$$\hat{N}_s = \frac{-i2M_p\Omega}{1 - \Omega^2 - M_p^2 + 2q\bar{q}} N_c. \quad (20)$$

In Fig.1 to Fig. 4, the frequencies of GAMs and SWs as well as the ratio between the sine and cosine components of density perturbation are plotted as functions of poloidal mach number M_p . Significant increases of frequencies are observed with respect to M_p . A small cosine (sin) component of density perturbation is present when $M_p > 0$ for GAMs (SWs), although it is zero in static plasmas. The density perturbation is a standing wave superimposed with a small amplitude traveling wave. To see more clearly, we write the density perturbation, e. g., for the GAMs

$$\begin{aligned} \hat{N} &= N_s \sin \theta e^{-i\omega t} + N_c \cos \theta e^{-i\omega t} \\ &= \hat{N}_s (1 - A) \sin \theta e^{-i\omega t} + A N_s e^{-i(\omega t + \theta - \pi/2)} \end{aligned} \quad (21)$$

with A the ratio between the amplitudes of the cosin and sin components.

If we taken the isothermal assumption for temperature, *i. e.* $\tilde{p} = T\tilde{\rho}/M_i$, then Eq.(16f) and Eq.(16g) give an identity since $\gamma = 1$. Then the solution Eq.(18b) is not necessarily assured. The LFZFs remain unchanged. The validity of the isothermal assumption for temperature is confirmed by the recent experimental observations²⁰.

3. SUMMARY AND DISCUSSION

In the present work, we investigated the axisymmetric electrostatic oscillations in tokamak plasmas with a dominantly poloidal equilibrium flow. In the MHD limit, the steady flow in a tokamak is given in the form of Eq. (2). In this form, a pure poloidal flow can never be achieved since the toroidal flow can never disappear. If the toroidal and poloidal flow velocities are comparable, the toroidal flow is given in the form of Eq. (13), in which the poloidally uniform part has little contributions in our nanalysis. We derived the equilibrium quantities in section II. Then, in section III, the linear eigenmodes were considered starting from the single fluid ideal MHD equations.

The frequency of the usual LFZF modes keeps unchanged offr the isothermal cases. But a finite frequency is acquired for the LFZFs using the adiabatic perturbation. We further predict that the frequencies of usual GAMs and sound wave branches both increase with the poloidal Mach number. The density perturbations have the form of standing waves superimposed with a small amplitude traveling wave. It is worthwhile to investigate these new phenomena of ZFs

in the ZF-turbulence interactions, for example, the collisionless damping rate might be changed due to the increase of the GAM frequency, etc.

We did not consider the radial structure of ZFs in the present work. Generally, a continuous spectrum, analogous to the shear alfenic wave continuum, forms due to the radial inhomogeneities¹⁹. People have observed the frequency dependence on the radial profiles, consistent with the theoretical prediction, in numerous experiments²¹. The radial structure of the zonal flow eigenmodes can be identified only when the kinetic effects such as finite Larmor radius and finite orbit width effects are included¹⁹. This is an issue left for future work.

A large numbers of experiments aiming at detecting zonal flows have been carried out in most tokamak devices world-widely²¹. However, few experiments can supply data to test the theoretical prediction in the present work. In Ref. [22], the profiles of the poloidal velocity, the GAM frequency and the temperatures were given for an ASDEX discharge. Estimate using these data can not give unambiguous verification of the theory in this paper. More data are required for the prediction in our work to compare with experimental observations.

ACKNOWLEDGEMENT

This work is supported by China Natural Science Foundation under contract No. 10775137, by Ministry of Science and Technology of China under contract No. 2009GB105001 and partly by the JSPS-CAS Core-University Program in the field of Plasma and Nuclear Fusion. The author appreciate helpful discussions with Prof. M. Furukawa and Prof. S. Wang.

REFERENCES

- ¹P. H. Diamond, S. -I. Itoh, K. Itoh, and T. S. Hahm, Plasma phys. Contr. Fusion 47, R35 (2005).
- ²K. Itoh, S. -I. Itoh, P. H. Diamond, T. S. Hahm, A. Fujisawa, G. R. Tynan, M. Yagi M and Y. Nagashima, Phys. Plasmas 13, 055502 (2006).
- ³N. Winsor, J. L. Johnson, and J. M. Dawson, Phys. Fluids 11, 2448 (1968).
- ⁴Z. Gao, K. Itoh, H. Sanuki, and J. Q. Dong, Phys. Plasmas 15, 072511 (2008).
- ⁵T. Watari, Y. Hamada, A. Fujisawa, K. Toi, and K. Itoh, Phys. Plasmas 12, 062304 (2005).
- ⁶D. Zhou, Phys. Plasmas 14, 104502 (2007).
- ⁷A. I. Smolyakov¹, C. Nguyen, and X. Garbet, Plasma Phys. Control. Fusion 50, 115008 (2008).
- ⁸S. Wang, Phys. Rev. Lett. 97, 085002 (2006); 97, 129902 (2006).
- ⁹C. Wahlberg, Phys. Rev. Lett. 101, 115003 (2008).
- ¹⁰C. Wahlberg, Plasma phys. Contr. Fusion 51,085006 (2009).
- ¹¹E. Frieman and M. Rotenberg, Rev. Mod. Phys. 32, 898 (1960).
- ¹²A. B. Hassam, Nucl. Fusion 36, 707 (1996).

- ¹³A. B. Hassam, and J. F. Drake, Phys. Fluids B 5,4022 (1993).
- ¹⁴F. L. Hinton, J. Kim, Y. -B. Kim, A. Brizard, and K. H. Burrell, Phys. Rev. Lett. 72, 1216 (1994).
- ¹⁵T. E. Stringer, Phys. Rev. Lett. 22,770 (1969).
- ¹⁶S. Pamela, G Huysmans¹, and S Benkadda, Plasma Phys. Control. Fusion 52, 075006 (2010).
- ¹⁷E. Hameiri, Phys. Fluids 26, 230 (1983).
- ¹⁸A. Ito, and N. Nakajima, Plasma Phys. Control. Fusion 51, 035007 (2009).
- ¹⁹F. Zonca, and L. Chen, Europhys. Lett. 83, 35001 (2008).
- ²⁰R. Nazikian, G.Y. Fu, M. E. Austin, H. L. Berk, R.V. Budny, N. N. Gorelenkov, W.W. Heidbrink, C. T. Holcomb, G. J. Kramer, G. R. McKee, M. A. Makowski, W. M. Solomon, M. Shafer, E. J. Strait, and M. A. Van Zeeland, Phys. Rev. Lett. 101, 185001 (2008).
- ²¹A. Fujisawa, Nucl. Fusion 49, 013001 (2009).
- ²²G D Conway, B Scott, J Schirmer, M Reich, A Kendl, and the ASDEX Upgrade Team, Plasma Phys. Control. Fusion 47, 1165 (2005).

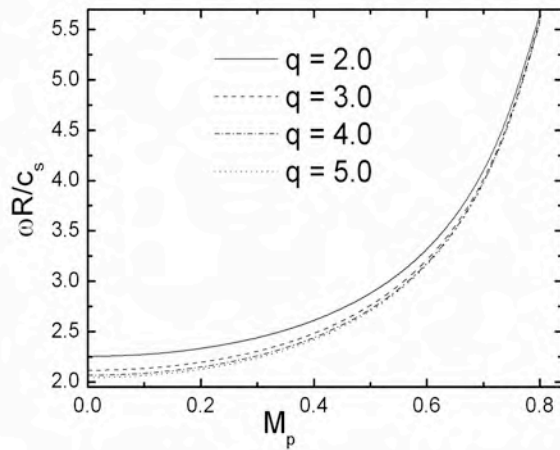


Fig. 1 The frequencies of GAMs plotted with respect to the poloidal Mach number for different safety factor

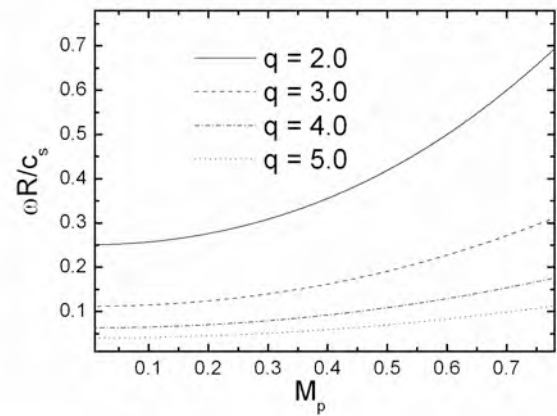


Fig. 2 The frequencies of the sound wave branch plotted with respect to the poloidal Mach number for different safety factor

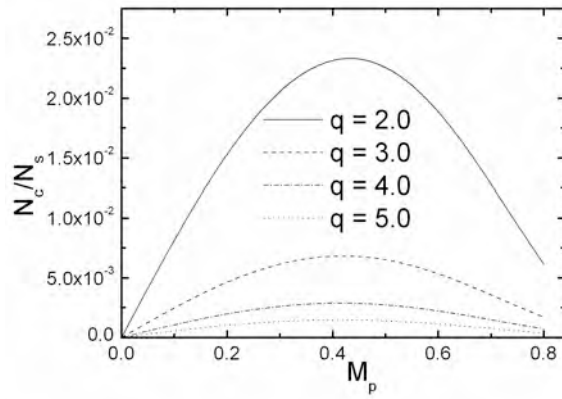


Fig. 3 The ratio between the sin and cosine components of density perturbation for GAMs

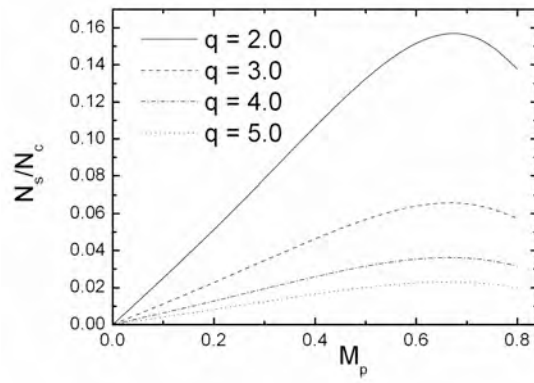


Fig. 4 The ratio between the cosine and sin components of density perturbation for SWs

Magnetic islands caused by microturbulence

A. Ishizawa* and N. Nakajima

National Institute for Fusion Science, Toki 509-5292, Japan.

(Dated: September 21, 2010)

Abstract

The process of magnetic island formation due to ion-temperature gradient (ITG) driven turbulence in a slab plasma is studied by means of numerical simulations of reduced two-fluid equations. ITG turbulence, which is a drift-wave turbulence, produces long-wavelength magnetic islands, even if the initial state is stable against tearing modes. Despite of the fact that the ITG is a short-wavelength instability, the length of magnetic islands is the same order as the system size. The island formation process is examined for several stability parameters of tearing modes. The long-wavelength magnetic islands are formed by merging of small-scale magnetic islands. Turbulent mixing due to electrostatic potential perturbation and electron pressure perturbation play a role in the formation process of the long-wavelength islands, however, the effect is not much stronger than the normal resistive diffusion. These features of island formation do not depend on stability parameter qualitatively.

PACS numbers: 52.35.Vd, 52.35.Py, 52.35.Qz, 52.35.Ra

*Electronic address: ishizawa@nifs.ac.jp

I. INTRODUCTION

Tearing modes are a magnetohydrodynamic (MHD) instability and are spontaneous magnetic reconnection that may occur in sheared magnetic configuration, such as a current sheet and a rational surface in magnetic confinement[1]. The stability parameter of tearing instabilities, Δ' , which reflects the free energy of the instability involving magnetic reconnection, determines the instability threshold and thus the formation of magnetic islands. An equilibrium is stable or unstable against tearing instabilities when Δ' is negative or positive, respectively. Tearing instabilities are current driven instabilities, and thus are unstable for long-wavelength perturbation and caused long-wavelength magnetic islands, which degrade magnetic confinement [2].

Turbulence can arise around a current sheet. For instance, small-scale turbulence is driven by temperature-gradient instabilities[3], and its magnetic fluctuations can give rise to magnetic reconnection[4]. Multi-scale interactions between micro-turbulence and macro-scale MHD including tearing modes, double tearing modes and magnetic islands have been studied analytically [5–9] and numerically [10–24]. Recently, we have found that turbulence can change the threshold of magnetic island formation[22]. We demonstrated that long-wavelength magnetic islands are produced by turbulence in a current sheet, even if the current sheet is so thick that the sheet is stable against spontaneous magnetic reconnection. The magnetic island is produced through energy transfer from small-scale turbulence. The threshold of magnetic island formation is usually given by the stability parameter of spontaneous magnetic reconnection Δ' at a current sheet, however, the results implies that the turbulence changes the threshold of magnetic island formation.

In this paper, we will investigate ion-temperature gradient (ITG) turbulence in a thick current sheet, which is stable against tearing modes, by means of numerical simulation based on MHD model and on two-fluid model. We examine two cases: one is that equilibrium is marginal to tearing modes, $\Delta' = 0$, the other case is that equilibrium is stable against tearing modes, $\Delta' = -3.4$. In our simulations turbulence is driven by ITG instabilities. Numerical simulations based on two-fluid model show that ITG turbulence causes long-wavelength islands. The length of magnetic island is the same order as the system size. The long-wavelength magnetic islands are formed by merging of small-scale magnetic islands.

The paper is organized as follows. Our two-fluid model is described in Sec. 2. Simulation

results are shown in Sec. 3. Magnetic island formation process are discussed in Sec. 4. Finally, summary is given in Sec. 5.

II. SIMULATION MODEL

In this section we introduce a reduced set of two-fluid equations, which is obtained by assuming strong guide magnetic field [12, 25] By assuming that plasma is uniform along the strong magnetic field that directs into z -direction, the reduced equations in two-dimensional plasma are obtained. The equations consists of the vorticity equation, the electron density equation, the parallel velocity equation, the generalized Ohm's law, and the ion temperature equation,

$$\left(\frac{\partial}{\partial t} + \mathbf{v} \cdot \nabla\right) \nabla^2 \Phi = -\mathbf{B} \cdot \nabla J - d_i \beta \nabla \cdot (\mathbf{v}_{di} \cdot \nabla \nabla \Phi) + \mu \nabla^4 \Phi, \quad (1)$$

$$\left(\frac{\partial}{\partial t} + \mathbf{v} \cdot \nabla\right) n = -\mathbf{B} \cdot \nabla v_{e\parallel} + \mu \nabla^2 n, \quad (2)$$

$$\left(\frac{\partial}{\partial t} + \mathbf{v} \cdot \nabla\right) v_{\parallel} = -\beta \mathbf{B} \cdot \nabla p + \mu \nabla^2 v_{\parallel}, \quad (3)$$

$$\frac{\partial \psi}{\partial t} = -\mathbf{B} \cdot \nabla \Phi + d_i \beta \mathbf{B} \cdot \nabla p_e + \eta J, \quad (4)$$

$$\left(\frac{\partial}{\partial t} + \mathbf{v} \cdot \nabla\right) T_i = -(\Gamma - 1)(\mathbf{B} \cdot \nabla v_{\parallel} + \kappa_L T_i) + \mu \nabla^2 T_i, \quad (5)$$

where $\mathbf{v} \cdot \nabla f = [\Phi, f]$, $\mathbf{B} \cdot \nabla f = -[\psi, f]$, $\mathbf{v}_{di} \cdot \nabla \nabla f = -[\nabla f, p_i]$, are written in terms of Poisson bracket $[f, g] = \partial_x f \partial_y g - \partial_x g \partial_y f$, where $\nabla = (\partial_x, \partial_y)$, and $\mathbf{B} = B_0 \mathbf{e}_z - \mathbf{e}_z \times \nabla \psi$, $\mathbf{v} = \mathbf{e}_z \times \nabla \Phi$, $\mathbf{v}_{di} = \mathbf{e}_z \times \nabla p_i$ are magnetic field, $E \times B$ drift velocity, ion diamagnetic velocity, respectively. In these equations Φ , ψ , n , $J = -J_z = \nabla^2 \psi$, v_{\parallel} , $v_{e\parallel} = v_{\parallel} + d_i J/n_{eq}$, T_i , T_e , $p_i = nT_i$, $p_e = nT_e$, $p = p_i + p_e$, are the electrostatic potential, the magnetic flux function, the electron density, the current density, the parallel ion velocity, the parallel electron velocity, the ion temperature, the electron temperature, the ion pressure, the electron pressure, the total pressure, respectively. Note that \parallel means parallel component along the guide magnetic field. The parameters $d_i = \rho_i/\sqrt{\beta}$, η , β , and L are the ion skin depth, the resistivity, the plasma beta, and the system size, respectively, where ρ_i is the ion Larmor radius. The term including $\kappa_L = \sqrt{\frac{8T_{eq}}{\pi}} |\mathbf{B}_{eq} \cdot \nabla|$ is the Landau damping term. the field quantities are divided into the initial equilibrium part and the rest of it as $f(x, y, t) = f_{eq}(x) + \tilde{f}(x, y, t)$, and it is assumed there is no equilibrium flow and no electron temperature fluctuation so that

$\psi = \psi_{eq} + \tilde{\psi}$, $\Phi = \tilde{\Phi}$, $n = n_{eq} + \tilde{n}$, $T_i = T_{eq} + \tilde{T}_i$, $T_e = T_{eq}$, $p_i = n_{eq}T_{eq} + T_{eq}\tilde{n} + n_{eq}\tilde{T}_i$, $p_e = n_{eq}T_{eq} + T_{eq}\tilde{n}$, respectively. We directly solve the reduced two-fluid equation Eqs. (1)-(5). Numerical method is as follows. Time advancement is made with the fourth-order Runge-Kutta method, and the x derivative is approximated by a finite-difference method, and Fourier decomposition is used in the y direction as $\tilde{f} = \sum_{k_y} \hat{f}(x, k_y, t) \exp(ik_y y)$. In this paper, nonlinear ion diamagnetic term in the vorticity equation is neglected because of numerical difficulty caused by third order derivative in this nonlinear term. The simulation box size is $(x, y) = (L, 2L)$. In x direction, 1024 uniform grids are employed, and 126 or 243 Fourier modes are employed in y direction. Parameters are set to be $\beta = 0.01$, $L/\rho_i = 80$, $\mu = 10^{-6}$, and $\eta = 2.35 \times 10^{-5}$.

Magnetic field configuration on the reconnection plane is assumed to be the Harris current sheet, $d\psi_{eq}(x)/dx = \tanh(x/L_s)$. The magnetic shear length, L_s , of the Harris sheet is associated with the gradient of current density and controls the strength of tearing modes, and small L_s , i.e. a thin current sheet, causes strong instability. The stability parameter of tearing instabilities $\Delta' = \frac{L}{2}[d \ln \tilde{\psi}/dx]_{0-}^{0+}$ is obtained by solving the linearized form of $\mathbf{B} \cdot \nabla J = \mathbf{B} \cdot \nabla \nabla^2 \psi = 0$. The uniform current density model $d\psi_{eq}(x)/dx = x/L_s$, which represents an infinitely thick current sheet, is also used. This profile has the neutral sheet at $x = 0$ and is absolutely stable against spontaneous magnetic reconnection.

III. MAGNETIC ISLANDS CAUSED BY TURBULENCE

We consider a plasma that is unstable against ion temperature gradient instability, which has the short-wavelength characterized by Larmor radius [3]. The instability is driven by ion temperature gradient and is controlled by the parameter $\eta_i = L_n/L_T$ which is proportional to the temperature-gradient, where L_T and L_n are temperature-gradient and density-gradient lengths, respectively. Both density and temperature gradients are assumed to be uniform, and L_n is the same as the system size, $L_n = L$, in our simulations. The instability grows exponentially at first, then the energy of the instability spreads in Fourier space via nonlinear mode coupling. The instability also produces strong zonal flow, which is the $k_y = 0$ mode, and the zonal flow then regulates the amplitude of the turbulence by means of its shear, and the system reaches a quasi-steady state.

Figure 1 shows color map of electrostatic potential and equi-contours of magnetic flux at

the quasi-steady state for the Harris sheet with $L_s/L = 0.22$, $\Delta' = 0$, and $\eta_i = 3.5$. Note that Δ' is calculated for the longest wavelength mode, $k = 1$, where the wavenumber is given by $k_y = \pi k/L$. It clearly shows magnetic islands appearing on the neutral sheet $x = 0$, even if there is no spontaneous magnetic reconnection $\Delta' = 0$. The wavelength of the magnetic island is much longer than the ion Larmor radius and is the same order as the system size, and the width is several times as large as the Larmor radius $\rho_i/L = 1/80$. The shape of the magnetic islands is deformed and is different from that of tearing modes because the turbulence causes fluctuations in the magnetic field.

IV. FORMATION PROCESS OF MAGNETIC ISLANDS

In this section we examine the process of magnetic island formation. Figure 2 shows the time evolution of magnetic flux on the neutral sheet, $x = 0$, for the uniform current density with (a) $\Delta' = -3.4$, and for the Harris sheet with (b) $\Delta' = 0$, where red region represents positive, and blue negative. The blue region represents the core parts of magnetic islands around O-points. At the beginning the color patterns show wave structure characterized by the wavelength of ion temperature gradient instability. After $t \approx 200$, large red and blue regions appear, and this means long-wavelength magnetic islands are formed. Especially, in the case $\Delta' = 0$, large red and blue region clearly appear as shown in Fig. 2 (b), because the tearing mode is marginally stable. Figure 3 shows the time evolution of the position of X-points and O-points for the uniform current density with (a) $\Delta' = -3.4$, and for the Harris sheet with (b) $\Delta' = 0$. The blue and black points represent X-points and O-points, respectively. Initially, there are many X- and O-points, and then some merge and disappear. After the large red and blue region appear in Fig. 2, sometimes X-points and O-points appear and disappear, because the turbulent perturbation causes random magnetic reconnection. This random magnetic reconnection is frequent even if the tearing instability is marginal, $\Delta' = 0$ as shown around $t \approx 750$ in Fig. 3 (b). Figures 2 and 3 also show the propagation of magnetic islands. At the beginning they propagate in the negative y direction, which is ion diamagnetic direction, because the ion temperature gradient instability propagates in the ion diamagnetic direction. Then, the magnetic islands propagate in the positive y direction, which is electron diamagnetic direction.

We examine each term of the generalized Ohm's law Eq. (4) in order to understand

the formation process of long-wavelength island. We consider the long-wavelength ($k = 1$) component of Eq. (4) on the neutral sheet $x = 0$ as

$$\frac{\partial \tilde{\psi}_1}{\partial t} = -(\tilde{\mathbf{v}} \cdot \nabla \tilde{\psi})_1 + d_i \beta (\tilde{\mathbf{v}}_{de} \cdot \nabla \tilde{\psi})_1 - \tilde{\mathbf{v}}_0 \cdot \nabla \tilde{\psi}_1 + d_i \beta \tilde{\mathbf{v}}_{de0} \cdot \nabla \tilde{\psi}_1 + \eta \tilde{J}_1, \quad (6)$$

where subscript 1 stands for $k = 1$ component. The left-hand-side of the equation represents production of long-wavelength ($k = 1$) magnetic flux on the neutral sheet. The first term in the right-hand-side $(\tilde{\mathbf{v}} \cdot \nabla \tilde{\psi})_1 = [\tilde{\Phi}, \tilde{\psi}]_1$ represents turbulent mixing by $E \times B$ flow. The second term represents turbulent mixing by electron diamagnetic flow $(\tilde{\mathbf{v}}_{de} \cdot \nabla \tilde{\psi})_1 = [\tilde{p}_e, \tilde{\psi}]_1$, where $\tilde{\mathbf{v}}_{de} = \mathbf{e}_z \times \nabla \tilde{p}_e$. The third and fourth terms represent the propagation due to zonal flow, $\tilde{\mathbf{v}}_0 \cdot \nabla \tilde{\psi}_1$, and the propagation due to equilibrium electron diamagnetic effect, i.e. ω_{*e} effect, respectively. The last term, $\eta \tilde{J}_1$, is the resistive diffusion term. Figure 4 shows the time evolution of the absolute values of these terms for the uniform current density with (a) $\Delta' = -3.4$, and for the Harris sheet with (b) $\Delta' = 0$. The $E \times B$ turbulent flow mixing and electron diamagnetic turbulent flow mixing terms are comparable to or larger than the resistive diffusion term in both cases. Hence, these turbulent flow mixing terms play a role in producing long-wavelength magnetic islands. The electron diamagnetic flow mixing term is usually larger than the $E \times B$ flow mixing term. Notice that the turbulent mixing is not so strong when the tearing instability is marginal as shown in Fig. 4 (b).

V. SUMMARY

In summary, we studied ITG turbulence in a current sheet and examined two cases: one is that equilibrium is marginal to tearing modes, $\Delta' = 0$, the other case is that equilibrium is stable against tearing modes, $\Delta' = -3.4$. We have found that ITG turbulence causes magnetic reconnection and produces long-wavelength magnetic islands, even if the sheet is so thick that there is no tearing modes. The long-wavelength magnetic islands are caused by energy transfer from small-scale turbulence due to ITG. The width of magnetic islands is several times as large as the ion Larmor radius, and their length is the same order as the system size. The long-wavelength magnetic islands are formed by the merging of small-scale magnetic islands produced by magnetic reconnection driven by turbulent fluctuation.

Our results suggest a mechanism of long-wavelength magnetic islands formation in a current sheet in addition to spontaneous and driven magnetic reconnections. When the

width of a current sheet is decreasing during a current sheet formation from a smooth magnetic configuration, turbulence produces long-wavelength magnetic islands at the very beginning of the formation before spontaneous or driven magnetic reconnection takes place.

Acknowledgments

The authors would like to thank Profs. R. Horiuchi and H. Sugama for their support. This work was partially supported by the JSPS-CAS Core University program in the field of 'Plasma and Nuclear Fusion'.

-
- [1] H. P. Furth, J. Killeen and M. N. Rosenbluth, *Phys. Fluids* **6**, 459 (1963).
 - [2] F.L. Waelbroeck, *Nucl. Fusion* **49**, 104025 (2009).
 - [3] W. Horton, *Rev. Mod. Phys.* **71**, 735 (1999).
 - [4] A. Zeiler, J. F. Drake, and B. N. Rogers, *Phys. Rev. Lett.* **84**, 99 (2000).
 - [5] D. Biskamp and H. Welter, *Phys. Letters*, **96A**, 25 (1983).
 - [6] P. H. Diamond, R. D. Hazeltine, Z. G. An, B. A. Carreras and H. R. Hicks, *Phys. Fluids* **27**, 1449 (1984).
 - [7] Sanae-I. Itoh, K. Itoh, and M. Yagi, *Phys. Rev. Lett.* **91**, 045003 (2003).
 - [8] C. J. McDevitt and P. H. Diamond, *Phys. Plasmas* **13**, 032302 (2006).
 - [9] A. Sen , R. Singh , D. Chandra , P. Kaw and D. Raju, *Nucl. Fusion* **49** 115012 (2009).
 - [10] A. Thyagaraja, P. J. Knight, M. R. de Baar, G. M. D. Hogeweij, and E. Min, *Phys. Plasmas* **12**, 090907 (2005).
 - [11] M. Yagi, S. Yoshida, S.-I. Itoh, H. Naitou, H. Nagahara, J.-N. Leboeuf, K. Itoh, T. Matsumoto, S. Tokuda and M. Azumi, *Nucl. Fusion* **45**, 900 (2005).
 - [12] A. Ishizawa and N. Nakajima, *Phys. Plasmas* **14**, 040702 (2007).
 - [13] A. Ishizawa and N. Nakajima, *Nuclear Fusion*, **47**, 1540 (2007).
 - [14] F. Militello, F. L. Waelbroeck, R. Fitzpatrick, and W. Horton, *Phys. Plasmas* **15** 050701 (2008).
 - [15] A. Ishizawa and N. Nakajima, *Physics of Plasmas*, **15**, 084504 (2008).
 - [16] A. Ishizawa and N. Nakajima, *Nuclear Fusion*, **49**, 055015 (2009).

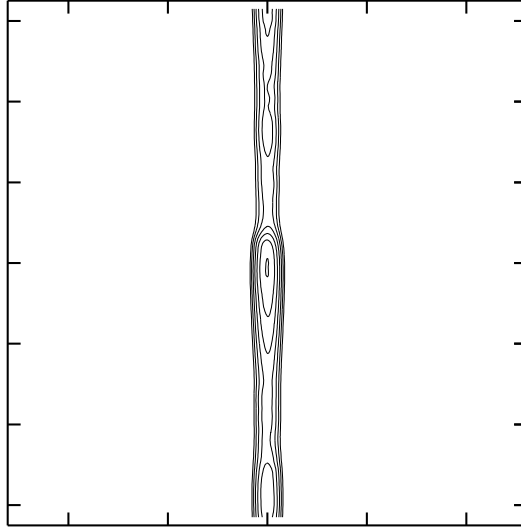


FIG. 1: Equi-contours of magnetic flux that indicates long-wavelength magnetic islands for the case $\Delta' = 0$.

- [17] E. Poli, A. Bottino and A.G. Peeters, Nucl. Fusion **49**, 075010 (2009).
- [18] M. Muraglia, O. Agullo, M. Yagi, S. Benkadda, P. Beyer, X. Garbet, S.-I. Itoh, K. Itoh, A. Sen, Nucl. Fusion **49**, 055016 (2009).
- [19] Jiquan Li, Y. Kishimoto, Y. Kouduki, Z. X. Wang, M. Janvier, Nucl. Fusion **49**, 095007 (2009).
- [20] F. L. Waelbroeck, F. Militello, R. Fitzpatrick, and W. Horton, Plasma Phys. Control. Fusion **51** 015015 (2009).
- [21] Z. X. Wang, J. Q. Li, Y. Kishimoto, J. Q. Dong, Phys. Plasmas **16**, 060703 (2009).
- [22] A. Ishizawa and N. Nakajima, Phys. Plasmas **17**, 072308 (2010).
- [23] A. Ishizawa and N. Nakajima, Phys. Plasmas **17**, 074503 (2010).
- [24] W. A. Hornsby, A. G. Peeters, A. P. Snodin, F. J. Casson, Y. Camenen, G. Szepesi, M. Siccino, and E. Poli, Phys. Plasmas **17**, 092301 (2010).
- [25] R. D. Hazeltine, M. Kotschenreuther, and P. J. Morrison, Phys. Fluids **28**, 2466 (1985).

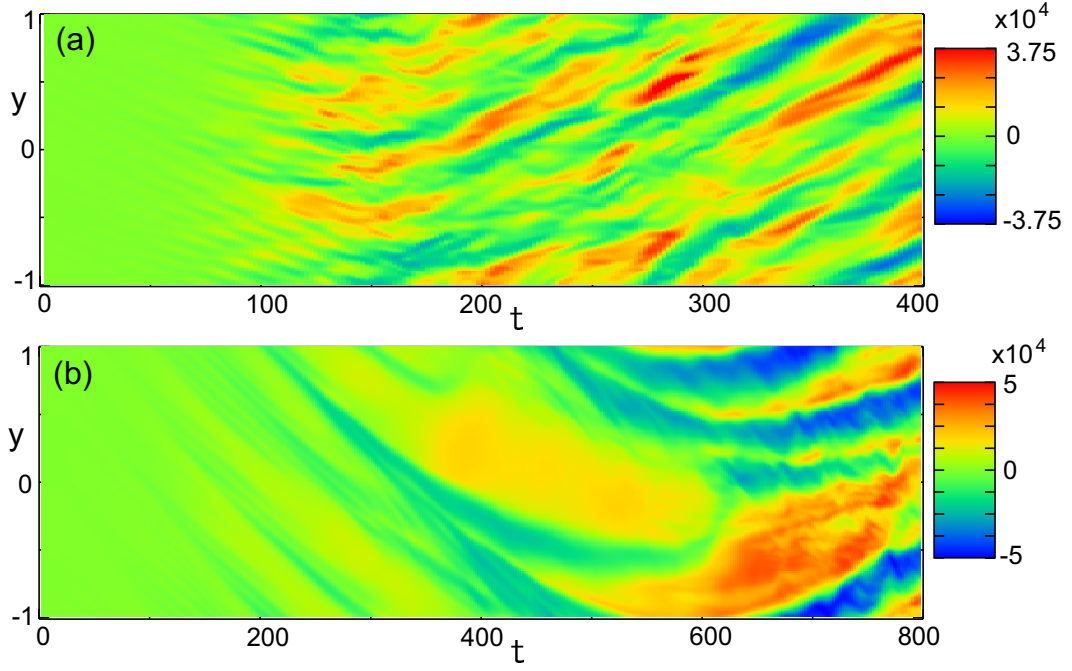


FIG. 2: Time evolution of magnetic flux on the neutral sheet, $x = 0$, for the case $\eta_i = 3.5$ and (a) $\Delta' = -3.4$, (b) $\Delta' = 0$. Blue region represents the core parts of magnetic islands around O-points.

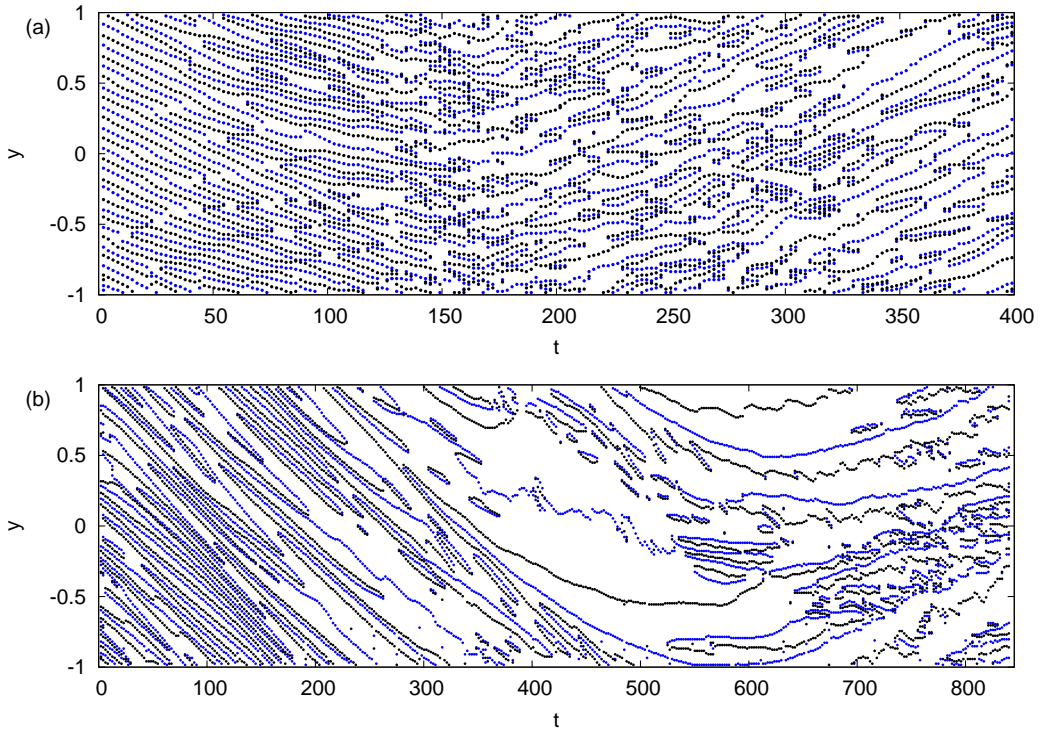


FIG. 3: Time evolution of X-points and O-points, for the case $\eta_i = 3.5$ and (a) $\Delta' = -3.4$, (b) $\Delta' = 0$. Black points are O-points and blue points are X-points.

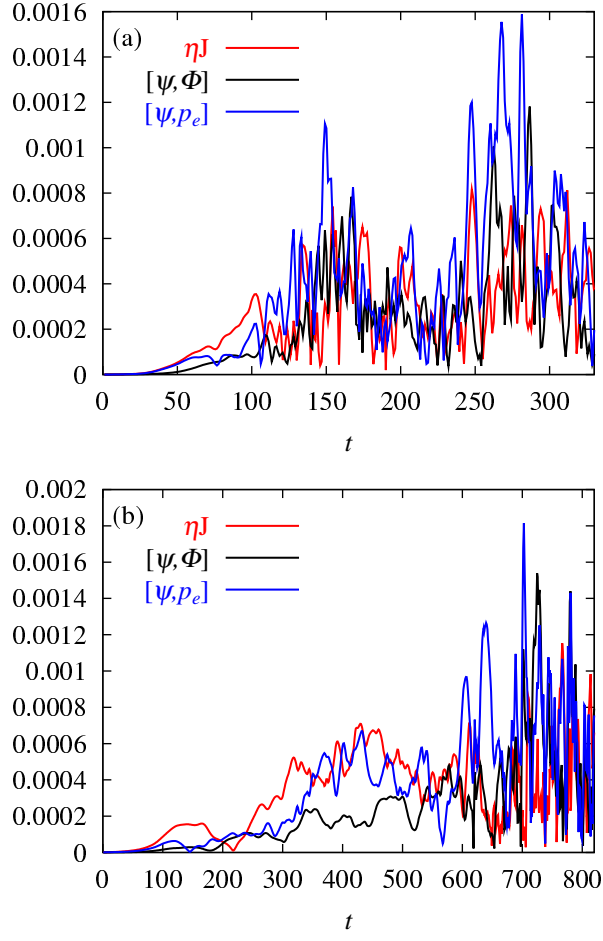


FIG. 4: Time evolution of absolute value of each term in the $k = 1$ (long-wavelength) component of Ohm's law on the neutral sheet for the case $\eta_i = 3.5$ and (a) $\Delta' = -3.4$, (b) $\Delta' = 0$.

Significant features of low frequency zonal flow and geodesic acoustic mode in the edge plasma of HL-2A tokamak

K. J. Zhao

Southwestern Institute of physics, P. O. Box 432, Chengdu, China

Abstract

A three dimensional Langmuir probe array set have completely proven the significant features of low frequency zonal flow (LFZF) and geodesic acoustic mode (GAM) in the HL-2A tokamak plasma by verifying the spatial characteristics and the nonlinear coupling with ambient turbulence. Besides, the radial wave number demonstrated clearly linear dispersion relation for the LFZFs and GAMs, consistently with the theoretical prediction. The spatio-temporal structures of zonal flow effect on ambient turbulence were identified that are similar to those observed in LFZFs and GAMs. The findings provide concrete evidence that the turbulence envelope modulation should be induced by the zonal flows, and strengthen the feasibility of the indirect method to detect the zonal flows through the density fluctuation envelopes that could be measured with various diagnostics.

PACS numbers: 52.35.Ra, 52.25.Fi, 52.35.Mw, 52.55.Fa

(Some figures in this article are in color only in the electronic version)

1. Introduction

Zonal flows (ZFs) are universal in turbulent systems such as magnetically confined laboratory and space plasmas as well as atmospheres of stars. The extensive studies in this field are aimed at understanding nonlinear processes responsible for the coherent structure formation and for anomalous cross-field transport induced by turbulent fluctuations.

It is widely accepted in recent years that the turbulence and the induced transport may be reduced or even suppressed by $\vec{E} \times \vec{B}$ sheared flows, such as mean flows and ZFs [1-3]. The ZFs are induced by ($m = 0, n = 0$) radial electric field fluctuations with finite radial scales, generated by nonlinear interactions in ambient turbulences (ATs). Here, m/n is the poloidal/toroidal mode number of the fluctuations. Two kinds of ZFs have been observed in toroidal plasmas, i.e., near zero low frequency zonal flows (LFZFs) [4-6], and oscillatory geodesic acoustic modes (GAMs) [7-8].

The GAMs have been extensively investigated in recent years [9-10], since they have finite frequency and larger density fluctuations than those of LFZFs that can be rather easily detected with various diagnostics. On the other hand, a few experimental studies of the LFZFs are available, since they can be detected only with limited diagnostics of plasma flow or space potential. The examples include the direct electric

field measurements in Compact Helical System (CHS) using two heavy ion beam probes (HIBP)[11] and potential fluctuation measurements in HL-2A using Langmuir probes (LPs)[12], and the indirect flow measurement in DIII-D using beam emission spectroscopy (BES) [13], while some experiments have reported their signatures [14-18]. At present, the symmetries of LFZFs, i.e., in poloidal and toroidal direction and finite radial wave length were measured in toroidal plasma [11-13]. The coexistence of LFZF and GAM has been confirmed in the edge of a tokamak plasma [13]. The nonlinear coupling between the ZF and AT has been analyzed by bicoherence analyses [15, 19-20]. Besides, the interactions have been observed as the modulation in the envelope of ATs [21-24]. For lower safety factor of less than 1, GAMs have not been observed [25].

The significant features of LFZFs and GAMs are unambiguously identified by verifying the toroidal and poloidal symmetries, and the radial scale of the LFZFs and GAMs, with three dimensionally displaced Langmuir probe arrays, simultaneously, in the edge plasmas of the HL-2A tokamak. The spatio-temporal structures of ZFs effect on ambient turbulence are analyzed and similar to those observed in LFZFs and GAMs, and well correlated with ZFs. The plausible nonlinear three wave coupling generation mechanism of the flows is also demonstrated.

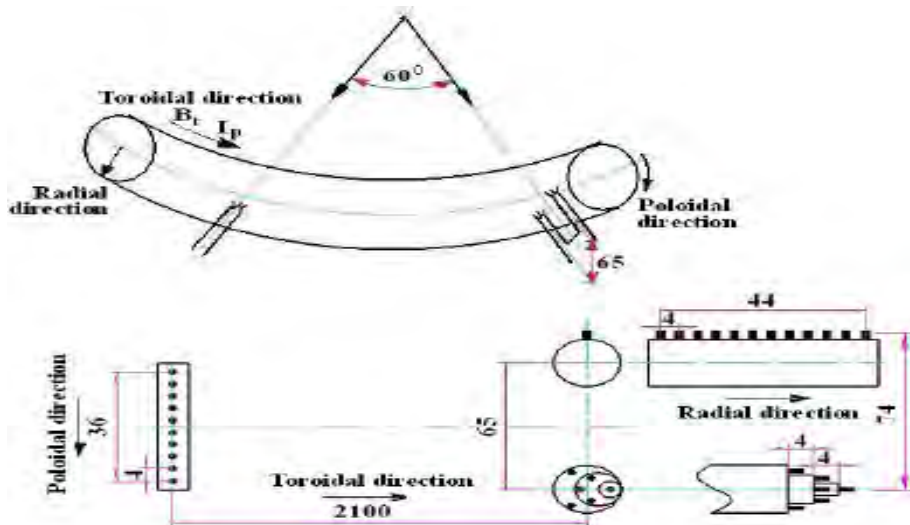


Figure 1. Layout and structure of the LP arrays.

The rest of this work is organized as follows: the experimental set up is given in section 2. The experimental results, described in section 3, include the coexistences of LFZFs and GAMs, envelope modulation, and the nonlinear three coupling between ZF and AT. Section 4 and 5 present the discussion and conclusion, respectively.

2. Arrangements of the LP arrays

The spatio-temporal fluctuations of the floating electrostatic potential were measured with three Langmuir probe (LP) arrays distributed poloidally and toroidally (see Figure.1) in the experiment. A 10 tip rake probe array with 4 mm tip separation was set up poloidally orientated and named poloidal probe (PP). A second rake probe array of 12 tips was mounted in the radial direction named radial probe (RP). A three

step Langmuir probe (TSLP) array of 6 tips [26] and the second rake probe array form a fast reciprocating probe set of 18 tips and a 65mm poloidal span, which was located in a poloidal cross section of 2100mm away from the first rake probe array in the toroidal direction. The length and diameter of each tip are 3 and 2mm. All of the probe sets were mounted at the outside middle plane of the tokamak up-down symmetrically. The PP and RP were used to measure the floating potential fluctuations while the TSLP array was for the measurements of the electron temperature and density in the experiment.

The major and minor radii of the HL-2A tokamak are $R = 1.65m$ and $a = 0.4m$, respectively. The experiments presented here were conducted in Ohmic heating deuterium plasmas of a circular cross section. The parameters specially set for the experiments are the toroidal magnetic field $B_t = 1.2-1.35T$, the plasma current $I_p = 150kA$, the line average electron density $\bar{N}_e \sim 1 \times 10^{19} m^{-3}$, the boundary safety factor $q_a = 3.5-4.0$, the discharge duration $t_d = 1.2s$. The collision frequency and the safety factor at the LP locations are estimated as $\nu_{ii} \sim 3 \times 10^3 / s$ and $q((r/a)=0.92) = 0.88 q_a$. No

significant signals were detected when the LPs were placed outside the $r=a$ surface.

The sample rate of the probe data is 1 MHz corresponding to Nyquist frequency of 500 kHz. The frequency resolution is 0.5 kHz in the following analysis unless otherwise stated.

3. The experimental results

3.1. The three dimensional characteristics of zonal flows

Figure 1 (a) presents the representative auto-power spectrum of the floating potential fluctuations at the inner and outer radial positions whose locations are 28mm and 24mm inside the last closed flux surface. Two distinct features are a large power fraction in low frequency range of 0-4kHz and a sharp peak at $f \sim 17$ kHz. The former is the focus of this work and will be demonstrated as a LFZF while the latter was already identified as a GAM [26-28]. In the case, the energy partition among the LFZF, the GAM and the A T, depending on the local plasma parameters and influencing transport phenomena, is roughly estimated as 0.21:0.23:0.56 and 0.19:0.31:0.50 for inner and outer positions, respectively. And the GAM fraction appears to increase as the

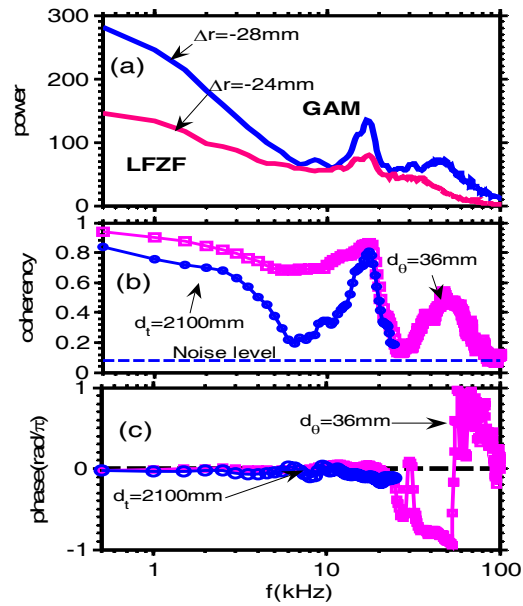


Figure 2. (color online). (a) Representative auto-power spectra of floating potentials at the inner and outer positions inside the last closed magnetic flux surface, (b) poloidal and toroidal coherence between floating potentials, (c) corresponding phase shifts.

safety factor increases, consistently with the simulation prediction [29].

The similar features were observed in the coherency spectra of the floating potential fluctuations over 36 and 2100 mm poloidal and toroidal distances (the lines with squares and circles) as shown in Figure. 2(b). The corresponding cross phase spectra are given in Fig. 2(c). Quite high (~ 0.8) coherencies and near zero phase shifts are apparent in the frequency range of less than 4 kHz, besides in the GAM frequency vicinity. On average over the half width of the LFZF spectrum, the poloidal and toroidal mode numbers were estimated as $m = 0.31 \pm 0.06$ and $n = 0.020 \pm 0.004$, respectively. This, in excellent agreement with theoretical and simulation predictions, unambiguously confirms the poloidal and toroidal symmetries of the fluctuations in this low frequency range in tokamak plasmas, as was done for the GAM alone before [18].

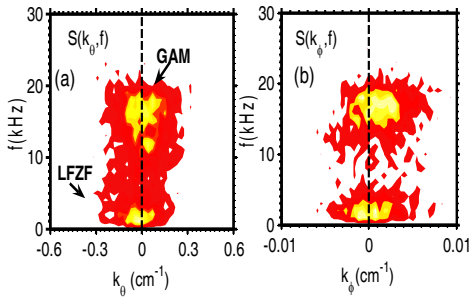


Figure 3. (a) and (b) are $S(k_\theta, f)$ and $S(k_\phi, f)$ of floating potential fluctuations.

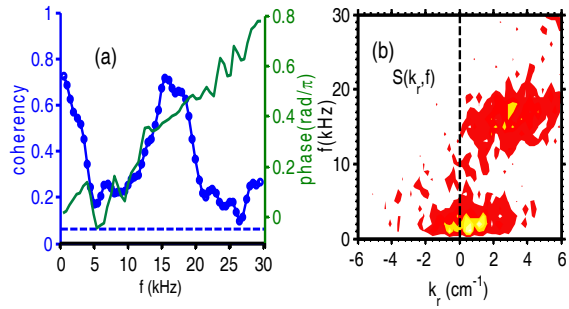


Figure 4. (a) Coherencies and phase shifts between floating potential fluctuations with poloidal/radial spans of 74/4mm, (b) corresponding to $S(k_r, f)$.

Here, $m=0.45 \pm 0.07$ and $n=0.33 \pm 0.05$ were also estimated simultaneously for the GAM.

Besides, the two point correlation measurements of the potential fluctuations may provide wave number-frequency characteristics of the zonal flows. Shown in Figures 3(a), (b) are the poloidal/toroidal wave number–frequency spectra, $S(k_\theta, f)/S(k_\phi, f)$,

where $S(k, f) = \frac{1}{M} \sum_{i=1}^m I[k - k_i(f)] S_{crsi}(f)$, evaluated with two point correlation

technique. Here, $I(a-b)=1$ if $a=b$, otherwise, $I(a-b)=0$, $S_{crsi}(f)$ and M represent the cross-correlation function and the number of realization, respectively. The feature of $k_\theta = k_\phi = 0$ in the frequency range of f less than 4 kHz is clearly demonstrated again.

The radial structure is also important for the identification of the ZFs. Figure 4 (a) provides the coherencies (cycle curve) and phase shifts (light curve) of floating potentials at two positions with poloidal and radial spans of 74mm and 4mm. Quite high coherency up to ~ 0.7 is shown again for the LFZFs and GAMs. And there are significant phase shifts in the low frequency range of less than 4kHz and GAM frequency range. The linear dispersion relations of the radial phase shifts are clearly demonstrated and consistent with the prediction of the theory. The phase velocities of

the LFZF and GAM are estimated as 0.25 km/s and 0.33 km/s, respectively. The group velocity of the former is the same as the phase velocity while it is 0.27 km/s for the latter. $S(k_r, f)$ is shown in figure 4 (b). The radial wave number and the half width of the $S(k_r)$ spectrum are roughly estimated as $k_r=0.5 \text{ cm}^{-1}$ and $\Delta k_r = 3.7 \text{ cm}^{-1}$, respectively, for the LFZF, in contrast with $k_{rGAM}=2.0 \text{ cm}^{-1}$ and $\Delta k_{rGAM} = 4.0 \text{ cm}^{-1}$ for the GAM.

3.2. The nonlinear coupling between zonal flow and ambient turbulence

The other condition for zonal flow to satisfy is the existence of the interaction with the AT or three wave coupling between ZF and AT. The bicoherence analysis, an indicator for the strength of nonlinear three wave coupling, can be used to prove the existence of the interaction between ZF and AT. The squared auto-bicoherence $\hat{b}^2(f_3)$

of the perturbations is calculated and shown in Figure. 4(a), plotted in the region between the lines of $f_1=f_2$ and $f_1=-f_2$ of the f_1 - f_2 plane. The enlarge picture in the frequency of less than 100kHz is also given in Figure 4.(b). The

values of $\hat{b}^2(f_3)$ about

$f_3=f_1-|f_2|<4\text{kHz}$ and $f_2<4\text{kHz}$ as well as $f_3=f_1-|f_2|\sim 17\text{kHz}$ and $f_2\sim 17\text{kHz}$ are higher than the rest, indicating that the nonlinear three wave coupling is a plausible creating mechanism for the LFZFs and GAMZFs. Figure 4.(c) provides the total bicoherence.

Similar features as the figure 2(a) are clearly shown again. The frequency resolution is 1 kHz in this analysis and the signals are significantly above the noise level in the LFZF and GAM frequency ranges. Therefore, the fluctuation less than 4kHz are low frequency zonal flow.

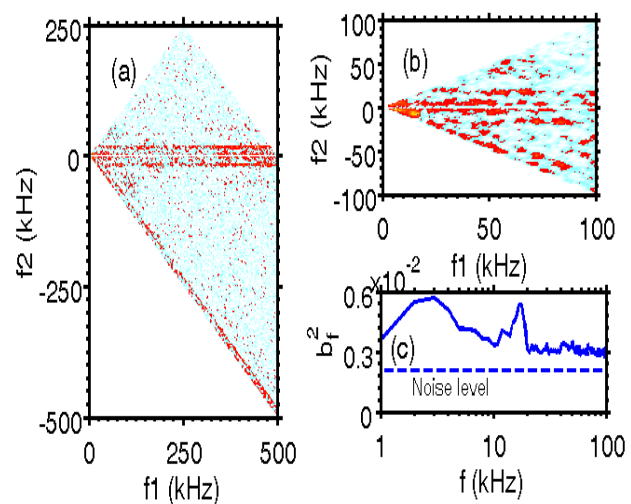


Figure5. (a) Auto-bicoherences of floating potentials plotted in f_1 - f_2 plane and (b) the enlarge picture, (c) the total bicoherence.

3.3. The local envelope modulation

The turbulence envelope modulation caused by the LFZFs, an important aspect of AT-ZF interactions, has been successfully demonstrated through the local envelope analyses of the potential fluctuations in the experiment. Figures 6(a) shows an example of the temporal evolution of the LFZF and the envelope of the turbulence of the frequency band from 300kHz to 500kHz, demonstrating a clear anti-phase correlation

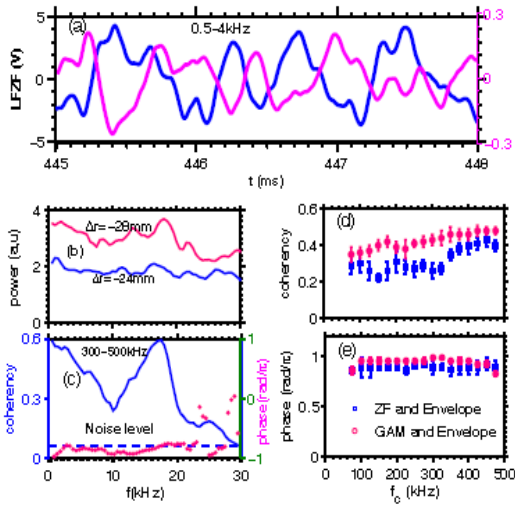


Figure 6. The local relation between ZFs and turbulence envelopes. (a) Waveforms of the LFZF and turbulence envelope, (b) the auto-power spectra of the turbulence envelopes evaluated for the frequency band from 300-500kHz, at inner and outer positions, (c) the coherency and cross phase spectra between the floating potentials and the turbulence envelopes at the inner position, (d) coherency and (e) cross phase between zonal flows (LFZF and GAM) and turbulence envelope versus the central frequency of the frequency band.

are the coherency and the cross phase spectra for the range of zonal flow frequencies (LFZFs of less than ~ 4 kHz and the GAM at ~ 17 kHz) as a function of the central frequency of the chosen frequency band. The band-width here is set to be 50 kHz. The increase of the coherency with the frequency and the invariance of the phase shift of $\sim \pi$ may indicate that the turbulence envelopes are all modulated by the LFZFs and the GAM and the modulation is stronger for higher frequency fluctuations. In addition, it is suggested that the modulation effects should be almost the same amount for the LFZF and the GAM in the edge of HL-2A tokamak plasmas.

between them, the signal of turbulence envelope is band pass filtered for LFZF frequency range of 0.5-4kHz). Figures 6 (b) and (c) show that the auto-power spectra of the turbulence envelope, the coherency and the cross phase between the ZFs and the turbulence envelope. The high coherencies up to ~ 0.6 and the phase shift of $\sim \pi$ statistically confirm the anti-phase correlation between the ZFs and the turbulence envelope. Therefore, it is obvious that the flows should have a significant impact on the turbulence. The interaction between ZFs and ATs, especially the effects of the former on the latter, is one of the key issues in the transport study of magnetized plasmas and worth more detailed investigation. Therefore, in addition to the envelope analysis for the band-width from 300 to 500 kHz, the similar analyses were conducted for the turbulence envelopes with various band ranges. Shown in Fig.6 (e) and (f)

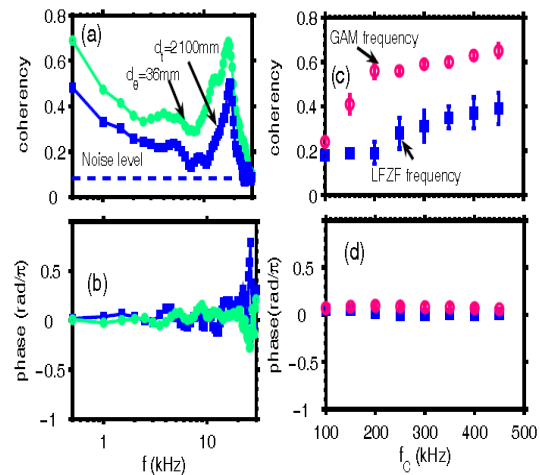


Figure 7. (a) Poloidal and toroidal coherency between turbulence envelopes (the light and dark lines) at two positions with separations of 36 and 2100mm in poloidal and toroidal direction, respectively, (b) corresponding cross phase, (d) coherency and (e) cross phase

3.4. The spatial characteristics of envelope modulation

To investigate the interaction between the flows and the turbulence further, the spatial features of the turbulent envelope were analyzed using the coherence between envelopes at two positions. The coherence spectra between two envelopes of the fluctuations in the frequency band from 300 to 500 kHz (the light circle and deep square lines), at two positions with poloidal and toroidal separations of 36 and 2100mm, respectively, are given in Fig.7(a). The high envelope-envelope coherencies (higher than 0.2) and the corresponding phase shifts close to zero in the LFZF frequency range in both the poloidal and toroidal directions indicate that the envelope has similar poloidal and toroidal scales as the LFZFs do. To be more specific, the poloidal and toroidal mode numbers of the envelope was estimated as $m=0.34\pm 0.02$, $n=0.1\pm 0.1$, respectively, which are close to the values estimated for the LFZF fluctuations above. In addition to 300-500 kHz frequency band, the similar analyses were conducted for the turbulence envelopes with various band ranges in the poloidal direction. Fig.7. (c) and (d) presented the coherence and the phase shift spectra for the range of the zonal flow frequencies. The band-width here is set to be 100 kHz. The increase of the coherence with the band frequency is notable and the near zero phase shifts over the frequency bands indicate that the turbulent envelopes at the zonal flow frequencies are poloidally symmetric. The toroidal symmetry of the turbulent envelopes was also identified with similar analysis as the GAMs do [28].

Figures 8 (a) shows the $S(k_r, f)$ spectrum of the turbulence envelope at two positions with 4mm spans in radial direction. The two distinct features in the LFZF and GAM frequency ranges are apparent and the wave vector-frequency spectra quite resembles that of floating potential fluctuations given in Fig.4(b). The spectral power density of the floating potential fluctuations and the turbulence envelope versus k_r at LFZF and GAM frequencies are given in Fig.8(c) and (d), respectively. The similarity of the $S(k_r)$ spectra for the floating potential and the turbulence envelope at the LFZF and GAM frequencies indicate that the radial scale of the envelope may be estimated the same as that of the ZFs.

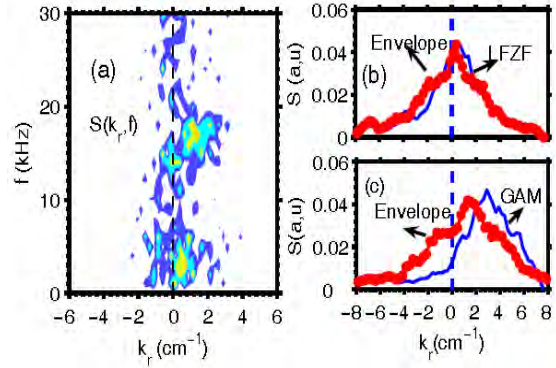


Figure8. (a) $S(k_r, f)$ spectrum of turbulence envelope as a function of radial wave number and frequency. (b) The comparison of radial wavenumber spectra between of the floating potential and turbulence envelope for the LFZF, and (c) that for GAM.

4. Discussion

The spatial calibration accuracy for the LP radial positions is about 1 mm. That may induce a finite wave vector component in the direction connecting the two poloidal LPs as $k \sim k_r / 36 = 0.01 \text{ cm}^{-1}$ and $m \sim 0.4$ from a finite radial wave vector $k_r = 0.5 \text{ cm}^{-1}$ when the poloidal wave vector is zero. This may explain the deviation of the measured poloidal feature of the LFZFs from the $m=0$ symmetry. Therefore, the observation, in excellent agreement with theoretical and simulation predictions, unambiguously confirms the poloidal and toroidal symmetries of the fluctuations in this low frequency range in tokamak plasmas, as was done for the GAM alone before [26].

It is worthwhile to discuss the detailed mechanisms of the turbulence modulation. One of the important origins, which should be distinguished from the ZF-AT interaction, is the Doppler effects due to the movements of the LFZFs and GAMs. If the fluctuation power is inhomogeneous with respect to the frequency in the plasma frame, the frequency modulation due to the Doppler effects in the laboratory frame should cause apparent modulation in the turbulence power of a frequency band. The modulation power due to the Doppler effect is expressed in the simulation for m as $\Delta P = (dP(f_0)/df) \delta f_{\max}$, over the turbulence power at the center of a band, $P(f_0)$,

where $f_{\max} = k_\theta(f_0)v_{ZF,\max}$. A rough estimate for the present experiment shows that the modulations are typically $\sim 1\%$ and $\sim 10\%$ due to the Doppler effects and the ZF, respectively, for the frequency band from 350 to 400 kHz. Therefore, the nonlinear interactions between ZFs and turbulences should be existent to explain the observed turbulence modulation.

One of the nonlinear interactions between ZFs and turbulence is the \mathbf{ExB} velocity shearing. The shearing rate can be roughly evaluated from the observations. The plasma velocities at the LFZF and the GAM are estimated as $V_{ZF} = 200 \text{ m/s}$ and $V_{GAM} = 300 \text{ m/s}$, respectively. The radial electrical field fluctuations of ZFs may be expressed as $E_r = E_{r0} e^{-(1/l_c + ikr)r}$, here, l_c and kr are radial correlation length and wave number of ZFs. Then the radial gradient of electrical field fluctuation is derived as $dE_r/dr = -E_{r0}(1/l_c + ik_r)e^{-(1/l_c + ikr)r}$. The corresponding to shearing rates are described by $\gamma_{ZF} = \sqrt{(1/l_c)^2 + (k_r)^2} V_{ZF}$. Then the calculated shearing rate is $\gamma_{LFZF} \sim 5 \times 10^4 / \text{s}$ for the LFZFs. Taking account of effective shearing rate effect, the shearing rate is estimated as $\gamma_{GAM} \sim 6 \times 10^4 / \text{s}$ for the GAMs. This suggests that the shearing effects of the LFZF and the GAM are comparable in this case. The decorrelation rate of turbulence is evaluated to be $\sim 3 \times 10^5 / \text{s}$. Therefore, the shearing

rates of both LFZF and GAM may be too small to give a significant reduction of the turbulence. In addition, it is plausible that the shearing effect may appear as the second harmonic frequency if the positive and negative sign of the shear should have the same effect on turbulence. As a result, some other nonlinear interaction between ZFs and turbulence, such as wave trapping, may be the major cause of the well correlated envelope modulation synchronized with the ZF oscillations.

Finally, the direct detection of ZFs (or electric field) can be carried out only with limited diagnostics i.e., LPs and HIBPs. However, both diagnostics are not easily applicable for present or future large devices with high temperature and strong confinement magnetic field. The indirect method to detect ZFs was proposed based on the local measurements of density fluctuation envelope and floating potential for GAM. The present observation shows that the modulation envelope of turbulence should really reflect the spatio-temporal characteristics of both LFZFs and GAMs. Therefore, the results presented here give a strong support of the feasibility of the indirect detection of ZF, which opens a way to proceed the turbulence and ZF researches in such high performance devices.

5. Conclusion

The significant features of LFZFs were identified by verifying the spatial characteristics, i.e., the symmetry in poloidal and toroidal direction, and the finite radial wave length with three-dimensional Langmuir probe arrays in the HL-2A tokamak experiments. The nonlinear couplings between ZF and AT indicate that the ZF may be created by the three wave coupling mechanism. The envelope modulation analyses show that the spatiotemporal structures of turbulence envelope are similar to those observed in LFZFs and GAMs, and well anti-phase correlated with the ZFs. The findings provide concrete evidence that the turbulence envelope modulation should be induced by the zonal flows, and strengthen the feasibility of the indirect method to detect the zonal flows through the density fluctuation envelopes that could be measured with various diagnostics. Besides, the radial wave number demonstrated clearly linear dispersion relation for the LFZFs and GAMs, consistently with the theoretical prediction. Besides, the radial wave number demonstrated clearly linear dispersion relation for the LFZFs and GAMs, consistently with the theoretical prediction.

Acknowledgments

The authors thank the HL-2A Team for operation of the machine. This work was partly supported by the National Natural Science Foundation of China Grants No. 10775044, and supported by the Sichuan Youth Foundation of Science and Technology, Grant No 09ZQ026-079, by the National Basic Research Program of China under Grant No 2008CB717806, and the National Magnetic Confinement Fusion Science Program Grant No 2010GB1060 08. This work was also partially supported by the JSPS-CAS Core-University Program in the field of 'Plasma and Nuclear Fusion'.

Reference

- [1] Z. Lin et al., *Science* 281, **1835** (1998).

- [2] P. W. Terry, Rev. Mode. Phys. **72**, 109 (2000).
- [3] H. Biglari, P. H. Diamond, and P. W. Terry, Phys. Fluids B**2**, 1 (1990).
- [4] P. H. Diamond et al., Plasma Phys. Controlled Fusion **47**, R35 (2005).
- [5] A. Hasegawa and M. Wakatani, Phys. Rev. Lett. **59**, 1581 (1987).
- [6] L. Chen, Z. Lin and R. B. White, Phys. plasmas, **7**, 3129 (2000).
- [7] N. Winsor, J. L. Johnson, and J. M. Dawson, Phys. Fluids **11**, 2448 (1968).
- [8] K. Hallatschek and D. Biskamp, Phys. Rev. Lett. **86**, 1223 (2001).
- [9] A. Fujisawa et al., Nucl. Fusion, **47**, S718 (2007).
- [10] A. Fujisawa, Nucl. Fusion, **49**, 013001 (2009).
- [11] A. Fujisawa et al., Phys. Rev. Lett. **93**, 165002 (2004).
- [12] A. D. Liu, et al., submitted to PRL.
- [13] D. K. Gupta et al., Phys. Rev. Lett. **97**, 125002 (2006).
- [14] G. S. Xu et al., Phys. Rev. Lett. **91**, 125001 (2003).
- [15] Y. Nagashima et al., Phys. Rev. Lett. **95**, 095002 (2005).
- [16] S. Coda, et al., Phys. Rev. Lett. **86**, 4835 (2000).
- [17] R. A. Moyer, et al., Phys. Rev. Lett. **87**, 135001 (2001).
- [18] Y. Hamada et al., Phys. Rev. Lett. **99**, 065005 (2007).
- [19] P. H. Diamond, et al., Phys. Rev. Lett. **84**, 4842 (2000).
- [20] Y. C. Kim and E. J. Power, IEEE Trans. Plasma Sci. **7**, 120 (1979).
- [21] M. Jakubowski et al., Phys. Rev. Lett. **89**, 265003 (2006).
- [22] T. Ido et al., Nucl. Fusion, **48**, S41 (2006).
- [23] A. Fujisawa et al., J. Phys. Soc. Jpn, **76**, 033501 (2007).
- [24] Y. Nagashima et al., Plasma Phys. Controlled Fusion, **49**, 1611 (2007).
- [25] M.A.Pedrosa et al., Phys. Rev. Lett. **100**, 215003 (2008).
- [26] K. J. Zhao et al., Phys. Rev. Lett. **96**, 255004 (2006).
- [27] T. Lan et al., Plasma Phys. Controlled Fusion **50**, 045002 (2008).
- [28] K. J. Zhao et al., Phys. plasmas, **14**, 122301 (2007).
- [29] N. Miyato et al., J.Li, Phys. Plasmas, **11**, 5557 (2004).

Heavy Ion Beam Probe Measurement in Turbulence Diagnostic Simulator

Naohiro KASUYA, Seiya NISHIMURA, Masatoshi YAGI ^{1,2)}, Kimitaka ITOH
and Sanae-I ITOH ¹⁾

National Institute for Fusion Science, 322-6 Oroshi-cho, Toki, Gifu 509-5292, Japan

¹⁾ *Research Institute for Applied Mechanics, Kyushu University, 6-1 Kasuga-kouen, Kasuga,
Fukuoka 816-8580, Japan*

²⁾ *Japan Atomic Energy Agency, 801-1 Mukoyama, Naka, Ibaraki 311-0193, Japan*

Development of experimental diagnostics in fusion plasmas enables to give high spatial and temporal resolution measurements of fluctuations. To verify the observation of fluctuations within their resolutions, it is helpful to use simulation data as a test field for the measurements, taking account of lines of sight of each diagnostic. A numerical measurement module simulating a heavy ion beam probe is developed, and numerical diagnostics of electrostatic potential and density fluctuations are carried out on 3-D turbulent data obtained by a global simulation of drift-interchange mode turbulence in helical plasmas. Deviation between measurements and local values is estimated, and it is found that characteristic structures can be detected in spite of screening effect by the finite spatial resolution.

Keywords: turbulence, structural formation, numerical simulation, heavy ion beam probe, fluctuation, spatial resolution

PACS: 52.65.-y, 52.70.-m, 52.35.Ra

1. Introduction

It is important to clarify the role of turbulent structures on anomalous transport in toroidal plasmas [1]. High resolution measurements of fluctuations have been carried out in experimental devices to make quantitative estimation of turbulent transport [2,3]. Numerical simulations of plasma turbulence are also carried out, and detailed analyses on the numerical turbulence fields can give good comparison with experimental results [4-6]. We have been developing a turbulence diagnostic simulator, which simulates plasma turbulence numerically [7]. Spatio-temporal data analyses as same in the experiments can be made on the simulation data [8], which aid the development of the data analysis technique to deepen our physical understandings.

In this article, the development of a module simulating a heavy ion beam probe (HIBP) measurement is described. HIBP is a powerful diagnostic in plasma experiments, which give an electrostatic potential and electron density in the core plasma with high spatio and temporal resolutions [9-11]. We carry out numerical HIBP measurements on three-dimensional (3-D) numerical simulation data of turbulence in toroidal plasma to find out how detected signals are influenced by fluctuations along the particle trajectory of the probe beam.

The article is organized as follows. In section 2, a reduced MHD model is explained for generation of turbulent fields in helical plasmas. In section 3, the setup of the HIBP module is described. In section 4, numerical diagnostics are carried out on the time series of the 3-D turbulent data, which is obtained by the nonlinear simulation, and comparison between numerical measurements and local values of the data are made. Finally we summarize our results in section 5.

2. Generation of a turbulent field

To provide turbulence data, the simulation code of the resistive drift wave turbulence in a linear

device, called ‘Numerical Linear Device’ [4] has been extended to calculate the drift-interchange turbulence in helical plasmas with a circular cross-section. The averaging method with the stellarator expansion [12,13] is applied to give a set of model equations as

$$\frac{\partial \nabla_{\perp}^2 u}{\partial t} = [u, \nabla_{\perp}^2 u] + \nabla_{\parallel} \nabla_{\perp}^2 A + [\Omega, P] + \mu \nabla_{\perp}^4 u, \quad (1)$$

$$\frac{\partial A}{\partial t} = \nabla_{\parallel} (u + \alpha P) + \eta \nabla_{\perp}^2 A, \quad (2)$$

$$\frac{\partial P}{\partial t} = [u, P] - C \nabla_{\parallel} \nabla_{\perp}^2 A + \eta_{\perp} \nabla_{\perp}^2 P + S, \quad (3)$$

where u is the stream function, A is the ζ component of the vector potential, P is the total pressure, $\nabla_{\parallel} = \partial / \partial \zeta + [\cdot, \Psi]$, $\Psi = A - (1/2) \nabla \langle \Phi \rangle \times \nabla \Phi \cdot \hat{\zeta}$, Φ is the magnetic potential, $\alpha = V_A / (2\Omega_{ci} a)$, $C = \gamma P_0 V_A / (\Omega_{ci} a)$, $\Omega = 2r \cos \theta / (\nabla \Phi)^2$ is the magnetic curvature, S is the pressure source, V_A is the Alfvén velocity, Ω_{ci} is the ion cyclotron frequency, a is the minor radius, γ is the specific heat ratio, η is the resistivity, μ and η_{\perp} are viscosities, \bar{f} is the average of f over the helical pitch length, and $[\cdot]$ is the Poisson bracket. The following normalizations are used in the model equations: $u / (\varepsilon a V_A) \rightarrow u$, $A / (\varepsilon a B_0) \rightarrow A$, $P / (\varepsilon a B_0^2 / \mu_0) \rightarrow P$, $t / t_A \rightarrow t$, and $r / a \rightarrow a$, where ε is the inverse aspect ratio and $t_A = a / \varepsilon V_A$ is the Alfvén time.

Equations (1) - (3) are solved in the toroidal coordinate with spectral expansion in the poloidal and toroidal directions. The boundary condition in the radial direction are set to $f = 0$ at $r = 0, 1$ when $m \neq 0$, and $\partial f / \partial r = 0$ at $r = 0, f = 0$ at $r = 1$ when $m = 0$, where f implies $\{u, A, P\}$, m is the poloidal mode number, and $r = 1$ gives an outer boundary of the plasma. In the initial state the pressure profile is given to be flat. The pressure source is fixed to be

$$S(r) = \frac{4S_0 \mu_N}{L_N^2} \left[1 - \left(\frac{r}{L_N} \right)^2 \right] \exp \left[- \left(\frac{r}{L_N} \right)^2 \right], \quad (4)$$

with $S_0 = 0.2$, $L_N = 0.6$ [m], which forms the profile peaked at $r = 0$. The magnetic potential is given by

$$\Phi = 2\Phi_l I_l(hr) \sin(l\theta + h\zeta), \quad (5)$$

where I_l is the modified Bessel function, l is the pole number of the helical winding, $h = M / R_0$, M is the pitch number, R_0 is the major radius, and Φ_l is a constant coefficient. The following parameters are used: $B = 2.0$ [T], $T_e = 1$ [keV], $a = 0.6$ [m], $R_0 = 3.75$ [m], $\mu = \eta = \eta_{\perp} = 1 \times 10^{-5}$, $l = 2$, $M = 10$, $\Phi_l = 0.2$. Rotational transform ι is given to be a monotonically increasing function with the radius from $\iota(0) = 0.41$ to $\iota(1) = 1.17$.

Simulations are performed with 1024 grids in the radial direction. Fourier modes $-64 \leq m \leq 64$, $-16 \leq n \leq 16$ are taken, where n is the toroidal mode number. Spatio-temporal data of turbulent fields are generated by this global simulation. Figure 1 (a) shows the time evolutions of the fluctuating energy of the electrostatic potential. Low m, n modes are excited in the linear growing phase, and saturation is obtained with energy exchange between various modes by nonlinear couplings. Figure 1 (b) shows the energy spectrum of the electrostatic potential on m in the nonlinear saturation state. The snapshots of the contours of the electrostatic potential and density at $t = 1000$ are shown in Fig. 2. Spatio-temporal data analyses are

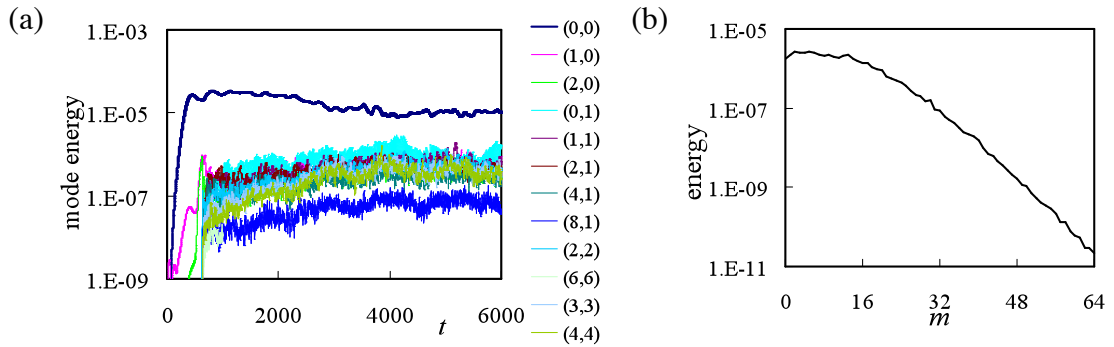


Fig. 1: (a) Time evolutions of the energy of Fourier modes. The fluctuation energies of the electrostatic potential are shown. (b) Potential energy spectrum on poloidal mode number m in the nonlinear saturation state.

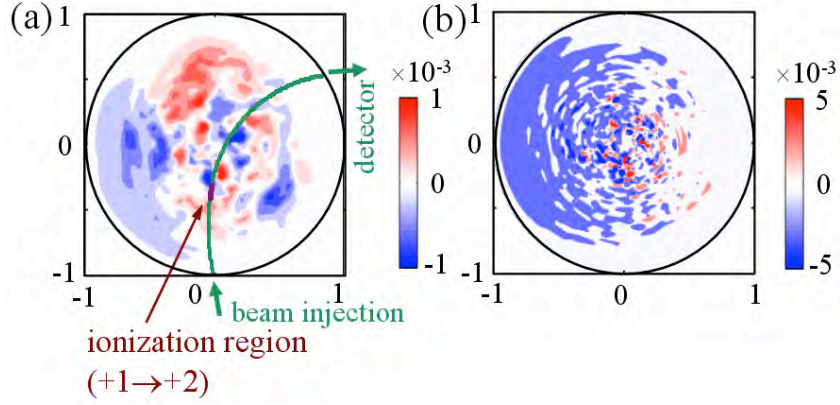


Fig. 2: Contours of (a) the electrostatic potential fluctuation and (b) the density fluctuation on the poloidal cross-section. These are the snapshots at $t = 1000$ in Fig. 1. The example of the HIBP beam trajectory (green line) with the ionization region (blown region) is also shown in (a).

carried out on this simulation data. Here, we assumed that the $E \times B$ flow velocity is larger than the diamagnetic flow velocity and the temperature is constant, so variables u and P represent the normalized electrostatic potential and density, respectively.

3. Simulation of a heavy ion beam probe

We have been developing several modules to simulate experimental diagnostics of turbulence. Time series of 3-D data from numerical simulations, as obtained in section 2, are analyzed with these modules. Here, analyses with a HIBP module are described.

3.1. Set up of a heavy ion beam probe module

A heavy ion beam probe is used to measure the electrostatic potential and the density in the core plasmas. The heavy ions such as Cs^+ and Au^+ are injected into the plasma, and the ions that are ionized from charge +1 to +2 in the plasma is detected as shown in Fig. 2 (a). The difference between the particle energy of the injected and detected ions corresponds to the potential at the ionized point, so the potential can be obtained. The trajectory of the ions changes in accordance with the ionization points, so the observation point can be identified. The intensity of the detected beam is affected by the ratio of ionization in the sample volume, and the attenuation along the trajectory, which is given to be [14]

$$I_d/I_0 = 2l_3 n \frac{\langle \sigma_{12} v_{th} \rangle}{v_b} \times \exp\left(-\int_{l_1} \frac{n \langle \sigma_1 v_{th} \rangle}{v_b} dl - \int_{l_2} \frac{n \langle \sigma_2 v_{th} \rangle}{v_b} dl\right), \quad (6)$$

where I_d and I_0 are the detected and injected beam current, $\langle \sigma_{12} v_{th} \rangle$ is the ionization rate, v_b is the velocity of the heavy ion, $l_{1,2,3}$ are path lengths of primary beam, secondary beam, and ionization region, respectively. The ionization rate is given by Lotz's empirical formula [15]. If the density is low, the attenuation along the trajectory is small, and the beam intensity can be assumed to obey the density at the ionization point.

In this way, the detected beam gives information of the potential and density at the ionization point. The HIBP module simulates this mechanism as the following way; the injection point, angle and energy, and detector position are set at first, and the trajectory of the injected ions is calculated in the fluctuating fields using the equation of motion. The charges of the ions are changed from +1 to +2 on the way to find the ionization point, from which the ions get into the detector position. Considering the finite beam width and detector size, the detector catches ions from not single ionization point but some region. The energies of ions and the beam intensity given by Eq. (6) are calculated, and averaged over the ionization region (sample volume) to give HIBP signals taking account of the spatial resolutions.

3.2. Benchmark of the module

We have been developing the HIBP module with the mechanism described in the previous

subsection. According to experiments [16], singly ionized gold ions (Au^+) are injected with the energy of 1.5 [MeV] as a probing beam. For the benchmark, a calculation on the mean fields, which are constant in the poloidal and toroidal directions, is carried out. The mean profiles of the potential and density at $t = 1000$ are subtracted from the data in Fig. 1, which is shown as the solid curves in Fig. 3. A scan of the detection position gives the radial profiles with the fixed injection condition. The radius is determined by averaging it over the sample volume. The detected ion energy and beam intensity give the potential and density, which are well reproduced in accuracy of 2% with the potential and 8% with the density, as shown with triangles in Fig. 3. This is the case with the beam width of 1cm and the detector size of 3cm. Note that the beam intensity is the integration along the sample volume determined by the detector size, so a large sample volume gives a large intensity accordingly, as shown in the detected beam intensity in Fig. 3. The beam intensity has to be divided by the size of the sample volume, which is also obtained by the numerical HIBP calculation, to obtain the corrected local density.

4. Numerical measurement

To produce a signal that can be comparable to experiments, a simulation of the HIBP, described in section 3, is carried out on the turbulent data, obtained in section 2.

4.1. Radial profiles

The numerical HIBP measurement is carried out on the fluctuation fields. Radial profiles are calculated using a snapshot data at first. The fluctuations of the potential and density at $t = 1000$, shown in Fig. 2, are analyzed. Figure 4 shows the calculated values at several points. The local values at the center of the sample volume are also shown. Comparison between them indicates that the calculated values agree well in the potential case, but large deviation exists in the density case. This is because the HIBP signal is given by averaging over the sample volume. As is shown in Fig. 2, the typical length of the fluctuations is larger in the potential than in the density. So the averaging screens the fine structures, which gives the large deviation in the density measurement.

4.2. Time evolutions

The data has time series, so time evolutions of quantities can be obtained. Figure 5 shows the time evolutions of (a) the potential, (b) detected beam intensity, (c) observation point and (d) size of the sample volume. These values are obtained by analyzing the fluctuation data with fixed injection and detection conditions. Figure 5 (c) indicates that the deviation of the observation point is 5 % at most. In addition to that, Fig. 5 (d) indicates that the size of the sample volume is around 8 % of the radius. Therefore, the potential and density fluctuations have the deviation of more than 10 % from the values on the fixed position in the sample volume. Figure 6 shows the comparison between the potential calculated with the HIBP measurement and that at the fixed point. The characteristic oscillation can be identified with the numerical HIBP signal, so the selected beam width and detector size are small enough to study the fluctuations. On the other hand, as in Fig. 7 (a), the deviation of the density is too large to reproduce the fluctuation at a fixed position. By reducing the beam width and detector size, the characteristic time evolution can be reproduced as in fig. 7 (b). The comparison of the spectra also shows that the spectrum of the density is well reproduced in the thinner beam case, though is not in the wider beam case, as in Fig. 8. In this way, the spatial resolution necessary to resolve the target fluctuation can be estimated with the numerical measurement.

4.3. Correlation analyses

The observation point can be selected by adjusting the condition of the beam injection and detection, and data at any multiple points are available. Correlation analyses are carried out using the signals. Figure 9 shows the two-point correlation of the potential between the different radii. There exists a broad mode in the radial direction at the frequency about 0.026, so there are the large correlation at $\Delta t = 0, 39t_A, 78t_A$, and so on. This characteristic is reproduced by using the numerical HIBP signals, as in Fig. 9. The fluctuation analysis shows that the numerical experiment is useful to obtain the results that can be compared with experiments.

5. Summary

In summary, we have carried out the nonlinear simulation of the drift-interchange turbulence in the helical plasma, and the numerical measurement simulating the HIBP on the data. The HIBP module calculates the electrostatic potential and density, taking account of the perturbation of the trajectories of the probe beam. The spatial resolution can be estimated, considering the finite beam width and detector size, and the calculation shows whether the given resolution is fine enough to resolve the target fluctuation. The example of the correlation analyses is also described to show the effectiveness for identification of the characteristic structure.

These results are obtained from one of the functions in the turbulence diagnostic simulator, which is the combination of the several turbulence codes and the several modules to simulate the experimental measurements. Integration of several modules will clarify the formation mechanism and the effect on transport with the quantitative analyses over the wide range in space and time.

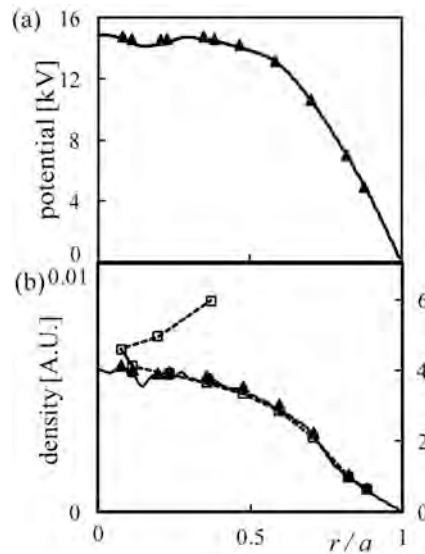


Fig. 3: Measurements of (a) the electrostatic potential and (b) density using the numerical HIBP on the mean fields at $t = 1000$ in the turbulent simulation. Triangles (\blacktriangle) and the solid line (-) indicate the numerical measurements and the mean profile, respectively. Open squares (\square) are the detected beam intensities, which are divided by the size of the sample volume to give the density.

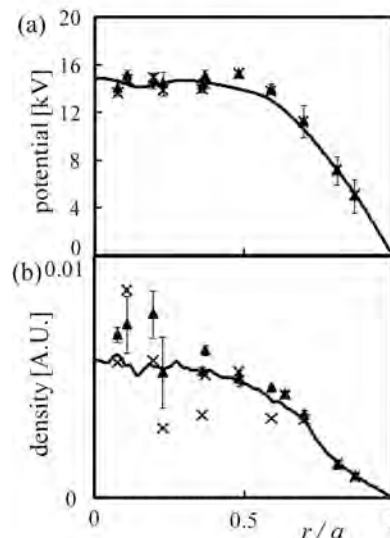


Fig. 4: Measurements of (a) the electrostatic potential and (b) density by using the numerical HIBP on the fluctuating field at $t = 1000$ in the turbulent simulation. Triangles (\blacktriangle), crosses (\times) and the solid line (-) indicate the numerical measurements, corresponding local values and the mean profile, respectively.

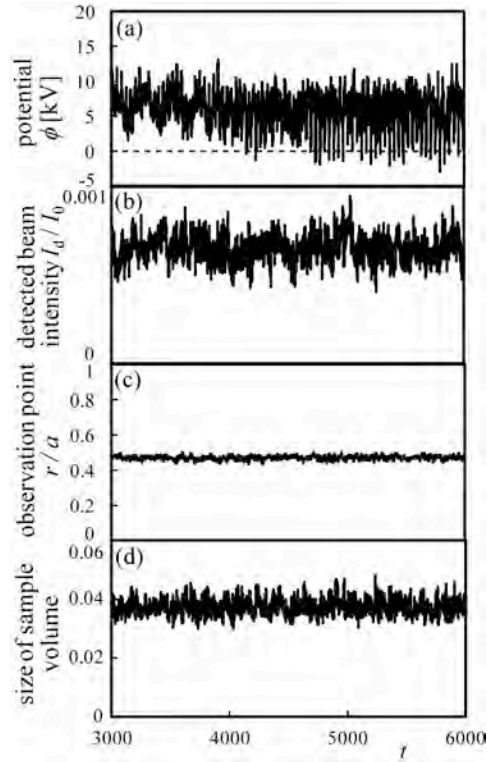


Fig. 5: Time evolutions of (a) the electrostatic potential, (b) detected beam intensity, (c) observation point and (d) size of the sample volume from the numerical HIBP measurement on the turbulent fields.

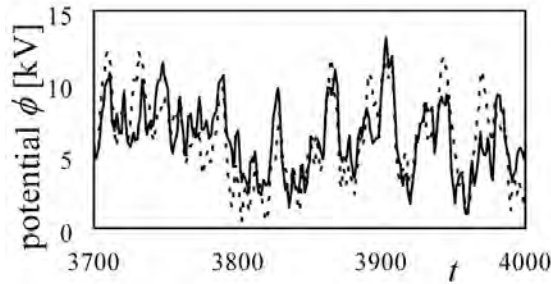


Fig. 6: Time evolutions of the electrostatic potential with the numerical HIBP measurement (solid line) and the local value at the fixed point in the sample volume (dashed line). This is the case with the beam width of 1cm and the detector size of 3cm.

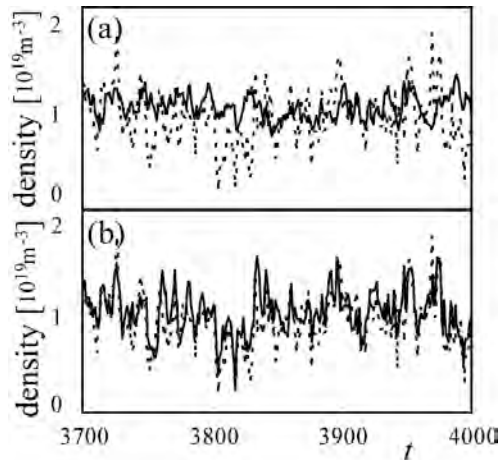


Fig. 7: Time evolutions of the density with the numerical HIBP measurement (solid line) and the local value at the fixed point in the sample volume (dashed line). These are the cases with (a) the beam width of 1cm and the detector size of 3cm, and with (b) the beam width of 0.5cm and the detector size of 1.5cm.

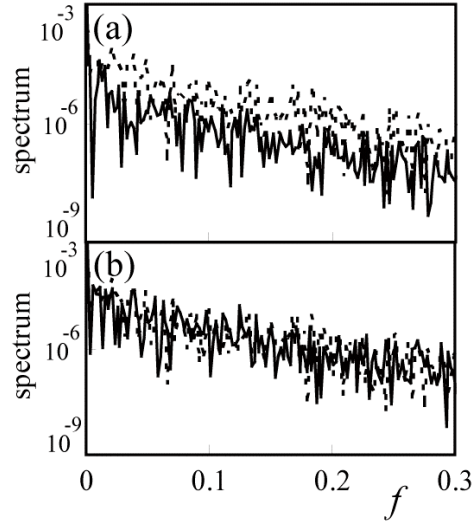


Fig. 8: Spectra of the density with the numerical HIBP measurement (solid line) and the local value at the fixed point in the sample volume (dashed line). These are calculated from the time series data in Fig. 7.

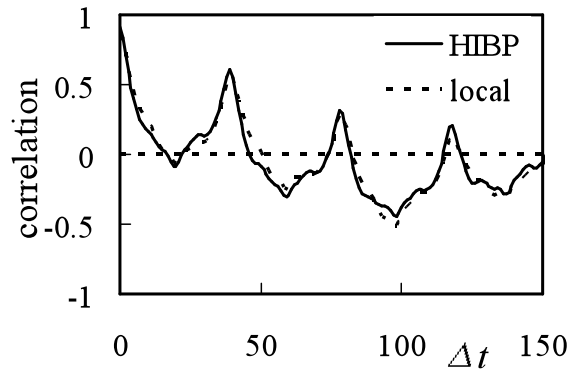


Fig. 9: Two-point correlation of the electrostatic potential between $r/a = 0.35$ and 0.45 , calculated from the values from the HIBP measurements (solid line) and the corresponding fixed positions (dashed line).

Acknowledgement

Authors acknowledge discussions with Prof. A. Fujisawa, Prof. K. Ida, Prof. A. Fukuyama, Dr. S. Inagaki, Dr. Y. Nagashima, and Dr. T. Yamada. This work is supported by the Grant-in-Aid for Young Scientists (20760581) and for Scientific Research (19360418, 21224014) of JSPS, the JSPS-CAS Core University program in the field of ‘Plasma and Nuclear Fusion’, by the collaboration program of NIFS (NIFS09KTAD009, NIFS09KDAD009, NIFS10KLHH315) and of RIAM of Kyushu University.

References

- [1] See reviews, e.g. P. H. Diamond, S.-I. Itoh, K. Itoh and T. S. Hahm, *Plasma Phys. Control. Fusion* **47**, R35 (2005).
- [2] A. Fujisawa, *Nucl. Fusion* **49**, 013001 (2009).
- [3] G. R. Tynan, A. Fujisawa and G. McKee, *Plasma Phys. Control. Fusion* **51**, 113001 (2009).
- [4] N. Kasuya, M. Yagi, S.-I. Itoh and K. Itoh, *Phys. Plasmas* **15**, 052302 (2008).

- [5] L. Lin, M. Porkolab, E. M. Edlund, J. C. Rost, C. L. Fiore, M. Greenwald, Y. Lin, D. R. Mikkelsen, N. Tsujii and S. J. Wukitch, *Phys. Plasmas* **16**, 012502 (2009).
- [6] J. Li and Y. Kishimoto, *Phys Plasmas* **17**, 072304 (2010).
- [7] N. Kasuya, S. Nishimura, M. Yagi, K. Itoh, S.-I. Itoh and N. Ohyaabu, *J. Plasma Fusion Res. SERIES* **9**, 523 (2019).
- [8] S. Nishimura, N. Kasuya, M. Yagi, K. Itoh, S.-I. Itoh and N. Ohyaabu, *Plasma Fusion Res.*, in press.
- [9] T. P. Crowley, *IEEE Trans. Plasma Sci.* **22**, 291 (1994).
- [10] G. A. Hallock, A. J. Wootton and R. L. Hickok, *Phys. Rev. Lett.* **59**, 1301 (1987).
- [11] A. Fujisawa, K. Itoh, H. Iguchi, K. Matsuoka, S. Okamura, A. Shimizu, T. Minami, Y. Yoshimura, K. Nagaoka, C. Takahashi, M. Kojima, H. Nakano, S. Ohsima, S. Nishimura, M. Isobe, C. Suzuki, T. Akiyama, K. Ida, K. Toi, S.-I. Itoh and P. H. Diamond, *Phys. Rev. Lett.* **93**, 165002 (2004).
- [12] J. M. Green and J. L. Johnson, *Phys. Fluids* **4**, 875 (1961).
- [13] M. Wakatani, *Stellarator and Heliotron Devices* (Oxford University Press, Oxford 1998).
- [14] H. Nakano, A. Fujisawa, A. Shimizu, S. Ohshima, H. Iguchi, Y. Yoshimura, and T. Minami, *Rev. Sci. Instrum.* **78**, 063502 (2007).
- [15] W. Lotz, *Astrophys. J.* **14**, 207 (1967).
- [16] T. Ido, A. Shimizu, M. Nishiura, H. Nakano, S. Kato, S. Ohshima, Y. Yoshimura, S. Kubo, T. Shimozuma, H. Igami, H. Takahashi, K. Toi, F. Watanabe, K. Narihara, I. Yamada and the LHD Experiment Group, *Plasma Sci. Tech.* **11**, 460 (2009).

Global and Kinetic MHD Simulation by the Gpic-MHD Code

Hiroshi Naitou¹, Yusuke Yamada¹, Kenji Kajiwara¹,
Wei-li Lee², Shinji Tokuda^{3,5}, Masatoshi Yagi^{4,5}

¹Graduate School of Science and Engineering, Yamaguchi University

²Princeton Plasma Physics Laboratory

³Research Organization for Information Science and Technology

⁴Research Institute for Applied Mechanics, Kyushu University

⁵Japan Atomic Energy Agency

Abstract

In order to implement large-scale and high-beta tokamak simulation, a new algorithm of the electromagnetic gyrokinetic PIC (particle-in-cell) code was proposed and installed on the Gpic-MHD code [Gyrokinetic PIC code for magnetohydrodynamic (MHD) simulation]. In the new algorithm, the vortex equation and the generalized ohm's law along the magnetic field are derived from the basic equations of the gyrokinetic Vlasov, Poisson, and Ampere system and are used to describe the spatio-temporal evolution of the field quantities of the electrostatic potential ϕ and the longitudinal component of the vector potential A_z . Particle information is mainly used to estimate second order moments in the generalized ohm's law. Because the lower order moments of the charge density and the longitudinal current density are not used explicitly to determine ϕ and A_z , the numerical noise induced by the discreteness of particle quantities reduces drastically. Another advantage of the algorithm is that the longitudinal induced electric field, $E_{Tz} = -\partial A_z / \partial t$, is explicitly estimated by the generalized ohm's law and used in the equations of motion. The particle velocities along the magnetic field are used (v_z -formulation) instead of generalized momentums (p_z -formulation), hence there is no problem of 'cancellation', which appear when estimating A_z from the Ampere's law in the p_z -formulation. The successful simulation of the collisionless internal kink mode by new Gpic-MHD with the realistic values of the large-scale and high-beta, revealed the usefulness of the new algorithm.

1. Introduction

The full understanding of experimentally observed global magnetohydrodynamic (MHD) phenomena in high temperature tokamak plasmas, inevitably requires investigations by the kinetic theory and simulation. There is no doubt that the MHD code with kinetic or extended MHD modifications can treat such phenomena. However, fluid-type simulation always encounters the problem of the “closure” which arises when deriving moment equations from the kinetic equations. The electromagnetic gyrokinetic PIC (particle-in-cell) code based on the gyrokinetic theory [1,2] is able to simulate such phenomena without the “closure” problem, although it needs huge computer resources because it must follow huge number of charged particles in the electromagnetic fields consisting of the external magnetic field and fields generated by charged particles themselves. In addition to the development of advanced algorithm, parallelization of gyrokinetic PIC codes on states-of-the art massive parallel computers is the crucial subjects. The parallelized code must have a good parallel performance up to more than $10^3 - 10^5$ cores. This article skips the parallelization techniques (for example see reference [3]) and concentrates on the development of the advanced algorithm.

More than a decade ago, we developed the gyrokinetic PIC code, `gyr3d` [4,5], based on the conventional gyrokinetic algorithm with δf scheme, in which (marker) particles represent only perturbed part of the velocity distribution functions, and successfully simulated collisionless $m=1/n=1$ (m, n are poloidal and toroidal mode numbers, respectively) internal kink mode that is the dominant mode related to the tokamak sawteeth crash phenomena (internal disruption). The `gyr3d` code was programmed for the three dimensional (3d) rectangular coordinate system, hence needed huge computer resources by two reasons. The first reason is that the time step size was forced to be quite small to resolve the quite fine time scale of unwanted high frequency shear Alfvén waves. The second reason is that we must have the fine scale spatial resolution to resolve a collisionless electron skin depth d_e , which is one of the characteristic lengths related to the physics of collisionless magnetic reconnection. Another characteristic length is an ion gyro-radius estimated by electron temperature ρ_s and becomes important when ρ_s is larger than d_e . By the limitation of computer resources, simulation was done with the parameters of $d_e/a \sim 0.1$ (a is a minor radius) and $\rho_s/d_e < 1$: the small scale

and low beta simulation. Note that here high beta means $\beta_e m_i / m_e = (v_{te} / v_A)^2 = (\rho_s / d_e)^2 > 1$, where β_e is the electron beta, m_i and m_e are the ion and electron masses, respectively, v_{te} is the electron thermal velocity, and v_A is the Alfvén velocity.

Recently we developed the gyrokinetic PIC code for MHD simulation, Gpic-MHD [3], with cylindrical geometry. The field quantities are represented with Fourier mode expansion both in axial and azimuthal directions. Nonuniform mesh is used in the radial direction so that we can accumulate the mesh around the rational surface. We can increase the time step by eliminating unwanted shear Alfvén modes in Fourier space. Due to the symmetry of the geometry we have 2d code with a single helicity and 3d code with multi-helicities. The 2d version of Gpic-MHD successfully simulated the collisionless internal kink mode [3]. The parameter range was extended from the gyr3d code but it could not access to the region with $d_e / a < 0.01$ and $\rho_s / d_e > 1$. The gyr3d and (conventional) Gpic-MHD codes use the generalized momentum $p_z = v_z + (q_s / m_s) A_z$ [q_s and m_s are the charge and mass for species s (electron or ion)] instead of the velocity v_z along the magnetic field. It was pointed out that the “cancellation” problem appears when estimating A_z from the Ampère’s law in the p_z -version. The “cancellation” problem causes the inaccuracy of the field solver when $d_e / a \ll 1$ and $\rho_s / d_e > 1$. One of solutions circumventing this problem is to use split-weight scheme [6,7], which is the advanced version of the δf scheme, where δf is decomposed into adiabatic and non-adiabatic responses. We have carefully revisited the formulation of split-weight scheme. In the split-weight scheme of p_z -version, to temporally advance particle weights, $\partial \phi / \partial t$ and $\partial A_z / \partial t$ must be evaluated by the vortex equation and generalized ohm’s law along the magnetic field.

It is natural to conceive that we can directly use the vortex equation and the ohm’s law for the spatio-temporal evolution of ϕ and A_z . Hence we proposed an alternative algorithm to the split-weight scheme. The new algorithm is very simple and uses these two equations to obtain ϕ and A_z . There is no need to use gyrokinetic Poisson equation and Ampère’s law. (They are used only to determine initial ϕ and A_z .) Because now we have accurate estimation of the induced electric field $-\partial A_z / \partial t$, we use the v_z -formulation. Also we use the conventional δf scheme. The information of particles is mainly used to estimate second order moment in the ohm’s law. The basic idea was

previously presented [8] and this article describes the details of the new algorithm.

The outline of this paper is as follows. The formulation of the new algorithm is summarized in section 2 as well as the essence of the conventional algorithm. The application to the collisionless internal kink mode simulation is described in section 3. The conclusions and discussion are given in section 4.

2. Proposal of new algorithm

The new algorithm of the electromagnetic gyrokinetic PIC code will be proposed in this section after the description of the conventional algorithm [2,4]. The basic gyrokinetic equations are derived using the ordering of

$$\frac{\omega}{\omega_{ci}} \sim \frac{\rho_{ii}}{L} \sim \frac{k_{\parallel}}{k_{\perp}} \sim \frac{e\phi}{T} \sim \frac{\delta B}{B_0} \sim O(\varepsilon), \quad (1)$$

where ω is the characteristic mode frequency, ω_{ci} is the ion gyro-frequency, ρ_{ii} is the thermal ion gyro-radius, L is the characteristic length of the equilibrium quantities, k_{\parallel} and k_{\perp} are the wave numbers parallel and perpendicular to the magnetic field, respectively, T is the plasma temperature, δB is the perturbed magnetic field, B_0 is the magnitude of a constant longitudinal magnetic field, and ε is the smallness parameter. We consider only the long wavelength limit of $k_{\perp}\rho_{ii} \sim O(\varepsilon)$, although the extension to the case of $k_{\perp}\rho_{ii} \sim O(\varepsilon^0)$ is not difficult. (The case of $k_{\perp}\rho_{ii} \sim O(\varepsilon^0)$ is important especially when we treat ion diamagnetic stabilization.) The lowest order tokamak model is employed; the plasma shape is the straight cylinder with periodic boundary condition in the axial direction.

The electric and magnetic fields are expressed by ϕ and A_z as

$$\mathbf{E} = -\nabla\phi - \frac{\partial A_z}{\partial t} \mathbf{b}, \quad (2)$$

$$\mathbf{B} = B_0 \mathbf{b} + \nabla A_z \times \mathbf{b}, \quad (3)$$

where \mathbf{b} is the unit vector in the direction of the longitudinal magnetic field (axial direction).

The gyrokinetic Vlasov equation for the v_z -formulation is

$$\frac{df_s}{dt} = \frac{\partial f_s}{\partial t} + \frac{d\mathbf{x}_s}{dt} \cdot \frac{\partial f_s}{\partial \mathbf{x}} + \frac{dv_{zs}}{dt} \frac{\partial f_s}{\partial v_z} = 0, \quad (4)$$

where $f_s = f_s(\mathbf{x}, v_z, t)$ is the velocity distribution function for the species s and

$$\frac{dx_s}{dt} = -\frac{\nabla\phi \times \mathbf{b}}{B_0} + v_z \mathbf{b}^*, \quad (5)$$

$$\frac{dv_{zs}}{dt} = -\frac{q_s}{m_s} \left(\mathbf{b}^* \cdot \nabla\phi + \frac{\partial A_z}{\partial t} \right), \quad (6)$$

where

$$\mathbf{b}^* = \mathbf{b} + \frac{\nabla A_z \times \mathbf{b}}{B_0}. \quad (7)$$

Eqs.(5) and (6) represent the characteristic of the gyrokinetic Vlasov equation. For simplicity we assume $q_i = e$. In the gyrokinetic PIC code, the equations for individual particles are identical to Eqs.(5) and (6). Some scientists prefers not to numerically estimate $\partial A_z / \partial t$ appearing in the right-hand-side of Eq.(6) and use p_z -formulation where

$$p_{zs} = v_{zs} + \frac{q_s}{m_s} A_z(\mathbf{x}_s, t). \quad (8)$$

The gyrokinetic Vlasov equation for p_z -formulation is given by

$$\frac{df_s}{dt} = \frac{\partial f_s}{\partial t} + \frac{d\mathbf{x}_s}{dt} \cdot \frac{\partial f_s}{\partial \mathbf{x}} + \frac{dp_{zs}}{dt} \frac{\partial f_s}{\partial p_z} = 0, \quad (9)$$

where

$$\frac{dp_{zs}}{dt} = -\frac{q_s}{m_s} (\mathbf{b} \cdot \nabla\phi - v_z \mathbf{b} \cdot \nabla A_z). \quad (10)$$

In Eq.(10) $\partial A_z / \partial t$ does not appear explicitly.

In the conventional gyrokinetic code, the field quantities of ϕ and A_z are obtained by the gyrokinetic Poisson equation and Ampere's law, respectively:

$$\frac{\omega_{pi}^2}{\omega_{ci}^2} \nabla_{\perp}^2 \phi = \frac{e}{\epsilon_0} \int f_e dv_z - \frac{e}{\epsilon_0} \int f_i dv_z, \quad (11)$$

$$\nabla_{\perp}^2 A_z = \mu_0 e \int v_z f_e dv_z - \mu_0 e \int v_z f_i dv_z, \quad (12)$$

for the v_z -formulation and

$$\frac{\omega_{pi}^2}{\omega_{ci}^2} \nabla_{\perp}^2 \phi = \frac{e}{\epsilon_0} \int f_e dp_z - \frac{e}{\epsilon_0} \int f_i dp_z, \quad (13)$$

$$\nabla_{\perp}^2 A_z = \mu_0 e \int \left(p_z + \frac{e}{m_e} A_z \right) f_e dp_z - \mu_0 e \int \left(p_z - \frac{e}{m_i} A_z \right) f_i dp_z, \quad (14)$$

for the p_z -formulation, where ω_{pi} represents the ion plasma frequency, and ϵ_0 and μ_0 are the vacuum permittivity and permeability, respectively. The system of Eqs.(9), (13), and (14) forms the basic equations of gyr3d and the conventional version of Gpic-MHD.

By taking a partial time derivative of Eq.(11), we have the vortex equation after some mathematical manipulations:

$$\frac{\partial}{\partial t} \nabla_{\perp}^2 \phi = -v_A^2 \mathbf{b}^* \cdot \nabla (\nabla_{\perp}^2 A_z) - \frac{\mathbf{b} \times \nabla \phi}{B_0} \cdot \nabla (\nabla_{\perp}^2 \phi). \quad (15)$$

Also, by taking a partial time derivative of Eq.(12), we have the ohm's law along the magnetic field:

$$\begin{aligned} \frac{\partial}{\partial t} \nabla_{\perp}^2 A_z = & \mu_0 e^2 \left(\frac{n_e}{m_e} + \frac{n_i}{m_i} \right) \left(\frac{\partial A_z}{\partial t} + \mathbf{b}^* \cdot \nabla \phi \right) - \frac{\mathbf{b} \times \nabla \phi}{B_0} \cdot \nabla (\nabla_{\perp}^2 A_z) \\ & - \mu_0 e \mathbf{b}^* \cdot \nabla \int v^2 f_e dv_z + \mu_0 e \mathbf{b}^* \cdot \nabla \int v^2 f_i dv_z. \end{aligned} \quad (16)$$

The basic idea of the proposed algorithm is to use Eqs.(15) and (16) to describe spatio-temporal evolution of ϕ and A_z . The particle information is mainly used to estimate second order momentum equations, which appear in the third and fourth terms in the right-hand-side of Eq.(16). It is important to notice that Eqs.(11) and (12) is only used when estimating the initial value of ϕ and A_z . Hence the numerical noise due to the discreteness of particles when we estimate zeroth and first order moments (charge and current densities), does not appear in the proposed algorithm. Although we use particle information to estimate lowest order moments of n_e and n_i which appear in the first term on the right-hand-side of Eq.(16), the effect is minimal because the particle information is used only to estimate perturbed part of the densities.

From Eq.(16) we also have accurate estimation of $\partial A_z / \partial t$, hence we can advance charged particles following Eq.(6). Hence we use the v_z -formulation for the new algorithm. The new version of Gpic-MHD is based on Eqs.(4), (15), and (16).

3. Simulation Results

For the simulation of the collisionless internal kink mode, we used the 2d Gpic-MHD code assuming single helicity. The conventional version is based on Eqs.(9), (13), and (14), while new version is based on Eqs.(4), (15), and (16). Both versions use the conventional δf method.

The computer we used is SR16000 [“plasma simulator” in NIFS (National Institute for Fusion Science)], which is the state-of-the-art scalar SMP (symmetric multiprocessing) cluster system. The total system of SR16000 is consisting of 128 nodes and each node includes 32 physical cores with SMP architecture. By using multithreading technology, one physical core is

equivalent to two logical cores.

First, the results of the conventional version of Gpic-MHD [3], are compared with the results of the new version for $d_e/a=0.06$ and $\rho_s/d_e=1$. For the safety factor profile, we used the monotonically increasing function given by $q(r)=q_0/[1-4(1-q_0)(r/a)^2]$ with $q_0=0.85$. The $q=1$ rational surface resides at $r/a=0.5$. The equilibrium current is generated by the shifted Maxwellian velocity distribution function of electrons. The selected aspect ratio is $R/a=18$ in order to hold the electron drift velocity less than electron thermal velocity. We verified that the both codes generated the almost identical results such as the linear growth phase succeeded by the nonlinear acceleration phase of the growth rate, and the observation of collisionless magnetic reconnection resulting in full reconnection. However it was difficult for the conventional version to obtain physically sound results when we further reduced d_e/a and increased ρ_s/d_e . One of reasons of this limitation is related to the ‘‘cancellation’’ problem. We found that the energy conservation is excellent for the new version.

To show that the new version of Gpic-MHD can approach large scale and high beta parameter range of present and future tokamaks, we made the series of simulation by reducing d_e/a from 0.016 to 0.002 with fixed value of $\rho_s/d_e=3$ and $R/a=18$. The obtained linear growth rates versus d_e/a is shown in Figure 1. The growth rate is normalized by $v_A/2\pi R$ with v_A estimated by B_0 . The number of azimuthal mesh is fixed as 64. The nonuniform radial mesh is used; the mesh is accumulated around the $q=1$ rational surface. The number of radial mesh is increased from 257 to 2049 as d_e/a becomes small (as the size of the system increases). The number of processes is 256 or 512 and the number of threads is 16. The ‘‘particle decomposition’’ is used for the process parallelization in which each process has a replica of the total field quantities. We used MPI (Message Passing Interface) for the processes and auto-parallelization for the threads. The number of the processes multiplied by the number of the threads is equivalent to the number of logical cores in execution. The number of particles per process is one million or 4 millions. For the largest scale case of $d_e/a=0.002$ we used 8192 logical cores and 2.048 billion particles with the wall clock time less than 10 hours. We verified that the obtained linear growth rates are proportional to d_e/a as the theory predicts: $\gamma \propto d_e^{1/3} \rho_s^{2/3}$ for $\rho_s/d_e \gg 1$ [9], which means $\gamma \propto d_e$ for the fixed value

of ρ_s/d_e . The results for the lower value of R/a also confirmed the same results (not presented here). We verified that we are able to simulate large-scale and high-beta tokamaks with the new algorithm, although in the limit of the straight tokamak. We believe that there will be no serious problem when we extend this algorithm to the toroidal geometry.

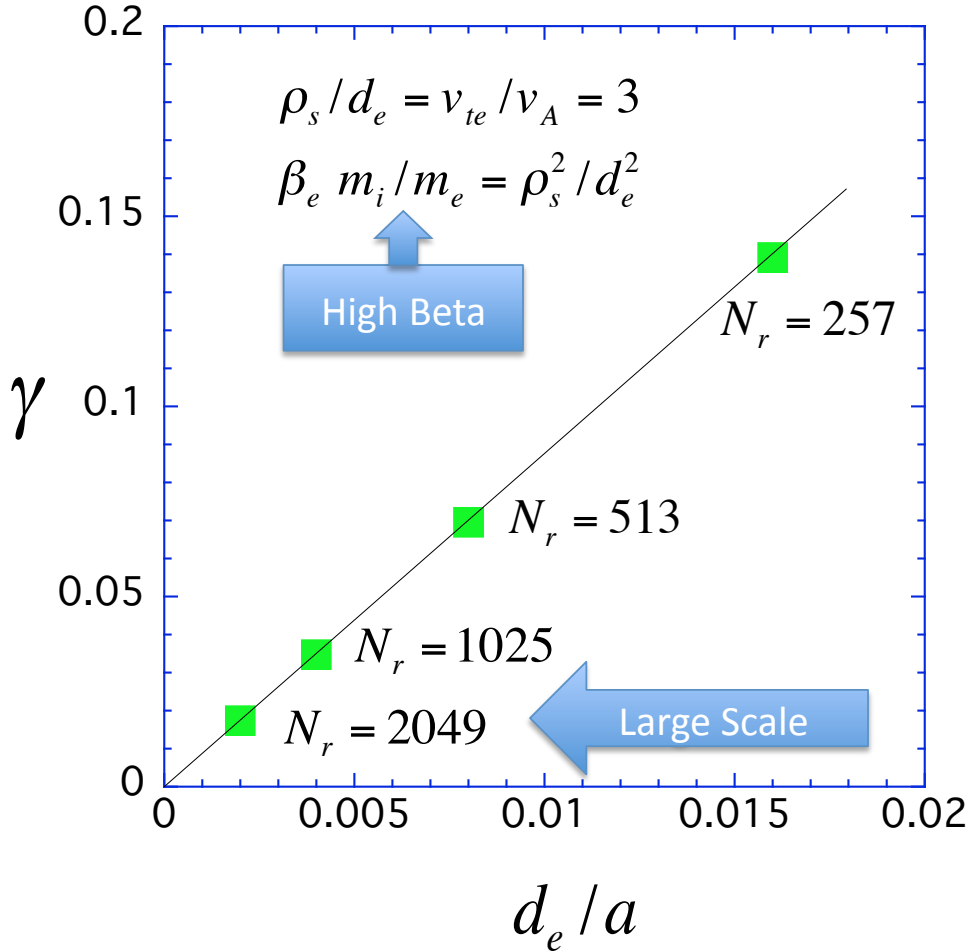


Fig.1 The growth rate versus normalized skin depth. N_r is the number of nonuniform radial meshes which is accumulated around the $q=1$ rational surface.

4. Conclusions and Discussion

The new algorithm for the electromagnetic gyrokinetic PIC code was proposed. In the new algorithm, the vortex equation and the generalized ohm's law along the magnetic field are derived from the basic equations of the

gyrokinetic Vlasov, Poisson, and Ampere system and are used to describe spatio-temporal evolution of ϕ and A_z . Particle information is mainly used to estimate the second order moments in the generalized ohm's law. Because the lower order moments, charge density and longitudinal current density, are not used explicitly to determine ϕ and A_z , the numerical noise induced by the discreteness of particle quantities reduces drastically. Another advantage of the algorithm is that the longitudinal induced electric field, $E_{Tz} = -\partial A_z / \partial t$, is explicitly estimated by the generalized ohm's law and used in the equations of motion. Because we use the v_z -formulation instead of the p_z -formulation, there is no problem of 'cancellation', which appear when estimating A_z from the Ampere's law in p_z -formulation with conventional δf method. The proposed algorithm was installed in the Gpic-MHD code. The simulation of collisionless internal kink mode by new Gpic-MHD demonstrated that we can simulate global and kinetic MHD mode with the realistic parameters of $d_e/a \sim 0.001$ and $\rho_s/d_e > 1$. Therefore the new Gpic-MHD can simulate large scale and high beta tokamak with kinetic effects, which are naturally included in the gyrokinetic PIC code.

There is one essential question of this algorithm, which we cannot answer at present. If we make a very long time scale runs with new Gpic-MHD, the equalities of gyrokinetic Poisson equation and Ampere's law are not assured. The equalities are only guaranteed in the limit of collisionless fluid in the phase space. Once the velocity distribution is approximated by the (marker) particles, the equalities hold only approximately; the difference will increase as time advances. Although up to now we have observed no unphysical phenomena, it is important that we will be very careful to verify the soundness of the simulation results especially in the very long time scale simulations. Because our algorithm is brand-new, the accumulations of well-benchmarked simulation results will finally decide the validity and usefulness of this algorithm.

The new algorithm proposed here gives the alternative to the split-weight method. There is also another alternative named the total characteristic method [10], in which δf estimated by (marker) particles is complemented with the fluid model to satisfy the conservation properties. We are interested in a similarity between two alternatives because both use the lower order moment equations, but the comparison in detail is outside the subject of this article.

From the basic equations of (4), (11), and (12), we can also derive the

gyro-reduced MHD equations as,

$$\frac{\partial}{\partial t} \nabla_{\perp}^2 \phi = -v_A^2 \mathbf{b}^* \cdot \nabla (\nabla_{\perp}^2 A_z) - \frac{\mathbf{b} \times \nabla \phi}{B_0} \cdot \nabla (\nabla_{\perp}^2 \phi), \quad (17)$$

$$\frac{\partial}{\partial t} A_z = -\mathbf{b}^* \cdot \nabla \phi + d_e^2 \frac{d}{dt} (\nabla_{\perp}^2 A_z) + \frac{T_{e0}}{n_{e0} e} \mathbf{b}^* \cdot \nabla n_e, \quad (18)$$

$$\frac{\partial}{\partial t} n_e = -\frac{\mathbf{b} \times \nabla \phi}{B_0} \cdot \nabla n_e - \frac{1}{e \mu_0} \mathbf{b}^* \cdot \nabla (\nabla_{\perp}^2 A_z), \quad (19)$$

where

$$\frac{d}{dt} = \frac{\partial}{\partial t} + \frac{\mathbf{b} \times \nabla \phi}{B_0} \cdot \nabla, \quad (20)$$

is a convective derivative. Based on these equation, we made GRM code [11,12], which is one of extended reduced-MHD codes. Hahm et al. first pointed out the close relation between the gyrokinetic equations and the reduced MHD equations [2]. Eq.(17) is the vortex equation [same as Eq.(11)]. Eq.(18) is the ohm's law along the magnetic field and can be derived from Eq.(18) with some approximation. The isothermal model is assumed for electrons in which electron pressure is approximated by $p_e = T_{e0} n_e$ (T_{e0} is the constant temperature). Eq.(19) describes the conservation of electrons. In the fluid point of view, the lower order moment equations of Eqs.(17) and (18) is closed by estimating second order moment (electron pressure) by the lowest order moment (electron density). In the same terminology, in the new algorithm we closes the moment equations [Eqs.(15) and (16)] by estimating second order moments by the particle information; we can say that we use the ‘‘particle closure’’ or ‘‘complete closure’’ because these equations are derived without approximation from the gyrokinetic equations and should be complete in the collisionless fluid limit in the phase space.

The simulation results presented in the previous section agreed very well with the results obtained by the GRM code. The linear growthrate given by the new Gpic-MHD code are slightly larger than the results by the GRM code. This may come from the fact that the perturbed electron temperature, which is naturally included in Gpic-MHD, has weak destabilizing effects on the internal kink mode.

We have a plan to make a toroidal version based on this new Gpic-MHD code in the near future. We believe that, in principle, the algorithm proposed in this article is applicable to the toroidal version.

Acknowledgements

This work was partially supported by the JSPS-CAS Core University program in the field of 'Plasma and Nuclear Fusion', Grant-in-Aid for Scientific Research (C) (20560766), collaboration programs between universities and JAEA (22K450), and universities and NIFS (NIFS09KTBL009).

References

- 1) W. W. Lee, *J. Comput. Phys.* **72**, 243-269 (1987).
- 2) T. S. Hahm, W. W. Lee, A. Brizard, *Phys. Fluids* **31**, 1940-1948 (1988).
- 3) H. Naitou, H. Hashimoto, Y. Yamada, S. Tokuda, M. Yagi, *J. Plasma Fusion Res. SERIES 8*, 1158-1161 (2009).
- 4) H. Naitou, K. Tsuda, W. W. Lee, R. D. Sydora, *Phys. Plasmas* **2**, 4257-4268 (1995).
- 5) H. Naitou, T. Sonoda, S. Tokuda, V. K. Decyk, *J. Plasma Fusion Res.* **72**, 259-269 (1996).
- 6) I. Manuilskiy, W. W. Lee, *Phys. Plasmas* **7**, 1381-1385 (2000).
- 7) W. W. Lee, J. L. V. Lewandowski, T. S. Hahm, Z. Lin, *Phys. Plasmas* **8**, 4435-4440 (2001).
- 8) H. Naitou, K. Kobayashi, H. Hashimoto, T. Andachi, W. W. Lee, S. Tokuda, M. Yagi, *Bull. APS 51st Annual Meeting of the Division of Plasma Physics*, Nov. 2-6, 2009, Atlanta, Georgia (2009).
- 9) F. Porcelli, *Phys. Rev. Lett.* **28**, 425-428 (1991).
- 10) Y. Todo, A. Ito, *Plasma Fusion Res.* **2**, 020-1-5 (2007).
- 11) H. Naitou, T. Kobayashi, K. Kuramoto, S. Tokuda, T. Matsumoto, *J. Plasma Fusion Res. SERIES 2*, 259-262 (1999).
- 12) H. Naitou, T. Kuramoto, T. Kobayashi, M. Yagi, S. Tokuda, T. Matsumoto, *J. Plasma Fusion Res.* **76**, 778-789 (2000).

Full Particle Simulation of a Tokamak Plasma with Open-field SOL-Divertor Region

T. Takizuka

Japan Atomic Energy Agency, Naka Fusion Institute, Naka 311-0193, Japan

Abstract In order to investigate the power and particle control with diveror system of fusion reactors, numerical simulations have been widely carried out. Fluid codes require further improvement of physics modeling for edge plasmas. The full particle simulation is powerful to study fundamental physics of open-field SOL-divertor plasmas as well as of the whole tokamak plasma including SOL-divertor region. PARASOL code with PIC method and binary collision model has been developed in JAERI and JAEA. Simulations with PARASOL code have been carried out for the above purpose. The one-dimensional (1D) version of PARASOL was applied to investigate the Bohm criterion, the supersonic flow, the SOL heat conduction, and so on. The ELM heat propagation was studied with the 1D-dynamic PARASOL. The two-dimensional version of PARASOL for the whole tokamak plasma with SOL-divertor region was useful to simulate the SOL flow pattern, the electric field formation etc. Based on PARASOL simulation results, physics modeling for the fluid simulation has been constructed.

1 Introduction

Power and particle control is one of the most important issues in the magnetic-confinement nuclear fusion research and development^[1]. Large heat flux to the divertor plates in the fusion reactors is worried about from the viewpoint of lifetime reduction of the divertor plates. In order to design the divertor equipment and to plan the operation scenario, numerical simulations have been widely carried out. The edge plasma including scrape-off layer (SOL) and divertor regions is very complicated due to many interactive processes among fuel plasmas, impurities, neutral particles, and wall-surfaces in the complex geometries of magnetic configuration and wall. Comprehensive divertor codes employing plasma fluid equations are used for the simulation of such a complex system^[2,3]. In the plasma fluid equations, however, several physics models are to be applied, such as the boundary condition of flow velocity at the divertor plate, the heat conduction parallel to magnetic field and so on^[2,3].

To examine the validity of the above physics models, kinetic studies are indispensable. One of the most powerful kinetic approaches is the particle simulation^[3~6]. There were many particle codes to study plasma physics phenomena with periodic condition along the magnetic field direction. We have been developing an electrostatic particle-in-cell (PIC) code called PARASOL (PARTicle Advanced simulation of SOL and divertor plasmas) and studying the basic physics of SOL-divertor plasmas. The PIC model handles the full particles unlike the δf model that assumes a fixed known background distribution function. The full particle simulation is able to realize a kinetic equilibrium far from the Maxwellian in edge plasmas, although it accompanies the large numerical noise^[7]. Because the relaxation process of velocity distributions is naturally important, Monte Carlo (MC) modeling for Coulomb collisions as well as for atomic-molecular reactions is introduced into PARASOL. PARASOL code now is applied to the simulation of a whole tokamak plasma with open-field SOL-divertor region. This paper reviews the history of the development of PARASOL code and the simulation study by using PARASOL.

2 Prehistory of PARASOL

In a scrape-off layer plasma touching the divertor plate, the self-consistent electrostatic field, i.e., sheath and pre-sheath field, plays an important role. Velocity distribution functions of electrons and ions are distorted remarkably from the Maxwellian. Therefore, the electrostatic particle model is suitable to study divertor plasmas.

As the first code of PIC model for divertor plasma simulation, we in JAERI (Japan Atomic Energy Research Institute, the predecessor of the present JAEA; Japan Atomic Energy Agency) developed a two-dimensional (2D) code before 1980. We found that in the SOL of a poloidal divertor tokamak the plasma flow together with the pre-sheath are formed due to the particle source supplied by the cross-field diffusion^[8]. In this code, a random-walk MC technique was introduced for the cross-field diffusion, while the collisional scattering in the velocity space was not taken into account.

Abreast of our earlier simulation, Chodura studied the transition layer between a plasma and a wall in an oblique magnetic field by using a one-dimensional (1D) collisionless PIC model. It was found that the magnetic pre-sheath is formed with the scale length of the ion Larmor radius^[9]. Note that the velocity distributions of electrons and ions were given at the upstream boundary in this model.

Coulomb collisions play a very important role in open-field plasmas. For instance, the collisional diffusion in the velocity space is the main mechanism to supply high-energy electrons. These electrons can escape to the divertor plate, while low-energy electrons are trapped in a SOL plasma by the sheath potential. Therefore we introduced to our PIC code a binary collision model, so-called Takizuka-Abe model^[10], utilizing MC techniques. Characteristics of SOL-divertor plasmas were studied by using the 1D version of this code. Dependence of plasma parameters, such as temperature, flow speed, pre-sheath potential, heat flux, etc., on the collisionality was investigated in detail. The pre-sheath with the scale length of the system size is formed by the collisional relaxation of the velocity distribution^[11]. In addition to the hot particle source in the central SOL region, recycling cold particles were supplied near the divertor plates. Effects of the recycling on the SOL plasma characteristics were also investigated^[12].

In this prehistoric era, 1976~1985, we used the single-CPU scalar computers, FACOM 230-75, FACOM M200 and FACOM M380, whose speeds were of the order of 10 MFLOPS. The number of simulation ions was only 2000~5000. It took several hours for a simulation run with $\sim 10^4$ time steps.

3 Model of PARASOL

After a long rest, the particle simulation activity on the tokamak edge plasma was revived under the NEXT (Numerical EXperiment of Tokamak) project^[13] started since 1995 in JAERI. Massively parallel computer systems have become available in JAERI. The particle code mentioned above was parallelized, and afterwards called PARASOL^[3,14~16]. A domain decomposition method with putting a master PE is adopted for the PARASOL parallelization, because this method is well suited to the Takizuka-Abe binary collision model.

The development of the PARASOL code, parallelization and extension of models, has been proceeded with under the NEXT project at first, and now under the integrated modeling project^[17,18]. A standpoint of PARASOL in the integrated modeling is to establish reliable physics models for the comprehensive divertor codes, such as SONIC developed in JAEA^[19~21].

The PARASOL code is fundamentally a time-dependent electrostatic PIC code incorporating a binary collision model. Physics model of PARASOL was described detailedly in previous papers^[3,15,16], and its schematic is shown here in Fig. 1.

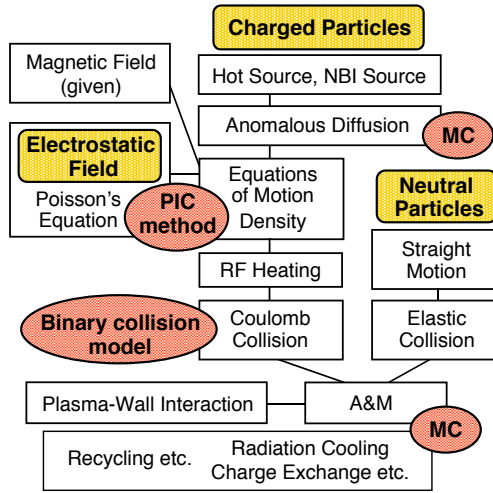


Fig.1 Schematic of physics model of PARASOL code

The simulation domain is surrounded by walls, and part of (or all) field lines of a given magnetic configuration intersect the walls. The system consists of charged particles and neutral particles. Ion orbits are fully traced in this given magnetic field, while guiding-center orbits are followed for electrons. The effect of drift in SOL-divertor plasmas is fully simulated by the PARASOL code. The full-orbit calculation provides a complete description of the ion polarization drift, which is essential for magnetic pre-sheath formation^[8,13]. The electrostatic potential, including the sheath potential at the plasma-wall boundary, is self-consistently calculated with a general PIC method. Although the system size L is very much larger than the Debye length λ_D in real plasmas, PARASOL simulations with the grid size Δ of the order of λ_D are available to study such plasmas with smaller values of $L/\lambda_D = 10^2 \sim 10^3$. This is because the characteristics of SOL-divertor plasmas under the quasi-neutral condition, except in the sheath region, are determined mainly by collisionality and normalized ion Larmor radius but insensitive to the L/λ_D value as shown in Fig. 2. As we put an artificially shortened system, we at the same time adopt a “collision cut-off technique” near the wall to keep the collisionless sheath condition.

At every time step after computing the collisionless motion, the velocity changes are given by the binary collision MC algorithm^[10]. A particle suffers binary collisions with an ion and an electron, which are chosen randomly in the same cell. The angle of the relative velocity is scattered in accordance with the Coulomb force. Total momentum and total energy are conserved intrinsically.

Present PARASOL code does not self-consistently simulate the turbulence driving the anomalous diffusion, because the system is limited to 1D or 2D. The anomalous transport across the magnetic field is simulated with an MC random-walk model.

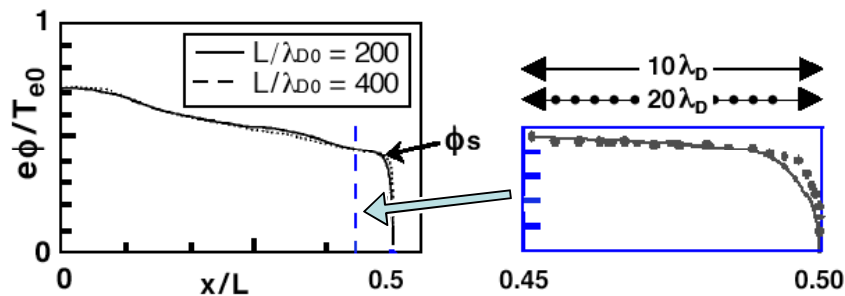


Fig.2 Potential profiles for different L/λ_D values. The same profiles are established except for sheath region $d < 5\lambda_D$ (right figure).

Several physics models for the source, sink, heating and cooling are provided in the PARASOL. For example in 1D PARASOL code, hot particle source is located in the central SOL region and cold particle source (corresponding to recycling particles) located near the divertor plate. Main sink of the particle is the flow into the divertor plate. Instead of the self-consistent tracing of neutral particles, atomic and molecular (A&M) reactions are often simulated with MC techniques. Energy loss corresponding to radiation cooling, momentum loss corresponding to charge-exchange reactions etc. are equipped.

Simulation results to be seen are averaged in time over a hundred time steps much longer than the plasma period. For the simulations of stationary plasmas, the averaging duration is more than a thousand time steps.

4 1D simulations

Boundary condition of the plasma flow velocity at the plasma-wall transition is to be clarified for the accurate fluid modeling. A simple one was the Bohm criterion, $V_{||} = C_s \equiv [(T_e + T_i)/m_i]^{1/2}$, where $V_{||}$ is the flow speed parallel to the magnetic field, C_s the sound speed, T_e (T_i) the electron (ion) temperature, and m_i the ion mass^[2]. Effects of radial electric field E_r , which generates $E \times B$ drift V_E towards the divertor plate, were investigated by the use of 1D PARASOL^[14]. The magnetic field line penetrates the plate obliquely with the pitch $\Theta = B_x/B \ll 1$ (x -direction is normal to the plate). Radial electric field was uniformly added. A boundary condition was found including the drift V_E : $V_x = \Theta V_{||} + V_E = \Theta C_{s*}$, where the specific sound speed $C_{s*} \equiv [(T_{e||} + \gamma_a T_{i||})/m_i]^{1/2}$ is defined by using the parallel temperature $T_{||}$ and an adiabatic index $\gamma_a \approx 3$ for $T_{i||}/T_{e||} < 1$. Figure 3 shows a simulation result, where the profiles of density n and parallel flow $V_{||}$ become asymmetric due to V_E . In accordance with the above boundary condition, the velocity towards plates V_x is almost symmetric between left and right, while the parallel velocity $V_{||}$ is remarkably asymmetric. The density becomes lower in a divertor region where $E \times B$ drift flows out from the plate. The asymmetry becomes large with the increase of V_E .

The flow speed at the sheath entrance is forced to exceed the specific sound speed when the divertor plasma is cooled below a critical value. This supersonic flow was really found by PARASOL simulation^[22]. The condition of supersonic is determined by an index of cooling, $C \equiv (R_r/R_p) (T_{\text{plate}}/T_{\text{throat}})^{1/2}$, where R_r is the particle flux amplification factor, R_p the momentum flux loss factor, and suffixes in T denote the positions at divertor plate and divertor throat. In the usual case of $C > 1$, the Mach number M at the plate is unity $M_{\text{plate}} = 1$, and at the throat $M_{\text{throat}} = C - (C^2 - 1)^{1/2}$ is less than unity. When divertor cooling is

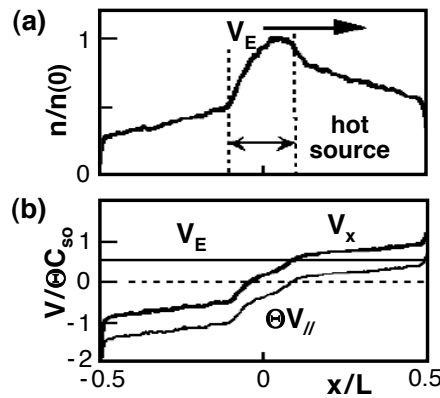


Fig.3 Profiles of (a) density n and (b) velocities V_E , $\Theta V_{||}$ and V_x for $\Theta = 0.2$ and $V_E = 0.55 \Theta C_{s0}$. Hot particle source is put in the central region ($-0.1 < x/L < 0.1$) and the plasma flows out to divertor plates at $x/L = \pm 0.5$. Sound speed C_{s0} is defined by the hot source electron temperature T_{e0} as $C_{s0} = (T_{e0}/m_i)^{1/2}$. Asymmetry in profiles is induced by the $E \times B$ drift

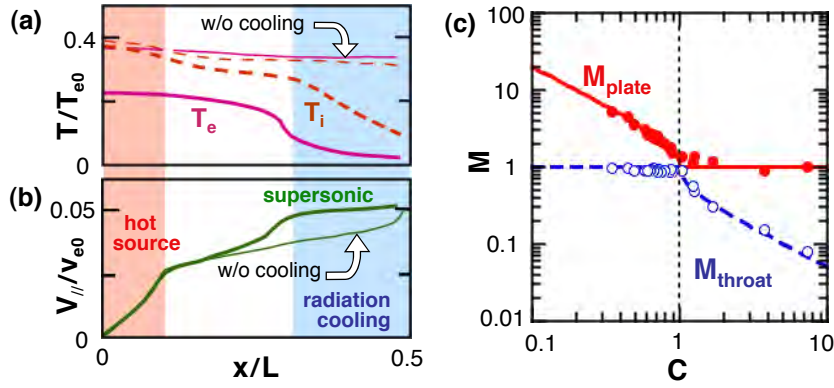


Fig.4 Profiles of (a) temperature T and (b) flow velocity $V_{||}$ for the case without cooling (solid lines) and the case with radiation cooling near the divertor plate (dashed lines). Supersonic flow arises in the cold divertor region. Dependence of Mach number M on cooling index C is shown in (c). Good agreement between simulation results (circles) and analysis expression (solid line for M_{plate} at the plate and dashed line for M_{throat} at the throat)

enhanced to $C < 1$, the Mach number $M_{\text{plate}} = C^{-1} + (C^{-2} - 1)^{1/2}$ becomes larger than unity while $M_{\text{throat}} = 1$. The simulation results agreed very well with these analytical expressions as demonstrated in Fig. 4(c) [22].

Computation time was about 8 hours with 64 PEs in Intel Paragon XP/S (75 MFLOPS/PE) for a run of above studies with 10^5 ions and 6×10^4 time steps. This was in the period 1996~2000. Compare with the small number of ions $< 5 \times 10^3$ used in the prehistoric era.

The heat conductive flux $q_{||}$ parallel to the magnetic field in a SOL plasma is considered for the fluid modeling to be a collisional diffusive one, usually given by the so-called Spitzer-Harm formula $q_{||} = q_{\text{SH}} \equiv -\kappa_{||} \nabla_{||} T \propto n^0 T^{7/2}$ ($\kappa_{||}$ is the thermal conductivity). When the collision mean-free-path l_{mfp} becomes longer than the SOL connection length $L_{||}$, the heat conduction is no more the diffusive transport but becomes the free-stream-like transport; $q_{||} \propto q_{\text{FS}} \equiv n T v_{\text{th}} \propto n T^{3/2}$ ($v_{\text{th}} \equiv (T/m)^{1/2}$ is the thermal speed). For the bridge from the short l_{mfp} case to the long l_{mfp} case, a harmonic average can be applied; $(q_{||})^{-1} = (q_{\text{SH}})^{-1} + (\alpha q_{\text{FS}})^{-1}$. Here α is the flux-limiting coefficient important to determine the collisionless SOL plasma transport. Results of divertor simulations with fluid modeling are sometimes affected much by the choice of α value. There have been many studies on the α value and resultantly wide-range of α values from much smaller than unity to the order of unity [23,24,15]. In order to clarify the reason of the spread of the α value, we have carried out the 1D PARASOL simulation [25~27]. The hot plasma is supplied in the central SOL region, and is lost to the divertor plates. The electron energy is cooled by radiation near the divertor plate. For the various plasma parameters, such as the ratio of l_{mfp} to the connection length $L_{||}$ and radiation loss fraction f_{rad} , the electron heat flux $q_{e||}$ is measured in the intermediate region between the source region and the radiation region. Figure 5(a) left shows the dependence of $q_{e||}$ on of l_{mfp} . It is found that the PARASOL simulation agrees with the fluid approximation of $q_{e||} = q_{\text{SH}}$ in the collisional regime, $l_{\text{mfp}}/L_{||} \ll 1$. On the other hand, the ratio $q_{e||}/q_{\text{SH}}$ decreases gradually with the increase of $l_{\text{mfp}}/L_{||}$ above unity. When we compare $q_{e||}$ with q_{FS} , the ratio $q_{e||}/q_{\text{FS}}$ is very small in the collisional plasma and increases with the increase of $l_{\text{mfp}}/L_{||}$. Finally in the collisionless regime, $l_{\text{mfp}}/L_{||} \gg 1$, $q_{e||}/q_{\text{FS}}$ saturates in a certain value. This value is measured for the electron flux-limiting coefficient α_e . We discover that one of major reasons of the spread in the α_e value is the functional dependence of α_e on the radiation loss fraction f_{rad} ; α_e is much smaller than unity for small f_{rad} case, α_e gradually increases with f_{rad} , and α_e becomes as large as the order of unity for large f_{rad} case as shown in Fig. 5(b).

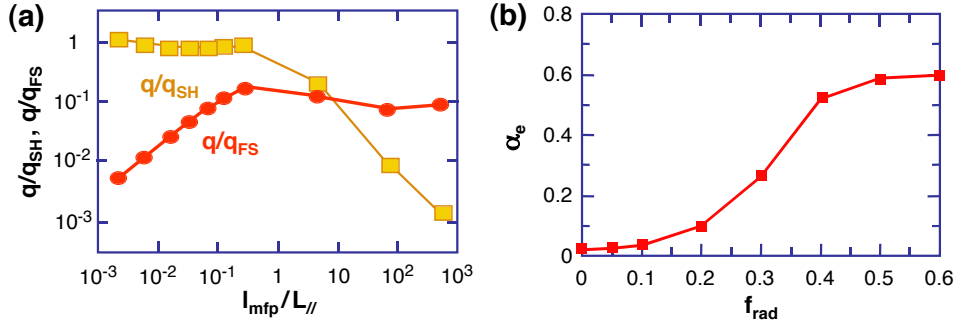


Fig.5 (a) Parallel heat conduction flux q normalized by q_{SH} (square symbols) and q_{FS} (circle symbols) depending on the ratio of mean free path l_{mfp} to connection length $L_{||}$ for radiation fraction $f_{rad} = 0.2$. (b) Heat flux-limiting coefficient of electrons $\alpha_e = q/q_{FS}$ in the long l_{mfp} limit increases with f_{rad}

5 1D dynamic simulation of ELM heat propagation

Enhanced heat flux to the divertor plates after an ELM crash in H-mode operation is really a crucial issue for the power and particle control in the tokamak reactor^[1]. Characteristic time of this heat flux is one of key factors of the influence on the plate. We have investigated the transient behavior of SOL-divertor plasmas after an ELM crash with the use of a 1D PARASOL^[28,30,31]. We adopt a simple model for an ELM crash. Before simulating an ELM crash, a slowly varying simulation is performed to achieve a stationary phase. During a stationary phase with N_{i0} ions in the system, an ELM crash suddenly supplies a large number of hotter particles (N_{ELM} pairs of electrons and ions) in a short period, $t_{ELM} < t < t_{ELM} + \tau_{ELM}$. These pairs are generated in the middle region of the SOL plasma. The shift from the center represents the ELM-source asymmetry. Temperatures of ELM-supplied electrons and ions, T_{eELM} and T_{iELM} , are higher than those of stationary source, T_{e0} and T_{i0} .

Influence of the collisionality and the recycling rate on characteristic times of the fast-time-scale response and of the slow-time-scale response was examined^[28]. Figure 6 shows that the fast-time-scale behaviors are affected by collisions. Supra-thermal electrons are supplied by the ELM crash. These electrons are lost rapidly from the central SOL region to the divertor plates. The resultant large heat flux Q_e appears at the plate soon after the crash for low collisionality. The loss of supra-thermal electrons induces the high sheath potential ϕ with the same fast-time-scale of Q_e . On the other hand the time scale of T_e is governed by the thermal electrons. In the early phase after the crash, Q_e and ϕ become soon very high but T_e is still low. This means the appearance of an extremely large heat transmission factor and higher sheath potential than that for Maxwellian electrons. When the collisionality increases, supra-thermal electrons are thermalized before reaching the plate. The large peak of Q_e in the early phase is reduced by collisions, and the heat transmission factor decreases gradually. The decrease of supra-thermal electrons in the collisional plasma makes the value of ϕ being proportional to T_e , $e\phi/T_e \sim 3$.

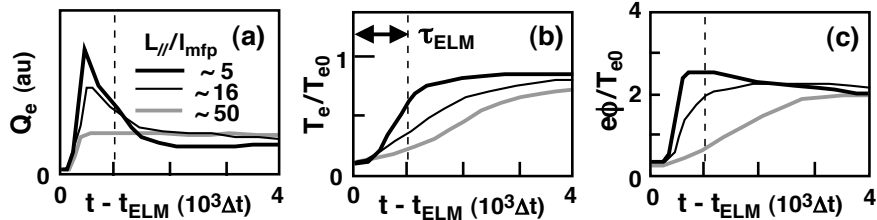


Fig.6 Fast-time-scale behaviors of (a) electron heat flux Q_e , (b) electron temperature T_e and (c) potential ϕ , in front of the divertor plate, for different collisionalities $L_{||}/l_{mfp}$. ELM source is given as $N_{ELM} = N_{i0}$ and $T_{eELM} = 2T_{e0}$

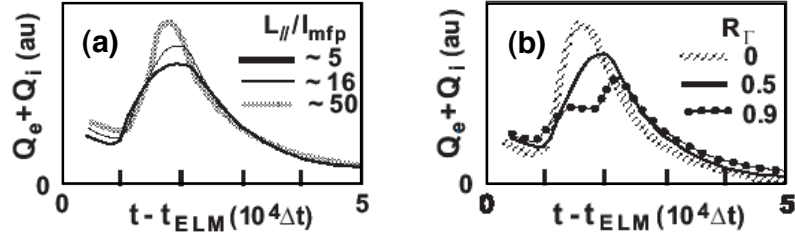


Fig.7 Slow-time-scale behaviors of total heat flux $Q_e + Q_i$ to the divertor plate for (a) different collisionalities $L_{||}/l_{mfp}$ and for (b) different recycling rates R_r .

As for the slow-time-scale behavior, there was a prediction that the time of the particle flux peak could depend on the collisionality^[29]. The simulation results did not support this prediction. Figure 7 shows the behavior of total heat flux $Q = Q_e + Q_i$ to the plate for (a) various collisionality $L_{||}/l_{mfp}$ and for (b) various recycling rate R_r . The characteristic time of Q is governed mainly by the sound speed in the central SOL region. The characteristic time of slow-time-scale behavior is insensitive to $L_{||}/l_{mfp}$ compared with the fast-time-scale behavior, though the peak values of Q are varied by $L_{||}/l_{mfp}$. On the other hand, the slow-time-scale phenomena are affected by the recycling condition. The time of the Q peak is delayed by the increase of R_r , though the arrival time of Q is not changed by R_r . This is because the recycling influences the enhanced fluxes only after the enhanced particle flux arrives at the plate. Large recycling makes the flow speed small in the central SOL region, and the Q peak is forced to be delayed.

Dynamics of SOL-divertor plasmas after an ELM crash, especially in the presence of the asymmetry, have also been studied^[30,31]. Asymmetry in the heat flux due to recycling asymmetry is extinguished by the symmetric ELM. On the other hand, ELM-source asymmetry brings the asymmetry in the heat flux. Electron heat propagation is governed by conduction, while majority of the heat is transported by convection with sound-speed time scale and its propagation time is linearly proportional to the parallel connection length^[30]. The peak heat flux to the near plate is larger as compared to the far plate. Even when the ELM heat flux is asymmetric, the induced SOL current brings the electron heat flux to suppress the imbalance of the heat deposition^[31].

The above 1D dynamic simulations of ELM propagation were carried out in the period 2003~2007. Computation time was about 1 hour with 128 PEs in SGI Altix 3700Bx2 (6 GFLOPS/PE) for a run with the number of ions $N_i > 10^5$ and time steps $K_t > 10^5$.

6 2D simulation of SOL flow patterns

Plasma flow in the SOL plays an important role for the power and particle control in fusion reactors, such as ITER. The flow is expected to expel Helium ashes and to retain impurities enhancing the radiative cooling in the divertor region, if the flow is directed towards the divertor plate. It has been experimentally observed, however, that the flow direction is sometimes opposite; from the plate side to the SOL middle side in the outer SOL region (low field side) of tokamaks. This backward flow is seen when the single null point is located in the ion ∇B drift direction, while it vanishes for the reversed null-point location^[32]. The SOL flow structure is affected by various physical factors. Among them the drift flow has been considered to be especially important for the flow-structure variation due to the change of null-point location. On this flow-structure problem, many simulation studies have been carried out with the fluid model (see references in [3]). Simulation results were compared with experimental results, but their agreements were not satisfactorily achieved and the essential physics mechanism of the SOL flow formation was not fully known. Kinetic simulations are considered to bring a breakthrough on this subject^[19]. Using the particle code PARASOL, we started to investigate the structure of SOL flow in 2D slab geometry^[33] and

in straight-tokamak divertor geometry^[34]. It was found that the SOL flow structure is much affected by the flow speed criterion at the 2D plasma-sheath interface. The asymmetry in the flow structure is induced, but the tendency of this asymmetry does not agree with the experimental observation in tokamak SOL plasmas.

We recently studied the SOL flow patterns with the PARASOL in the axisymmetric toroidal geometry shown in Fig. 8(a)^[16]. The number of simulation ions N_i was 10^6 in the 2D spatial cells 320×512 . The hot source is given uniformly in the core region. Hot particles diffuse out to the SOL region and flow into the divertor plates. Achieved steady-state profiles of electron density n_e and electron temperature T_e are shown in Fig. 8 (b) and (c), respectively. The SOL flow pattern in this steady state was investigated.

Figure 9 shows the 2D structures of the flow parallel to the magnetic field ($V_{||}$) in a tokamak with an aspect ratio $A = 5.5$ and the downward ion ∇B drift. The flow pattern is changed by the position of a null point; (a) UN (upper-null) configuration or (b) LN (lower-null) configuration. In the figure, the co-flow to the plasma current (anti-clockwise in the poloidal cross-section) and the counter-flow (clockwise) are represented by arrows. For the UN case with the ion ∇B drift away from the null point, the parallel flow velocity $V_{||}$ is directed to the divertor plate both in the inner (high-field-side) and outer (low-field-side)

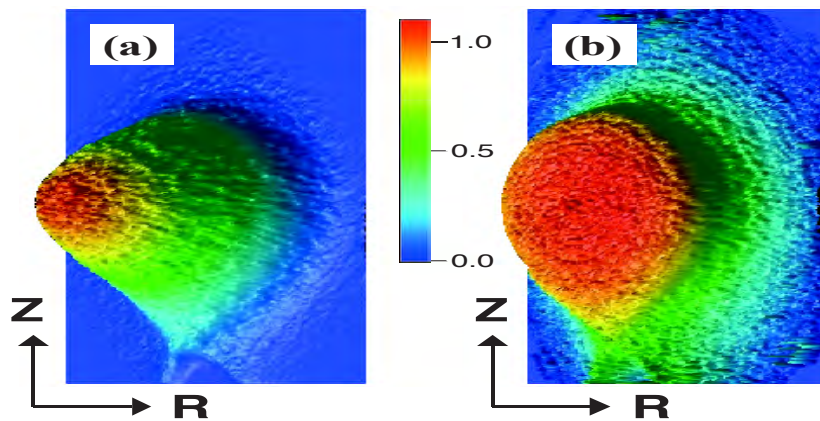


Fig.8 (a) Axisymmetric 2D geometry for PARASOL simulation of SOL flow patterns in tokamak plasma with divertor configuration. Bird-eye view of steady-state profiles of (b) electron density and (c) electron temperature

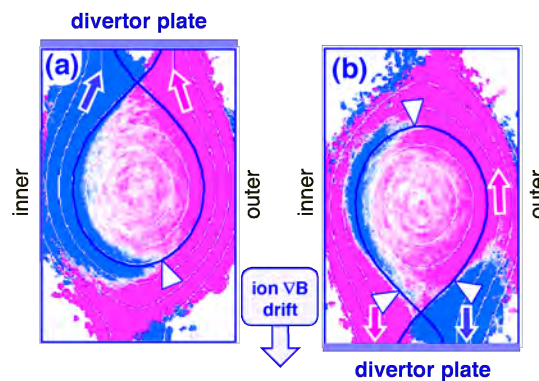


Fig.9 2D structures of parallel flow $V_{||}$ in a tokamak with $A = 5.5$. Flow pattern is varied by the null-point location; (a) UN configuration with the ion ∇B drift away from the null point or (b) LN configuration with the ion ∇B drift toward the null point. Inner divertor plate is in the left side and outer plate is in the right side for each figure. Stagnation points ($V_{||} = 0$) are important information to distinguish the flow patterns, and those just outside the separatrix are indicated by open triangles

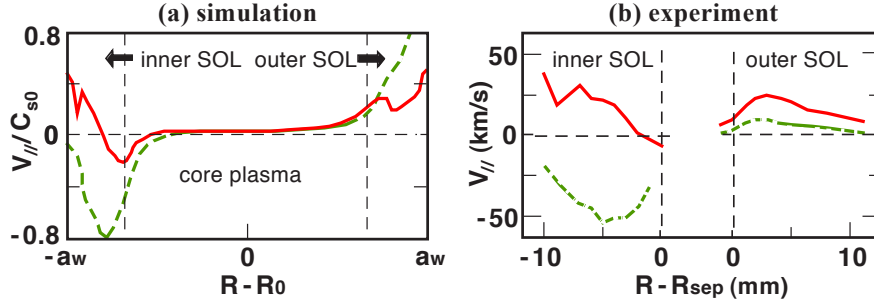


Fig.10 Radial profiles of $V_{||}$ for UN configuration (dashed green line) and LN configuration (solid red line). Vertical dashed line denotes the position of separatrix. PARASOL simulation result (a) is the equatorial profile. Experimental results of Alcator C-Mod (from figure 5 in [35]) are shown in (b) where $V_{||}$ profiles in the inner SOL and the outer SOL are separately plotted

SOL regions and the stagnation point ($V_{||} = 0$) is located symmetrically at the bottom. On the other hand for the LN case with the ion ∇B drift toward the null point, $V_{||}$ in the outer SOL region has a backward flow pattern (anti-clockwise flow near the outer mid-plane). The stagnation point moves below the mid-plane of the outer SOL. It is noted that an island of the backward flow is observed in the inner SOL near the separatrix (clockwise flow near the inner mid-plane separatrix). Comparing with the experimental results from Alcator C-Mod [35], we confirmed the PARASOL simulation results being very similar to them qualitatively and quantitatively as shown in Fig. 10.

In order to find the essential factors to form the SOL flow pattern, we carried out the simulations by artificially cutting the electric field \mathbf{E} . Collisional interaction between ions and electrons is maintained. It is interestingly found that the change in the stagnation-point positions is small between for the full simulation and for the $\mathbf{E} = 0$ simulation; the stagnation point lies near the symmetric bottom position in the UN configuration, and the three stagnation points keep their positions in the LN case. On the contrary, we observed a clear change in the flow pattern when compared the full simulation and $\mathbf{E} = 0$ simulation for the straight-tokamak ($A = 1000$); in the full simulation the SOL flow pattern is fully asymmetric with a single stagnation point is located much far from the center, while in the $\mathbf{E} = 0$ simulation a completely symmetric flow pattern is realized [16].

In the artificial simulation with $\mathbf{E} = 0$, the plasma flow is determined only by ion motions w/o \mathbf{E} . Above simulations for the medium aspect ratio case demonstrated that the change in the SOL flow pattern with \mathbf{E} and w/o \mathbf{E} was not large. Therefore, we can infer that the SOL flow pattern in standard tokamaks with $A < 5$ is governed mainly by the ion orbits rather than by the self-consistent electric field.

Based on the above simulation results, we presented a new model of the edge plasma flow by introducing the “ion-orbit-induced flow”. We take account of the finite ion orbit effect to the fluid equations. The guiding center orbit of an ion is horizontally shifted from a magnetic surface in a tokamak by the curvature- ∇B drift. An ion with the co- $v_{||}$ is shifted outward (to the low field side), while an ion with the counter- $v_{||}$ is shifted inward (to the high field side). Say a banana orbit of a trapped ion drifted out from the core generates the co-flow in the outer SOL region. In a UN configuration, this “ion-orbit-induced flow” is an additive flow to the original SOL flow towards the upper divertor plate in the outer SOL. On the contrary, in a LN configuration, the “ion-orbit-induced flow” is a subtractive flow from the original SOL flow towards the lower divertor plate in the outer SOL. This “ion-orbit-induced flow” causes the variation of flow patterns in the UN- and LN- divertor configurations. A new analytic model of “ion-orbit-induced flow” for the fluid equations is presented in Ref. [36].

7 Formation of radial electric field in tokamak plasmas

It is widely recognized that the electric field (or $E \times B$ drift flow shear) significantly affects the transport of the magnetically confined plasma, but it has not fully been understood how the electric field is formed. The stationary electrostatic field is determined so that electron and ion particle transports are balanced. In an open-field configuration, such as SOL-divertor plasmas, electrons flow out faster to the wall, and the SOL plasma potential becomes positive against the wall. On the other hand, in an axisymmetric closed-field configuration such as a tokamak core plasma, the cross-field transport is mainly ambipolar, and it is not obvious which flows out faster. The effect of SOL region on the core region is not fully clarified as well. Using 2D PARASOL code, we studied the structure of electrostatic field in a whole tokamak plasma including open-field SOL-divertor region^[37].

Even for a straight-tokamak without any neo-classical effect, we found that a stationary structure of the electrostatic field is formed depending on the magnitude of normalized ion Larmor radius $\rho^* \equiv \rho_i/a$. Figure 11 shows two types of the potential profile, (a) convex profile for small ρ^* and (b) hollow profile for large ρ^* . Note that the density profile is unchanged by the ρ^* value. In the SOL region, electrons are lost faster than ions, the charge density is positive, and the potential ϕ becomes positive. In the core plasma near the separatrix, the charge density is still positive continuously from the SOL. When ρ^* is small enough, the positively charge-up state is maintained even in the central region. Resultantly whole ϕ profile forms monotonically upward convex. When ρ^* is large, the ion diffusion can exceed the electron diffusion. It has been evaluated that the classical diffusion is brought by collisions between unlike particles. When ρ^* is large and an ion feels the second derivative of ion density, the ion diffusive movements can be generated by the ion-ion collision. This effective diffusion coefficient of ions is roughly given by $D_{i,\text{eff}} \approx \nu_{ii} \rho_i^4 (n_i^{-1} d^2 n_i / dr^2)$. As a result, ions escape faster than electrons across the field line in the core region. The charge density, which is positive near the separatrix, tends to be negative in the central region. The ϕ profile thus becomes hollow. The saturation mechanism of the growing negative E_r is brought by the shift of guiding center of an ion just born from the ionization of a neutral. The shift is given by $\Delta r = E_r / B \Omega_i$ and the resultant current can reduce E_r . Finally a stationary hollow profile of ϕ is formed.

The structure of electrostatic field is changed much by the toroidal configuration of tokamak plasmas. Figure 12 shows the radial profiles of ϕ ; (a) ρ^* dependence for straight-tokamak ($A = 1000$), (b) aspect ratio A dependence for small $\rho^* = 0.022$ with constant $\Theta = 0.2$, (c) magnetic field pitch Θ dependence for $A = 5.5$, and (d) ρ^* dependence for $A = 5.5$ and $\Theta = 0.2$. It is clearly seen in Fig. 12(b) that the hollow profile of ϕ appears easily in the usual tokamak plasma with finite aspect ratio. The hollow becomes deeper with decreasing A . The major cause to create the hollow ϕ profile could be the trapped ions; their fraction $F_{\text{trap}} \sim 1/A^{1/2}$ and banana orbit size $\rho_{\text{banana}} \sim \rho_i/A^{1/2}\Theta$. As Θ decreases and ρ_{banana} increases, the hollow becomes deeper. Similarly, as ρ^* increases and ρ_{banana} increases, the hollow becomes deeper.

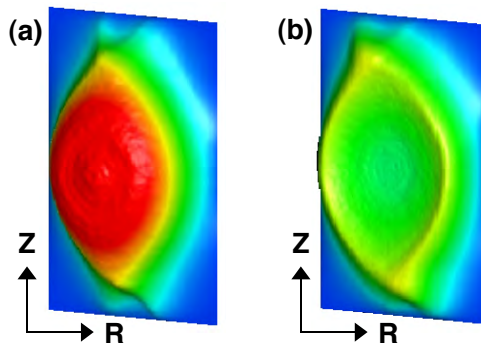


Fig.11 Bird-eye view of stationary profile of electrostatic potential for (a) small $\rho^* = 0.022$ and for (b) large $\rho^* =$

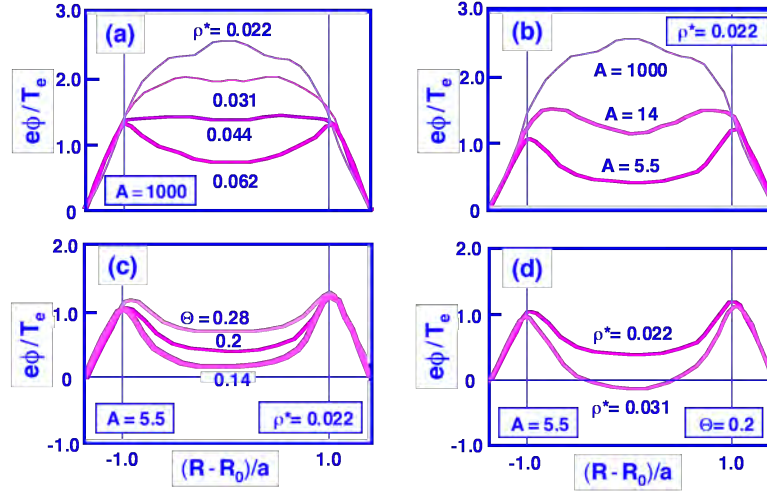


Fig.12 Radial profiles of electrostatic potential ϕ ; (a) ρ^* dependence for $A = 1000$, (b) A dependence for $\rho^* = 0.022$, (c) Θ dependence for $A = 5.5$ and $\rho^* = 0.022$, and (d) ρ^* dependence for $A = 5.5$ and $\Theta = 0.2$. Vertical thin lines denote the position of separatrix

It should be noted that there is small differences between ρ_{banana} dependence and ρ^* dependence. The effect of ρ_{banana} works near the edge region to steepen the ϕ gradient (strengthen the negative E_r), changes little the flat ϕ profile in the central region. On the other hand the effect of ρ^* changes the hollow ϕ profile globally.

The ϕ profile (E_r profile) is changed remarkably by the plasma rotation in tokamaks. This phenomenon was simulated by the PARASOL^[38]. As a model of neutral beam injection, pairs of energetic ion and cold electron are supplied in the central core region (beam-injection region). Large numbers of warm ions and electrons are poured into the plasma periphery. Radial profiles of electron density n_e , electron temperature T_e and ion temperature T_i in the steady state are shown in Fig. 13. Cases of co- or counter- injection into a straight- or standard- tokamak are compared in Fig. 14. Profiles of rotation velocity $V_{||}$ are shown in Fig. 14 (a,b), which are changed little by the aspect ratios. Profiles of potential ϕ are shown in Fig. 14 (c,d). In a straight tokamak ($A = 1000$), the ϕ profile in the beam injection region is changed by the injection direction, while the ϕ profile outside the beam-injection region is unchanged by the rotation direction. In a standard tokamak ($A = 5.5$), the ϕ profiles are completely different between for co-rotation and for the counter-rotation; positive E_r in the whole core region for co-rotation while negative E_r for counter-rotation.

In some simulation codes to study edge-SOL-divertor plasmas in a tokamak, an inner boundary condition is sometimes put artificially to reduce computational resources, such as $\phi = \phi_{\text{core}}$ on an arbitrary magnetic surface inside the core plasma. If one puts such an internal boundary condition for ϕ , one can never observe the variation of ϕ profiles demonstrated above.

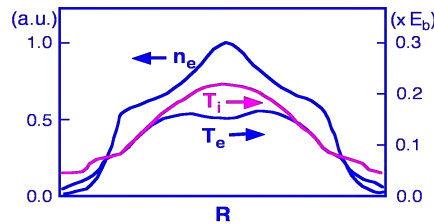


Fig.13 Radial profiles of n_e , T_e and T_i . The beam with energy E_b is injected in the central region.

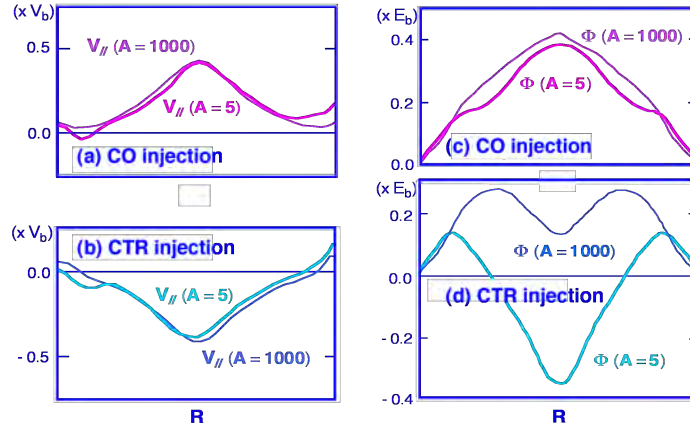


Fig.14 Radial profiles of rotation velocity and potential for co- or ctr- injection in straight- or standard- tokamak. Scale of $V_{||}$ is beam speed $V_b = (2E_b/m_i)^{1/2}$, and scale of $\Phi \equiv e\phi$ is beam energy E_b

The early 2D PARASOL simulations in the period 2001~2002^[33,34] took the computation time ~ 5 hours with 64 PEs in SGI Origin 3800 (1 GFLOPS/PE) for a run with the number of ions $N_i = 10^6$ and time steps $K_t = 5 \times 10^4$. The 2D toroidal PARASOL simulations in the period 2006~2008^[16,37,38] took the computation time ~ 5 hours with 64 PEs in SGI Altix 3700Bx2 (6 GFLOPS/PE) for a run with the number of ions $N_i = 10^6$ and time steps $K_t = 2 \times 10^5$.

8 Summary

In order to investigate the power and particle control with diveror system of fusion reactors, numerical simulations have been widely carried out. Fluid codes require further improvement of physics modeling for edge plasmas. The full particle simulation is powerful to study fundamental physics of open-field SOL-divertor plasmas as well as of the whole tokamak plasma including SOL-divertor region. PARASOL code with PIC method and binary collision model has been developed in JAERI and JAEA. After a prehistory during 1976~1985 and a long rest during 1986~1994, we revived the development of PARASOL in earnest with the massively parallel computing since 1995. The objects of the PARASOL simulation have been widened with the progress of the computer. Simulation model of the PARASOL is briefly explained in this review. Simulations with PARASOL code have been actively carried out to study various physics of the SOL-divertor plasma. The 1D version of PARASOL was applied to investigate the Bohm criterion, the supersonic flow, the SOL heat conduction, and so on. The ELM heat propagation was studied with the 1D-dynamic PARASOL. The 2D version of PARASOL for the whole tokamak plasma with SOL-divertor region was useful to simulate the SOL flow pattern, the electric field formation etc. Based on PARASOL simulation results, we have constructed physics modeling for the fluid simulation.

Acknowledgment

The author wishes to thank Dr. K. Shimizu, Mr. M. Hosokawa, Dr. A. Froese, and Prof. M. Yagi for the continuous collaborations on PARASOL simulation studies. Especially acknowledging Mr. Hosokawa for the development of PARASOL code. The author is grateful for collaborators on the modeling and simulation of SOL-divertor plasmas; Dr. H. Kawashima, Dr. K. Hoshino, Dr. N. Hayashi, Dr. M. Honda, Dr. T. Ozeki, Prof. A. Fukuyama and Prof. Y. Tomita. This work was supported partly by the JSPS-CAS Core-University Program in the field of "Plasma and Nuclear Fusion", and partly by the Grant-in-Aid for

References

- 1 Loarte A, et al. 2007, Progress in the ITER Physics Basis, Chapter 4: Power and Particle Control, Nucl. Fusion, 47: S203
- 2 Stangeby P C. 2000, The Plasma Boundary of Magnetic Fusion Devices, Taylor & Francis, New York
- 3 Takizuka T. 2010, Plasma Interaction in Controlled Fusion Devices: 3rd ITER International Summer School, AIP Conference Proceedings 1237: 138
- 4 Hockney R W, Eastwood J W. 1981, Computer Simulation Using Particles, McGraw-Hill, New York
- 5 Birdsall C K. 1991, IEEE Trans. Plasma Sci., 19: 65
- 6 Verboncoeur J P. 2005, Plasma Phys. Control. Fusion 47: A231
- 7 Cohen R, Xu X Q. 2008, Contrib. Plasma Phys., 48: 212
- 8 Takizuka T, et al. 1981, Plasma Physics and Controlled Nuclear Fusion Research (Proc. 8th Int. Conf. Brussels, 1980), IAEA, Vienna, 1: 679
- 9 Chodura R. 1982, Phys. Fluids 25: 1628
- 10 Takizuka T, Abe H. 1977, J. Comput. Phys., 25: 205
- 11 Takizuka T, Tani K, Azumi M, Shimizu K. 1984 J. Nucl. Mater., 128&129: 104
- 12 Takizuka T, Tani K, Azumi M. 1987, Particle Simulation of Divertor Plasma, Proc. US-Japan Workshop on Advanced Plasma Modeling, Nagoya, 1985, Research Report, IPP Nagoya University, IPPJ-818
- 13 NEXTE project, <http://www-jt60.naka.jaea.go.jp/english/theory/intro/>
- 14 Takizuka T, Hosokawa M. 2000, Contrib. Plasma Phys., 40: 471
- 15 Takizuka T, Hosokawa M, Shimizu K. 2001 Trans. Fusion Technol., 39: 111
- 16 Takizuka T, Shimizu K, Hayashi N, Hosokawa M, Yagi M. 2009, Nucl. Fusion, 49: 075038
- 17 Hayashi N, JT-60 Team. 2010, Phys. Plasmas, 17: 056112
- 18 Fukuyama A, Yagi M. 2005, J. Plasma Fusion Res., 81: 747 (in Japanese)
- 19 Kawashima H, Shimizu K, Takizuka T, et al. 2006, Plasma Fusion Res., 1: 031
- 20 Kawashima H, Shimizu K, Takizuka T. 2007 Plasma Phys. Control. Fusion, 49: S77
- 21 Shimizu K, Takizuka T, et al. 2009, Nucl. Fusion, 49: 065028
- 22 Takizuka T, Hosokawa M, Shimizu K. 2001, J.Nucl. Mater., 290-293: 753
- 23 Fundamenski W. 2005, Plasma Phys. Control. Fusion, 47: R163
- 24 Tskhakaya D, et al. 2008, Contrib. Plasma Phys., 48: 89
- 25 Froese A, Takizuka T, Yagi M. 2010, Plasma Fusion Res., 5: S1017
- 26 Froese A, Takizuka T, Yagi M. 2010, Contrib. Plasma Phys., 50: 285
- 27 Froese A, Takizuka T, Yagi M. 2010, Plasma Fusion Res., 5: 26
- 28 Takizuka T, Hosokawa M. 2006, Contrib. Plasma Phys., 46: 698
- 29 Loarte A, et al. 2003, J. Nucl. Mater., 313-316: 962
- 30 Takizuka T, Hosokawa M. 2007, Trans. Fusion Sci. Technol., 51: 271
- 31 Takizuka T, Oyama N, Hosokawa M. 2008, Contrib. Plasma Phys., 48: 207
- 32 Asakura N, ITPA SOL and Divertor Topical Group, 2007, J. Nucl. Mater., 363-365: 41
- 33 Takizuka T, Shimizu K, Hayashi N, Hosokawa M. 2001, Proc. 18th IAEA Fusion Energy Conf., Sorrento, 2000, IAEA, Vienna, CD-ROM IAEA-CSP-8/C: THP1 /22
- 34 Takizuka T, Hosokawa M, Shimizu K. 2003, J. Nucl. Mater., 313-316: 1331
- 35 LaBombard B, et al. 2004, Nucl. Fusion, 44: 1047
- 36 Takizuka T, Hoshino K, Shimizu K, Yagi M. 2010, Contrib. Plasma Phys., 50: 267
- 37 Takizuka T, Hosokawa M. 2007, Two-dimensional Full Particle Simulation of the Formation of Electrostatic Field in a Tokamak Plasma, presented at 11th IAEA Technical Meeting on H-mode Physics and Transport Barriers, Tsukuba, <http://www-jt60.naka.jaea.go.jp/h-mode-tm-11/index.html>
- 38 Takizuka T, Honda M. 2008, Modeling of Rotation, presented at 1st ITPA Transport & Confinement TG meeting, Milan

Edge Impurity Transport Study in Stochastic Layer of LHD and Scrape-off Layer of HL-2A

M. Kobayashi 1), S. Morita 1), C.F. Dong 1), Y. Feng 2), S. Masuzaki 1), M. Goto 1), T. Morisaki 1), H.Y.Zhou 1), H. Yamada 1), Y. Tomita 1), G. Kawamura 1) and the LHD experimental group 1)

1) National Institute for Fusion Science, Toki 509-5292, Japan

2) Max-Planck-Institute fuer Plasmaphysik, D-17491 Greifswald, Germany

Z. Y. Cui 3), Y. D. Pan 3), Y. D. Gao 3), P. Sun 3), Q. W. Yang 3) and X. R. Duan 3)

3) Southwestern Institute of Physics, P. O. Box 432, Chengdu 610041, China

E-mail contact of main author: kobayashi.masahiro@lhd.nifs.ac.jp

Abstract. Edge impurity transport has been investigated in the stochastic layer of LHD and the scrape-off layer (SOL) of HL-2A, as a comparative analysis based on carbon emission profile measurement and three-dimensional edge transport simulation. The 3D simulation predicts impurity screening effect in the both devices, but with different behavior against collisionality and the impurity source location. The difference is attributed to topological effects of the field lines in the stochastic layer and X-point poloidal divertor SOL. The carbon emission (CIV) profile in the stochastic layer of LHD shows clear signature of impurity movement towards downstream at high density range, in reasonable agreement with the 3D code simulation predicting impurity screening. Comparison of CIV profile measurements in HL-2A with the modelling implies that there exists either additional impurity source than the divertor sputtering or another screening effect at the upstream (X-point) such as strong poloidal flow formation, which is not taken into account in the present model.

1. Introduction

Understanding of edge impurity transport is one of the most critical issues in magnetically confined fusion devices, in order to keep a purity of core plasma by reducing the impurity influx through LCFS (last closed flux surface), to identify material migration process and to control the impurity radiation pattern/intensity for achieving stable radiative/detached divertor operation. Divertor optimization to satisfy the required functions, heat load mitigation, control of impurity transport and the fuel/helium ash pumping, is still an open issue for future reactors. While the tokamak X-point poloidal divertor is being optimized in the direction of closed divertor structure in the 2D axi-symmetric geometry [1], there is also another approach to explore a possibility of the large flexibility of 3D magnetic field geometry with symmetry breaking, which naturally occurs in the helical devices due to the coil configuration [2,3] or in the non-axisymmetric tokamaks with the externally applied resonant magnetic perturbation field [4,5,6]. The 3D configuration usually introduces stochasticity of magnetic field structure in the edge region, where one expects substantial difference in the transport properties compared to those in the axi-symmetric tokamak scrape-off layer, in terms of coupling between transport components of parallel and perpendicular to magnetic field lines. In this paper, we attempt to analyze the effects of the different magnetic field geometries on the edge impurity transport by comparing the stochastic layer of LHD (Large Helical Device) and the scrape-off layer (SOL) of HL-2A. The analyses are based on the carbon emission profile measurements with the EUV and VUV spectroscopy installed in LHD and HL-2A and on the 3D edge transport code simulations implemented in the both devices.

2. Edge magnetic field structure and plasma parameter range in LHD and HL-2A

Fig.1 shows magnetic field configuration of LHD and HL-2A in terms of the connection length (L_C) distribution. LHD is a heliotron configuration with poloidal winding number of $l=2$ and toroidal field period of $n=10$. It has major radius of 3.9 m and averaged minor radius

of ~ 0.7 m [2]. To realized a confinement magnetic field without net toroidal current, the two coils winds around the plasma helically in toroidal direction. This coil configuration creates stochastic magnetic field structure at the edge region due to the overlapping of magnetic island chains. The stochasticity introduces long connection length flux tubes, more than 1 km, which interact with short flux tubes while traveling towards divertor plate. HL-2A tokamak has a X-point poloidal divertor configuration with closed shape divertor chamber. The major radius is 1.65 m and minor radius is ~ 0.4 m, respectively [7], and the L_C in the SOL is around 40 m.

While in the HL-2A SOL the parallel transport is dominant process to deliver the plasma particle and energy to the divertor plate, in the stochastic layer of LHD the plasma is transported radially, where a substantial fraction of perpendicular transport contributes, because of the very small ratio of $B_r/B_t \sim 10^{-4}$, with B_r and B_t being radial and toroidal magnetic field. For the energy transport, when the edge plasma parameters satisfies the condition [8],

$$n/T^{5/2} > \Theta^2 \kappa_{//0} / \chi_{\perp}, \quad (1)$$

here $\kappa_{//0}$ and χ_{\perp} are parallel heat conductivity coefficient and perpendicular heat conductivity, respectively, and $\Theta \approx B_r/B_t$. For the value of Θ above, the ion energy transport easily satisfies the eq.(1) in the LHD stochastic layer. Another effect of the stochasticity on the transport is perpendicular loss of parallel momentum. This is caused by the interaction between counter-acting parallel flows, which results from the magnetic field geometry of the stochastic field [9]. Such flow alternation is also measured in experiments [10]. This process breaks down the pressure conservation along flux tubes, which is usually considered to hold in the tokamak SOL. The momentum loss along the flux tubes alters the transport characteristics and leads to the rather modest downstream parameter (T_{down} , n_{down}) dependence on n_{up} (upstream density) [9],

$$T_{down} \propto n_{up}^{-1 \sim -2/3}, n_{down} \propto n_{up}^{1 \sim 1.5} \quad (2)$$

while for the standard case of X-point tokamaks we have $T_{down} \propto n_{up}^{-2}$, $n_{down} \propto n_{up}^3$, much more sensitive to n_{up} . The modest dependence in the stochastic layer delays the detachment transition towards higher upstream density, i.e. higher collisionality.

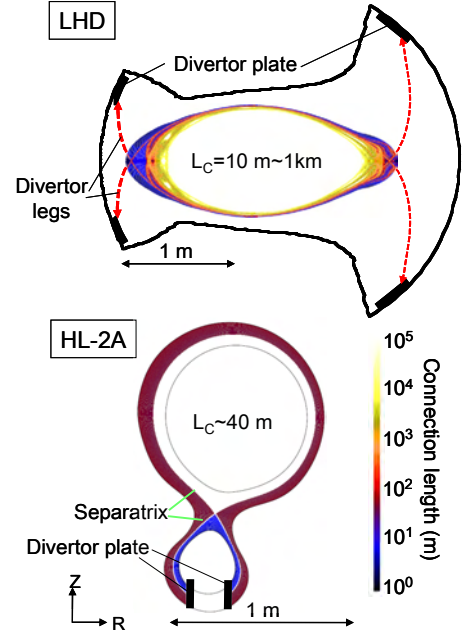


FIG.1 Connection length distribution and divertor configuration in LHD and HL-2A. The length is scaled with different colours.

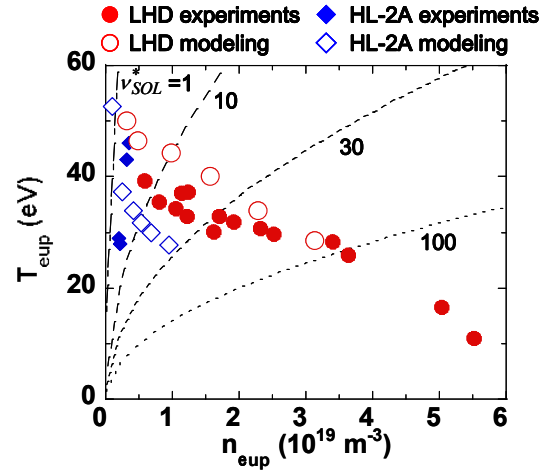


FIG.2 Edge plasma parameter range in LHD stochastic layer and HL-2A scrape-off layer. The lines indicate the SOL collisionality, v_{SOL}^* (defined in the text). Circles and diamonds represent LHD and HL-2A data. Closed and open symbols indicate the data from experiments and modellings, respectively. The upstream location is taken at the edge surface layer at outboard side for LHD and at outboard mid-plane for HL-2A.

For the present analyses, the NBI heated plasmas with 4 to 8 MW of LHD and the ohmic discharges with plasma current up to 380kA with input power ~ 300 kW of HL-2A, have been compared. Fig.2 shows the range of edge plasma parameter (T_{eup} , n_{eup}) in the two devices. The upstream position is defined at the last closed flux surface (LCFS) on the outer mid-plane for HL-2A and outboard side edge surface layers (laminar region) for LHD, where the clustered long flux tubes starts to interact with the short ones and to exhibit SOL-like parallel flow towards divertor. Contours of the SOL collisionality, $v_{\text{SOL}}^* \equiv L_{\parallel} / \lambda_{ee}$, is also indicated, where λ_{ee} is the electron mean free path and L_{\parallel} is a characteristic scale length along magnetic field, which is either the half of L_C for HL-2A or the Kolmogorov length for LHD, both of them are estimated at about 20 m. Unfortunately the experimental data of T_{eup} and n_{eup} in HL-2A is sparse, but the modeling results supplement the information. In the case of HL-2A, we have an upper boundary for the edge parameters around $v_{\text{SOL}}^* = 20$, where the computation indicates detachment onset. It is also consistent with experimental observation [11]. The access to the higher $v_{\text{SOL}}^* \sim 100$ in LHD before detachment onset is not only due to the higher heating power, but also due to the modest change of T_{down} , n_{down} , eq.(2), i.e. T_{down} decreases slowly against n_{up} as discussed above. The consequence of these features on the edge impurity transport is discussed later.

3. 3D edge transport modelling of LHD and HL-2A

In order to investigate the transport properties, we have implemented the 3D edge plasma transport code, EMC3[12]-EIRENE[13], in both LHD and HL-2A. EMC3 solves the fluid conservation equations of mass, parallel momentum, energy of electron & ion, together with impurity, in arbitrary 3D geometry of magnetic field and divertor/first wall shape. The divertor recycling of neutrals is treated by the kinetic transport model by EIRENE also in the 3D geometry. In the frame of fluid approximation, the parallel motion of impurity is considered to be in force balance in steady states as follows [14],

$$0 = -\frac{1}{n_z} \frac{\partial T_i n_z}{\partial s} + m_z \frac{V_{i\parallel} - V_{z\parallel}}{\tau_s} + ZeE_{\parallel} + 0.71Z^2 \frac{\partial T_e}{\partial s} + 2.6Z^2 \frac{\partial T_i}{\partial s}, \quad (3)$$

where $T_z = T_i$ is assumed and $V_{i\parallel}$, $V_{z\parallel}$, τ_s , m_z being the parallel velocity of background ion and impurity, the slowing down time of impurity colliding with background ions, mass of impurity, respectively. The terms on the right hand side represent the impurity pressure gradient, friction force exerted by the background parallel plasma flow, electric field and electron & ion thermal force (temperature gradient force), respectively. s is the coordinate along the magnetic field. In perpendicular direction, pure diffusion is assumed and the

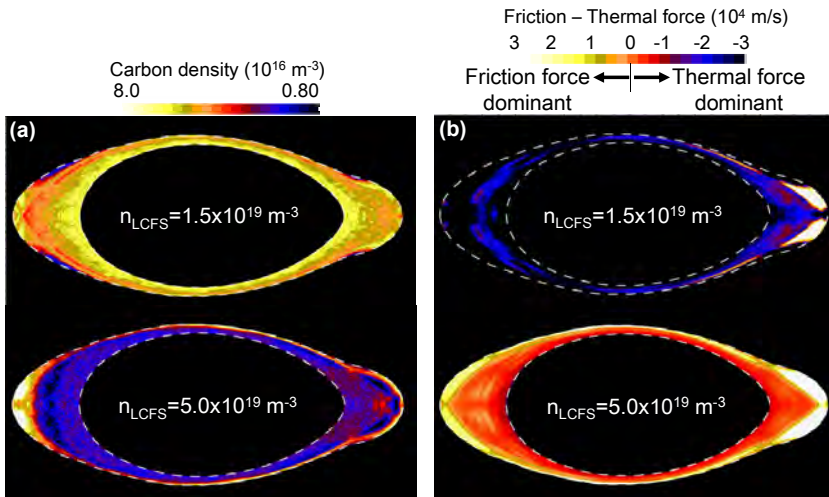


FIG.3 (a) carbon density distribution in LHD for different n_{LCFS} obtained by the 3D modellings. (b) Friction-Thermal force balance as explained in eq.(4). The yellow and black colours represent friction force and thermal force dominant region, respectively. The dashed lines indicate computation boundary.

diffusion coefficient is set to be same as those of background plasma. As often discussed, the dominant forces in the equation are the friction force and the ion thermal force, the second and the forth terms on the right hand side. Since usually the background plasma flow is directed towards divertor plates, the friction force sweeps the impurity to the divertor region, while due to the $\nabla_{//}T$ which directs towards upstream the thermal force leads to build up of impurity at the upstream region. In the both devices, the divertor plates are made of graphite and it is the main source of carbon, which is an impurity species treated in the present modelling. The neutral impurity source from the divertor plate is distributed according to the plasma particle deposition pattern with a certain sputtering coefficient, C_{sput} . For the present analysis, C_{sput} is a free parameter and fixed to 2% for LHD while for HL-2A it has to be changed to get agreement with the experiments, as discussed later. The ejection energy from the material surface is set to be 0.05 eV for all cases. Although the rather complex dissociation process of hydrocarbon is beyond the scope of this paper, the major results of the analyses will not change even if it is taken into account.

Resulting carbon density distribution in LHD is plotted in Fig.3 together with the friction-thermal force balance,

$$V_{z//} \approx V_{i//} + \frac{\tau_s}{m_z} \left(2.6Z^2 \frac{\partial T_i}{\partial s} + 0.71Z^2 \frac{\partial T_e}{\partial s} \right), \quad (4)$$

where the electric field and pressure gradient terms are neglected because they are usually small. At the low density, $n_{\text{LCFS}}=1.5 \times 10^{19} \text{ m}^{-3}$, the carbons are distributed around the LCFS, Fig.3 (a) (upper), due to the large inward velocity by the thermal force as shown in Fig.3 (b) (upper), where the entire region is covered by the thermal force dominant region. At the high density, $n_{\text{LCFS}}=5.0 \times 10^{19} \text{ m}^{-3}$, on the other hand, the carbons are pushed back to the periphery, due to the increasing friction force, Fig.3 (b) (lower), resulting in the impurity screening, as shown in Fig.3 (a) (lower). It is noted that the friction dominant region is distributed in all poloidal direction surrounding the stochastic layer. This provides effective screening for the impurity coming from all directions.

The results of HL-2A are plotted in Fig.4 for the different density cases. Similarly to the LHD case, the higher density leads to the impurity screening. At the low density case, the region above the X-point is deeply in the thermal force dominant while the near the divertor plate is friction dominant. In spite of the dominant friction force near the divertor plates, any small leakage of impurity out of the friction dominant region builds up at the upstream due to the strong thermal force above X-point. Increasing density strengthens the friction force near divertor plate and weakens the thermal force above X-point. This gives rise to a good screening. However, it is also

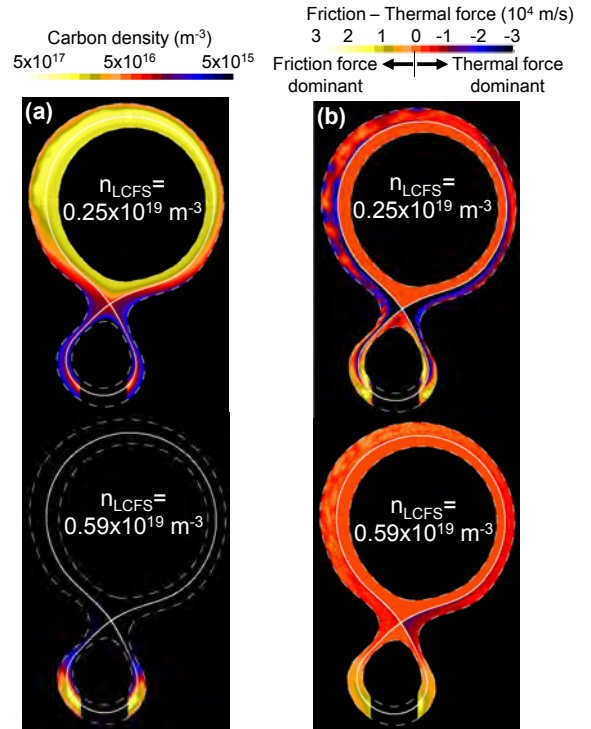


FIG.4 (a) carbon density distribution in HL-2A for different n_{LCFS} obtained by the 3D modellings. (b) Friction-Thermal force balance as explained in eq.(4). The yellow and black colours represent friction force and thermal force dominant region, respectively. The white solid lines and the dashed lines indicate separatrix and computation boundaries, respectively.

noted that the residual thermal force can not be removed completely around/above X-point at the highest density just before the detachment transition, as shown in Fig.4 (b) (lower). This indicates that the SOL is relatively weak to the impurity injected around upstream, i.e. impurity source at the first wall.

As a measure of a degree of the screening, the ratio, $n_{up}^{imp} / n_{down}^{imp}$, is plotted in Fig.5 as a function of v_{SOL}^* , where n_{up}^{imp} and n_{down}^{imp} are the impurity density at upstream (LCFS) and near divertor plates, respectively, summed up over all charge states. When the ratio becomes below unity, it can be considered that the screening starts. The impurity source is distributed not only at the divertor plate but also at the first wall uniformly for the both devices to see the effect of source location. In HL-2A, the ratio decreases rapidly above $v_{SOL}^* \sim 5$, down to 0.1 showing strong screening against the divertor source. This is understood as due to the strong dependence, $T_{down} \propto n_{up}^{-2}$, $n_{down} \propto n_{up}^3$, which brings the downstream SOL to deeply in the friction dominant regime, where the parallel flow towards divertor plate is also available driven by the sink action at the target. On the other hand, it is found that the HL-2A SOL has no screening effect against the first wall source, as anticipated from Fig.4 (b) (lower). This is again related to the strong dependence of T_{down} and n_{down} , which brings the divertor plasma to detachment regime while the upstream remaining at rather low v_{SOL}^* . Also, almost no flow acceleration is available at the upstream in the frame of the present model, in which the driver of the flow is only the ionization source and the sink action at the divertor plates, both of them are localized near divertor region.

In the case of LHD, the stochastic layer has screening effect against both divertor and first wall source, although the reduction of the ratio is not as large as those of HL-2A. The effect is explained by the combination of the following processes: the modest dependence, $T_{down} \propto n_{up}^{-1 \sim -2/3}$, $n_{down} \propto n_{up}^{1 \sim 1.5}$ helps the upstream goes to higher v_{SOL}^* , i.e. higher density as discussed above. Due to the dependence of eq.(2), the downstream density is relatively low and never exceeds the upstream density [9,15]. This allows the recycling neutrals to escape from the divertor region, penetrating deep in the edge region. This giving rise to substantial upstream ionization source, which provides flow acceleration towards divertor. The current open divertor configuration in LHD also helps the recycling neutrals escape from the divertor region. At the inner radial location where the remnant islands exist with very small internal field line pitch, $B_r / B_t \sim 10^{-4}$, as discussed in the section 2, the enhanced perpendicular energy transport channel, $n \chi_{\perp} \partial T / \partial r$, compensates the parallel ones along the braiding magnetic fields. This process avoids developing large $\nabla_{\parallel} T$, i.e. thermal

force, at high collisionality. Since the $\frac{\text{friction force}}{\text{thermal force}} \propto \frac{M n_i}{|\nabla_{\parallel} T_i| T_i}$ with M being Mach number,

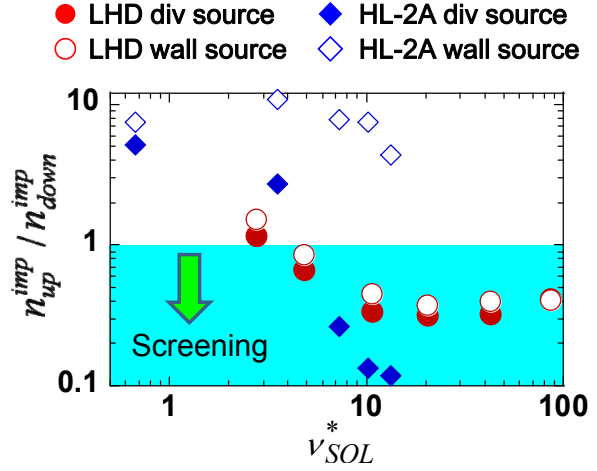


FIG.5 Impurity screening effect measured by the ratio $n_{up}^{imp} / n_{down}^{imp}$ obtained in modelling. The smaller the value is, the larger the screening effect. Circles for LHD, diamonds for HL-2A. Closed and open symbols represent divertor source and first wall source, respectively.

the above three process favors larger friction force dominating over the thermal force. This is the reason for the formation of the friction dominant region at the upstream, screening the impurity from both first wall and divertor plates. While the modest dependence of downstream parameters brings about the collisional upstream SOL, however, the collisionality at the downstream can not be increased as in the tokamak SOL due to the low downstream density. Therefore, the reduction of the ratio, $n_{up}^{imp} / n_{down}^{imp}$, remains small compared to that of HL-2A. The analysis shows that the perpendicular interaction of flux tubes in the stochastic layer alters the plasma characteristics, and provides different behaviors of impurity screening effect against v_{SOL}^* and the source location.

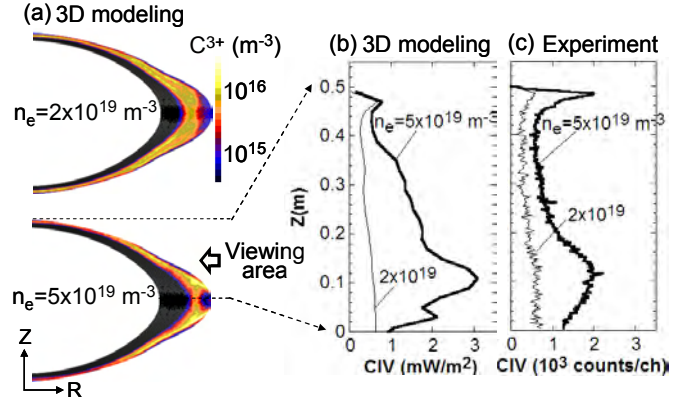


FIG.6 (a) C^{3+} carbon density (emitting CIV) distribution obtained by the modelling in LHD, and chord-integrated CIV profiles obtained by (b) modelling and (c) experiments for two different densities, as a function of vertical coordinate, Z .

4. Experimental observation

VUV, EUV spectroscopy systems have been installed in LHD [16] and in HL-2A [17] respectively, in order to investigate edge impurity transport. Fig.6 (a) shows the C^{3+} carbon density distributions for the low and high density cases ($n_{LCFS}=2.0$ and $5.0 \times 10^{19} \text{ m}^{-3}$), where the edge region changes from thermal force dominant to friction force dominant regime. At the low density case the C^{3+} carbon distributes almost uniformly in poloidal direction as seen in Fig.6 (a) (upper). At the high density case, on the other hand, the screening effect pushes impurity towards the flux tubes of divertor legs, resulting in strong poloidal modulation of the distribution as shown in Fig.6 (a) (lower). The change is reflected on the vertical profile of the line integrated CIV (1548 Å) emission in horizontal view. Profiles obtained from the modelling results are plotted in Fig.6 (b), where one sees a clear change of the profiles from a flat to peaked one with increasing density. The peak around $Z=0.1$ m corresponds to the location of divertor legs. Similar change of the emission profiles with increasing density is observed in the experiments obtained in the same viewing area, as shown in Fig.6 (c). The results indicate existence of the impurity screening effects in experiments. Emission of CIII (977 Å), CIV and CV (40.27 Å) was also measured. The density dependence of the each line emission was analyzed using the 3D edge transport code when the screening occurs, using the same viewing area as the experiments. Here the intensity of CIII and CIV are interpreted as a proxy for the source, and CV as a proxy for the impurity at deeper radial position. It is found that the behavior of measured emission agrees well with the model prediction with impurity screening [9, 18], i.e. slight increase of CIII and CIV, decrease of CV against density scan. From these results, at the moment qualitative trend of screening is confirmed in LHD.

In HL-2A, line integrated CIV profile measurements have been conducted. The obtained profiles are plotted in Fig.7, together with the viewing angle of the spectroscopy shown in the right figure. Z coordinate starts at the center of plasma and increases downward. At the very low density, profile becomes almost flat in Z direction. In terms of the modelling, this is interpreted as due to the distribution of CIV emission which is almost uniform but slightly intense at the inboard side that contributes to make the profile flat. In this low density case, the thermal force is dominant above X-point, as shown in Fig.4 (b), and is stronger at the

outboard side than at inboard side because of the in-out asymmetry of the configuration, i.e. the shorter field line length from divertor to mid-plane at outboard side, and larger energy flux through LCFS is assumed at the outboard side due to the narrower flux surface distance (Shafranov shift). This gives rise to the in-out asymmetry of the thermal force and of the impurity density distribution, larger at inboard side. Increasing density

leads to the peaked CIV profile around $Z=0.35$ m in experiments with the concomitant increase of emission itself. In the modelling, the peak also appears at high density but the location is shifted outward, $Z=0.40$ m. The peak comes from the localized emission around X-point as shown in Fig.7 (c) (lower), which is due to the screening effect at high density. As for the deviation of the peak location, we need further careful check of the reconstruction of magnetic flux surface and the calibration of the viewing lines of experiments and modelling. It is found that, in order to reproduce the increased emission at the high density case observed in the experiments, it is necessary to increase the impurity source from the divertor, sputtering coefficient from 1% to 10%, as indicated in Fig.7 (b). Introducing first wall impurity source (distributed uniformly) gives rise to a flat profile as shown in Fig.7 (b) with dashed line, due to the residual thermal force above X-point as discussed in section 3, although the measured profile always peaked at high density. The comparison between the experimental data and the modelling implies either that, there is additional impurity source other than the divertor sputtering, or that there exists another screening effect above X-point, which is not included in the present modelling such as large poloidal flow formation as observed and analyzed in tokamak devices [19, 20], if the first wall source is assumed to explain the emission increase in the experiments.

5. Summary

The edge impurity transport properties have been investigated by comparing the LHD stochastic layer and the HL-2A scrape-off layer. The 3D edge transport code EMC3-EIRENE has been implemented for the both machines, and the profile measurements of carbon emission has been performed using the EUV, VUV spectroscopy in the both devices. Comparison of the simulation results shows clear difference in the screening process between LHD and HL-2A. In the HL-2A, the strong screening effect appears suddenly above $v_{SOL}^* \sim 5$ for divertor impurity source. But almost no screening effect on the first wall source due to the

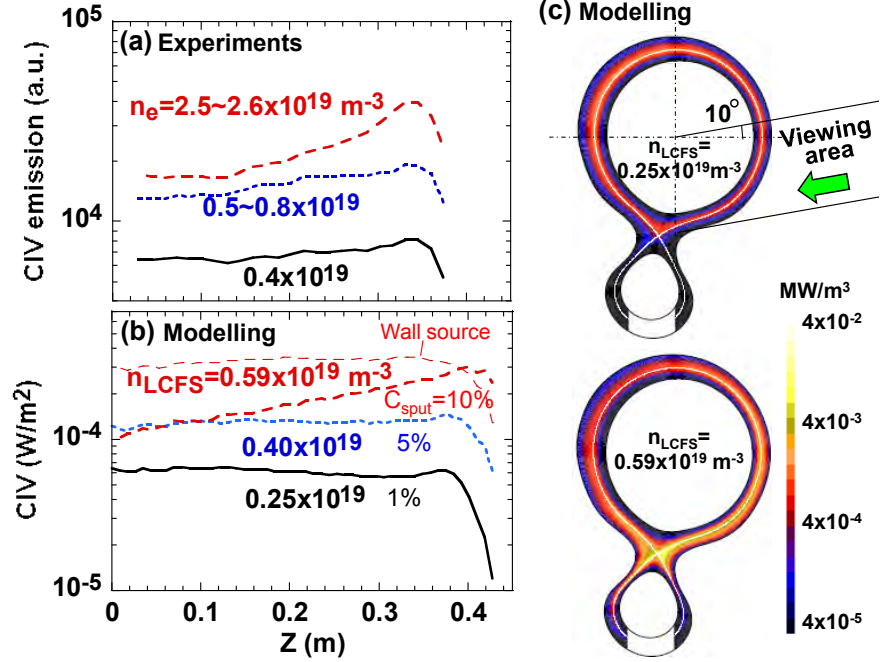


FIG.7 Line integrated CIV profiles obtained in HL-2A for different densities. (a) Experiments, (b) Modelling, (c) CIV distribution obtained by the modelling together with viewing area of spectroscopy. In the modelling, sputtering coefficient is varied as indicated in (b). The result of first wall impurity source is shown by dashed line in (b).

residual thermal force at the upstream (above the X-point) even at the highest density just before detachment onset. In the case of LHD, the screening also appears above $v_{SOL}^* \sim 5$, where the effect seems to be weaker than those of HL-2A. The screening is, however, available also for the first wall source. This is due to the enhanced perpendicular transport in the stochastic layer, which can bring the entire upstream region into friction dominant regime.

The comparison of the modelling with the spectroscopy measurements shows reasonable agreement in LHD in terms of the CIV emission profiles and CIII, CIV, CV intensity against density scan, indicating the existence of the screening effect. In the HL-2A case, the interpretation of the experimental data in terms of the present impurity transport model is not straightforward. The comparison between the experimental data and the modelling implies either existence of additional impurity source other than the divertor sputtering, or of another screening effect at the upstream (above X-point), which is not included in the present modelling such as large poloidal flow formation.

For answering the uncertainty found in the present analyses and for investigating quantitative behavior of the impurity, we need further systematic and organized experiments between LHD and HL-2A.

Acknowledgements

The authors wish to thank the LHD and HL-2A operation group for their excellent technical support. The authors are grateful for the support for the computational resources: Plasma Simulator SR16000 L2 powered by HITACHI Ltd, and AMD Opteron-InfiniBand Cluster Machine, by Grant-in-Aid for Science Research on Priority Areas (Area 465, No.18070005) from MEXT Japan. The computational work is partly supported by the NIFS budget code NIFS10ULPP016. This work was partly supported by the JSPS-CAS Core-University Program in the field of "Plasma and Nuclear Fusion".

References

- [1] "Progress in the ITER physics Basis: Chapter 4 : Power and particle control", Nucl. Fusion **47** (2007) S203.
- [2] OHYABU, N. et al., Nucl. Fusion **34** (1994) 387.
- [3] GRIGULL, P. et al., Plasma Phys. Control. Fusion **43** (2001) A175.
- [4] GHENDRIH, PH. et al., Nucl. Fusion, **42** (2002) 1221.
- [5] FINKEN, K.H. et al., Nucl. Fusion **47** (2007) 522.
- [6] EVANS, T. et al., Nature Phys. **2** (2006) 419.
- [7] YANG, Q.W. et al., Nucl. Fusion **47** (2007) S635.
- [8] FENG, Y. et al., Nucl. Fusion, **46** (2006) 807.
- [9] KOBAYASHI, M. et al., Fusion Sci. Technol. **58** (2010) 220.
- [10] EZUMI, N. et al., J. Plasma Fusion Res., **8** (2009) 429.
- [11] YAN, L.W. et al., J. Nucl. Mater. **390-391** (2009) 246.
- [12] FENG, Y. et al., Contrib. Plasma Phys. **44** (2004) 57.
- [13] REITER, D. et al., Fusion Sci. Technol. **47** (2005) 172.
- [14] STANGEBY, P.C., and ELDER, J.D., Nucl. Fusion **35** (1995) 1391.
- [15] MASUZAKI, S., et al., J. Nucl. Mater. **313-316** (2003) 852.
- [16] DONG, C.F. et al., Rev. Sci. Instrum. **81** (2010) 033107.
- [17] CUI, Z. et al., Rev. Sci. Instrum. **81** (2010) 043503.
- [18] KOBAYASHI, M. et al., Proceedings of 22nd IAEA FEC (13-18th Oct. 2008, Geneva), EX/9-4. <http://www-pub.iaea.org/MTCD/Meetings/fec2008pp.asp>
- [19] ASAKURA, N. and ITPA SOL and Divertor Topical Group, J. Nucl. Mater. **363-365** (2007) 41.
- [20] TAKIZUKA, T. et al., Nucl. Fusion **49** (2009) 075038.

Modelling of Edge Plasma on JT-60U Tokamak by Using SOLPS5.0 code

YiPing Chen¹, H.Kawashima², N.Asakura², K.Shimizu², H.Takenaga²

¹Institute of Plasma Physics, Chinese Academy of Sciences, Hefei, Anhui, China

²Japan Atomic Energy Agency, Naka-shi, Ibaraki-Ken, 311-0193, Japan

ABSTRACT

The edge plasma transport code SOLPS5.0 is used for modelling edge plasmas on JT-60U tokamak. The modelling results are matched to the experimental measurement of the edge plasmas in L-mode and H-mode shots and the radial transport coefficients at the edge have been obtained by fitting the experimental measurement with the results of the transport code.

1 Introduction

The transport of edge plasma has become one of the key issues in the research on magnetic confinement fusion. Some transport codes of edge plasma, for example, SOLPS, UEDGE, EDGE2D-NINBUS, SONIC, have been developed in the world and they have become the important tools in the transport study of edge plasmas. UEDGE is mainly used in USA, EDGE2D-NINBUS is specified for using on JET and SONIC is mainly used in Japan. SOLPS is widely used on the tokamaks in the world, for example, ITER, JET, ASDEX Upgrade, TCV, JT-60U, EAST, HL-2A. The important input data in the transport codes includes the radial particle transport coefficient D , radial ion and electron heat transport coefficients χ_i and χ_e . Due to the uncertainties associated with the transport coefficients D , χ_i and χ_e , some assumption for D , χ_i and χ_e usually are made in the modelling of edge plasmas with the transport codes. Modelling of edge plasmas in the experimental shots on the experimental devices and comparing the modelling results to the experimental measurement are usually used for the validity study of the transport models or the radial transport coefficients in the transport codes. Fitting the modelling results to the experimental measurement by changing the radial transport coefficients in the codes usually is used for the transport analysis, by which the radial transport coefficients can be obtained by matching the code results directly to the experimental measurement.

2 Edge plasma modelling and the radial transport coefficients on JT60U tokamak

JT-60U is one of the large tokamaks in the world, the main parameters on the device are major radius $R=3.4\text{m}$, minor radius $a=1.0\text{m}$, toroidal field $B_t=4\text{T}$, plasma current $I_p=3\text{MA}$, plasma volume $V_p=90\text{m}^3$, pulse length $T_p=65\text{s}$. The experimental measurement of L-mode shot 39090 and H-mode shots 37851, 37856 on JT-60U tokamak are used for the present modelling with SOLPS5.0. The plasma current I_p , the average electron density n_e and D_α trace versus time in the shots 39090 and 37856 are shown in Fig.1. The main parameters in the shots are shown in the table 1. In the table 1, I_p , V_l and B_t are the average plasma current, the loop voltage and the toroidal magnetic field respectively. R_{axis} is the axis position. P_{OH} and P_{NBI} are the Ohmic and NBI heating power respectively. The total power flux to the computation region is $P=P_{OH}+P_{NBI}$. F_{pump}^{exp} , G_{core}^{exp} and G_{puff}^{exp} are the pumping speed, total particle flux from the core boundary to the computational region and the gas puffing flux respectively. Although total energy flux from the core boundary to the computational region P can be obtained according to the experimental measurement, for electron and ion energy fluxes to the computational region, P_e and P_i , no exact experiment data is available since a separation of P_e and P_i is not possible in the experiment measurement, so, for the present modelling an assumption that $P_e=P_i=0.5\times P$ is made. The ratio P_i/P_e would affect the modelling results. The power in the ion channel usually is larger than in the electron channel when using neutral beams, so, the ratio P_i/P_e may be larger than 1 when NBI is used for heating plasmas, but, how large it is and how it affects the modelling results become two important problems and they should be studied. Fig.1 shows the computational meshes in the computational domain and in the divertor region respectively. The computational meshes are orthogonal.

B2.5-SOLPS5.0 [1-4] is a two-dimensional edge plasma transport code and it is widely used for modelling tokamak edge plasma. The complete description about physics model included in the code can be found [1], it mainly includes, plasma and neutrals are treated by fluid model, the electric potential equation coupled with the fluid equations allows self-consistent treatment of the electric field, completed and self-consistent treatment of all classical drifts and currents naturally arise in the computational region, full account of perpendicular direction is no more confused with poloidal direction, drift (including ExB drift) is included, atomic and molecular processes, including ionization, recombination, charge exchanges and so on, are taken into account. B2.5I-SOLPS5.0[5,6] which includes experiment measurement data fitting routines based on same physics model [1] is used for modelling experimental shots and fitting experiment measurement data from JT-60U plasma experiment device in order to obtain the radial transport coefficients from the

experiment. The modelling and fitting are carried out in the plasma edge computational regions, the plasma species include ion, electron and neutrals without the impurities, drift and neoclassic transport are not taken into account for simplification. The actual MHD equilibrium in the discharges are available for the modelling and fitting. The fitted experiment measurement data includes the experimental profiles of plasma temperature and density at the midplane, neutral flux density near the outer wall, total particle flux and power flux from the core plasma to the edge computation region, pumping speed, so, the modelling and fitting are based on particle and power balance in the shots. By changing the radial transport coefficients in the code and minimizing residual between modelling results and experiment measurement data, finally the radial transport coefficients for the shots can be obtained.

Table 1: shot parameters from JT-60U experiment for modelling

shot #	time s	R m	a m	Gas	mod	$\frac{q}{g}$ $10^{19}/m^3$	I_p MA	V_l V	B_t T	R_{axis} m	R_{sep} m
39090	6.4	3.418	0.970	D ₂	L-mode	1.85	1.959	0.484	3.076	3.462	3.054
37851	7.0	3.440	0.957	D ₂	H-mode	1.70	0.998	0.212	1.893	3.532	3.056
37856	7.0	3.418	0.970	D ₂	H-mode	1.93	0.997	0.153	1.898	3.527	3.058

P_{OH} MW	Heat	P_{heat} MW	P MW	F_{pump}^{exp} $10^{21}/s$	G_{core}^{exp} $10^{21}/s$	$G_{0,wall}^{exp}$ $10^{21}/s$
0.948	NBI	4.500	5.448	2.720	0.440	2.280
0.212	NBI	4.300	4.512	0.421	0.421	0.000
0.153	NBI	5.600	5.753	0.549	0.549	2.472

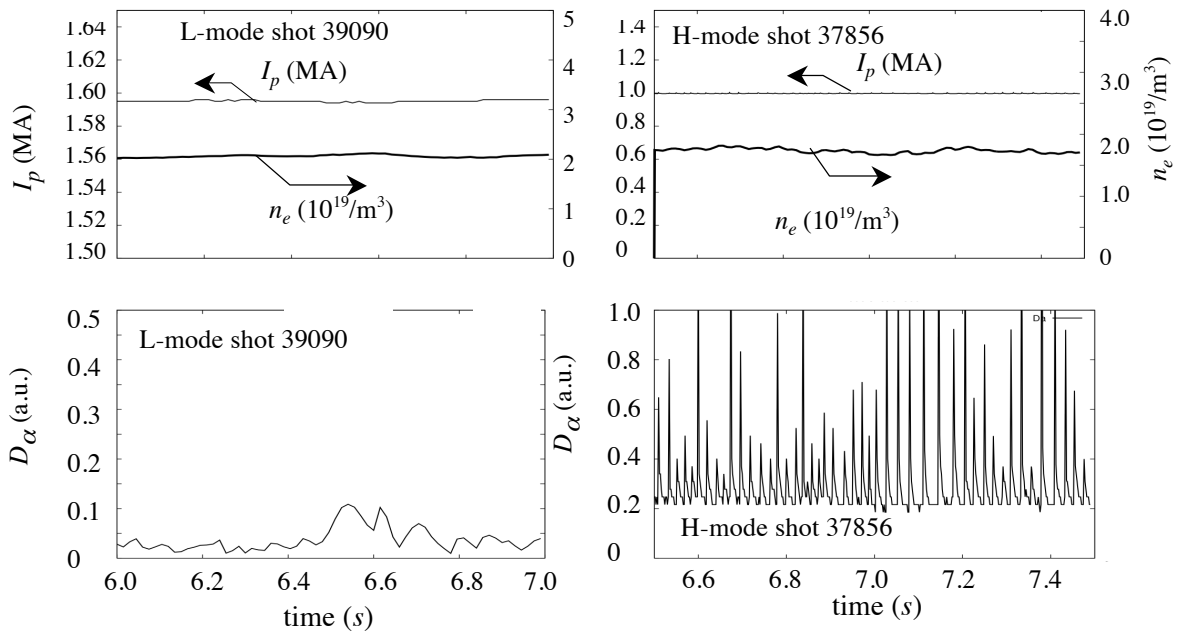


Figure 1: Plasma current I_p , average electron density n_e and D_α trace versus time in L-mode shot 39090 and H-mode shot 37856.

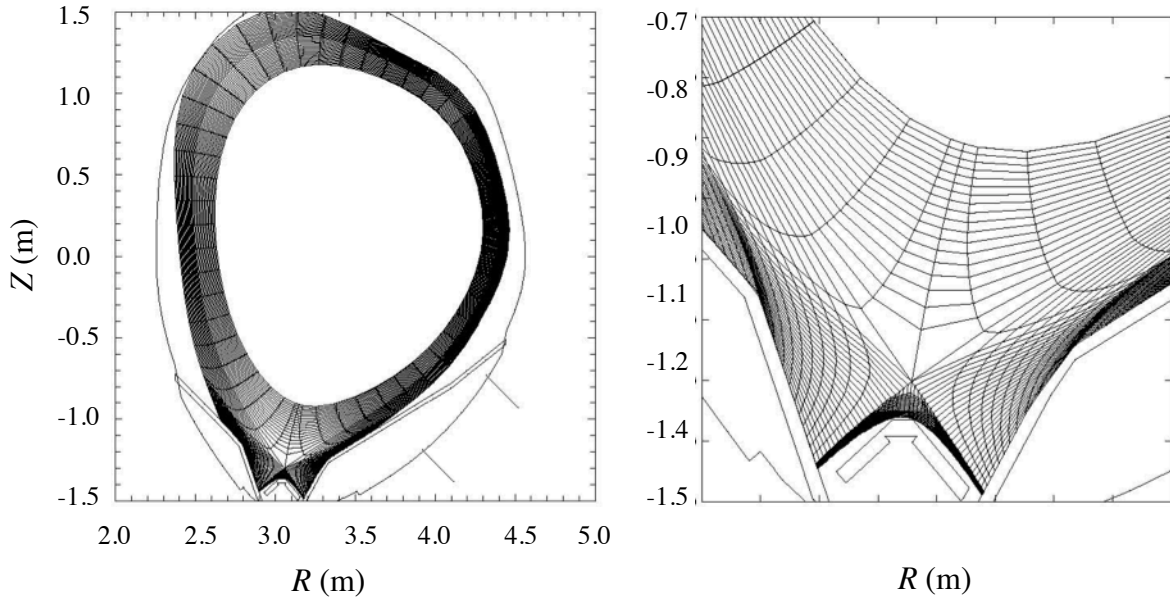


Figure 2: Computational domain with the number of radial and poloidal mesh points 36x96 and the Computational mesh in the divertor region.

Fig.3 shows the profiles at the midplane from the experimental measurement of plasma density, electron and ion temperature respectively for L-mode shot 39090 and H-mode shots 37851, 37856. The profiles from the code results by fitting the experimental measurement and the radial transport coefficients obtained from the fitting are also shown in the figures. Because the profile of ion temperature is not available in the computational region, it is assumed that the radial ion heat transport coefficient χ_i and radial electron heat transport coefficient χ_e are equal, i.e. $\chi_i = \chi_e$. The fitting results show that the experimental data are well fitted by updating the radial particle transport coefficient D and radial electron heat transport coefficient χ_e . A dynamic Monte-Carlo treatment may be more reasonable for neutrals, but running the B2.5I-SOLPS5.0 with Eirene[7], which includes a dynamic Monte-Carlo treatment for neutrals, would enlarge the CPU time and produce noise in the results. The noise would make the judgment of convergence and the calculation of residuals by the code itself during the fitting more difficult. A good way for the dynamic Monte-Carlo treatment of neutrals can be considered by using the radial transport coefficients D , χ_e and χ_i from the B2.5I-SOLPS5.0 fitting, and running the coupling version B2.5-Eirene.

The fitting results show that the radial particle transport coefficient D has large drop within the Edge Transport Barrier (ETB) in the H-mode shots and the radial transport coefficients may drop to neoclassic level, but, what kind of microturbulence is suppressed is under discussion. The fitting results show the radial electron and ion heat transport coefficients χ_e and χ_i , the obvious drop within the Edge Transport Barrier (ETB) in the H-mode shots 37851 and 37856 has no found, the values of χ_e and χ_i near the outer wall are very large, which should be further studied in the next step.

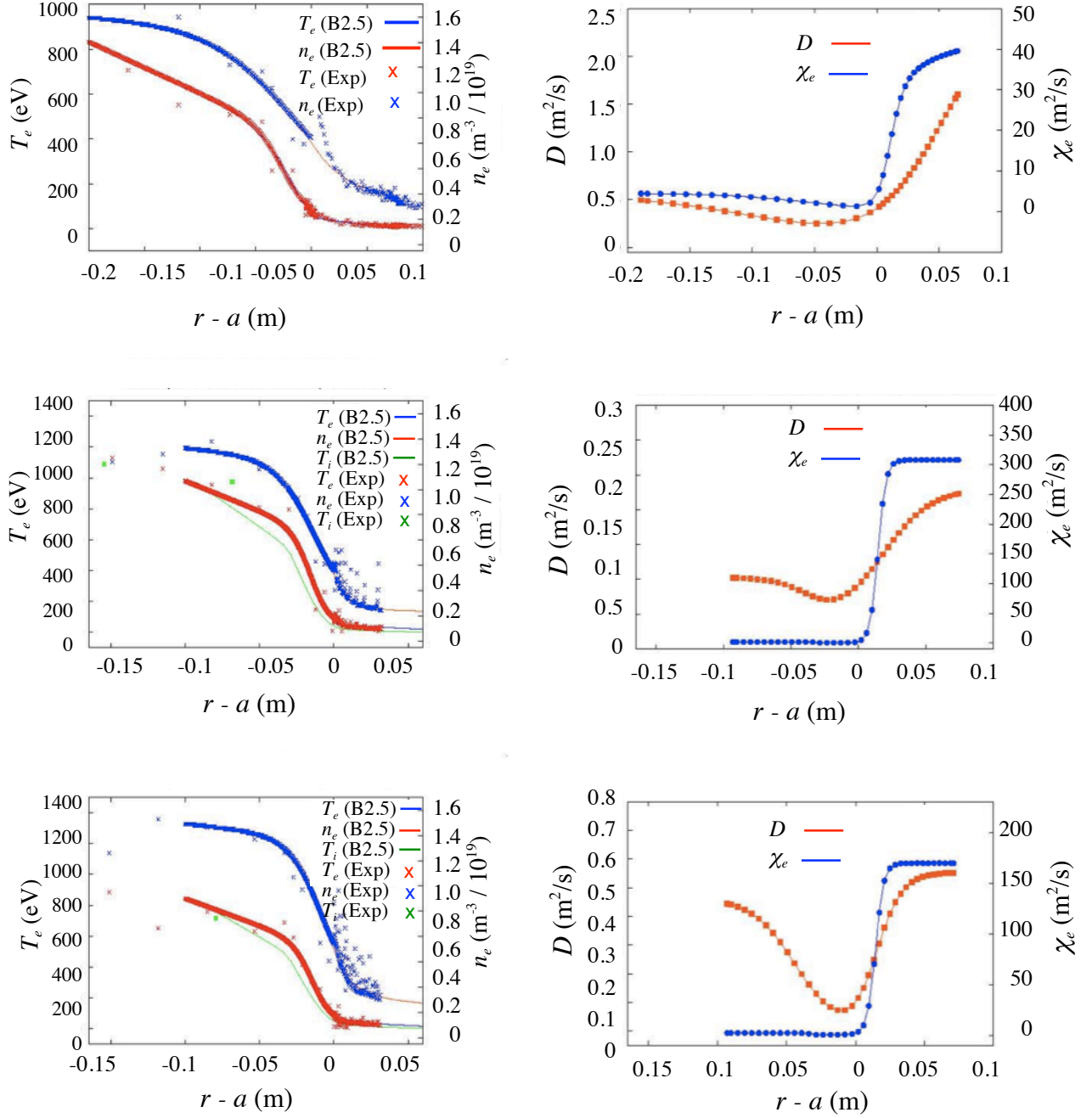


Figure 3: Fitting results of experimental data of the L-mode shot 39090 and the H-mode shots 37851, 37856 from JT- 60U, profiles of radial particle transport coefficient D and radial electron heat transport coefficient χ_e at the midplane from the fitting.

For the Type I ELMy H-mode shots 17151 and 17396 on ASDEX Upgrade[9] and for Type III ELMy H-mode shot on TCV[10] the measured profiles of plasma parameters at the midplane also have been matched by the full B2-Eirene modelling results for the transport analysis and the radial transport coefficients D , χ_e have been obtained. The modelling and match results also showed the radial transport coefficients D and χ_e have large drop within the Edge Transport Barriers (ETBs). The edge plasma transport code EDGE2D was used for modelling type I ELMy H-mode shot 58569 on JET and matching the modelling results to the

experimental temperature and density profiles by varying the perpendicular heat conductivities $\chi_{e,i}$ and the particle transport coefficient D in the code, a good agreement between the code results and the measurement data is obtained by using D and χ_e with three different plateau values respectively for three different regions and the assumption of $\chi_i = \chi_e$ [11]. From the Fig.2 in Ref.[11] for JET shot 58569, after dropping to lower value within the ETB $\chi_{e,i}$ increase again and reach to $1 \text{ m}^2 \text{ s}^{-1}$. The profiles of radial transport coefficients from H-mode shots on ASDEX Upgrade, JET and TCV are very similar to the profiles of D and χ_e obtained from the present fitting results of H-mode shot 37851 and 37856 on JT-60U tokamak.

3 Summary

The profiles of radial particle transport coefficient D , radial electron and ion heat transport coefficients χ_e, χ_i have been obtained by modelling plasma experiments and fitting the experimental data from L-mode shot 39090 and H-mode shots 37851 and 37856 in JT-60U tokamak with NBI and Ohmic heating. The radial transport coefficients D, χ_e and χ_i from the fitting have a radial dependence and they consist of qualitatively different parts. From the experimental results, it can be seen that in H-mode shots 37851 and 37856 steep gradients and pedestals near the separatrix have been formed in the plasma parameter profiles. From the modelling and fitting results at the pedestal region, the radial transport coefficient D and χ_e shows larger drops compared with the radial transport coefficients at other sections in the profiles. For the radial electron and ion heat transport coefficients χ_e and χ_i , there is no obvious drop within the Edge Transport Barrier (ETB) in the H-mode shots 37851 and 37856, the values of χ_e and χ_i near the outer wall are very large, which should be further studied in the next step. For L-mode shot 39090, the obvious drop of D and χ_e has not found.

Acknowledgments

This work was partially supported by the JSPS-CAS Core University program in the field of 'Plasma and Nuclear Fusion' and partially supported by National Natural Science Foundation of China (No.10975158). The authors greatly appreciate Max-Planck-Institut für Plasmaphysik in Garching for providing the SOLPS5.0 code package

References

- [1] R. Schneider, X. Bonnin, K. Borrass, D.P.Coster, H. Kastelewicz, D.Reiter, V.A.Rozhansky, B.J.Braams, Contrib. Plasma Phys.,46, NO.1-2,3-191(2006).
- [2] D.P.Coster, X.Bonnin, et al., J. Nucl. Materials, 337-339(2005)366-370.

- [3] Braams, B. et al., *Contrib. Plasma Phys.* 36, 276 (1996).
- [4] V.A. Rozhansky, S.P. Voskoboinikov, E.G. Kaveeva, D.P. Coster, R. Schneider, Simulation of tokamak edge plasma including self-consistent electric fields, *Nuclear Fusion*, Vol.41, No.4(2001) 387-401.
- [5] D.P.Coster, J.W.Kim, G.Haas, B.Kurzan, H.Murmann, J.Neuhauser, H.Salzmann, R.Schneider, W.Schneider, J.Schweitzer, and the ASDEX Upgrade Team, Automatic evaluation of edge transport coefficients with B2-SOLPS5.0, *Contributions to Plasma Physics*, 40(3-4),334-339(2000); 7th PET Conference, Tajimi, Gifu, Japan, 4.-6. October, 1999.
- [6] J.-W. Kim, D.P. Coster, J. Neuhauser, R.Schneider, and the ASDEX Upgrade Team, ASDEX Upgrade edge transport scallings from the two-dimensional interpretative code B2.5-I, *J. Nucl. Mater.* 290-293(2001)644-647; 14th PSI, Rosenheim, Germany,22.-26. May 2000.
- [7] D.Reiter, et al., *J.Nucl.Mater.* 196-198(1992)80.
- [8] V V Parail, Energy and particle transport in plasmas with transport barriers, *Plasma Phys. Control. Fusion* 44(2002)A63A85.
- [9] L.D.Horton, A.V.Chankin, Y.P.Chen, et al., Characterization of the H-mode edge barrier at ASDEX Upgrade, *Nucl. Fusion* 45(2005)856-862.
- [10] B.Gulejov'a, et al., *J.Nucl.Mater.* 363-365(2007)1037.
- [11] A Kallenbach, Y Andrew, M Beurskens, G Corrigan, T Eichl, et al., EDGE2D modelling of edge profiles obtained in JET diagnostic optimized configuration, *Plasma Phys. Control. Fusion* 46(2004) 431-446.

Monte Carlo simulation of carbon redeposition on LHD first wall

Kawamura G.¹, Tomita Y.¹, Kobayashi M.¹, Tokitani M.¹, Masuzaki S.¹, Kirschner A.²

¹National Institute for Fusion Science, Toki 509-5292, Japan

²Institut für Plasmaphysik, Forschungszentrum Jülich GmbH, Germany

Abstract Deposition of impurities on surfaces of plasma confinement devices is one of essential issues in present devices and also future fusion devices. In the Large Helical Device (LHD), it is necessary to reveal fundamental characteristics of impurity transport and deposition by simulation studies along with experimental studies. In the present paper, simulation scheme of carbon deposition on the first wall of LHD and results are discussed. The geometry of the LHD divertor and the configuration of the plasma are newly implemented to the Monte Carlo code ERO. The profiles of the background plasma are calculated numerically by a 1D two-fluid model along a magnetic field line. Spatial distributions of the carbon impurities are investigated for a typical set of plasma parameters in LHD. The simulation results indicate that the deposition is caused by neutral carbon particles from two facing divertor plates. The divertor opposite to the first wall makes less contribution than the adjacent one because of the ionization in the divertor plasma. Chemically sputtered impurities cause more deposition near the divertor than physical ones because atomic processes of methane molecules lead to isotropic particle velocities.

Keywords: Impurity, deposition, divertor, ERO

PACS: 52.40.Hf, 52.25.Vy

1. Introduction

Deposition of impurities on surfaces of plasma confinement devices is one of essential issues for long-time discharges and reduction of tritium inventory in present devices and also future fusion devices. In the Large Helical Device (LHD)^[1], which is the largest heliotron-type plasma confinement device, distributions of impurities in deposition layers of divertor plates and material probes placed on the first wall have been investigated^[2-4]. The main components of the deposited impurities are carbon and iron during the main and glow discharges, respectively. Although the deposition itself does not cause a problem to the plasma directly, a long-term accumulation of impurities on the device surfaces can harm the plasma if the deposited films peel off into the plasma. In order to understand the characteristics of the impurity deposition, estimate and control impurity behaviors, simulation studies are necessary along with experimental investigations. In the present paper, simulation scheme of carbon deposition on the first wall of LHD and fundamental characteristics of the simulated carbon deposition are discussed.

We employed the ERO code^[5] to reveal how impurity carbon is transported and where it deposits. The Monte Carlo code ERO traces impurity atoms and molecules in simulation space with a number of atomic

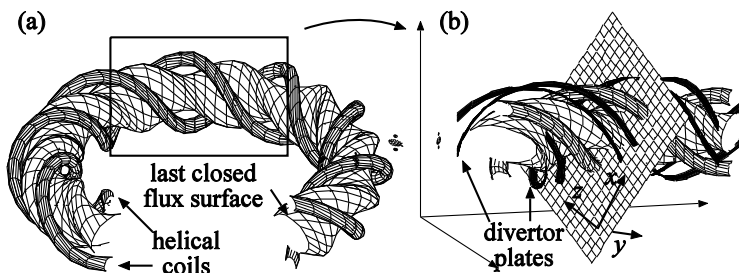


Fig. 1: (a) Schematic illustration of the plasma and the helical coils in the LHD. (b) enlarged illustration of the rectangular section. A plane with x - z axes represents a cross section of LHD divertor chamber used in the ERO code.

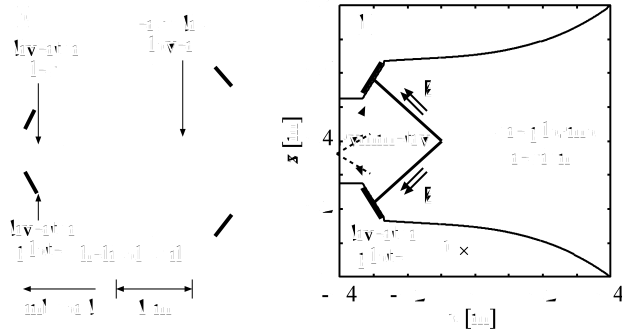


Fig. 2: (a) a poloidal cross section of the LHD plasma and the first wall. (b) the x - z plane used in the ERO code. The latter plane was generated by a CAD system and the perpendicular direction to the figure, i.e. along the y -axis, is locally uniform.

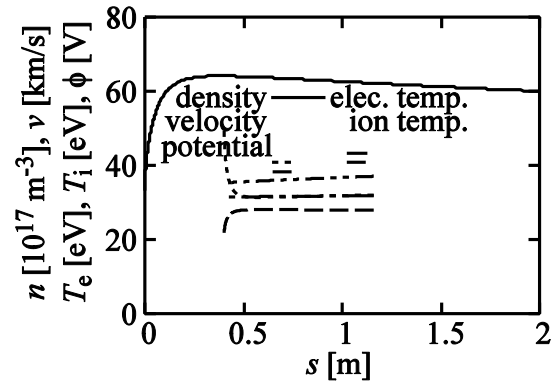


Fig. 3: Plasma profiles along the magnetic field for a typical set of plasma parameters.

Density, velocity, electron and ion temperatures and electrostatic potential are shown. The divertor plate and the upstream boundary are located at $s=0$ and 2 [m], respectively.

processes such as ionization and dissociation. The electromagnetic force and the collisional forces due to the background hydrogen plasma in the simulation box are involved in the calculations. A new implementation of the surface configuration in LHD has been introduced in the code. Figure 1 shows the LHD plasma surrounded by a pair of helical coils and four series of divertor plates. The rectangular section drawn in Fig. 1(a) is enlarged in Fig. 1(b). Two pairs of divertor plates are located between the helical coils and face the tips of the elliptic flux surfaces. We chose a helical cross section as the simulation box and carried out the simulation in 2D space with the assumption of uniformity along the perpendicular direction to the plane.

The detail of the simulation box and the background plasma used in the simulation are explained in Sec. 2. Deposition profiles obtained from the simulation are given in Sec. 3 and their characteristics are discussed there. Finally, conclusions are presented in Sec. 4.

2. Simulation model of the impurity transport in LHD divertor

Figure 2(a) shows a poloidal cross section of the plasma and the first wall of the LHD. The core plasma is surrounded by an ergodic layer characterized by stochastic magnetic fields. The divertor plates are placed approximately half meter away from the core plasma and connected with the ergodic layer through divertor legs. In order to reduce the dimension of the simulation box, the plane drawn in Fig. 1(b) was employed as a 2D simulation box, x - z . Figure 2(b) shows the x - z plane with a simplified plasma configuration. The plane is selected to be normal to the divertor plates and the first wall. We can safely assume the up-down symmetry to reduce the size of the simulation box to the bottom half by introducing virtual reflections of impurity particles at the upper boundary, $z=0.4$ [m]. The magnetic field in each divertor leg is assumed to be uniform with incident angle of 82° from the surface normal of the divertor plate. The perpendicular direction, i.e. y -direction, is assumed to be uniform, and thus periodic boundary condition is employed. Impurity particles are removed from the simulation when they move into the core plasma region shown as dotted lines in Fig. 2(b).

Material surfaces in the ERO code are described by a series of short line segments. They are used to calculate deposition, reflection and material mixing on the divertor plate and also the first wall. We used a polynomial function for the first wall, i.e. -0.27 [m] $< x < 0.4$ [m], and a straight line segment for the divertor plate, i.e. -0.33 [m] $< x < -0.27$ [m]. The outer region of the device wall, i.e. -0.4 [m] $< x < -0.33$

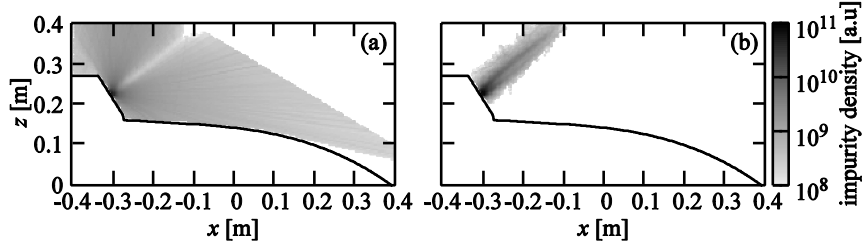


Fig. 4: Impurity density distributions; (a) neutral carbon atom, C, and (b) carbon ion, C⁺.

[m], was simplified as a horizontal line. These configurations were taken from a CAD diagram of the cross section. The main component of the divertor plate is carbon and that of the first walls is iron. Throughout discharges in a whole campaign, carbon atoms sputtered from the divertor plate deposit on the first wall and thus the surface near the divertor plate is covered by deposition layers^[3]. Therefore in the simulation we chose carbon as the initial material of divertor plate and also the first wall.

A background plasma is assumed in the simulation box and causes ionization and collisional forces on impurity particles. In order to implement the LHD divertor plasma in the code, we employed a new plasma model which consists of one dimensional two-fluid equations and neutral transport equations^[7,8]. The model involves balance equations of hydrogen ion flux, momentum and heat flux, and also heat conduction, thermal force and interactions between ions and neutral atoms. Numerical solutions of the model are used as a function of distance along the magnetic field from the strike-point to an arbitrary point in the simulation box. The solution is employed only on the center line of the divertor leg and the perpendicular profile to the line is given by Gaussian profile, $\exp(-l^2/\lambda^2)$, where the perpendicular distance and characteristic width were denoted by l and $\lambda=1$ [cm], respectively.

Plasma profiles for a typical set of parameters are shown in Fig. 3. The solution was obtained for boundary conditions as follows; the input heat power along the magnetic field from the upstream boundary is 10 [MW/m²], the upstream plasma density is 6×10^{18} [m⁻³] and the wall surface is electrically floating. The distance from the strike-point along the magnetic field is denoted by s , i.e. $s=0$ [m] corresponds to the strike-point. The plasma has steep profiles near the surface, i.e. $s < 0.3$ [m], while approximately uniform away from the surface. The steep gradients of potential profiles and large velocity yield significant parallel electric field and friction force on impurities, respectively. Since both of them push the impurity toward the divertor plate, they play a role of impurity confinement in the divertor leg. We note that a potential drop caused by the Debye sheath, $\approx 3T_e/e$ typically, is not shown in the figure but calculated and included in the code as an additional electrostatic force normal to the surface.

3. Simulation results of the impurity deposition

The ERO code traces impurity particles of various charge state and chemical species such as C, C⁺, C²⁺, C³⁺, C⁴⁺, CH, CH₂⁺ and so on. We note that C⁵⁺ and C⁶⁺ are not generated because of insufficient electron temperature for further ionization. The spatial profiles of neutral carbon atom, C, and carbon ion, C⁺ are, for instance, shown in Fig. 4(a) and Fig. 4(b), respectively. Since carbon is easily ionized by electrons, the neutral carbon is quite low density in the divertor leg. The perpendicular width of the leg is, however, relatively short and thus a certain amount of carbon atoms can penetrate the plasma without ionization and reach the first wall directly. If ionization takes place, the plasma flow and electric field push the impurity ions toward the surface and cause the localization of impurities near the surface for the plasma parameters used here, see Fig. 4(b). Although other results for different plasma parameters are not given in the present paper, we confirmed that high-density plasma tends to confine the impurities efficiently in the divertor region.

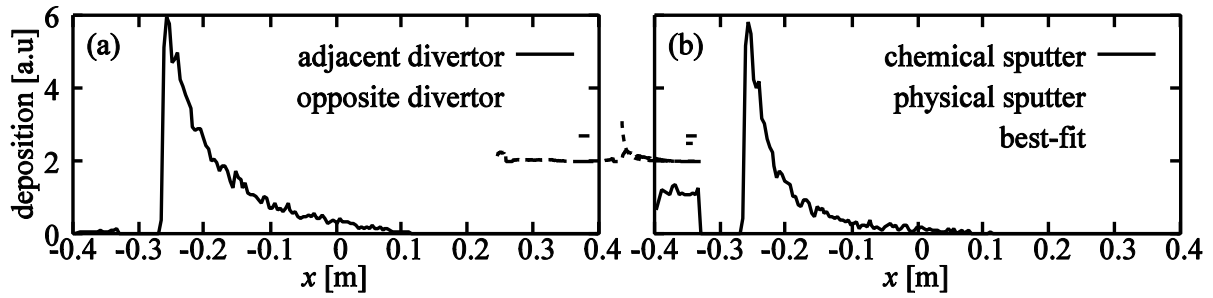


Fig. 5: Deposition profiles of carbon; (a) comparison of source positions, (b) comparison of chemical/physical sputtering. The best-fit curve is given by $0.012(x+0.3)^{-2}$ in the range of $x > -0.33$.

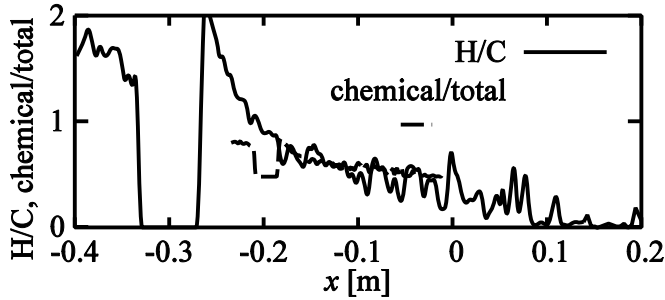


Fig. 6: Fraction of hydrogen atoms to the carbon atoms, i.e. $H/C = ([CH] + 2[CH_2] + 3[CH_3]) / [total\ C]$, and fraction of chemically sputtered carbon to the total carbon are shown.

The direct deposition of neutral carbon atoms depends on the plasma configuration and geometry of the divertor. The relative position and intensity of the impurity source are important to understand how impurities are distributed and how the deposition layer is formed on the first wall. The deposition profiles on the wall are shown in Fig. 5(a). The solid and dashed lines represent the number of carbon atoms per area of each surface mesh coming from the adjacent and opposite divertors, respectively. The divertor plate region, $-0.33\ [m] < x < -0.27\ [m]$, is omitted in the figure because the plasma-wetted surface has large erosion and there are no net depositions. The deposition caused by the opposite divertor is much less than that caused by the adjacent one on the first wall, while opposite divertor makes a major contribution in the outer region, i.e. $x < -0.33\ [m]$. The difference comes from the geometry of the LHD divertor shown in Fig. 2(b). The outer region is located behind the divertor and thus the impurities come only from the opposite divertor. If the amount of deposition is determined only by geometrical reason, the deposition on the first wall due to the opposite divertor must be at the same level as that on the outer region, but that is not the case. The reason is the presence of another divertor leg between the first wall and the opposite divertor plate. Since ionization in the plasma prevents the impurity particles from reaching the first wall, the deposition is significantly reduced.

The composition of the deposition layer is strongly affected by the impurity species. Figure 5(b) shows the amount of carbon resulting from chemical and physical sputtering. Their profiles differ from each other especially near the divertor plate. The chemically sputtered carbon has a sharp peak at $x \approx -0.25$, while physical one does not have a peak and the decay length to the x -direction is much longer. The dotted line in the figure is an inverse-square curve and coincides with the deposition profile of the chemically sputtered carbon. That implies the incident particles had isotropic velocities when they were generated near the strike point. At the same time the fact that charged particles cannot leave the plasma for the first wall indicates that the deposition is caused by neutral radicals and atoms, i.e. CH_3 , CH_2 , CH and C . That is consistent with the isotropic velocity distribution because the generation of the neutral particles requires atomic processes such as ionization and dissociative recombination, which lead to isotropic particle velocities.

In Fig. 5(a), a peak is observed on the deposition caused by the adjacent divertor. There is a reason for the similarity of the peak to that of the chemically sputtered carbon. Since the chemical species are ionized more easily than carbon atoms, they hardly penetrate the divertor leg. As a result, the chemical sputtering from the adjacent divertor is dominant and the deposition profile near the divertor plate is determined by

the chemical sputtering.

Since the deposition is caused by radicals and carbon atoms, the components of the deposition layer differ according to location. Fraction of hydrogen atoms to the carbon atoms is shown in Fig. 6. Also the fraction of the chemically sputtered particles to the total carbon atoms is shown in the same figure. These two profiles are approximately proportional to each other and the ratio is two. That implies averaged H/C of the deposited particles, i.e. C, CH, CH₂ and CH₃, originated in the chemical sputtering is approximately two independently of location and the distribution is determined only by the fraction of the chemically sputtered carbon to the total carbon.

4. Conclusions

The geometry of the LHD divertor and the configuration of the divertor plasma were implemented in the Monte Carlo code ERO in order to study impurity distribution on the first wall. The plane, x - z in Fig. 1 and 2, was employed as the simulation box. We used a background plasma profile calculated by a two-fluid model for a typical set of boundary parameters and carried out Monte Carlo simulations. The profiles of various charges of carbon atoms and methane molecules and radicals were obtained and we found that impurity ions experience the friction force and electric force toward the divertor plate and thus they are localized near the divertor plate.

The depositions on the first wall were expected to originate from the two impurity sources at the adjacent and opposite divertor plates but we obtained much less amount of deposition from the opposite divertor plate than that of the adjacent one. The reason is the ionization in the divertor leg between the first wall and the opposite divertor plate. A part of carbon atoms and almost all of methane molecules are ionized and trapped in the plasma and thus the deposition from the opposite divertor plate is reduced significantly.

Deposition from chemically and physically sputtered carbon was compared with each other and we obtained characteristic distribution of hydrocarbons with a sharp peak next to the divertor plate. Since the methane is ionized quite easily, the deposition of the hydrocarbons are caused by radicals generated by dissociation of methane molecules in the plasma. Therefore their velocities become nearly isotropic and yield the different distribution compared with the physically sputtered carbon with the cosine distribution.

The fundamental characteristics of the spatial distribution of carbon impurity has been investigated in the paper. They are important bases of further studies such as parameter survey of the background plasma and also useful clues to understand the impurity distributions in the actual device. Comparisons with experimental observations, more detailed plasma-wall interactions with TRIM code and impurity transport study in the divertor leg will be future issues.

Acknowledgments

This work was supported in part by a Grant-in-Aid for scientific research from Ministry of Education, Science and Culture of Japan (No. 19055005). This work was partially supported by the JSPS-CAS Core University program in the field of 'Plasma and Nuclear Fusion.'

¹ Oyabu N., Watanabe T., Ji H., *et al.* 1994, Nucl. Fusion, 34:387

² Sagara A., Masuzaki S., Morisaki T. *et al.* 2003, J. Nucl. Mater., 313-316: 1

³ Nobuta Y., Yamauchi Y., Hirohata Y. *et al.* 2004, J. Nucl. Mater., 329-333: 800

⁴ Hino T., Nobuta Y., Yamauchi Y., *et al.* 2003, J. Nucl. Mater., 313-316: 167

⁵ Kirschner A., Philipps V., Winterb J. and Kögler U. K., 2000, Nucl. Fusion, 40: 989.

⁶ Eckstein W.. 1991, *Computer Simulation of Ion-Solid Interaction*, Springer-Verlag, Berlin

⁷ Kawamura G., Tomita Y., Kobayashi M. and Tskhakaya D., 2010, J. Plasma Fus. Res., 5: S1020

⁸ Kawamura G., Tomita Y., Kobayashi M. and Tskhakaya D., 2009, J. Plasma Fus. Res. Series, 8: 455

Second stable regime of internal kink modes excited by barely passing energetic ions in tokamak plasmas

H. D. He¹, J. Q. Dong^{2,1}, G. Y. Fu³, G. Y. Zheng¹, Z. M. Sheng², Y. X. Long¹,
Z. X. He¹, H. B. Jiang¹, Y. Shen¹ and L. F. Wang¹

¹Southwestern Institute of Physics, Chengdu, China

²Institute for Fusion Theory and Simulation, Zhejiang University, Hangzhou, China

³Princeton Plasma Physics Laboratory, Princeton, USA

The internal kink (fishbone) modes, driven by barely passing energetic ions (EIs), are numerically studied with the spatial distribution of the EIs taking into account. It is found that the modes with frequencies comparable to the toroidal precession frequencies are excited by resonant interaction with the EIs. Positive and negative density gradient dominating cases, corresponding to off- and near-axis depositions of neutral beam injection (NBI), respectively, are analyzed in detail. The most interesting and important feature of the modes is that there exists a second stable regime in higher β_h (= pressure of EIs / toroidal magnetic pressure) range, and the modes may only be excited by the barely passing EIs in a region of $\beta_{th1} < \beta_h < \beta_{th2}$ (β_{th} is threshold or critical beta of EIs). Besides, the unstable modes require minimum density gradients and minimum radial positions of NBI deposition. The physics mechanism for the existence of the second stable regime is discussed. The results may provide a means of reducing or even preventing the loss of NBI energetic ions and increasing the heating efficiency by adjusting the pitch angle and driving the system into the second stable regime fast enough.

I. INTRODUCTON

The effects of energetic ions (EIs) on plasma instability and confinement in toroidal devices have been a major subject of theoretical and experimental studies in recent decades. The fish-bone like internal kink modes excited by trapped EIs have been observed in perpendicular neutral beam injection (NBI)¹ as well as ion cyclotron resonance heating (ICRH) experiments.²⁻³ These modes have been analytically and numerically investigated in detail and shown to be resonantly excited by precession of deeply trapped EIs.⁴⁻⁷ Besides the low frequency fish-bone modes, high frequency internal kink modes, being resonantly destabilized by passing EIs, have also been observed in tangential NBI experiments.⁸ These instabilities usually result in loss of the EIs, and consequently degradation of confinement and efficiency of plasma heating. Therefore, it is crucially important to control and to avoid the instabilities in advanced tokamak experiments. On the other hand, experimental and theoretical studies have shown that a population of energetic trapped ions can result in plasma completely stable to both sawtooth oscillations and the fishbone mode.⁹⁻¹¹

In this work, the unstable modes driven by barely passing EIs are investigated, taking the spatial density distribution of EIs into account. The frequency of the modes is found to increase dramatically when the radial profile of the EI density changes from off-axis peaking

to near-axis peaking. The mode growth rate as a function of β_h , has a maximum and, therefore, there exists a second stable regime in higher β_h range. In Sec. II, the dispersion relation for internal kink mode considering spatial distribution of EIs is derived. Two critical betas of EIs are analytically given. In Sec. III, the numerical solution of the dispersion relation is discussed based on HL-2A cross section equilibrium configuration parameters. In addition, the Nyquist technique is employed to demonstrate the existence of the second stable regime. In Sec. IV, the possible physical mechanism for the formation of the mode is presented. And in Sec. V are the conclusions and discussion.

II. DISPERSION RELATION

A larger-aspect-ratio tokamak plasma consisting of core and hot (energetic) components is considered. The inverse aspect ratio is $\varepsilon = a/R \ll 1$ (here a and R are minor and major radii of the torus, respectively). The following orderings are assumed in this paper in accordance with tokamak experiments: $\beta_{pc} \sim O(1)$, $\beta_{ph} \sim O(\varepsilon)$, (β_{pc} is the poloidal beta value of the core component), and the temperature ratio between the core and hot components, $T_c/T_h \sim O(\varepsilon^2)$. Therefore, the density ratio between the energetic and the core components is estimated as $n_h/n_c \sim O(\varepsilon^3)$. By making use of these assumptions, a dispersion function is obtained as,⁴⁻⁵

$$D(\xi) = \delta W_{MHD} + \delta W_k + \delta_I, \quad (1)$$

Where $\delta_I = -\frac{1}{2}\omega^2 \int d^3x \rho_m |\xi|^2$ is the inertial term, δW_{MHD} and δW_k are MHD and kinetic contributions, respectively, given by the following two equations,

$$\delta W_{MHD} = -\frac{1}{2} \int d^3x \left[\frac{|\delta B_\perp|^2}{4\pi} - \frac{j_{||}}{c} (\bar{\xi}_\perp^* \times \bar{e}_{||}) \cdot \delta \bar{B}_\perp - 2(\bar{\xi}_\perp \cdot \nabla P)(\bar{\xi}_\perp^* \times \bar{\kappa}) + \frac{B^2}{4\pi} |\nabla \cdot \bar{\xi}_\perp + 2\bar{\xi}_\perp \cdot \bar{\kappa}|^2 + \gamma P_c |\nabla \cdot \bar{\xi}_\perp|^2 \right], \quad (2)$$

$$\delta W_k = 2^{9/2} \pi^3 m_h \int R B r dr \int d\alpha \int_0^\infty dE E^{5/2} K_b \frac{\bar{J}_0^* Q \bar{J}_0}{\omega_d - \omega}. \quad (3)$$

Here, $K_b = \frac{1}{2\pi} \oint \frac{d\theta}{\sqrt{1-\alpha B}}$, $Q = (\omega \frac{\partial}{\partial E} + \hat{\omega}_{*h}) F$, $J = \frac{\alpha B}{2} \nabla \cdot \bar{\xi}_\perp - (1 - \frac{3\alpha B}{2}) \bar{\xi}_\perp \cdot \bar{\kappa}$ with $\bar{\kappa} = \bar{b} \cdot \nabla \bar{b}$ being the curvature of the magnetic field line, E is energy of EIs, $\hat{\omega}_{*h} = \frac{\omega_{*h}}{T_h}$, T_h is temperature of EIs. $\omega_{*h} = -i \frac{T_h}{m_h \omega_0} (\bar{b} \times \nabla \ln F) \cdot \nabla$ is the diamagnetic drift frequency of EIs, $\bar{A} = (\oint A dl / |v_{||}|) / (\oint dl / |v_{||}|)$ is an average over a field line, $\alpha = \mu / E$ (μ is magnetic moment) and ω_0 are the pitch angle and cyclotron frequency of the EIs, respectively, and $F(r, \alpha, E) = n(r) \delta(\alpha - \alpha_0) g(E)$ is the distribution function of the EIs. In addition, the transit frequency ω_t is neglected in Eq. (3) due to the fact that barely passing EIs are considered only. The radial density profile is assumed to be $n(r) \sim e^{-\sigma^2 (r-r_0)^2}$ and a

slowing-down energy distribution $g(E) = E^{-3/2}$ is employed for the EIs. $\omega_d = (Eq/r\omega_0 R)K_c$ is the bounce averaged precession frequency of the EIs. K_c is a function of the first and the second kinds of complete elliptic functions E and K

$$K_c = 1 + 2k^2 \left[\frac{E(1/k)}{K(1/k)} - 1 \right] + 4k^2 s \left[\frac{E(1/k)}{K(1/k)} - \frac{\pi}{2K(1/k)} \sqrt{1 - 1/k^2} \right] \quad (4)$$

with the argument $k^2 = (1/\alpha_0 - 1 + r/R)/(2r/R)$ for passing particles,¹²⁻¹³ here, and $s = rdq/qdr$ is magnetic shear. The average beta value of the EIs inside the $q=1$ flux surface may be expressed as

$$\beta_h = \int d^3x 8\pi (\int d^3v EF) / B^2 V = c_\beta \int r dr d(\alpha B) Ef(r, \alpha, E) K_b dE, \quad (5)$$

Where V is the volume of plasma column, $f(r, \alpha, E) = 2^{5/2} R \sqrt{EF}(r, \alpha, E) / N_p$ is the normalized distribution function, N_p is the total number of the EIs, and $c_\beta = \frac{2\pi^2 N_p}{RB^2 r_s^2}$. The

third term on the right hand side in Eq.(2) indicates that the contribution of the hot particles to δW_{MHD} is $\delta W_{MHD,h} = -\int d^3x (\tilde{\xi}_\perp \cdot \nabla P)(\tilde{\xi}_\perp^* \cdot \kappa)$. In order to minimize the dispersion function Eq.(1), an appropriate trial function is constructed as $\tilde{\xi}_\perp = (\bar{e}_r + i\bar{e}_\theta)\xi_0 \exp(i\theta - i\phi)$ inside the $q=1$ flux surface of radius r_s and $\tilde{\xi}_\perp = 0$ outside the surface. Note, the toroidal and poloidal wave vectors as well as the radial structure of the mode under consideration are all fixed with this trial function. Following the minimizing procedure described in Refs.4-5, the dispersion relation is obtained as following from Eqs.(1-3),

$$0 = D(\omega) \equiv -i \frac{\omega}{\omega_A} + \delta \hat{W}_c + \delta W_{MHD,h} + \delta W_k, \quad (6)$$

where the normalization $\delta \hat{W} = 2R \delta W / (\pi B^2 r_s^2 \xi_0^2)$ has been introduced and

$$\delta \hat{W}_c = 3\pi \Delta q (r_s / R)^2 (13/144 - \beta_{ps}^2) \text{ is obtained }^{14} \text{ with } \beta_{ps} = -\left(\frac{R}{r_s}\right)^2 \int_0^{r_s} r^2 \beta' dr$$

, $\Delta q = 1 - q(0)$, and $\beta = 8\pi P / B_0^2$ is the beta value of the core component. After integrated over energy E and pitch angle α , Eq. (6) becomes,

$$0 = D(\omega) \equiv -i \frac{\omega}{\omega_A} + \delta \hat{W}_c + \delta W_{k0} + \delta W_{k1}. \quad (7)$$

Here, the responses $\delta \hat{W}_{k0}$ and $\delta \hat{W}_{k1}$ are damping and driving terms and given by the following two equations, respectively,

$$\delta \hat{W}_{k0} = \frac{\beta_h R n(r_s)}{2r_s a'} \left(\frac{2E}{K} - 1 \right) + \frac{\beta_h R}{2r_s a'} \hat{C} \int_0^1 n(\hat{r}) \sqrt{\frac{1}{\hat{r}}} d\hat{r} \quad (8)$$

$$\delta \hat{W}_{k1} = -\frac{\beta_h R}{2r_s a'} \left(\frac{2E}{K} - 1 \right)^2 \frac{\Delta n}{qK_c} \left[1 + \Omega \ln \left(1 - \frac{1}{\Omega} \right) \right] + \frac{\beta_h R}{2r_s a'} \Omega (\hat{A} - \hat{B} - \hat{B} \Omega \frac{\partial}{\partial \Omega}) \int_0^1 n(\hat{r}) \sqrt{\hat{r}} \ln \left(1 - \frac{1}{\Omega \hat{r}} \right) d\hat{r} \quad (9)$$

with $a' = \int_0^1 n(\hat{r}) \sqrt{\hat{r}} d\hat{r}$, $\Omega = \omega / \omega_{ds}$, $\Delta n = n(r_s) - n(0)$. We can evaluate the threshold beta of EIs by letting $\Omega = \Omega_r + i\gamma$, $\gamma \rightarrow 0$. Considering that $\ln(x) = \ln|x| + i\pi$ when $x < 0$, an

expression for the threshold beta can be easily obtained as following by letting $\text{Im} D(\omega) = 0$,

$$\beta_{h,\text{crit}} = \frac{2r_s a' \omega_{ds}}{\pi \omega_A R (\hat{A} - \hat{B} - \hat{B} \Omega_r \frac{\partial}{\partial \Omega_r}) \int_0^{1/\Omega_r} n(\hat{r}) \sqrt{\hat{r}} d\hat{r}}, \quad (10)$$

where $\Omega_r > 1$ has to be determined by substituting Eq. (10) back into the real part of Eq. (7).

A non-uniform normalized spatial density distribution profile $n(\hat{r}) \sim e^{-\sigma^2(\hat{r}-\hat{r}_0)^2}$ with $\hat{r} = r/r_s$ is considered. In order to get an analytic expression similar to the previous results,^{4,5} the domain $\hat{r} \in [0, 1]$ is divided into N sub-domains $[\hat{r}_j, \hat{r}_j + \Delta\hat{r}]$, $j=1,2,\dots,N$, where the spatial density profile is fitted with the linear form $n(\hat{r}) = k_j \hat{r} + c_j$ for simplicity. Here, $\Delta\hat{r} = \frac{1}{N}$, $k_j = \frac{n(\hat{r}_{j+1}) - n(\hat{r}_j)}{\Delta\hat{r}}$, $c_j = n(\hat{r}_j) - k_j \hat{r}_j$, $\hat{r}_j = (j-1)\Delta\hat{r}$. Then, in Eqs. (8-9) the integration over radial distance can be conveniently substitute by the following summations,

$$\delta\hat{W}_{k0} = \frac{\beta_h R [n(r_s)(2E/K - 1) + a_1 \hat{C}]}{4r_s a_0} \quad (8')$$

$$\begin{aligned} \delta\hat{W}_{k1} = & -\frac{\beta_h R}{4r_s a_0} \left(\frac{2E}{K} - 1 \right)^2 \frac{\Delta n}{qK_c} \left[1 + \Omega \ln \left(1 - \frac{1}{\Omega} \right) \right] + \frac{\beta_h R}{2r_s a_0} \sum_{j=1}^N \left\{ \frac{k_j}{5} [(\hat{A} - \hat{B})\Omega U(5, a, b) - \right. \\ & \frac{2\hat{A}(b^3 - a^3)}{3} - 2(\hat{A} + \hat{B})\frac{b-a}{\Omega} + (\hat{A} + \frac{3\hat{B}}{2})\frac{V(a, b)}{\Omega} - \hat{B}\Omega^2 \frac{\partial U(5, a, b)}{\partial \Omega} + \hat{B} \frac{\partial U(1, a, b)}{\partial \Omega}] \\ & \left. + \frac{c_j}{3} [(\hat{A} - \hat{B})\Omega U(3, a, b) + (\hat{A} + \hat{B}/2)V(a, b) - 2(\hat{A} + \frac{\hat{B}}{2})(b-a)] \right\}. \quad (9') \end{aligned}$$

Here, $a = \sqrt{\hat{r}_j}$, $b = \sqrt{\hat{r}_{j+1}}$, $U(n, x, y) = y^n \ln(1 - \frac{1}{\Omega y^2}) - x^n \ln(1 - \frac{1}{\Omega x^2})$,

$$V(x, y) = \frac{1}{\sqrt{\Omega}} \ln \frac{(\sqrt{\Omega}x - 1)(\sqrt{\Omega}y + 1)}{(\sqrt{\Omega}x + 1)(\sqrt{\Omega}y - 1)}.$$

The normalized \hat{A} , \hat{B} , \hat{C} , and a_0 , a_1 are given as,

$$\hat{A} = \left(\frac{1-2k^2}{K_c} - \frac{1}{\alpha} \right) \left(\frac{2E}{K} - 1 \right) \left[\frac{d}{dk^2} \left(\frac{E}{K} \right) + \frac{1}{2K} \frac{d(2E-K)}{dk^2} \right] + \frac{(2E/K-1)^2}{2K_c} \left(1 - \frac{1-2k^2}{K_c} \frac{dK_c}{dk^2} \right), \quad (11)$$

$$\hat{B} = \frac{(2E/K-1)^2}{2K_c} \left[\left(\frac{1-2k^2}{K_c} - \frac{1}{\alpha} \right) \frac{dK_c}{dk^2} - 2 \right], \quad (12)$$

$$\begin{aligned} \hat{C} = & \left(\frac{2E/K-1}{K_c} - 1 \right) \left[\frac{1}{2} \left(\frac{2E}{K} - 1 \right) + \frac{1-2k^2}{2K} \frac{d(2E-K)}{dk^2} \right] + \\ & \frac{(2E/K-1)(1-2k^2)}{2K_c} \left[\frac{d}{dk^2} \left(\frac{2E}{K} \right) - \frac{(2E-K)}{K_c K} \frac{dK_c}{dk^2} \right], \quad (13) \end{aligned}$$

$$a_0 = \sum_{j=1}^N \left(k_j \frac{b^5 - a^5}{5} + c_j \frac{b^3 - a^3}{3} \right), \quad a_1 = \sum_{j=1}^N \left[\frac{2}{3} k_j (b^3 - a^3) + 2c_j (b-a) \right]. \quad (14)$$

III. NUMERICAL RESULTS

To be specific, we consider a neutral beam injection experiment (injection energy $E_b=60\text{KeV}$) on the HL-2A tokamak¹⁵ with a circular cross section equilibrium configuration. The other parameters are the toroidal magnetic field $B_T=1.68\text{T}$, the major radius $R=165\text{cm}$, the

minor radius $a=40\text{cm}$, the magnetic shear $s=0.003$, the Alfvén frequency $\omega_A = 4.31 \times 10^6 \text{ s}^{-1}$, $\hat{r}_0=0.72/0.25$ corresponding to the cases that positive/negative radial gradient of the energetic ion density dominates (i.e. off-axis/near-axis NBI heating, respectively). $\delta\hat{W}_c = 0.003$ (i.e. MHD is stable) and the $q=1$ surface is located at $r_s=a/2$. Under these conditions, the particles with $0 < \alpha_0 < 1 - r_s / R$ (or $k > 1$) are passing particles.

The formulas and the numerical code are checked and the results in previous works^{4, 5} are recovered when $\sigma = 0$ and deeply trapped EIs are considered.

The dispersion relation, Eq. (7) is numerically solved and an unstable mode is found to be driven by barely passing EIs. The real frequency ω_r and growth rate γ of the mode versus β_h are given in Fig.1 where the lines with open circles denote modes in the high frequency range whereas the lines without symbols do that in the low frequency range. Meanwhile, the dashed, the dash-dotted and the solid lines correspond to $\sigma=6, 7, 7.5$, respectively, with $\alpha_0=0.8, \hat{r}_0=0.25$ for the modes with higher frequencies, and $\alpha_0=0.8, 0.78, 0.76$, respectively with $\sigma=2.5, \hat{r}_0=0.72$ for the modes with lower frequencies. Generally speaking, the modes are unstable in the lower and higher frequency ranges for off-axis peaking and near-axis peaking density profiles, respectively. The striking feature of the modes studied here is that there exists a second stable regime in the higher β_h parameter range and, therefore, there are two threshold beta values, β_{th1} and β_{th2} . The instability is excited by barely passing energetic ions when the condition $\beta_h > \beta_{th1}$ is satisfied. The growth rate increases first, and then decreases gradually after reaching a maximum when β_h increases. Finally, the mode becomes stable when $\beta > \beta_{th2}$. The result resembles that for the ideal MHD ballooning mode with the plasma β there replaced by β_h here.⁹⁻¹¹ The real frequency of the mode is comparable to the toroidal precession frequency ω_d indicating the resonant excitation of the mode energetic ions. The expression of ω_d above indicates that it is inversely proportional to radial position r . Therefore, the modes in high and low frequency ranges are driven unstable, respectively, when the radial profile of the EI density changes from near-axis peaking to off-axis peaking, corresponding to near-axis heating and off-axis heating of NBI, respectively (See Fig. 3 for more details). This figure also indicates that the higher the σ value, corresponding to higher density gradient, the wider the unstable range of β_h for fixed $\alpha_0=0.8$, and $\hat{r}_0=0.25$. On the other hand, the lower the α_0 value, corresponding to smaller pitch angle, the wider the unstable range for fixed $\sigma=2.5, \hat{r}_0=0.72$ and the parameter α_0 domain studied here.

Shown in Fig. 2 are the real frequency ω_r and growth rate γ as functions of beam energy E_b with $\beta_h = 0.002$ and $\alpha_0 = 0.8$. The lines with circles correspond to near-axis heating with $\hat{r}_0=0.25, \sigma=7$ and the other lines correspond to off-axis heating with $\hat{r}_0=0.72, \sigma=2.5$. It is clear that the growth rate increases monotonically with increasing beam energy when β_h is kept constant. Consequently, there exists a critical E_b for both near-axis and off-axis heating cases. In addition, the critical beam energy for near-axis heating case is about 3/5 of that for off-axis heating case.

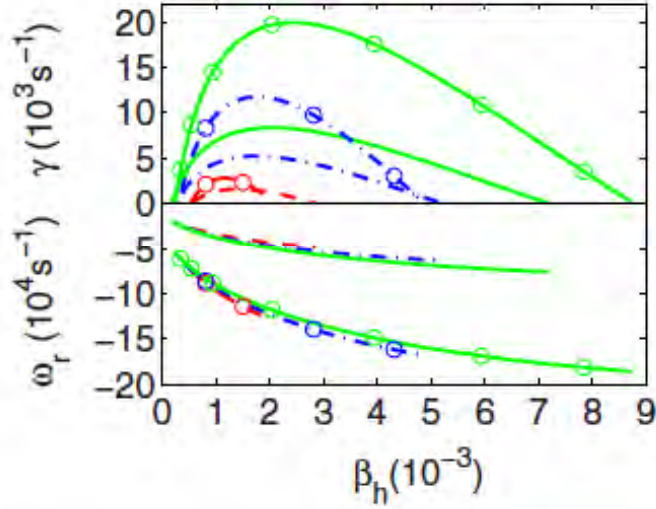


FIG. 1. The mode real frequency ω_r and growth rate γ as functions of β_h , the lines with circles and without symbols denote the modes in high frequency and low frequency ranges, respectively.

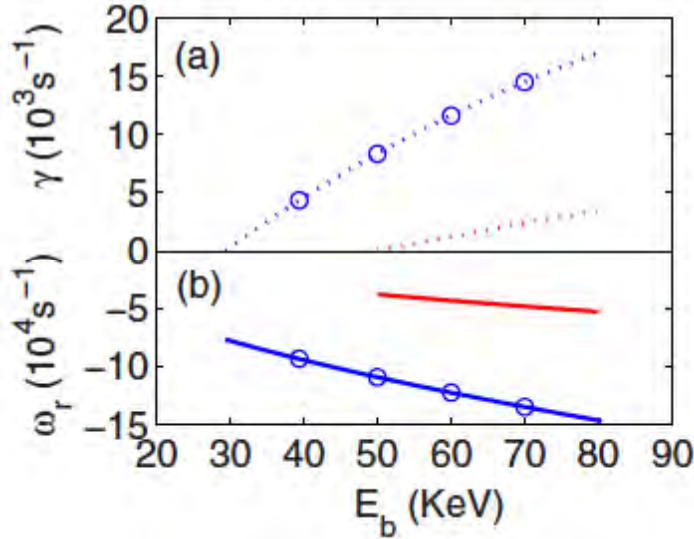


FIG. 2. The real frequency ω_r and growth rate γ as functions of the beam energy E_b for off-axis heating and near-axis heating.

Given in Fig.3 are the dependences of the real frequency (the solid lines) and the growth rate (the dash-dotted lines) on the deposition position \hat{r}_0 (the lines with triangles) of NBI for $\sigma=7.5$ and on the density gradient parameter σ (the lines with circles) for $\hat{r}_0=0.25$. The results clearly indicate that there exists a critical value, $\hat{r}_0 = \hat{r}_{0crit}$. When $\hat{r}_0 > \hat{r}_{0crit}$, the mode is excited and the growth rate increases first, reaches a maximum value, and then decreases with further increase of \hat{r}_0 . The real frequency monotonically decreases with increasing of \hat{r}_0 from high frequency range to low frequency range. The formula $-\omega_r \sim c / \hat{r}_0$ (here c is a scaling constant) fits the numerical results quite well as shown by the dotted line, showing the same scaling with \hat{r}_0 as the precession frequency ω_d does. The growth rate and the real frequency of the mode for $\hat{r}_0=1.0$ are both much lower than the maxima reached at $\hat{r}_0 \sim 0.3$ and 0.2 , respectively. This indicates that the mode is easier to be destabilized for $\partial F / \partial r < 0$

dominating (near-axis heating) case than for $\partial F / \partial r > 0$ dominating (off-axis heating) case. For both off-axis and near-axis heating cases, the resonant energy exchanging between the hot ions and the modes plays an essential role in excitation of the mode with frequency comparable to ω_d .

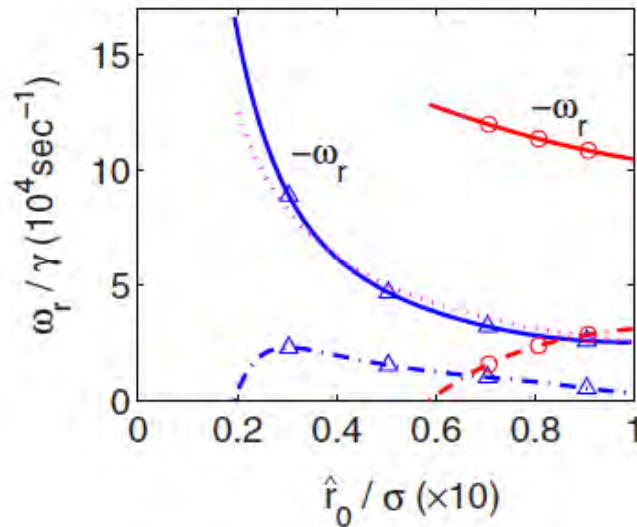


FIG. 3. The real frequency ω_r (the solid lines) and growth rate γ (the dash-dotted lines) as functions of \hat{r}_0 (the lines with triangles) and density gradient parameter σ (the lines with circles) with $\alpha_0=0.8$, $\beta_h=0.002$. $\hat{r}_0=0.25$ for the lines with circles and $\sigma=7.5$ for the lines with triangles. The dotted line is a fit of $-\omega_r \sim c / \hat{r}_0$

In addition, the lines with circles indicate that a minimum $\sigma_{crit} \sim 6$ is also necessary to drive the mode unstable while the real frequency $\omega_r \sim 1.2 \times 10^5 / s$ does not vary much up to $\sigma \sim 10$ for $\hat{r}_0=0.25$. The minimum $\sigma_{crit} \sim 2.5$ is also required to drive the mode unstable and the real frequency $\omega_r \sim 4 \times 10^4 / s$ does not vary much up to $\sigma \sim 10$ for $\hat{r}_0=0.72$ (not shown here).

Shown in Fig.4 are the stability diagrams in the $\beta_h - \sigma$ plane. The solid and dotted lines correspond to $\hat{r}_0=0.72$ and $\hat{r}_0=0.25$, respectively, with $\alpha_0=0.80$ for both cases. The $\beta_h - \sigma$ plane is divided into unstable and stable regions by each curve. The mode is unstable and stable above and below the corresponding line, respectively, in each case. Beta values on the curves are critical beta values $\beta_{h,crit}$ for each case. There are two critical beta values for a given σ in each case. The ranges in Fig.4 marked with numbers 1, 2 and 3 for off-axis heating case (I, II and III for near-axis heating case) are called the first, the second stable ranges and the unstable ranges, respectively. In each first stable range, the mode can be driven on the condition that the hot particle beta is higher than the critical value. On the contrary, the mode becomes stable when beta is higher than the second critical value and enters into the second stability range. From Fig.4 we can see that the first threshold beta value of energetic ions decreases with increasing σ whereas the second one increases with increasing σ for both near- and off-axis heating cases. This indicates that the mode is difficult to be driven unstable but easy to enter the second stability regime for flat density profiles of EIs. It is the opposite for peaked density profiles. In addition, steeper density profiles are needed to drive the modes in high frequency range (i.e. in near-axis heating case) than that in low frequency range (i.e. off-axis heating case).

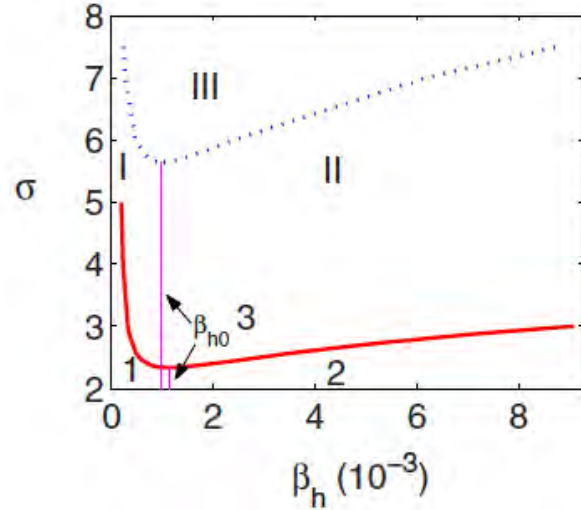


FIG.4. The stability diagrams in the $\beta_h - \sigma$ plane. The solid and dotted lines are for the modes in off-/near-axis heating cases with $\hat{r}_0=0.72/0.25$ and $\alpha_0=0.80$.

Furthermore, it is numerically found that there exist minimum values of density gradient parameter $\sigma = \sigma_{min}$ in the vicinity of $\beta_h = \beta_{h0} \sim 1.0 \times 10^{-3}$ for the both. The barely passing EIs can destabilize the modes through wave-particle resonance only when $\sigma > \sigma_{crit}$.

Nyquist technique is employed to further check the results presented above. Shown in Fig. 5 are the Nyquist diagrams plotted in the complex $D(\omega)$ plane. The dashed and the dash-dotted lines are for two β_h values in the first and second stable regions, whereas the dotted line is for one β_h in the unstable region. The diagrams clearly demonstrate that there is indeed an unstable mode (the curve encircles the original point once) only when β_h is higher than the first threshold beta value and lower than the second one. Otherwise, there are no unstable modes (the curve does not encircle the original point). Therefore, results in Fig.(1) are confirmed.

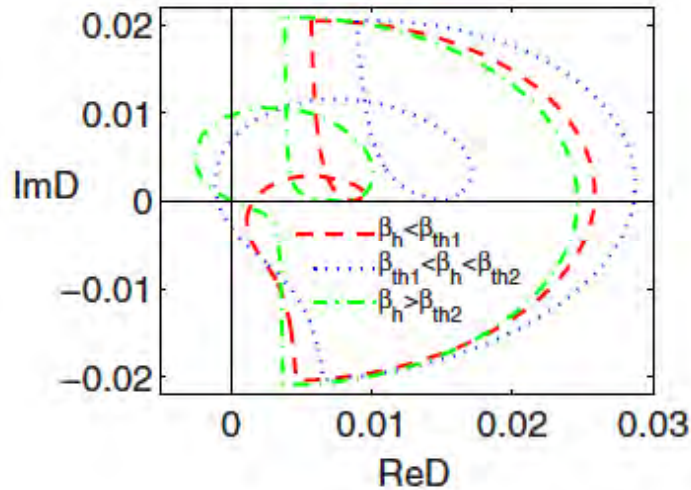


FIG.5 the Nyquist diagrams plotted in the complex D plane. The dashed, dash-dotted and dotted lines are, respectively, for the first, the second stable regions and the unstable region.

IV. THE POSSIBLE PHYSICAL MECHANISM

It is worthwhile to discuss the physical mechanism for the formation of the second stable regime of the modes more in detail. Taking an off-axis heating case with $\sigma=2.5$, $\hat{r}_0=0.72$ as an example, shown in Fig.6 (a) is the damping term $\delta\hat{W}_{k0}$ in Eq. (7) as a function of α_0 covering both passing and trapped ranges for $\beta_h=0.002$. The results indicate that the damping effect of $\delta\hat{W}_{k0}$ in the passing range (the solid line) is much stronger than that in the trapped range (the broken line). This may mean that the modes excited by passing EIs are easier to enter into the second stability region than that done by trapped EIs. On the other hand, roughly speaking, the real part of the driving term $\delta\hat{W}_{k1}$ in Eq.(7) provides necessary free energy for inducing the unstable modes. The exciting condition for the unstable modes to develop may be estimated as $\delta\hat{W}_c + \delta\hat{W}_{k0} + \text{Re}(\delta\hat{W}_{k1}) < 0$ from Equation (7). That is, the free energy provided by the driving term is greater than the damping term $\delta\hat{W}_{k0}$ plus core MHD term $\delta\hat{W}_c$. Shown in Fig.6 (b) is the dependence of $\delta W_k^R = \delta\hat{W}_c + \delta\hat{W}_{k0} + \text{Re}(\delta\hat{W}_{k1})$ on β_h . The solid and broken lines are for barely passing ions with $\alpha_0=0.76$ and barely trapped ions with $\alpha_0=0.93$, respectively. δW_k^R decreases monotonically, meaning the mode becomes more unstable, with increasing of β_h for barely trapped EIs of $\alpha_0=0.93$. In contrast, δW_k^R decreases first, reaches a minimum and then increases with increasing of β_h for barely passing EIs of $\alpha_0=0.76$. In addition, we learn from equation (8) that the damping term depends on β_h linearly and is independent of the mode frequency and growth rate. Consequently, the contribution of damping term is trivial for small β_h and predominant for large β_h . This is the reason why the absolute value of δW_k^R in Fig.6 (b) increases with increasing β_h in the small β_h range and decreases in the large β_h range. As a result, the mode is driven unstable for small β_h . On the other hand, the destabilizing effect of energetic ions can be greatly weakened by the damping term $\delta\hat{W}_{k0}$ for large beta. Therefore, it is understandable that the growth rate in Fig.1 increases for small beta and decreases after reaching a maximum γ for large beta when β_h increases. It is also clear that there is not a second stable regime for the internal kink (fishbone) modes driven by deeply trapped EIs since the free energy δW_k^R monotonically increases with β_h for trapped EI case.

The main features of the modes, such as possessing second stable regime, remain for radial density profile, $n(\hat{r}) \sim e^{-\sigma^2(\hat{r}^2 - \hat{r}_0^2)^2}$, which provide zero density gradient at the original point of $\hat{r}_0 = 0$ and prevents non-physical factors.

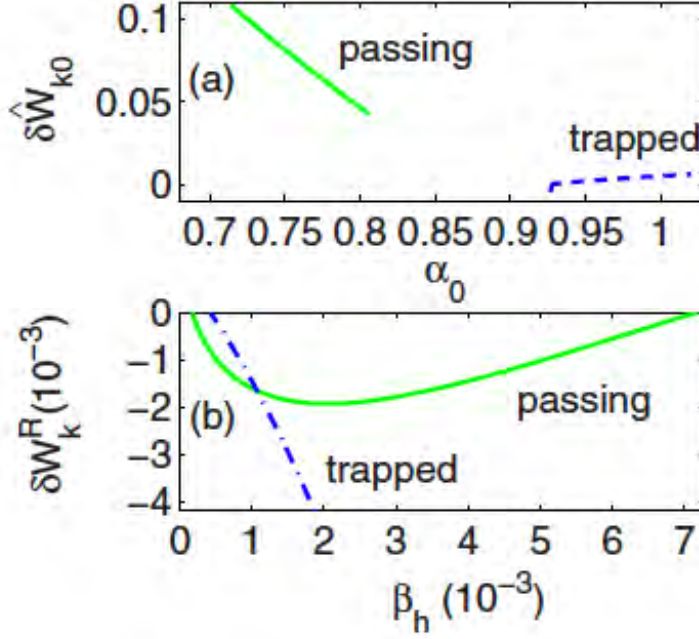


FIG. 6. (a) $\delta\hat{W}_{k0}$ as a function of pitch angle α_0 for trapped (the broken lines) and passing ions (the solid lines) with $\beta_h=0.002$ and (b) δW_k^R as a function of β_h with $\alpha_0=0.76$ for barely passing ions and $\alpha_0=0.93$ for barely trapped ions. The other parameters are $\sigma=2.5$, $\hat{r}_0=0.72$.

V. CONCLUSIONS AND DISCUSSION

In summary, the internal kink (fishbone) mode induced by barely passing energetic ions is investigated numerically. It is found that the mode is resonantly excited by the energetic ions and the mode frequency is comparable to the toroidal precession frequency ω_d . Therefore the mode frequency is low in the case of positive density gradient $\partial F / \partial r > 0$ dominating case (off-axis NBI deposition) whereas is high in the case of negative density gradient $\partial F / \partial r < 0$ dominating (near-axis NBI deposition), corresponding to the fact that the toroidal precession frequency is inversely proportion to radial position r . The most interesting result found in this work is that there exists a second stable regime for the mode in the higher β_h parameter range and there are two threshold beta values, β_{th1} and β_{th2} . The mode may be excited by barely passing energetic ions in the range of $\beta_{th1} < \beta_h < \beta_{th2}$ only. The results are also confirmed with Nyquist technique. The positive free energy (i.e. the damping term in the dispersion relation) increases with increasing beta of EIs and drives the plasma into the second stable regime near the second stability threshold beta value. The physics mechanism for the existence of the second stability range is the competition between the driving and damping forces related to magnetic gradient and curvature drifts as well as density gradient. Besides, there exist a minimum density gradient parameter and a minimum deposition position of NBI for the mode to be unstable.

The results of this work may provide a way to reduce or even prevent the loss of NBI energetic ions through fishbone modes and to increase the NBI heating efficiency by adjusting the pitch angle and driving the system into the second stable regime fast enough.

Explicit expressions for β_{th1} and β_{th2} as functions of plasma parameters only (independent of the mode frequency) are desirable but difficult to be obtained. Nevertheless, numerical solutions are possible. The real and imaginary parts of Eq. (7) are

$$\begin{aligned} \text{Re } D(\omega) = & \delta\hat{W}_c + \frac{\beta_{h,crit} R}{2r_s a'} \hat{C} \int_0^1 n(\hat{r}) \sqrt{\frac{1}{\hat{r}}} d\hat{r} - \frac{\beta_{h,crit} R}{2r_s a'} \left(\frac{2E}{K} - 1\right)^2 \frac{\Delta n}{qK_c} \left[1 + \Omega_r \ln\left(1 - \frac{1}{\Omega_r}\right)\right] + \frac{\beta_{h,crit} R n(r_s)}{2r_s a'} \quad \text{and} \\ & \times \left(\frac{2E}{K} - 1\right) + \frac{\beta_{h,crit} R}{2r_s a'} \Omega_r (\hat{A} - \hat{B} - \hat{B} \Omega_r \frac{\partial}{\partial \Omega_r}) \int_0^1 n(\hat{r}) \sqrt{\hat{r}} \ln\left(\frac{1}{\Omega_r \hat{r}} - 1\right) d\hat{r} = 0, \quad (15) \end{aligned}$$

$$\text{Im } D(\omega) = -\frac{\omega_{ds}}{\omega_A} \Omega_r + \frac{\beta_{h,crit} R}{2r_s a'} \pi \Omega_r (\hat{A} - \hat{B} - \hat{B} \Omega_r \frac{\partial}{\partial \Omega_r}) \int_0^1 n(\hat{r}) \sqrt{\hat{r}} d\hat{r} = 0. \quad (16)$$

respectively, for where $\Omega_r > 1$. An expression for $\beta_{h,crit}$ is formally given in Eq. (10) from Eq. (16). By inserting $\beta_{h,crit}$ from Eq. (10) into Eq. (15), an equation for Ω_r is obtained. Therefore, we can get two roots of Ω_r by numerically solving equation (15). Substituting the two roots back into equation (10), the lower and the upper threshold betas can be conveniently obtained. In this way, we get $\Omega_{r1} = 1.85$, $\Omega_{r2} = 5.35$ and $\beta_{th1} = 2.53 \times 10^{-4}$, $\beta_{th2} = 5.40 \times 10^{-3}$, respectively, for the case of off-axis heating with $\alpha_0 = 0.78$, which is in good agreement with the results shown in Fig. 1.

ACKNOWLEDGMENTS

The discussions with Drs. J. Q Li, Y. Kishimoto, R. White and L. Chen are gratefully acknowledged. This work is supported by National Basic Research Program of China under grant No. 2008CB717806 and ITER Project in China under grant No. 2009GB105005, and also partly supported by the JSPS-CAS Core-University Program in the field of Plasma and Nuclear Fusion.

¹K. McGuire, R. Goldston, M. Bitter, K. Bol, K. Brau, D. Buchenauer, T. Crowley, S. Davis, F. Dylla, H. Eubank, H. Fishman, R. Fonck, B. Grek, R. Grimm, R. Hawryluk, H. Hsuan, R. Hulse, R. Izzo, R. Kaita, S. Kaye, H. Kugel, D. Johnson, J. Manickam, D. Manos, D. Mansfield, E. Mazzucato, R. McCann, D. McCune, D. Monticello, R. Motley, D. Mueller, K. Oasa, M. Okabayashi, K. Owens, W. Park, M. Reusch, N. Sauthoff, G. Schmidt, S. Sesnic, J. Strachan, C. Surko, R. Slusher, H. Takahashi, F. Tenney, P. Thomas, H. Towner, J. Valley, and R. White, Phys. Rev. Lett. **50**, 891 (1983).

²K. L. Wong, M. S. Chu, T. C. Luce, C. C. Petty, P. A. Politzer, R. Prater, L. Chen, R. W. Harvey, M. E. Austin, L. C. Johnson, R. J. La Haye, and R. T. Snider, Phys. Rev. Lett. **85**, 996 (2000).

³X.T. Ding, Yi. Liu, G.C. Guo, E.Y. Wang, K.L. Wong, L.W. Yan, J.Q. Dong, J.Y. Cao, Y. Zhou, J. Rao, Y. Yuan, H. Xia, Yong Liu and the HL-1M group, Nucl. Fusion. **42**, 491 (2002).

⁴L. Chen and M. N. Rosenbluth, Phys. Rev. Lett. **52**, 1122 (1984).

⁵R. B. White, L. Chen, F. Romanelli, and R. Hay, Phys. Fluids. **28**, 278 (1985).

⁶C. Z. Cheng, Phys. Fluids B. **2**, 1427 (1990).

⁷F. Zonca, P. Buratti, A. Cardinali, L. Chen, J.-Q. Dong, Y.-X. Long, A.V. Milovanov, F. Romanelli, P. Smeulders, L. Wang, Z.-T. Wang, C. Castaldo, R. Cesario, E. Giovannozzi, M. Marinucci and V. Pericoli Ridolfini, Nucl. Fusion. **47**, 1588 (2007).

⁸W. W. Heidbrink, K. Bol, D. Buchenauer, R. Fonck, G. Gammel, K. Ida, R. Kaita, S. Kaye, H. Kugel, B. LeBlanc, W. Morris, M. Okabayashi, E. Powell, S. Sesnic, and H. Takahashi, Phys. Rev. Lett. **57**, 835 (1986).

⁹R. B. White, P. H. Rutherford, P. Colestock and M. N. Bussac, Phys. Rev. Lett. **60**, 2038 (1988).

¹⁰R. B. White, M. N. Bussac and F. Romanelli, Phys. Rev. Lett. **62**, 539 (1989).

¹¹M. N. Rosenbluth, S. T. Tsai, J. W. Van Dam, and M. G. Engquist, Phys. Rev. Lett. **51**,

1967 (1983).

¹² M. Rosenbluth and M. L. Sloan, *Phys. Fluids*, **14**, 1725 (1971).

¹³ J.W. Connor, R.J. Hastie, and T. J. Martin, *Nucl. Fusion*, **23**, 1702 (1983).

¹⁴ M. N. Bussac, R. Pellat, D. Ederly and J. L. Soule, *Phys. Rev. Lett.* **34**, 1638 (1975).

¹⁵ Y. Liu, X.T. Ding, Q.W. Yang, L.W. Yan, D.Q. Liu, W.M. Xuan, L.Y. Chen, X.M. Song, Z. Cao, J.H. Zhang, W.C. Mao, C.P. Zhou, X.D. Li, S.J. Wang, J.C. Yan, M.N. Bu, Y.H. Chen, C.H. Cui, Z.Y. Cui, Z.C. Deng, W.Y. Hong, H.T. Hu, Y. Huang, Z.H. Kang, B. Li, W. Li, F.Z. Li, G.S. Li, H.J. Li, Q. Li, Y.G. Li, Z.J. Li, Yi Liu, Z.T. Liu, C.W. Luo, X.H. Mao, Y.D. Pan, J. Rao, K. Shao, X.Y. Song, M. Wang, M.X. Wang, Q.M. Wang, Z.G. Xiao, Y.F. Xie, L.H. Yao, L.Y. Yao, Y.J. Zheng, G.W. Zhong, Y. Zhou and C.H. Pan, *Nucl. Fusion*, **45**, S239 (2005).

Integrated Modeling of Tokamak Plasmas by TASK Code

A. Fukuyama, S. Murakami, A. Wakasa and H. Nuga
Department of Nuclear Engineering, Kyoto University, Kyoto, Japan

In order to describe time evolution of tokamak core plasmas, the integrated tokamak modeling code, TASK, has been developed. It is composed of analyses of equilibrium, transport, wave physics, and momentum distribution function, and interface to couple them with each other. The features of each component are described and typical simulation results for ITER are presented. The kinetic integrated modeling under development is also mentioned.

1 Introduction

In order to predict the performance of future magnetic fusion devices, to optimize their operation scenario, and to design DEMO fusion reactors, it is necessary to develop a reliable tool which describes a whole plasma including core, edge, SOL, and divertor plasmas as well as plasma-wall interaction over a whole discharge including startup, sustainment, probabilistic incidents, and shut down. Since the time scale extends from the order of 10 ns of the electron cyclotron wave to the order of 1000 s of the discharge, and the spatial scale from the order of 10 μm of the Debye length to the order of 10 m of the device size, it is practically impossible to describe a whole plasma and a whole discharge by a single simulation code. Therefore we have to utilize an integrated simulation combining modeling codes which describe specific phenomena and interact with each other.

Several activities are in progress in the world in order to develop such integrated modeling codes for toroidal burning plasmas. In Japan, the Burning Plasma Simulation Initiative (BPSI) has been working since 2003 [1]. It is a research collaboration among universities, National Institute for Fusion Science (NIFS), and Japan Atomic Energy Agency (JAEA). Main targets of this initiative includes development of a framework for integrated simulation, pioneering new physics models required for integrate modeling, and introducing advanced computing technique to integrated codes. As a core code of this activity, the integrated tokamak modeling code, TASK, has been developed and is evolving for a more advanced and reliable tool simulating magnetic fusion plasma.

The purpose of this paper is to describe the present status of the integrated code, TASK, and present recent results of the analysis. The outline and the present structure of TASK are described in section 2, and important components of TASK and their typical results are presented in section 3. The last section briefly describes the kinetic integrated modeling under development.

2 The integrated code TASK

The integrated code, TASK (Transport Analyzing System for tokamaK) [2], is a core code of the integrated modeling in BPSI. It has a modular structure for easier maintenance of the code and includes reference implementation of the BPSI data-exchange interface (BPSD) and the BPSI

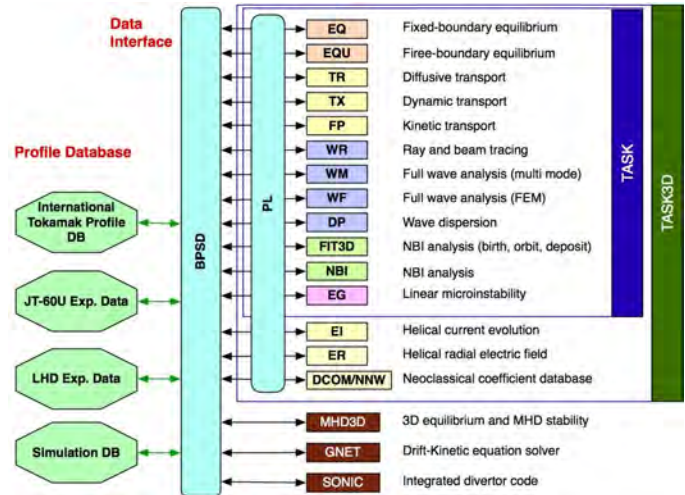


Figure 1: Present structure of the TASK code and related codes

execution interface (BPSX) which will be explained later. It has high portability and works on various UNIX-like environments from laptop computers to large-scale cluster computers. The source code has been stored in a CVS version control system for collaborative development and is freely downloadable from the web site [3]. A part of the code has been parallelized using the MPI library.

The present structure of the TASK code and related codes is shown in Fig.1. The original TASK components are enclosed by a rectangular denoted by TASK. The components in the extended rectangular denoted by TASK3D [4] are used in the simulation of the plasma in a three-dimensional (3D) configuration, such as Large Helical Device (LHD). Coupled simulations with external codes, 3D MHD equilibrium and stability code (MHD3D), drift kinetic equation solver (GNET), and integrated divertor code (SONIC) are planned.

The components are designed to exchange simulation data through the BPSD interface. The BPSD data-exchange interface defines standard datasets which describes the status of the device and the plasma, e.g., MHD equilibrium profile (magnetic field, metric), fluid description of the plasma (density, temperature, velocity), kinetic description of the plasma (momentum

Physical quantity	Variable name	Unit
time	plasmaf%time	[s]
number of radial grid	plasmaf%nrmax	
number of species	plasmaf%nsamax	
species identifier	plasmaf%ns_nsa(nsa)	
normalized radius	plasmaf%rho(nr)	
inverse of safety factor	plasmaf%qinv(nr)	
plasma density	plasmaf%data(nr,nsa)%pn	[m ⁻³]
plasma temperature	plasmaf%data(nr,nsa)%pt	[eV]
toroidal flow velocity	plasmaf%data(nr,nsa)%pu	[m/s]

Table 1: Example of a BPSD data structure defined as a derived type of Fortran90; fluid quantities of plasma

Name of subroutine	Role of subroutine
XX_main	Main program for stand-alone operation
XX_init	Definition and default value of input parameters
XX_parm	Read input parameters
XX_menu	Command processor for user interface
XX_prep	Initialize profiles in time evolution
XX_exec	Calculate and advance time by a time step
XX_calc	Calculate without time advance
XX_gout	Output calculated data in text or in graphics
XX_save	Save present status data in a file
XX_load	Load saved status data from a file

Table 2: Standard subroutine names for BPSX interface. XX denotes the name of the component.

distribution function), wave field distribution, transport coefficients, and source terms. The dataset is implemented using the derived type of Fortran90 and the locality of the data is taken into account. An example of the data structure, fluid quantities of plasma, is indicated in Table 1. The BPSD interface also defines a few simple application programming interfaces (API) to set data, get data, save data in a file, load data from a file, and so on. Since the number of the BPSD API is restricted in order to keep simplicity, more universal and efficient interfaces are implemented in the library TASK/PL.

The BPSD interface also includes the data interface with experimental and simulation data. Several kinds of ASCII data files, e.g. the UFILE form [5], and the experiment database library MDSplus [6] are available. The International Tokamak Profile Database developed [7] by ITPA activity has been used to examine the thermal transport models in tokamak plasmas [8].

The BPSX execution interface is still under development. Most of the components include basic routines with unified subroutine names as shown in Table 2. Interface routines control the execution sequence of the fundamental subroutines. This interface will be extended to the use of graphical framework interface, such as Kepler [9], and web interface.

3 Components of TASK

3.1 Equilibrium

MHD equilibrium of an axisymmetric plasma is described by Grad and Shafranov (GS) equation. TASK has two equilibrium components, EQ and EQU. TASK/EQ solves GS equation with a fixed plasma boundary condition for given pressure and safety-factor profiles. Using the solution of GS equation or reading the equilibrium data from a file, TASK/EQ calculates the magnetic flux coordinates and metric data. The other component EQU, originally developed by M. Azumi [10], solves GS equation with a free boundary condition for given separatrix points by iteration starting from initial poloidal coil currents. Figure 2 illustrates contours of the poloidal magnetic flux calculated by TASK/EQ and TASK/EQU for ITER plasmas.

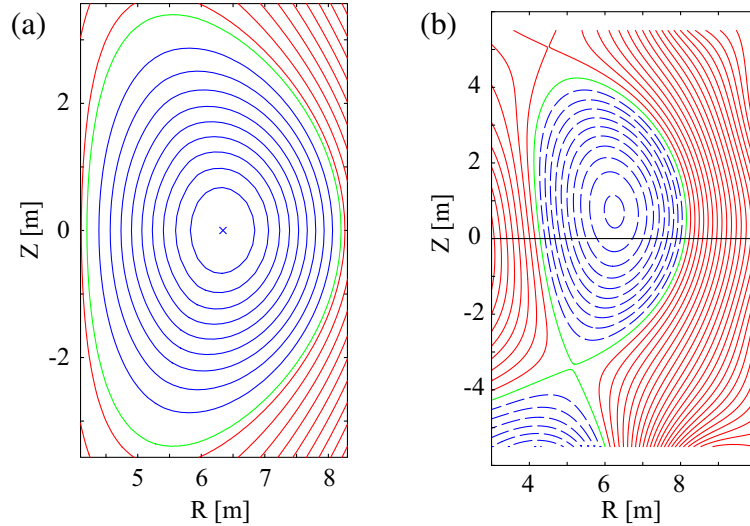


Figure 2: Contours of poloidal magnetic flux calculated by (a) TASK/EQ (fixed boundary) and (b) TASK/EQU (free boundary) for 15MA ITER plasma.

Model	Equation	Variables	TASK/
Fluid model	Diffusive transport equation	$n(\rho, t), v_\phi(\rho, t), T(\rho, t)$	TR
	Dynamic transport equation	$n(\rho, t), \mathbf{u}(\rho, r), T(\rho, t)$	TX
Kinetic model	Bounce-averaged drift-kinetic equation:	$f(p, \theta_p, \rho, t)$	FP
	Axisymmetric gyrokinetic equation	$f(p, \theta_p, \rho, \chi, t)$	
	Gyrokinetic equation	$f(p, \theta_p, \rho, \chi, \zeta, t)$	
	Full kinetic equation	$f(p, \theta_p, \phi_g, \rho, \chi, \zeta, t)$	

Table 3: Levels of transport modeling

3.2 Transport

Transport components usually describe the time evolution of the plasma in transport time scale. There are several levels of transport modeling as shown in Table 3. The most accurate two modelings, full-kinetic and gyrokinetic, usually describe the turbulence self-consistently and require very large amount of computing resources. On the other hand, conventional transport modeling (TASK/TR, [8]) solves the diffusive transport equation accompanied with the flux-gradient relation. Since the flux-gradient relation is derived from the stationary solution of the equation of motion, a quick change of the transport may not be described self-consistently. The dynamic transport modeling (TASK/TX, [11]) solves the flux-surface-averaged multi-fluid equations coupled with Maxwell's equations. Since the equations of motion and Poisson's equation are solved simultaneously, the plasma rotation and the radial electric field are self-consistently calculated without the assumption of the quasi-neutrality. In order to describe the heating and current drive which usually produce energetic particles and modify the momentum distribution function, the kinetic transport modeling (TASK/FP) solves the bounce-averaged Fokker-Planck equation for the momentum distribution function including the radial transport.

Figure 3 shows an example of heat transport simulation by TASK/TR for the ramp-up phase of ITER inductive operation using the CDBM05 turbulent transport model [8].

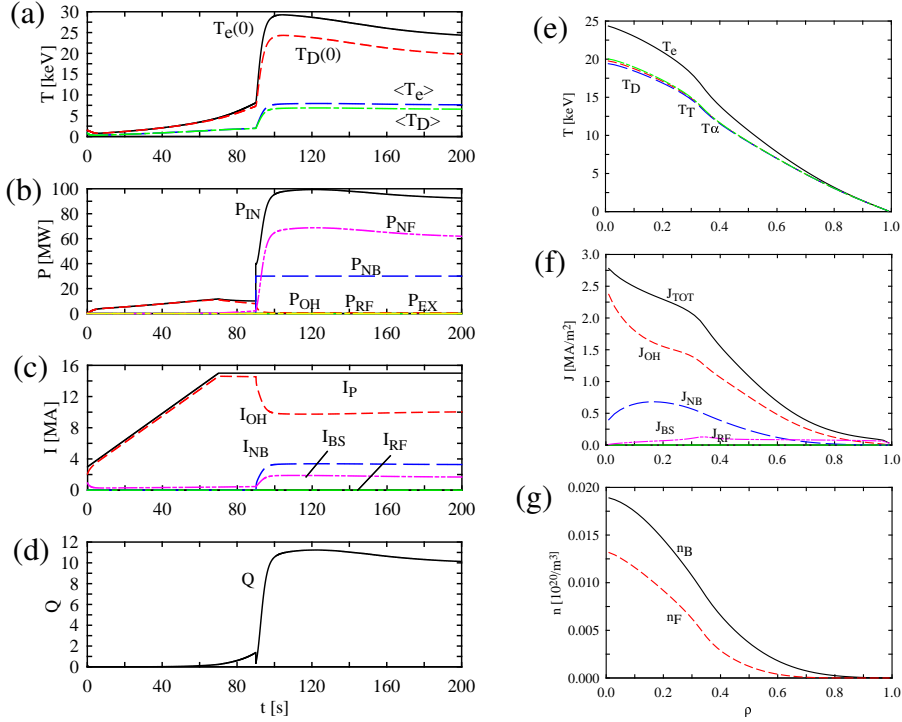


Figure 3: Time evolution of (a) central temperature, (b) heating power, (c) plasma current and (d) fusion power multiplication factor, and radial profiles of (e) temperature, (f) current density and (g) energetic ion density, n_B due to NBI and n_F due to fusion reaction, at $t = 200$ s calculated by TASK/TR for ITER inductive operation.

3.3 Wave analysis

There exist various kinds of electromagnetic (EM) fields in tokamak plasma, excited internally or externally, with wide ranges of frequency, growth rate and wave number. In order to describe the excitation, propagation and absorption of EM fields, several modeling schemes have been used in toroidal plasmas as indicated in Table 4.

The ray tracing component, TASK/WR, solves the ray equation in the Hamiltonian form to calculate the ray position and the wave number from the dispersion relation which corresponds to the Hamiltonian. It also uses the dielectric tensor component, TASK/DP, to calculate the dispersion relation. The TASK/WR is applicable to beam tracing [12] in which the radius of

Scheme	Time dependence	Spatial dependence	TASK/
Wave optics	Initial value problem	FEM/FDM	—
	Boundary value problem	Fourier analysis	—
		Fourier & FEM/FDM	WM
		FEM/FDM	WF
Geometrical optics	Initial value problem	Ray tracing	WR
		Beam tracing	WR

Table 4: Types of wave modeling: FEM and FDM denote the finite element method and the finite difference method, respectively.

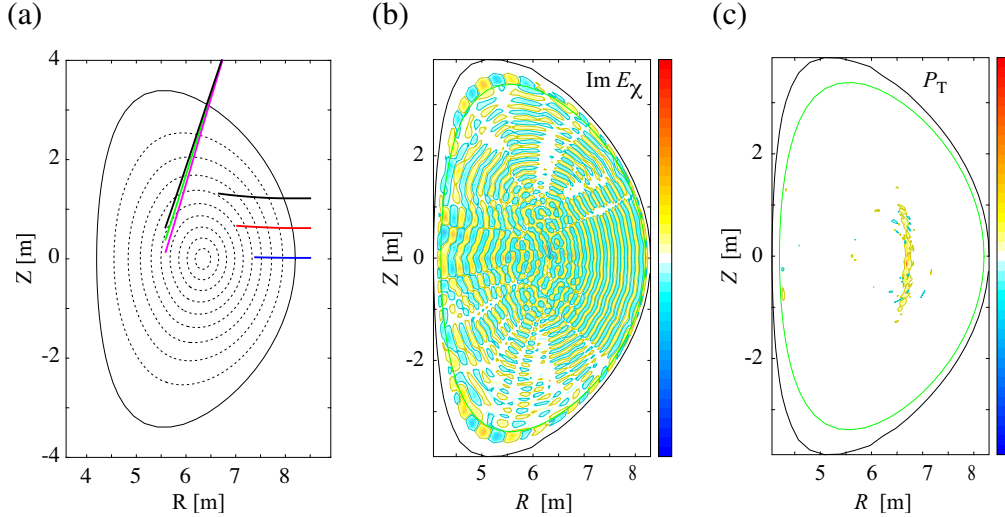


Figure 4: (a) Ray tracing analysis of electron cyclotron waves by TASK/WR and full wave analysis of ion cyclotron waves by TASK/WM, (b) the poloidal component of the wave electric field and (c) the power density absorbed by triton at the second harmonic cyclotron resonance.

the wave beam and the curvature radii of the equi-phase wave surface are also calculated. The TASK/WR has been applied to the electron cyclotron heating and current drive [13] as well as the lower-hybrid current drive.

The full wave analysis component, TASK/WM, solves Maxwell's equation as a boundary-value problem. It uses the Fourier expansion in the poloidal and toroidal directions and the finite element method (FEM) in the radial direction. Various models of dielectric tensor are available in the component TASK/DP; resistive MHD, collisional multi-fluid, uniform kinetic, and drift kinetic. For the kinetic models, not only the Maxwellian velocity distribution but also any form of equilibrium velocity distribution function, such as the output of the Fokker-Planck analysis can be used through numerical integration in velocity space. At present, the finite gyro radius effect is evaluated from the fast wave approximation. The TASK/WM has been used in the analysis of heating and current drive in the ion cyclotron range of frequency [14]. Since the wave frequency can be complex in TASK/WM, it is applicable to the eigenmode analysis by maximizing the volume integral of the square of the wave amplitude for given excitation proportional to the electron density. It has been applied to the analysis of Alfvén eigen modes [15]. Another full wave component, TASK/WF, using three-dimensional FEM is under development for the analysis of waves with shorter wave length.

Figure 4 illustrates the ray trajectories of the electron cyclotron waves calculated by TASK/WR and the wave structure of the ion cyclotron waves calculated by TASK/WM for ITER plasmas.

3.4 Momentum distribution function

The heating and current drive by waves, neutral beam, and alpha particles modify velocity distribution functions of heated particle species and produce energetic particles which affect the transport and stability of the plasma and the heating mechanism itself. The three-dimensional Fokker-Planck component, TASK/FP [16], is used to analyze the modification of momentum distribution functions of particle species s , $f_s(p_{\parallel}, p_{\perp}, \rho, t)$, where p_{\parallel} and p_{\perp} are the parallel and perpendicular components of the momentum relative to the equilibrium magnetic field at the lo-

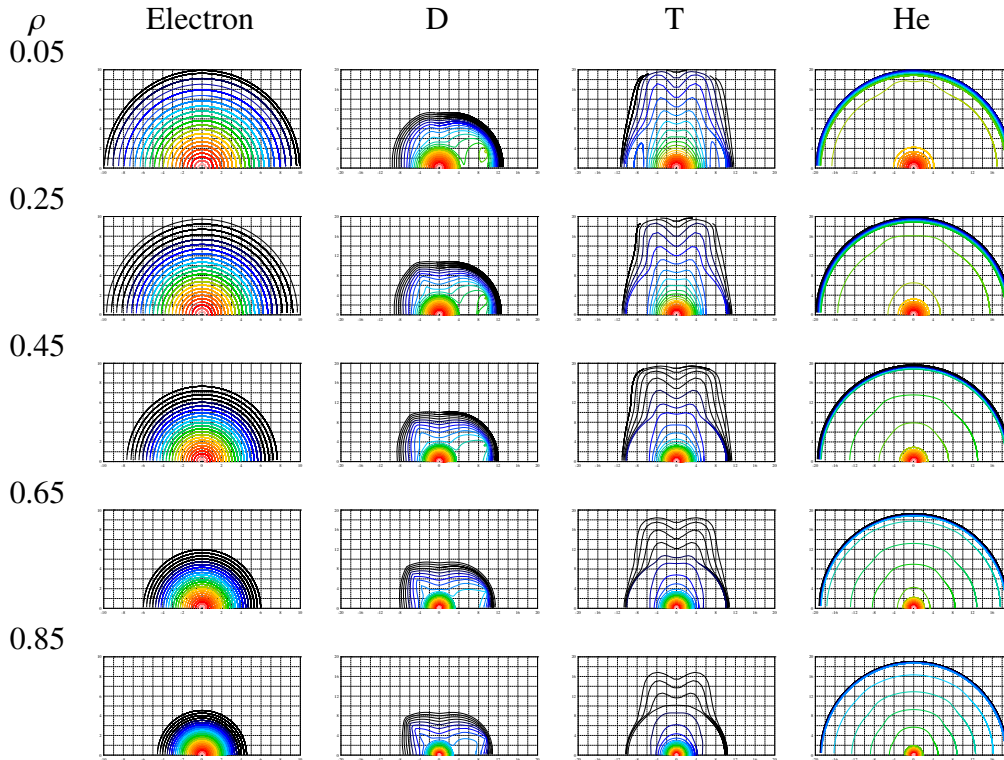


Figure 5: Contours of the momentum distribution function at different minor radius and different particle species. The horizontal and the vertical axes indicates the parallel and the perpendicular momentum normalized by the thermal momentum.

cation of minimum magnetic field strength on the magnetic surface specified by the normalized radius ρ .

It solves the bounce-averaged drift-kinetic equation for multi-species f_s simultaneously. The drift kinetic equation is averaged over the bounce motion for trapped particles and the circular motion for passing particles. The equation includes the Coulomb collision term which describes the collisional interaction between different species as well as the self-interaction relaxing the distribution of the Maxwellian. Since the conserves not only momentum but also energy, the quasilinear wave interaction term which is evaluated from the wave electric field calculated by TASK/WR and TASK/WM, the radial transport terms due to turbulent diffusion and pinch, and the source and sink term due to neutral beam injection and nuclear fusion reaction.

Figure 5 shows the momentum distribution function of electrons, deuterons (D), tritons (T), and Helium ions (He) at various radius in ITER plasmas. The calculation includes ICRF heating of electrons and T, NBI heating of D, and fusion reactions of DT and DD. Radial diffusion with given radial profile is assumed and 50 radial points are used.

3.5 Other components

The TASK code includes some other components; FIT3D for neutral beam trajectory, energetic ion generation, finite orbit width, and deposition, NBI for simple version of NBI analysis, and EG for linear micro instability analysis for turbulent transport estimation. It also common libraries for numerical integration, spline interpolation, fast Fourier transform, spatial functions, matrix solver, and parallel processing. A free graphic library, GSAF, is also developed and can

be installed separately.

4 Kinetic integrated modeling

In order to describe burning plasma more accurately and self-consistently, we are now developing a kinetic integrated version of TASK which is based on the kinetic description of the bounce-averaged momentum distribution functions. The transport is analyzed by the Fokker-Planck component TASK/FP and the heating and current drive as well as global stabilities are analyzed by the full wave component TASK/WM including the effect of energetic particles calculated by TASK/FP. It will give us more precise evaluation of fusion reaction and energetic-particle-driven global instabilities.

Acknowledgements

This work is supported by Grant-in-Aid for Scientific Research (S) (20226017) from JSPS, Japan.

References

- [1] A. Fukuyama, M. Yagi, J. Plasma and Fusion Res., **81** 747 (2005) [in Japanese].
- [2] A. Fukuyama, Murakami, M. Honda, Y. Izumi, M. Yagi, N. Nakajima, Y. Nakamura, T. Ozeki, Proc. of 20th IAEA Fusion Energy Conf. (Vilamoura, 2004), IAEA-CSP-25/CD/TH/P2-3 (2004).
- [3] TASK, <http://bpsi.nucleng.kyoto-u.ac.jp/task/>.
- [4] N. Nakajima, M. Sato, Y. Nakamura, A. Fukuyama, S. Murakami, A. Wakasa, K. Y. Watanabe, S. Toda, and H. Yamada, Fusion Sci. Tech., **58** 289 (2010).
- [5] M. Vachharajani, <http://w3.ppp1.gov/pshare/help/ufiles.htm>.
- [6] MDSplus, <http://www.mdsplus.org/>.
- [7] M. Roach et al., Nucl. Fusion, **48** 125001 (2008).
- [8] M. Honda and A. Fukuyama, Nucl. Fusion, **46** 580 (2006).
- [9] Kepler Project, <http://www.keplerproject.org/en/Kepler>
- [10] M. Azumi, G. Kurita, in: Proc. 4th Symp. on the Computing Methods in Applied Sciences and Engineering, Paris, 335 (1979).
- [11] M. Honda, A. Fukuyama, J. Comp. Phys., **227**, 2808 (2008)
- [12] G.V. Pereverzev, Phys. Plasmas, **4** 3529 (1998).
- [13] A. Fukuyama, Fusion Eng. Des., **53** 71 (2001).
- [14] A. Fukuyama, E. Yokota and T. Akutsu, Proc. of 18th IAEA Fusion Energy Conf. (Sorrento, 2000), IAEA-CN-77/THP2/26 (2000)
- [15] A. Fukuyama and T. Akutsu, Proc. of 19th IAEA Fusion Energy Conf. (Lyon, 2002), IAEA-CN-94/TH/P3-14 (2002)
- [16] H. Nuga, A. Fukuyama, J. Plasma and Fusion Res. Series, **8** 1125 (2009).

Simulation of ECR startup and comparison to experimental observations in SUNIST

Yi Tan¹, Zhe Gao¹, Long Wang²

¹ Department of Engineering Physics, Tsinghua University, Beijing, China

² Institute of Physics, Chinese Academy of Sciences, Beijing, China

E-mail: tanyi@sunist.org

Abstract: Electron cyclotron resonance heating is an effective method to startup the plasma current in spherical tokamaks (STs). It has been shown on many STs that the transient process at the beginning of ECR startup discharges can affect the startup results significantly, especially for short microwave pulses. This paper presents the experimental observations of two types of ECR startup on SUNIST: one with electron density spikes but very low plasma current, and the other one without electron density spikes but higher plasma current. The mechanism of the formation of spikes is studied by a series of parameter scan experiments, i.e., resonant layer scan and vertical field scan. It was found that the long wave length of microwave, the drift process of over dense electrons and the perpendicularly installed microwave antenna are all responsible for these interesting phenomena. The experimental configuration is modeled as an exciter-reflector system and is analyzed in one dimension. The continuous equations for each cell of the space between the inner and the outer wall are given. The reflection ratio of microwave is simply calculated with the assumption as optics. After careful tuning of the coefficients, the simulation results that are comparable to experimental observations are obtained thus the physical images conjectured from experiments are confirmed.

PACS: 52.55.Fa, 52.55.Wq, 52.50.Sw

Introduction

Spherical tokamaks have higher beta, compact size and lower cost when compared to conventional tokamaks. However, these advantages are guaranteed from the ultra limited space for center post, in which the capability of the central solenoid (CS) is greatly decreased. This makes STs hard to startup solely with the flux swing provided by CS. For this reason, research of non-inductive startup in STs is a hot topic. Many non-inductive methods have been applied to and studied in STs, e.g., merging and compressing (applied to START[1], TS-3/4[2], MAST[3], UTST[4]), coaxial helicity injection (CHI, applied to HIT[5], NSTX[6]), and electron cyclotron heating (ECR, applied to CDX[7], LATE[8-12], TST-2[13, 14], MAST[15], SUNIST[16], CPD[17], et al). Since ECR startup doesn't need special design to the tokamak machines (former two methods both require special structures or shapes of the device for operation), it has attracted the widest research interests on STs.

Although some uncertainties of the mechanism still exist, the brief processes of ECR startup have been explicit. First, when a microwave is injected to a vessel with prefilled gas and an appropriate magnetic field, the gas is ionized by ECRH. Then, as long as electrons and ions (weakly ionized

plasma) generated, electrons move along the helical field lines (the composite of toroidal field and vertical field) with asymmetrical lifetime. The electrons with different lifetime in two opposite drift directions form a plasma current flow (therefore at this stage plasma current are pressure driven; $N_{||}$ and poloidal flux swing are not necessary). If the microwave injection continues, the plasma pressure increases, as well as the plasma current. When a threshold is reached, the plasma current suddenly jumps to a much higher value because the magnetic field generated by the increased plasma current improves confinement and increases the plasma pressure more. This positive feedback make the current jump happen. Previous open field lines are partially transitioned to closed flux surfaces. After current jump, a tokamak like plasma torus is formed. At this stage, the mechanism of current drive becomes typical ECCD and therefore $N_{||}$ is required if one want to drive current further.

SUNIST is a small spherical tokamak. Its major radius, minor radius, toroidal field are 0.3 m, 0.23 m, and < 0.15 T respectively. ECR startup experiments have been conducted on SUNIST. A 2.45 GHz / 100 kW / 10 ms magnetron microwave source is used in the experiments. To make the electron cyclotron frequency match the frequency of microwave, the toroidal field is adjusted from 875 to 1200 Gauss. Before the injection of microwave, the vacuum vessel is prefilled with Hydrogen to $1E-3 \sim 1E-2$ Pa by a pulse controlled piezo-valve. The main diagnostics used include a Rogowski coil, a set of poloidal flux loops, visible light photodiodes, an 8 mm interferometer and a fast camera. The hardware arrangement of these experiments is shown in Figure 1. After a long term of wall conditioning, optimal ECR startup results are obtained when the filling pressure is as low as $1E-3$ Pa and the vertical field is about 15 Gauss. As shown in Figure 2, about 2 kA of plasma current can be routinely started up shortly (several milliseconds) after the injection of microwave and maintained till the end of microwave pulse.

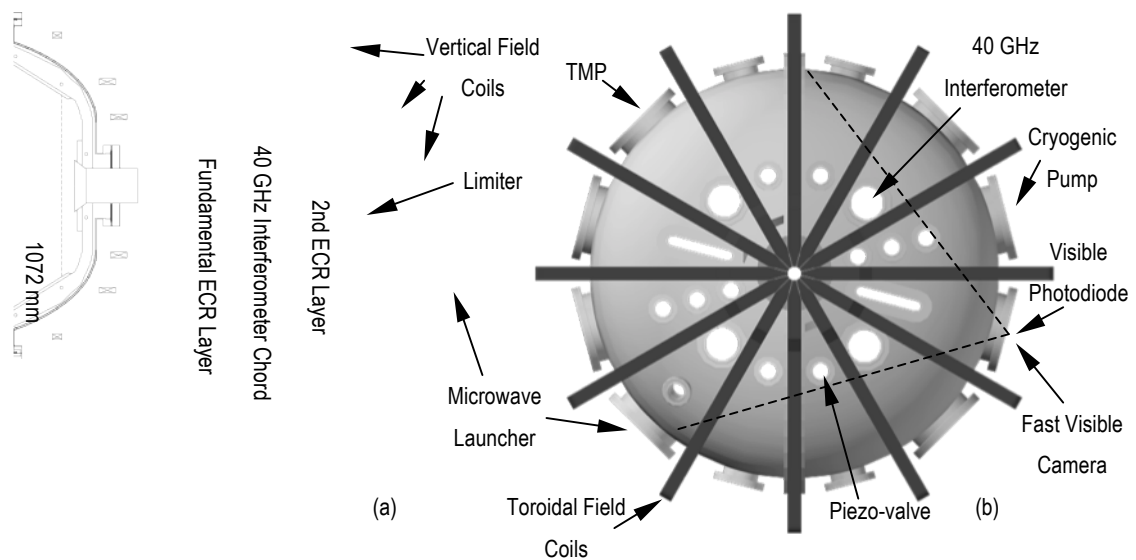


Figure 1. The experimental setup for electron cyclotron wave start-up experiments on SUNIST. (a) Side view illustrating the radial positions of fundamental and second electron cyclotron resonance (ECR) layers and the interferometer chord, the poloidal position of the microwave launcher, and the poloidal limiters. (b) Top view showing the toroidal positions of main equipment and diagnostics.

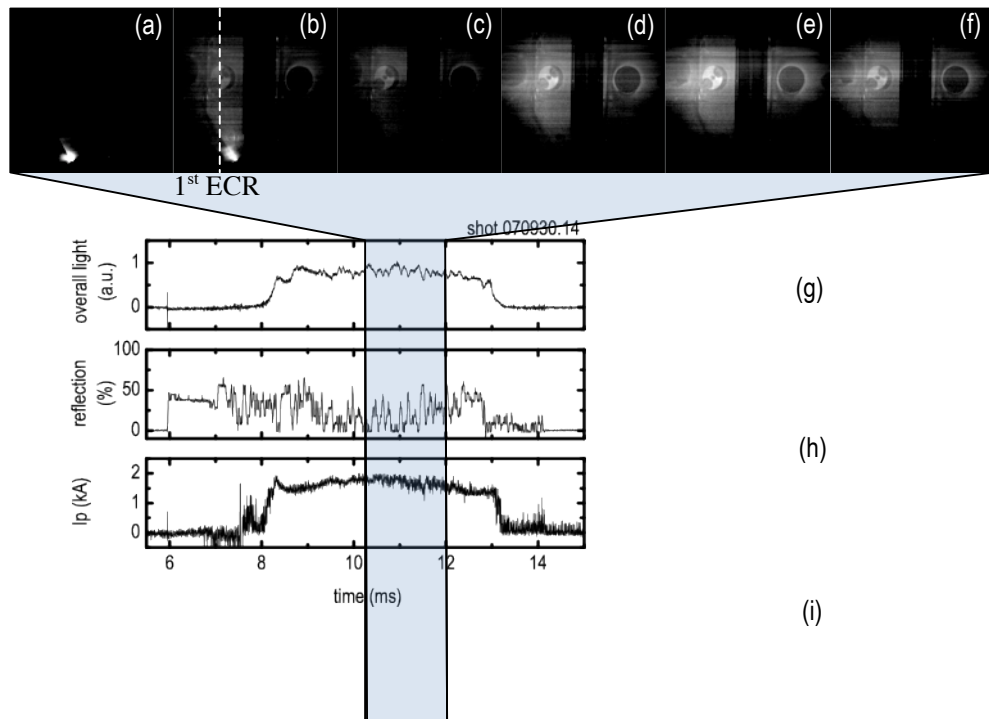


Figure 2. Pictures of visible light (a) ~ (f) and dependence of overall visible light emission (g), microwave reflection (h) and plasma current (i) on time in a typical discharge with filling pressure $P_{H_2} \sim 1 \times 10^{-3}$ Pa, vertical field $B_V \sim 12$ G and microwave power ~ 40 kW. The pictures are taken with intervals of 0.2 ms.

The transition of current jump is essential to get good startup efficiency. However, many factors can affect succeeding current jumps. On SUNIST, the poloidal field generated by the plasma current is estimated to be ~ 20 G and is larger than the biased vertical field (~ 15 G). This implies that partially closed flux surface may have formed. However, the experimental results of vertical field scanning revealed an $I_p \sim 1/B_V$ scaling (Figure 3), which means that the plasma current is still pressure driven. These conflicts may be interpreted as follows: in our experiments the plasma pressure, and therefore the plasma current, increase very fast and almost reaches the threshold of current jump; however the pulse length of microwave limited the evolution of plasmas before current jump really occurs. For this reason, although current jump is prohibited by the short pulse length, the rapid formation of plasma current (which is not very common at this power injection level in STs) is still of interests. To investigate the mechanism of fast plasma current formation, the transient process of startup need to be understood.

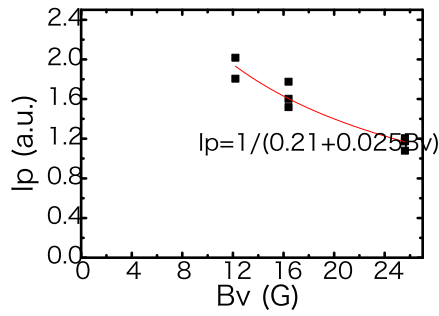


Figure 3. The plasma current as a function of vertical field. The red curve is fitted from the experimental data (black bricks).

From a number of shots we can find two types of startup with quite different time evolution of the plasma current (Figure 4). Type I shots were obtained with relatively higher gas filling pressure ($> 5E-3$ Pa). The distinct feature of type I shots is the spike of both the waveforms of plasma current and electron density at the very beginning of discharges. However, after the spike plasma current can not be maintained and decays fast. In contrary, type II shots were obtained with lower gas filling pressure ($\sim 1E-3$ Pa) and didn't have spikes. Constant plasma current (the waveform has a flat top from the beginning to the end of pulse) can be maintained in type II shots. It seems that the beginning of discharge is spiky or not determines the whole process of startup as well as the plasma current waveform. This phenomenon on SUNIST is not unique. Similar results have been widely observed on other STs, including LATE (both 2.45 GHz and 5 GHz experiments), TST-2 (both 2.45 GHz and 8.2 GHz experiments) and CPD (8.2 GHz). Especially for CPD, in its latest campaign the power of microwave (8.2 GHz) is gradually increased, not step applied, to avoid the spikes at the beginning of the waveforms of plasma current and electron densities. The spikes are common features of ECR startup on STs and have important effects on the plasma current. However, the transient process of ECR startup has not yet been studied in detail; the determination of such two types of shots is not well understood. In this paper, the ECR startup transient processes in SUNIST are modeled based on a series of parameters scanning experiments and simulated. The comparison between the simulation results and experimental observations are presented as well.

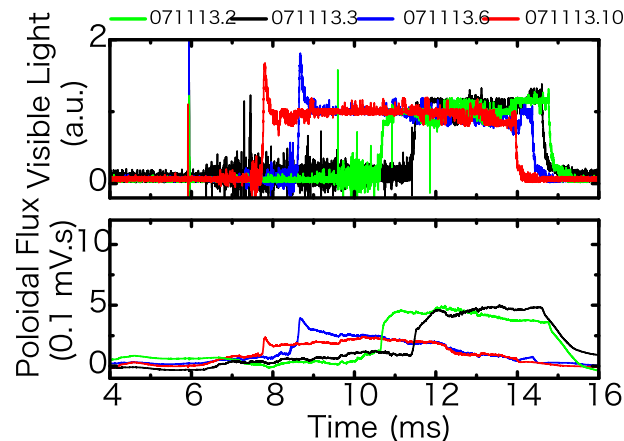


Figure 4. Two types of shots: with and without spikes at the beginning of H_{α} emission. The plasma current (poloidal flux) in the shots that have spikes are not sustainable.

Parameters Scan and Modeling

Several assumptions are made before introducing the model. First, the ionization ratio during the whole pulse duration is low and at any time there are plenty of neutral particles that can be ionized. If we compare the density of molecular in gas ($2.7E17 \text{ m}^{-3}$ for $1E-3 \text{ Pa}$) and the cutoff density of 2.45 GHz microwave ($7E16 \text{ m}^{-3}$), this assumption is obvious. Second, the electron temperature is low. In the breakdown phase, collision is frequent and the electrons heated by ECR loss their energy to neutral particles quickly. Thus T_e is kept low, or in practice zero, in the model. The third assumption, H_α emission is roughly proportional to the electron density, is directly derived from previous two assumptions. With this assumption the H_α emission signal, which is faster and more reliable than interferometer signals, is used to represent the electron density in the following experiments and analysis. The fourth assumption comes from a special feature of the antenna system on SUNIST. Because the antenna is almost perpendicularly installed on a window in the equatorial plane, its launching direction is normal to the toroidal direction. Thus we can assume that the reflection of microwave reflects the radial position of cutoff layers, although the relationship may not be proportional. With these assumptions, the main structure of ECR startup can be modeled as an exciter-reflector system. Refining of the model is completed by scanning parameters experimentally. Both radial position of the EC resonant layer and the strength of vertical field are scanned.

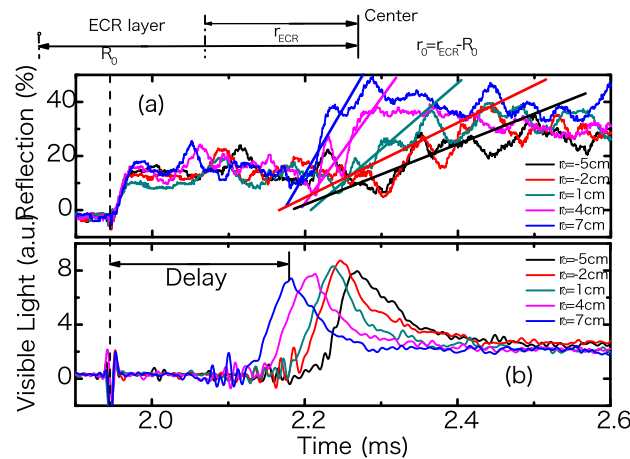


Figure 5. Traces of microwave reflections (a) and H_α emissions (b) in ECR layer scan.

Figure 5 shows the results of resonant layer scanning from $R_0 - 5 \text{ cm}$ to $R_0 + 7 \text{ cm}$ (R_0 is the radial position of magnetic axis). As long as the resonant layer moves inward, the slope of the traces of microwave reflection (lines with the same color as signal traces are used to mark the averaged slopes) decreases but the delay of H_α emission increases. However the final values of both microwave reflection and H_α emission are respectively close no matter where the ECR layer is. Regarding to the installation of the antenna, the property of microwave reflection is deduced to be caused by the drift and diffusion process across field lines of the over dense plasmas. When the toroidal field decreases, the ECR layer is located away from the antenna. The drift velocity is proportional to $|E|/|B|$. The distance between the ECR layer and the antenna is proportional to $1/|B|$.

In this case, the time needed to drift from ECR layer to antenna is determined by the electrical field generated by charge separation. For the electrons moving along helical field lines composed by toroidal field and vertical field with the same parallel velocities, its speed along vertical direction is determined by $|B_z|/|B_T|$. For smaller toroidal field, the vertical speed of electrons is faster and then the compensation to charge separation is larger. Therefore, inner plasmas need more time than outer plasmas to drift and diffuse towards the launching face of the antenna and to make large fraction of microwaves reflected. On the other hand, the power density of microwave varies at different positions of ECR layer since the horn antenna used in the experiments has an E-plane / H-plane launch angle of 61 / 81 degrees. The time needed for ionization depends on the power density is the reason why Ha emission delays as the ECR layer move inward (away the antenna). The deductive cause of the spikes of Ha emission is the long wave length (e.g., ~ 12 cm for 2.45 GHz, more than a half of the minor radius of SUNIST) of low frequency microwaves used in the experiments. Damped waves in a large evanescent region behind the cutoff layer can still transfer energy to and heat up electrons effectively. Gases continue to be ionized even the cutoff density reaches. Therefore the electron density may rise up to be higher than the cutoff density. Indeed, this phenomena is quite common in ECR ion sources.

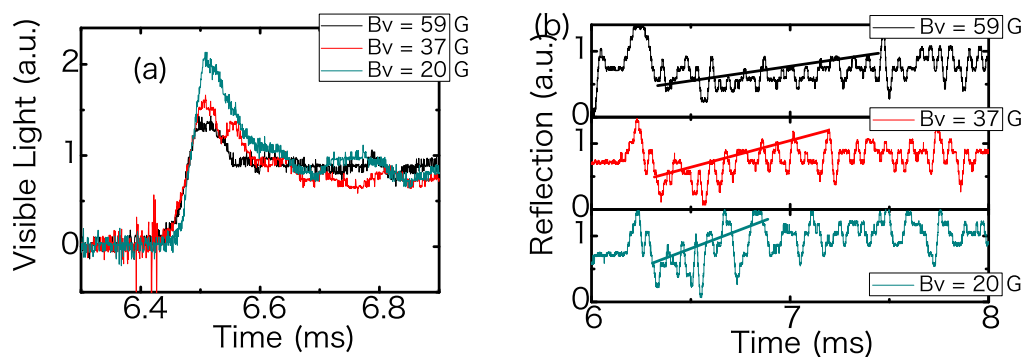


Figure 6. Traces of microwave reflections (a) and H_α emissions (b) in vertical field scan.

The scan of vertical field reveals an important loss channel of electrons (Figure 6). In this scan the slope of microwave reflection also shows a strong relationship to vertical field (Figure 4 b). But in this case the radial position of ECR layer is fixed. The difference of slope can not be explained by drift process across field lines any more. From Figure 4 (a) it can be found that the maximum amplitude of Ha emission has a negative correlation to the strength of vertical fields, although both input power and the power density are identical in these shots. The electron loss along vertical field lines should be responsible for the relationship. As described before, the vertical velocity of electrons is proportional to the strength of vertical field. Thus large vertical field causes faster electron loss along field lines and reduces the amplitude of Ha emissions.

Based on the above parameters scans, we can abstract a clearer model than the exciter-reflector one: electrons are generated at the ECR layer, drift/diffuse in the radial directions and get lost along vertical field lines. Over dense plasmas are rapidly formed in the ECR region before making microwave reflected. Large fraction of microwave are reflected only when the over dense plasmas move close to the antenna. This conjectured process has been partially confirmed by the images taken by a fast camera. From Figure 7 (f) ~ (k), a quite similar process is shown. Therefore, we

have enough confidence to make a simple but reasonable model and simulate the experimental results.

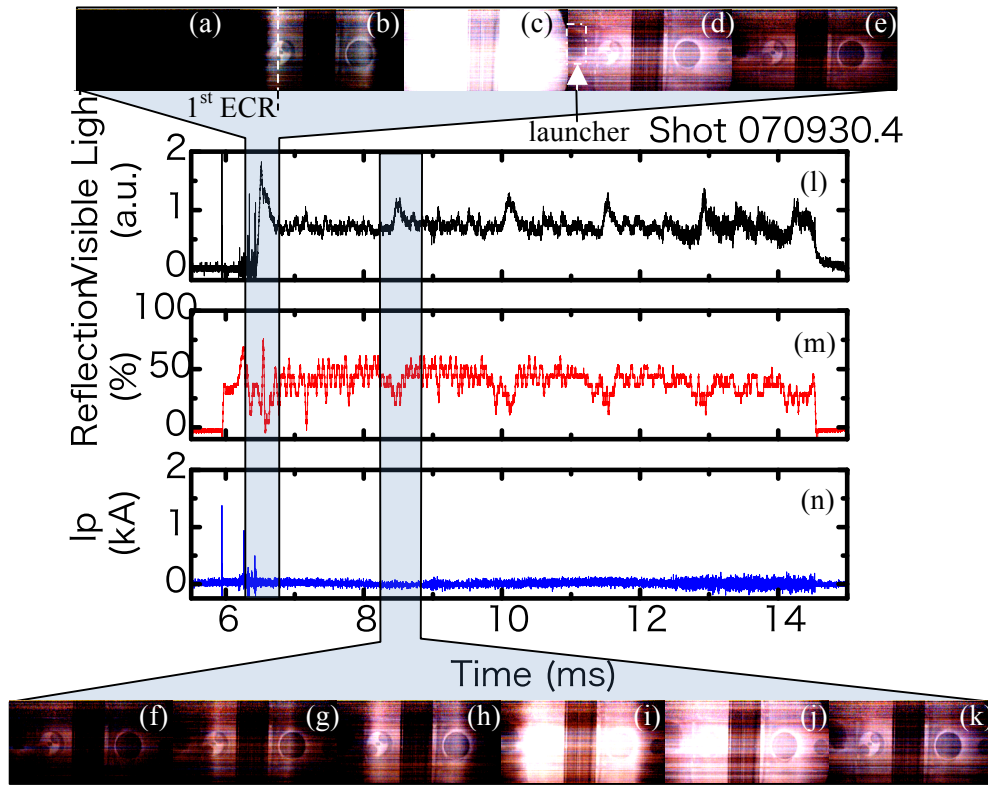


Figure 7. Pictures of visible light (a) ~ (k) and the time dependences of overall visible light emission (l), microwave reflection (m) and plasma current (n) in a typical discharge with filling pressure $P_{H_2} \sim 5 \times 10^{-3}$ Pa, vertical field $B_V \sim 20$ Gauss and microwave power ~ 40 kW. The pictures are taken with intervals of 0.1 ms.

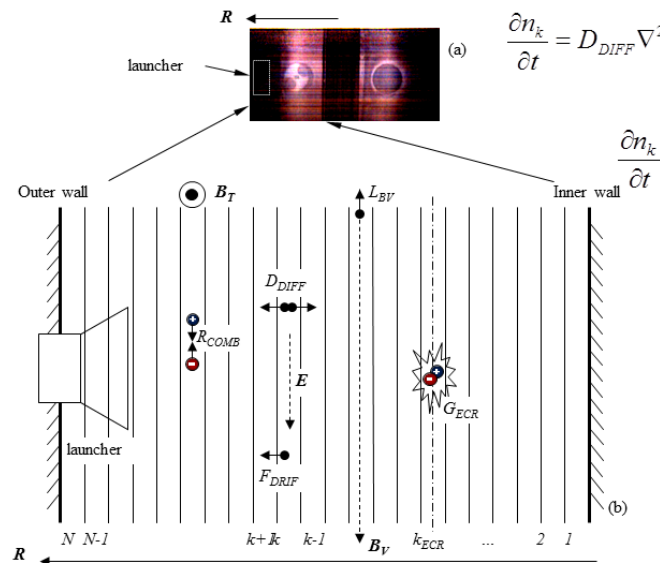


Figure 8. The one dimensional model used to analyze the transient process of ECR startup.

As shown in Figure 8, the space between the outer and inner wall of the vacuum vessel is divided

into vertical cells. The microwave antenna is located near the outer wall and the ECR layer is placed in any cell determined by the toroidal field. For simplicity, ionization can only happen in the ECR cell so the source term only exists in this cell. But diffusion, radial and vertical drifts happen in any cells. One can write the continuous equations for the cells as:

$$\frac{\partial n_k}{\partial t} = D_{\text{DIFF}} \nabla^2 n_k - F_{\text{DRIF}} \nabla n_k - L_{\text{BV}} n_k \quad (k \neq k_{\text{ECR}}) \quad (1)$$

$$\frac{\partial n_k}{\partial t} = D_{\text{DIFF}} \nabla^2 n_k - F_{\text{DRIF}} \nabla n_k - L_{\text{BV}} n_k + G_{\text{ECR}} n_k \quad (k = k_{\text{ECR}}) \quad (2)$$

where n_k is the electron density in k cell, D_{DIFF} is the diffusion rate (here we assume it constant), F_{DRIF} is the drift velocity (its composition is complex but here is also assumed constant), L_{BV} is the loss rate along vertical field lines and G_{ECR} is the ionization ratio that is proportional to the power density of microwave. To simplify the calculation of microwave reflection, the cut off layer is treated as a plane mirror and the microwave antenna is treated optically with the same radiating and receiving angles. The equation of reflection ratio is:

$$r_{\text{REF}} = \frac{W}{4d \tan \frac{\alpha}{2} + W} \frac{L}{4d \tan \frac{\beta}{2} + L} \quad (3)$$

where r_{REF} is the reflection ratio, W and L are the width and length of launching surface of the antenna respectively, α and β are the E-plane and H-plane launching angles respectively, and d is the distance from the cut off layer to the launching surface.

Simulation and Comparison

Because many coefficients in the continuous equations are uncertain, we need firstly to manually assign values and tune them by comparing the simulation results to experimental observations. When the coefficients are fixed experiments comparison are meaningful. Figure 9 (a) is the simulation of an oscillating shot as in Figure 7. Figure 9 (b) is the simulation of resonant layer scan like Figure 5. Both simulations are qualitatively agreed with the experimental results.

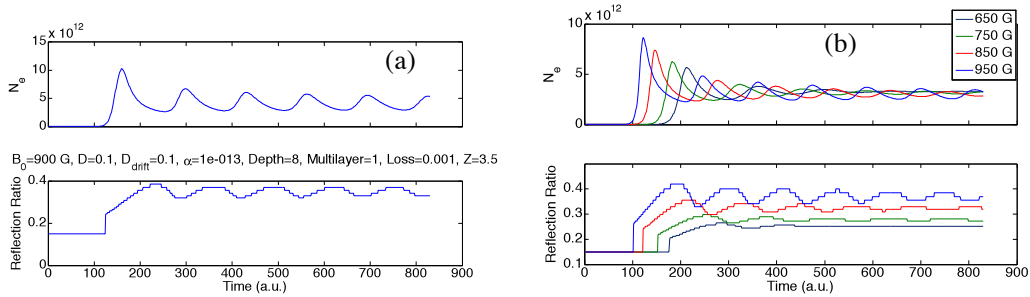


Figure 9. The simulation results of an oscillating shot (a) and the scan of resonant layer (b).

Conclusion

The transient process of ECR startup on SUNIST is successfully modeled and simulated. The

results are comparable to experimental observations. Simulated type 1 shots are qualitatively agreed with experiments. However, there are too many uncertain coefficients in the continuous equation and the model doesn't fully catch the dynamics of ionized electrons. Thus further study on this modeling is still on going.

Acknowledgements

This work is supported by the Major State Basic Research Development Program from MOST of China under Grant No. 2008CB717804, NSFC under Grant No. 10535020 , as well as the Foundation for the Author of National Excellent Doctoral Dissertation of PR China under Grant No. 200456. This work is partially supported by the JSPS-CAS Core University program in the field of 'Plasma and Nuclear Fusion'.

References

1. Sykes, A., et al., *First results from the START experiment*. Nuclear Fusion, 1992. **32**(4): p. 694-699.
2. Ono, Y., et al., *High-beta characteristics of first and second-stable spherical tokamaks in reconnection heating experiments of TS-3*. Nuclear Fusion, 2003. **43**(8): p. 789-794.
3. Sykes, A., et al. *Plasma formation without a central solenoid in a Spherical Tokamak*. 2004.
4. Ono, Y., et al. *Initial Operation of UTST High-Beta Spherical Tokamak Merging Device*. in *48th Annual Meeting of the Division of Plasma Physics*. 2006: American Physical Society.
5. Raman, R., et al., *Demonstration of Plasma Startup by Coaxial Helicity Injection*. Physical Review Letters, 2003. **90**(7): p. 075005.
6. Raman, R., et al., *Efficient Generation of Closed Magnetic Flux Surfaces in a Large Spherical Tokamak Using Coaxial Helicity Injection*. Physical Review Letters, 2006. **97**(17): p. 175002.
7. Forest, C.B., et al., *Internally generated currents in a small-aspect-ratio tokamak geometry*. Physical Review Letters, 1992. **68**(24): p. 3559.
8. Uchida, M., et al., *Formation of ST Plasmas by ECH on LATE*. Plasma Science & Technology, 2004. **6**(4): p. 2364-2366.
9. Maekawa, T., et al., *Formation of spherical tokamak equilibria by ECH in the LATE device*. Nuclear Fusion, 2005. **45**(11): p. 1439-1445.
10. Maekawa, T., et al., *Formation of low aspect ratio torus equilibria by ECH in the LATE device*. Plasma Science and Technology, 2006. **8**(1): p. 95-98.
11. Yoshinaga, T., et al., *Spontaneous formation of closed-field torus equilibrium via current jump observed in an electron-cyclotron-heated plasma*. Physical Review Letters, 2006. **96**(12): p. -.
12. Yoshinaga, T., et al., *A current profile model for magnetic analysis of the start-up phase of toroidal plasmas driven by electron cyclotron heating and current drive*. Nuclear Fusion, 2007. **47**(3): p. 210-216.
13. Takase, Y., et al., *Plasma current start-up experiments without the central solenoid in the TST-2 spherical tokamak*. Nuclear Fusion, 2006. **46**(8): p. S598-S602.
14. Ejiri, A., et al., *ECH and HHFW start-up experiments on the TST-2 spherical tokamak*. Fusion

- Science and Technology, 2007. **51**(2T): p. 168-170.
15. Gryaznevich, M., V. Shevchenko, and A. Sykes, *Plasma formation in START and MAST spherical tokamaks*. Nuclear Fusion, 2006. **46**(8): p. S573-S583.
 16. He, Y.X., et al., *Preliminary Experiment of Non-Inductive Plasma Current Startup in SUNIST Spherical Tokamak*. Plasma Science and Technology, 2006. **8**(1): p. 84-86.
 17. Yoshinaga, T., et al. *Non-Inductive Current Start-up Experiment by ECH in the CPD Device. in 13th International Workshop on Spherical Torus*. 2007. Fukuoka.

Monte Carlo study of the H/C ratio of impurities depositing on the bottom of the toroidal gaps between divertor tiles

Dai Shuyu ^a, Sun Jizhong ^a, M. KOMM ^b, Wang Dezhen ^{a*}

^a School of Physics and Optoelectronic Technology, Dalian University of Technology,
DaLian 116024, China

^b Institute of Plasma Physics, Academy of Sciences of the Czech Republic v.v.i., Association
EURATOM/IPP.CR, Za Slovankou 3, 18000 Prague, Czech Republic

Abstract

The castellated structure will be used at the divertor region to maintain the thermo-mechanical stability in ITER. Hydrocarbons generated by chemical erosion depositing in the gaps between the divertor tiles can cause tritium retention. In order to investigate the deposition behavior of impurities, we carry out simulations to study impurities transport, collisions and deposition in the toroidal gaps of shaped cells. The simulation results on several scenarios with different magnetic field configurations, plasma temperatures and densities show that they have a significant influence on the H/C ratio of deposited species on the bottom of the toroidal gaps: The magnetic field with a smaller incident angle can reduce the H/C ratio of deposited species noticeably; when the plasma density exceeds a certain value, the H content in deposited impurities on the bottom of the toroidal gaps becomes negligible.

Keywords: Monte Carlo methods, impurities, divertor, nuclear fusion

PACS: 52.65.Pp, 52.25.Vy, 52.55.Rk

1 Introduction

The plasma-facing divertor armor in the International Thermonuclear Experimental Reactor (ITER) will be castellated by splitting them into cells to maintain the thermo-mechanical stability [1]. The castellated cells are bombarded by high heat fluxes of ions and neutrals from the core plasma, which leads to the erosion of the plasma facing components (PFCs). The erosion by energetic particles determines the lifetime of PFCs and creates a source of impurities, which cool and dilute the plasma. The experiments in TEXTOR have clearly shown carbon accumulation and fuel retention in the limiter gaps with castellated configuration [2-6]. Continuous accumulation can give rise to remarkable tritium retention due to the shortage of effective cleaning techniques [7-11]. A better knowledge of hydrocarbons deposition in the gaps is essential for optimizing the shape of the castellation cells to minimize tritium retention.

Recently, in company with experimental works, some simulation studies have been carried out about impurity deposition in the gaps of rectangular cells and in the poloidal gaps of shaped cells [12,13]. However, few simulation works on the deposition of impurities in the toroidal gaps of shaped cells can be found. More studies in this respect are in need. Experiments observed that the deposits exist on the bottom of the gaps using a tungsten castellated limiter with rectangular and roof-like shaped cells in TEXTOR [5-6]. Regrettably, the relevant information is limited on account of diagnostic difficulty. A complementary means is to use computer simulation. In this study, the simulation of impurities transport, collisions and deposition in the toroidal gaps of roof-like shaped cells at divertor region has been performed using a three-dimensional Monte Carlo (MC) code. With the MC code, the studies on the influence of magnetic field configuration and plasma conditions on impurities deposition allow us to gain insight into the tritium retention in the toroidal gaps. This work will focus on the impurities deposition, in particular, the H/C ratio of deposited species on the bottom of the toroidal gaps between divertor tiles.

2 Models

In this study, we apply our MC code to the analysis of impurities transport, collisions and deposition in the toroidal gaps of shaped cells. A schematic of the toroidal gap of roof-like shaped cells is illuminated in Figure 1. The geometrical dimensions of the shaped cells (10x10x12/15 mm) and the width of the cell gap (0.5 mm) are chosen the same as the experiments performed in TEXTOR [5-6]. The simulation region is the toroidal gap between roof-like shaped cells, and the toroidal gap is a plasma-open region, which is unlike the case of the poloidal gap acting as plasma-shadowed areas. Since the magnetic field lines are

parallel to the sides of the gap as in the experiments, the gap is filled with the plasma. Thus, we can assume the background plasma to be spatially uniform as a zero-order approximation for simplicity. Moreover, sheath acceleration does not occur in the gap [13]. The angle of magnetic field lines making with the z direction (i.e. the toroidal direction) is defined as α . In the simulation, ion-to-electron temperature ratio $\tau = T_i / T_e$ is assumed to be 2 [14-16], and the magnetic field strength is 2.25 T.

We briefly review the simulation procedure as follows: all methane molecules (CH_4) are released from a random position at the entrance of the gap of shaped cells. We use a half-maxwellian velocity distribution corresponding to a temperature of 0.1 eV with velocity cut-off only in the direction of x -axis positive direction. The collision probability of hydrocarbons with the plasma electrons and ions is determined by the plasma temperature and the plasma density [17]. As a result of CH_4 colliding with the plasma electrons and ions, many neutral and ionized fragments are produced through chains of successive reactions. The reactions involving CH_4 and its fragments (i.e. carbon and hydrocarbons) include electron-impact direct and dissociative ionization of CH_y , electron-impact dissociative excitation of CH_y neutrals, electron-impact dissociative excitation of CH_y^+ ions, electron-impact dissociative ionization of CH_y^+ ions, electron dissociative recombination with CH_y^+ ions, proton-impact ionization and charge exchange. These cross sections are calculated by the fitting formulas given by Janev and Reiter [18]. The cross section data for $\text{H}^+ + \text{C} \rightarrow \text{H}^+ + \text{C}^+$ is taken from Ref. [19]. When a particle is charged, it gyrates due to Lorentz force in the magnetic field; when a particle is neutral, it moves along straight lines. When an ionized particle reaches the sides of the gap, we assume it sticks to the sides of the gap as done in the ERO code [20]. When a neutral particle comes to the sides of the gap, whether it either sticks or reflects is decided by comparing a random number with each reflection coefficient. The energy- and species-dependent reflection coefficients for fragments (i.e. carbon and hydrocarbons) are taken from modified MolDyn calculations [21-22]. All reactive fragments are tracked until they deposit in the gap or escape from the gap.

3 Results and discussion

3.1 Comparison between simulation and experiment

Litnovsky et al recently have done an experiment using a tungsten castellated limiter with two different shapes of castellation exposed in the scrape-off layer (SOL) plasma in TEXTOR. Two types of castellation (i.e. rectangular and roof-like shaped cells) were installed on the double-roof limiter that was introduced to TEXTOR by the limiter lock

system. After exposure, several surface and elemental analyses have revealed the advantages of using shaped castellations to reduce the amount of deposited deuterium and carbon compared with no-shaped ones. More detailed information about the experiment can be seen in Ref. [4-6]. Due to non-perfect alignment of the toroidal gaps with respect to the magnetic field under experimental conditions, there usually exists a small offset angle between the toroidal gaps and the magnetic field; we take this offset angle as 1° in the simulation.

Figure 2 shows the distribution of carbon atoms deposition rate in the toroidal gap of shaped cells. The circle and triangle symbols represent the simulated results and normalized experimental data [5], respectively. The experimental data has been normalized by the total carbon atom density. By the comparison, we can see that the simulation reproduces the experimental deposition profile very well. As shown in Fig.2, we notice that the deposition profile has a great difference between plasma-shadowed side and plasma-viewing side. There are two reasons for such a difference: (1) non-perfect alignment of the toroidal gaps with respect to the magnetic field; and (2) the gyration radii of the carbon ions are comparable to the gap width. These reasons are strongly related to the experimental conditions; their detailed explanations are presented in Ref. [4-6].

3.2 Deposition on the bottom of the toroidal gaps

Two incident angles of magnetic field $\alpha = 20^\circ$ (the same with that in experiments [2-6]) and $\alpha = 5^\circ$ (a preferred angle for ITER) are considered for all different plasma temperatures and plasma densities. In the simulation, all plasma parameters are guaranteed not to violate the conditions that the maximum pressure does not exceed 10^{-3} bar in the gap [6], and only carbon/hydrocarbon species generated from collisions are taken into account.

Figure 3(a) shows the H/C ratios of deposited species with different plasma temperatures on the bottom of the toroidal gap. The hydrocarbons produced by chemical erosion have low energy so that the gyration radii of the ionized particles are small compared with the gap width [7]. As a result, the ionized particles can get deep into the gap and even deposit on the bottom of the toroidal gap. At a lower temperature, fewer plasma background species carry the kinetic energy over the dissociation reaction threshold energy, and consequently, the happening probability of the dissociation reactions during the lifetime of the hydrocarbon molecules is smaller. As a result, the substance depositing on the bottom of the gap contains more hydrogen component at the lower temperature. In addition to the effect of plasma temperature, we assess the extent to which the incident angle α of magnetic field affects the H/C ratio of deposited species on the bottom of the gaps. As can be seen from Fig. 3(a), there is a significant difference in the H/C ratios between $\alpha = 20^\circ$ and $\alpha = 5^\circ$ under

otherwise identical conditions. It is easily understood that the ionized particles have a longer flight distance along the magnetic field lines at a smaller angle by simple geometry knowledge. Hence, the ionized particles undergo more collisions at the incident angle of $\alpha = 5^\circ$ than that at the incident angle of $\alpha = 20^\circ$. To further quantify our explanation, we calculate the statistical distribution of collision numbers of particles depositing on the bottom of the toroidal gap during their transport processes, which is plotted in Figure 3(b). Clearly, the particles in the case of $\alpha = 5^\circ$ undergo more collisions than that in the case of $\alpha = 20^\circ$.

Apart from plasma temperature, it is necessary to check whether the plasma density has a strong influence on the H/C ratio of deposited species on the bottom of the toroidal gap. Figure 4 shows the deposited species ratio with different plasma densities on the bottom of the toroidal gap. As shown in Figure 4(a) and (b), we can see that the ionized particles account for most deposited species on the bottom of the gap. The ionized particles move along the magnetic field lines with small gyration radii and get to the bottom easily. However, the neutral particles don't have the constraint of Lorentz force in the magnetic field, and the motion direction of the neutral particles is fairly random; they have much more chance of depositing on the side wall and few of them reach the bottom of the gap. Figure 5 displays the H/C ratios of deposited species at different plasma densities on the bottom of the toroidal gap. The collision probability is larger at a higher plasma density. This fact results in the decrease in the H/C ratio of deposited species at a higher density. As a consequence, the H/C ratio of deposited species decreases as the plasma density increases, as shown in Fig. 5. Another unexpected result is that the H/C ratio of deposited species on the gap bottom is remarkably smaller for $\alpha = 5^\circ$ than that for $\alpha = 20^\circ$ when plasma density is below $1 \times 10^{18} \text{ m}^{-3}$ in Fig. 5. At the smaller incident angle of magnetic field, the ionized species travel a longer distance and experience more dissociation collisions. However, when the plasma density exceeds $1 \times 10^{18} \text{ m}^{-3}$, this angular effect becomes gradually unnoticeable. At a higher plasma density, almost all hydrogen atoms of the ionized species are stripped by the collisions. Thus, the difference of the H/C ratio of deposited species between $\alpha = 5^\circ$ and $\alpha = 20^\circ$ gradually decreases as the plasma density rises. When the plasma density is over $5 \times 10^{18} \text{ m}^{-3}$, the H/C ratios of deposited species drop approximately to zero for both $\alpha = 5^\circ$ and $\alpha = 20^\circ$. The carbon atoms and carbon ions account for the major components of the impurities depositing on the bottom of the toroidal gap. This result suggests that when the fusion device runs at a high plasma density, the issue of the hydrogen (its isotopes) retention due to the redeposition of hydrocarbons on the bottom of the toroidal gap should not be as severe as it is envisaged.

4. Conclusions

In this work, a three-dimensional Monte Carlo code has been used to simulate impurities transport, collisions and deposition in the toroidal gaps of roof-like shaped cells. The Monte Carlo code was benchmarked first by the comparison of the simulation result with the corresponding experimental one obtained in TEXTOR. The code was then used to simulate various cases about the deposition of impurities in the toroidal gaps with different magnetic field configurations and plasma conditions. On the bottom of the toroidal gap, it was also found that the H/C ratio of deposited species is smaller at a higher plasma temperature. Further, the simulation results show that the incident angle of magnetic field has a remarkable influence on the H/C ratio of deposited species on the bottom of the toroidal gap: the magnetic field with a smaller incident angle can reduce the H/C ratio remarkably. When the plasma density exceeds $5 \times 10^{18} \text{ m}^{-3}$ in this study, the H/C ratio of deposited species drops to a negligible value. This result may suggest that the issue of the hydrogen isotopes retention due to the redeposition of hydrocarbons on the bottom of the toroidal gap should not be as severe as that predicted by simple extrapolation of the results from current fusion devices when the future fusion device performs at a much higher plasma density.

Acknowledgements

This work was supported by National Basic Research Program of China under grant No: 2008CB717801 and 2009GB106002. Authors would like to express their appreciation to Feng Wang and Shengguang Liu for his assistance in computation. This work was partially supported by the JSPS-CAS Core University program in the field of 'Plasma and Nuclear Fusion'.

References

- [1] W. Daener, M. Merola, P. Lorenzetto, et al., 2002, Fusion Eng. Des. 61-62: 61.
- [2] A. Litnovsky, V. Philipps, P. Wienhold, et al., 2005, J. Nucl. Mater. 337-339: 917.
- [3] A. Litnovsky, V. Philipps, A. Kirschner, et al., 2007, J. Nucl. Mater. 367-370: 1481
- [4] A. Litnovsky, V. Philipps, P. Wienhold, et al., 2007, Phys. Scr. T128: 45
- [5] A. Litnovsky, V. Philipps, P. Wienhold, et al., 2009, J. Nucl. Mater. 386: 809
- [6] A. Litnovsky, P. Wienhold, V. Philipps, et al., 2009, J. Nucl. Mater. 390: 556
- [7] G. Federici, C. H. Skinner, J. N. Brooks, et al., 2001, Nucl. Fusion. 41: 1967
- [8] G. Federici, J. N. Brooks, M. Iseli, et al., 2001, Phys. Scr. T91: 76.
- [9] R. A. Causey, J. N. Brooks, G. Federici, 2002, Fusion Eng. Des. 61-62: 525
- [10] C. H. Skinner, J. P. Coad, G. Federici, 2004, Phys. Scr. T111: 92

- [11] J. Roth, E. Tsitrone, T. Loarer, et al., 2008, Plasma Phys. Control. Fusion. 50: 103001
- [12] K. Inai, K. Ohya, 2007, J. Nucl. Mater. 363-365: 915
- [13] K. Inai, K. Ohya, Y. Tomita, et al., 2009, J. Nucl. Mater. 390-391: 119
- [14] C. S. Pitcher, P. C. Stangeby, 1997, J. Nucl. Mater. 39: 779
- [15] M. Kocan, R. Panek, J. Stockel, et al., 2007, J. Nucl. Mater. 363-365: 1436
- [16] M. Kocan, J. P. Gunn, J. Y. Pascal, et al., 2009, J. Nucl. Mater. 390-391: 1074
- [17] V. Vahedi, M. Surendra, 1995, Comput. Phys. Commun.. 87: 179
- [18] R. K. Janev, D. Reiter, 2002, Phys. Plasmas. 9: 4071
- [19] P. C. Stancil, J. P. Gu, C. C. Havener, et al., 1998, J. Phys. B. 31: 3647
- [20] W. Bohmeyer, D. Naujoks, A. Markin, et al., 2005, J. Nucl. Mater. 337-339: 89
- [21] D. A. Alman, D. N. Ruzic, 2003, J. Nucl. Mater. 313-316: 182
- [22] D. A. Alman, D. N. Ruzic, 2004, Phys.Scr. T111: 145

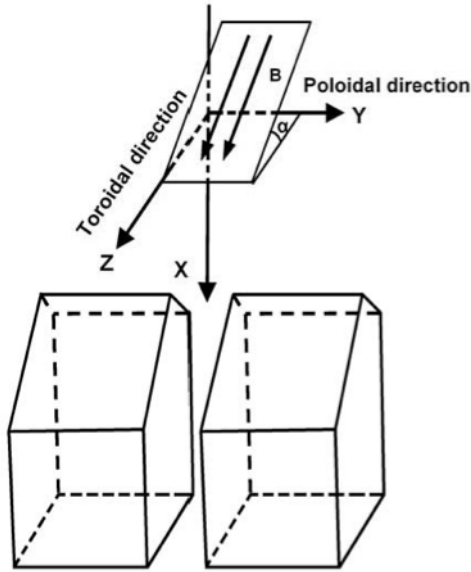


FIG. 1. Schematic of the toroidal gap of roof-like shaped cells. The coordinate axes, toroidal direction and poloidal direction are schematically shown.

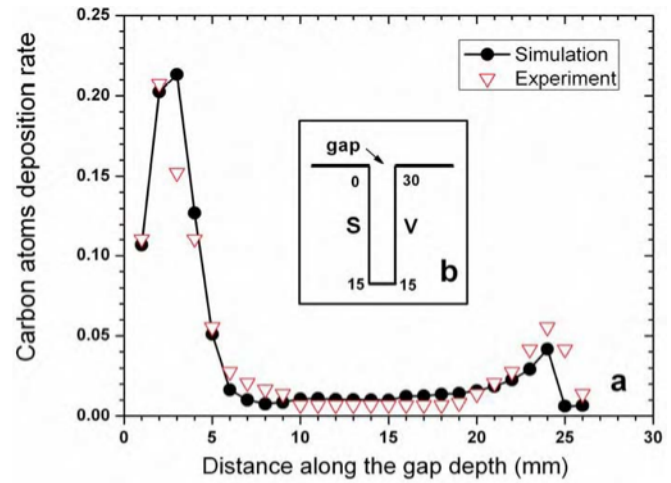


FIG. 2. (a) The distribution of carbon atoms deposition rate for simulation (circle) and experiment (triangle) as a function of the distance along the gap depth ($T_e = 25$ eV, $n_e = 10^{18} \text{ m}^{-3}$). (b) Cross-sectional view of the shaped cells along the poloidal direction: S-plasma-shadowed side (0-15 mm), V-plasma-viewing side (15-30 mm). The beginning of the abscissa axis corresponds to the edge of plasma-shadowed side.

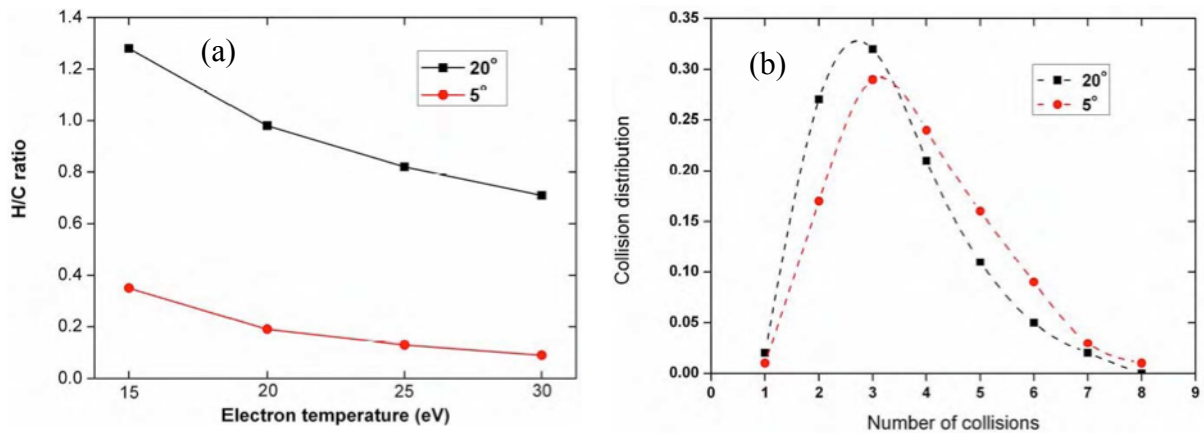


FIG. 3. (a) The atomic ratio of H/C of deposited species with different plasma temperatures on the bottom of the toroidal gap ($n_e = 10^{18} \text{ m}^{-3}$), and (b) the distribution of the collision number of deposited species on the bottom of the toroidal gap ($T_e = 25$ eV).

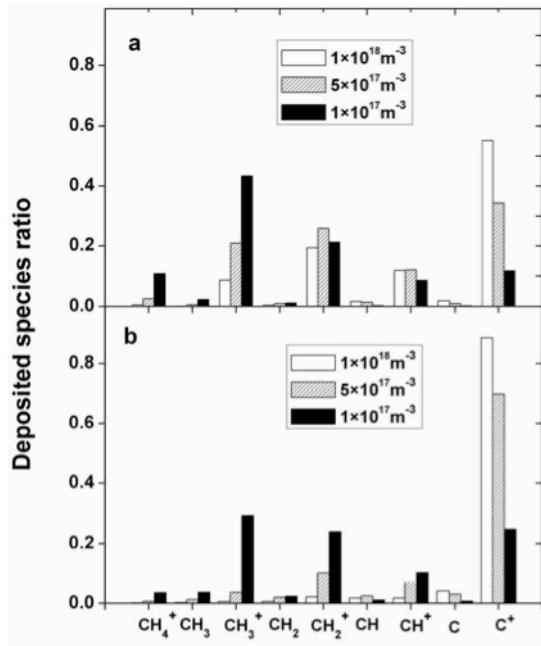


FIG. 4. The deposited species ratio with different plasma densities on the bottom of the toroidal gap for (a) $\alpha = 20^\circ$ and (b) $\alpha = 5^\circ$.

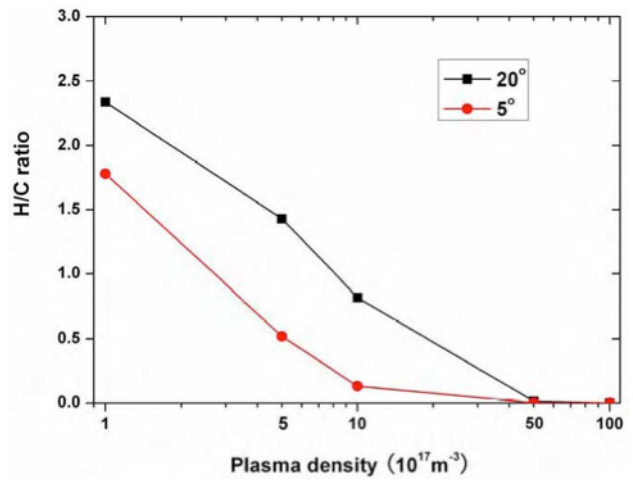


FIG. 5. The atomic ratio of H/C of deposited species with different plasma densities on the bottom of the toroidal gap ($T_e=25$ eV).

The simulation of erosion and deposition behavior on EAST

Qian Xu^a, K. Ohya^b, Z. S. Yang^a, K. Inai^b, G.-N. Luo^{a*}

^a*Institute of Plasma Physics, Chinese Academy of Sciences, P.O. Box 1126, Hefei 230031, China*

^b*Institute of Technology and Science, The University of Tokushima, Tokushima 770-8506, Japan*

Abstract

Using the typical edge plasma parameters of the Experimental Advanced Superconducting Tokamak (EAST), the erosion and deposition behavior of the SiC coating were calculated with the modified Erosion and Deposition based on Dynamic model (EDDY code). Compared to those on the non-doped graphite, it's found that less deposition and erosion occurred on the SiC coating. Further benchmarking experiments on EAST have been planned.

1. Introduction

Carbon-based materials have been widely used as Plasma-Facing Materials (PFMs) for the properties such as low atomic number (Z), superior thermal shock resistance and potentially high thermal conductivities. However, carbon-based materials have high chemical erosion rates due to hydrocarbon formation [1]. In order to reduce the chemical erosion rates, one kind of multi-element doped graphite GBST1308 (1%B₄C, 2.5%Si, 7.5%Ti) with $\sim 100 \mu\text{m}$ thick SiC gradient coatings was chosen as the PFM in the Experimental Advanced Superconducting Tokamak (EAST) [2]. As we know, physical sputtering, chemical erosion and re-deposition of carbon-based PFMs are unavoidable during the discharges, and the related knowledges are not yet understood well for our SiC/C-PFM. The sputtered/eroded neutral solid particles are ionized or dissociated through their collisions with plasma electrons in the SOL. The particles, particularly C ions, are deposited after their gyromotion and dissociation and modify the surface composition, which, in turn, alters the sputtering yield of modified material. In order to simulate the dynamic erosion and deposition processes on the PFMs, a three-dimensional dynamic Monte Carlo simulation code, Erosion and Deposition based on Dynamic model (EDDY), was developed by K. Ohya recently [3]. The EDDY code has been successfully used to study the erosion and re-deposition behavior of graphite and tungsten materials under various edge plasma conditions in several fusion devices such as JT-60U, TEXTOR, ITER-FEAT [4-6].

In this work, we modified the code to simulate the 2-dimensional erosion and deposition patterns in EAST, and compared the erosion and deposition behavior

* Corresponding author. E-mail: gnluo@ipp.ac.cn

between SiC coating and pure carbon using typical edge plasma parameters from the following four aspects: (1) erosion depth and deposition thickness; (2) depth profiles; (3) carbon reflection coefficient; (4) carbon and silicon sputtering yields. The input parameters include carbon chemical sputtering yield Y_{ch} , impurities concentration in SOL f_C/f_{Si} , electron density n_e and electron temperature T_e .

2. Method

In the code, the velocities distribution of the ions in SOL plasma is assumed to be Maxwellian, and the ions are accelerated towards the PFM by the sheath potential. The interactions of ions and solid are calculated by binary collision approximation. EDDY also simulates the transport of released impurities and hydrogen isotopes in the background plasma. The chemically sputtered hydrocarbons C_xH_y ($x=1-3$) may undergo more complicated processes than simple ionization of those physically sputtered atoms and reflected hydrogen isotopes atoms. Successive ionization and dissociation processes are followed by combining kinetic equation analysis with Monte Carlo simulation. Some particles redeposit promptly or after migration in the plasma. As a result, erosion and deposition patterns are calculated on the material surface. Detailed models are described in Ref. [3].

Table 1 Parameters used in the calculations

Magnetic field strength, B(T)	2
Angle between plasma sheath and surface, θ (deg)	30
Angle between magnetic field line and surface, ϕ (deg)	1
Charge of incident ions	C^{2+}/Si^{3+}
Carbon sputtering yield, Y_{ch}	$Y_{ch}=2\%, 8\%$
Impurities concentration, f_C/f_{Si}	$f_C=2\%, 5\%$ $f_{Si}=2\%$

The interaction between the edge plasma and the first wall occurs on the SiC coating before the coating is removed away. For simplicity, we herein take the stoichiometric composition of SiC into account, i.e., concentrations of 50% and 50% for C and Si, respectively. The simulation time for one discharge is 7 seconds. Moreover, in order to follow the transport of Si atoms and their redeposition on the surface, additional rate coefficients for ionization of Si [7] are introduced into EDDY. Other input parameters used in this simulation are summarized in Table 1.

3. Results and discussion

Figure 1(a) shows the thickness dynamic change on the SiC coating with typical

parameters of $T_e=20$ eV and $n_e=10^{18}$ m⁻³ in EAST [8], in comparison with that of non-doped graphite as shown in Fig. 1(b). The results show that, for high f_C (5%) in the plasma and low Y_{ch} (2%) of the wall material, deposition of C is the major process on the surface. With introducing the Si impurity into the plasma ($f_{Si}=2\%$), more deposition is observed. On the other hand, low f_C (2%) or high Y_{ch} (8%) leads to the surface recession. However, despite of the erosion of the surface, carbon impurities in plasma are deposited on the surface, as shown in Fig. 2(b).

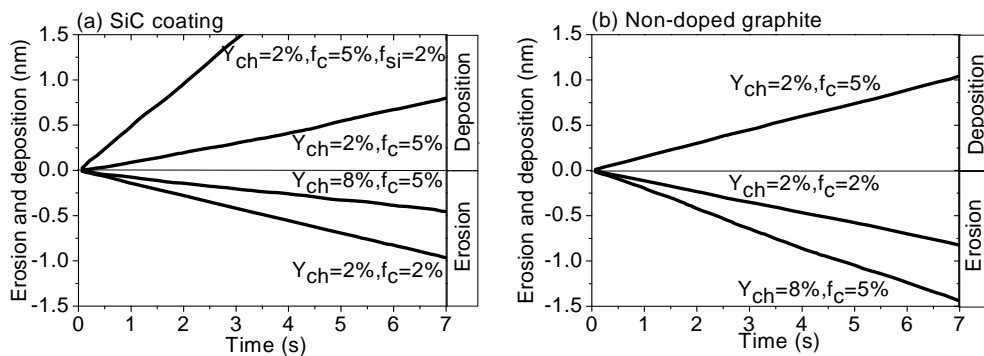


Fig. 1. Erosion depth and deposition thickness of (a) SiC coating and (b) non-doped graphite during plasma exposure at different values of Y_{ch} and f_C and f_{Si}

It should be noted that for $Y_{ch}=2\%$, less deposition on the SiC coating is observed in comparison with that on the non-doped graphite, whereas for $Y_{ch}=8\%$, less erosion on the SiC coating is observed. The former is due to an enhanced reflection of C on the SiC coating, as calculated and shown in Fig. 3(a). The latter is because C atoms are eroded by both chemical sputtering and physical sputtering, while Si atoms in the SiC coating are only eroded by physical sputtering. Otherwise, the physical sputtering does not affect very much the erosion behavior at such low electron temperature.

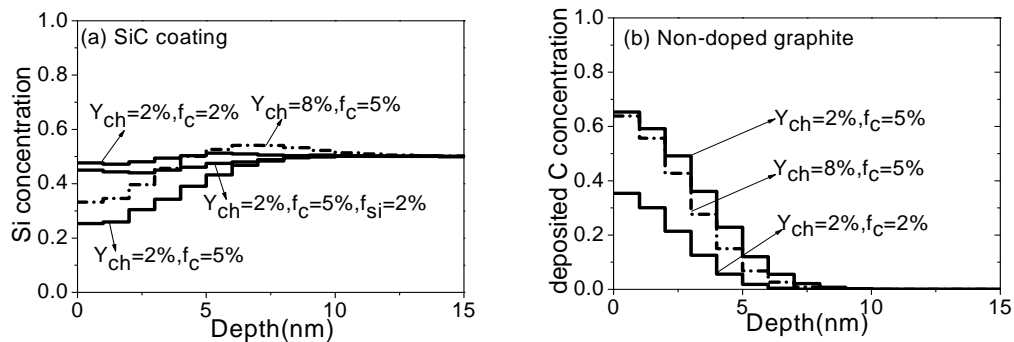


Fig. 2. Depth profiles of (a) Si in the SiC coating and (b) deposited carbon concentration on non-doped graphite after plasma exposure at different values of Y_{ch} and f_C and f_{Si}

As shown in Fig. 2(a), Si concentration in the coating is strongly reduced near the surface after the plasma exposure, especially for $f_C=5\%$. This is due to the deposition of

C impurities on the surface. For high $Y_{ch}=8\%$, Si concentration is more than the initial value (50%) near the depth of 7 nm. It is because chemical sputtering of C is the dominant process at such high Y_{ch} (8%), and the C concentration in the coating is much lower than 50%. Furthermore, additional Si impurity in the plasma and deposited C suppresses the change of Si concentration, then Si concentration is near to the initial value (50%) for the depth $>10\text{nm}$.

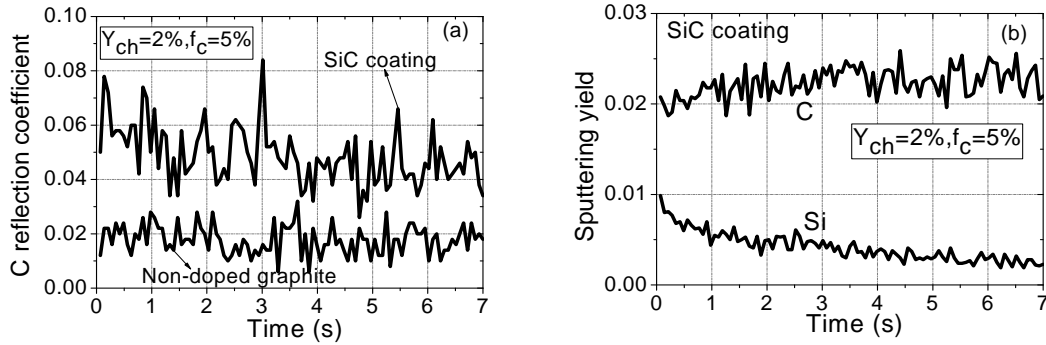


Fig.3. Dynamic changes of carbon reflection coefficient on SiC coating and non-doped graphite (a) and carbon and silicon sputtering yield of SiC coating (b) during plasma exposure

In Fig. 3(a), it should be noted that the C reflection coefficient on the SiC coating decreases little by little before 4 seconds of plasma exposure time, whereas despite of the scattering, that on the non-doped graphite is kept to be constant. The dynamic change on the SiC coating is caused by the increasing deposition of C impurities. This causes the C (Si) sputtering yield on SiC coating to increase (decrease) with increasing exposure time again (Fig. 3(b)).

4. Conclusions and Future issues

In order to analyze the erosion and deposition behavior on the SiC coated, multi-element doped graphite wall of the EAST, rate coefficients for the ionization of Si atoms sputtered from the coatings were introduced into the EDDY code to follow the transport of Si in the edge plasma. Assuming a chemical sputtering yield Y_{ch} of 2%, less deposition of carbon on the SiC coating has been found in comparison with on the non-doped graphite surface. Furthermore, less erosion on the SiC coating has also been observed for higher Y_{ch} (8%) with assumption of no chemical sputtering of Si atoms in our simulations. The carbon deposition on the SiC coating reduces both C reflection and Si physical sputtering, but increases C physical and chemical sputtering.

These predictive results present important information for better understanding and controlling of the plasma performance. However, more efforts are still necessary to further demonstrate the co-relationship of the major parameters Y_{ch} , f_c and f_{Si} and their impacts onto the erosion and re-deposition on the SiC coating, and some benchmarking

experiment in EAST would be conducted.

ACKNOWLEDGEMENTS

This work has been partially supported by the JSPS-CAS Core-University Program in the field of “Plasma and Nuclear Fusion”.

References

- [1] G. Federici and C.H. Skinner, et al, Nuclear Fusion 41 (2001) 1967.
- [2] C.Y. Xie, J.L. Chen, J.G. Li, Q.F. Fang, Journal of Nuclear Materials 363-365 (2007) 282.
- [3] K. Ohya, Phys. Scripta T124 (2006) 70.
- [4] K. Ohya and R. Kawakami, et al, Jpn. J. Appl. Phys. 40 (2001) 5424.
- [5] K. Ohya and K. Inai, et al, Journal of Nuclear Materials, 363-365 (2007) 78.
- [6] K. Ohya and A. Kirschner, Phys. Scr. T138 (2009) 014010.
- [7] M. A. Lennon et al. Report of the Culham Laboratory, CLM-R270 (1986).
- [8] T. Ming, W. Zhang, J. Chang, G. Xu, S. Ding, N. Yang, X. Gao, H. Guo, Fusion Engineering and Design 84 (2009) 57.
- [9] H.Y. Guo, S.Z. Zhu, J.G. Li, Plasma Science & Technology. 8 (2006) 633.

Theoretical modeling of hydrogen retention and recycling in plasma-facing graphite

Liu Shengguang, Sun Jizhong, Dai Shuyu, Wang Dezhen *

Key Laboratory of Materials Modification by Laser, Ion and Electron Beams
(Ministry of Education), School of Physics and Optoelectronic Technology,
Dalian University of Technology, Dalian, 116024, China

Abstract

The graphite and carbon fibre composites used as plasma facing components in fusion devices are composed of graphitic crystallites, connected by intercrystalline voids. The porous structure gives rise to great complexity to understand the hydrogen transport behaviour in graphite. In this work dynamic Monte Carlo simulations are carried out to understand the dependence of the hydrogen retention, re-emission, and thermal desorption on the void fraction of graphite. The results show that the void fraction plays an important role in hydrogen retention and release behaviour.

Keywords: void fraction, retention, re-emission, thermal desorption PACS: 52.65.Pp, 66.30.Xj, 68.43.Vx, 81.05.Uw

*Author to whom correspondence should be addressed; E-mail: wangdez@dlut.edu.cn

1 Introduction

Carbon-based materials are attractive candidates for the plasma facing components in current and future thermonuclear fusion devices. As well known, there is growing concern that application of carbon-based materials eventually causes unacceptable hydrogen/its isotope recycling and tritium inventory. The accumulation of tritium in the vessel wall materials of thermonuclear fusion devices is a major safety issue [1, 2]. Therefore, the understanding of retention and release of hydrogen in graphite is important for fusion plasma density control and the determination of tritium inventory in future devices.

The graphite used as plasma facing components in fusion devices are porous and consists of crystallites separated by intercrystalline voids [3, 4]. These voids provide a large internal surface area inside graphite where the hydrogen interstitial atoms can diffuse and react with each other, which finally affects the hydrogen isotope inventory, recycling behaviour and chemical erosion. Such porous structure does give rise to great complexity to understand the hydrogen transport behaviour in graphite. Although many macroscopic models have been proposed [5-7], these models ignore the effects of the porous structure on the inventory and transport of hydrogen in graphite. A few microscopic studies such as molecular dynamics simulation and density functional theory calculations [8-10] were carried out on the hydrogen diffusion in crystalline graphite. Though they can give many insights into the microscopic mechanism, they are not suitable for studying the evolution process of a large scale system to reflect the structural effects.

Recently, a multi-scale dynamic Monte Carlo model was developed by Rai et al. to study atomic hydrogen inventory and diffusion in porous graphite [11, 12]. In present work, we modify the model to evaluate the effects of the void fraction on the hydrogen retention, re-emission and thermal desorption processes in graphite.

2 Theoretical model

A porous graphite is constructed theoretically by using Poisson distribution to specify the mean side length of a random-shaped sub-structure. The sub-structure is created by populating basic building blocks (called cells here) to fill up a given volume. The smoothness of the sub-structure depends on the cell size. If the sub-structure is crystallite, random orientations are specified. After each populating action, the remaining void volume is checked against a predefined void fraction of void volume over the substructure volume. The process is repeated until the required void fraction is reached. More details of constructing the porous structure are described in Ref. [12].

The atomic hydrogen diffusion in graphite involves many processes. The main

processes contributing to the hydrogen transport [11, 12] are: (i) trapping–detrapping; (ii) recombination, dissociation and molecule formation; (iii) desorption from graphite surface, (iv) incident hydrogen deposition profile; (v) trans-granular diffusion and (vi) diffusion along voids. The corresponding activation energies are summarized in Table 1. The recombination between hydrogen atoms is handled using the Smoluchowski boundary condition [11, 12] by checking the distance between the atoms. If this distance gets shorter than a critical distance, they recombine to form a molecule. The distance was considered to be in the range 0.17-0.27 nm [5]. A value of 0.2 nm is used in the current simulation. The hydrogen molecules are assumed to be infinitely fast on the crystallite surface [5, 6] but unable to move within the crystallites [5, 21] due to the small interlayer spacing within the graphite crystallites (~0.3 nm).

The dynamic Monte Carlo simulation of the diffusion process is reviewed briefly as follows: The diffusion is considered to be a thermally activated process, which can be any of events summarized in table 1. The probability of an event performed depends on its jump rate, which is given by

$$R = r_0 \exp(-E_d / k_B T) \quad (1)$$

where r_0 is the attempt frequency, E_d is the detrapping energy, k_B is the Boltzmann constant, and T is the substrate temperature. The happening probability of each event is weighted by using the BKL algorithm [13]. When an event takes place, an action is taken to let the associated particle walk a distance of L randomly in the porous graphite. In the course of the diffusion, the hydrogen atom can be caught by a trap with a predefined probability. Then the total of simulation time advances by a time step

$$\Delta t = -\log(r) / \sum N_i R_i \quad (2)$$

where r is a uniform random number between 0 and 1, N_i is the particle number of species i , and R_i is the jump rate of species i .

The main modifications to the previous model are (i) the TRIM code [14] is coupled into the diffusion model to get a self-consistent deposition profile; (ii) the hydrogen molecule is released right away once it forms due to fast diffusion on the crystallite surface; (iii) The interested quantities are time-varying, not just quasi steady-state quantities [12].

3 Results and discussion

A porous granule of $100 \times 100 \times 200 \text{ nm}^3$ in the X , Y , and Z directions is constructed. The volume of the cubic cell to create the porous structure is chosen to be 0.125 nm^3 , and the mean side length of crystallites is 10 nm. The hydrogen ion temperature T_i considered in present simulation is 30 eV with an electrostatic sheath potential of $3T_i$. The probability that

hydrogen atoms are caught by a trap site is set to 0.0075. The depth profile of ions is given by TRIM calculations. The periodic boundary conditions are applied to the X and Y directions.

3.1 Hydrogen retention

Figure 1 shows the hydrogen retention versus temperature under different void fractions. At temperature lower than 1000 K, most of incident hydrogen species stay inside the target; at temperature above than 1000 K, the hydrogen retention fraction drops rapidly. Compared with the diffusion in crystallites, hydrogen atomic desorption and detrapping have much higher activation energy. The recombination of hydrogen atoms takes place mostly within crystallites. Because the formed hydrogen molecules can not diffuse to the crystallites surface due to small interlayer spacing in crystallites, and consequently, high values of retained fraction are observed at low temperature. When the temperature rises over 1000 K, higher probability of atomic hydrogen desorption and detrapping results in the rapid reduction of the retained fraction.

In addition, it is also found that the incident hydrogen species retain inside more in the larger void fraction at a given temperature above 1000 K. At higher void fraction, there exists larger internal surface area for hydrogen adsorption, and hydrogen atom can diffuse along the void surface easily deep into the graphite. Therefore, at a higher void fraction, a higher retention fraction of incident particles is observed.

3.2 Re-emission of hydrogen

Figure 2 shows the re-emitted flux as a function of temperature at void fractions 2%, 6% and 9%. As can be seen, the released flux is made up mainly of molecular hydrogen at lower temperatures and atomic hydrogen at higher temperatures. The results are in agreement with the experimental results [22] and theoretical calculations [5]. At low temperatures, the desorption energy of hydrogen atoms is too high for them to release, but they can diffuse on the surface and recombine to form hydrogen molecules. These molecules have a very low desorption energy and diffuse to the substrate surface almost immediately, and are therefore thermally released. As the temperature increases, atomic hydrogen desorption from the crystallite surfaces gradually becomes an important process and atomic hydrogen release can be observed, too. Due to atomic hydrogen release, there are fewer hydrogen atoms available for molecule formation. As a result, molecular hydrogen release drops at higher temperatures.

As a matter of fact, the released flux is determined by the competition between diffusion, recombination and trapping-detrapping, which further depend on the internal structure of the graphite. It can be seen from Fig. 2 that the temperature at which both atomic and molecular hydrogen species are released with an equal amount shifts towards lower temperature as the void fraction decreases. The increase of the void fraction increases means

larger area of internal surface, which provides more trapping sites to capture the atoms. Therefore, at a fixed flux, the incident atoms have more chance to recombine with the trapped hydrogen atoms on the crystallites surface in higher void fraction graphite. Consequently, the released flux of hydrogen molecules increases with the void fraction.

3.3 Thermal desorption

Figure 3 shows the desorbed amount of H_2 as a function of substrate temperature under different void fractions. We note a thermal desorption phenomenon in the previous experimental studies that the desorption rate of H_2 molecules sometimes exhibits single peak [22, 23], sometimes exhibits double peaks [24, 25]. Nevertheless, the number of desorption peaks depending on the graphite structure has never been discussed before. From Fig. 3, it can be seen that the void fraction is strongly linked to the number of desorption peak. When the void fraction is 1.5%, only single desorption peak is observed around 1000 K. As the void fraction increases, another minor peak appears around 820 K. When the void fraction is 9%, the minor peak grows, comparable to the main peak at 1000 K.

The two desorption peaks may be attributed to the coexistence of two main types of traps containing one or two H atoms (in form of CH and CH_2 complexes). In the present simulation, the implanted hydrogen atoms exist in two states, solute state and trapped state. Hence, three different atomic reactions – solute hydrogen and solute hydrogen, solute hydrogen and trapped hydrogen, and trapped and trapped hydrogen – lead to the recombination between hydrogen atoms. When a recombination event takes place between two solute hydrogen atoms, the formed hydrogen molecules behavior very differently: When the hydrogen molecule is located on the crystallite surface, it is released right away; when it is located in the crystallite, it is retained inside due to the small interlayer spacing within the graphite crystallites (~ 0.3 nm). If the recombination event takes place between solute hydrogen atom and trapped hydrogen atom or between two trapped hydrogen atoms, the two hydrogen atoms coexist in a trap site in the form of CH_2 complex. For a trap site containing one hydrogen atom only, it is assumed that the trapped hydrogen exists in the form of CH complex. The two types of traps have different temperature stabilities (the detrapping energy of CH complex is 2.7 eV while the detrapping energy of CH_2 is 2.3 eV), which may be the reason responsible for the appearance of double peaks. The hydrogen release under 820 K is contributed mainly by the hydrogen molecules resulting from the CH_2 complexes already available on the crystallite surfaces; whilst the hydrogen release above 820 K is contributed predominantly by the hydrogen molecules resulting from the reactions between detrapped hydrogen atoms and the CH complexes.

Figure 4 presents the hydrogen retention fractions in two types of traps at 400 K. It can

be seen that as the void fraction increases, the hydrogen retention fraction in the trap containing two hydrogen atoms increases while the fraction in the trap containing one hydrogen atom decreases. The low-temperature peak is contributed mainly by the CH₂ complex as mentioned above. Therefore, the low-temperature peak becomes more obvious as the void fraction increases. The result shown in Fig. 4 can be understood as follows: at the same temperature and dose, when the void fraction is larger, more hydrogen atoms can be trapped on the crystallite surfaces, which leads to more reactions forming CH₂ complexes by the mobile atom recombining with another trapped atom. Thus, proportionately, more atoms are retained on the crystallite surfaces in the form of CH₂ complexes rather than in the form of CH complexes than at a smaller void fraction. The larger proportion of CH₂ will lead to higher amplitude of the low temperature release peak. This explains why the low temperature release peak grows as the void fraction increases.

The interpretation mentioned above is supported by the results from experimental and theoretical studies. In a previous experimental study, Atsumi's et al. [26] concluded that the deuterium in the graphite exists in both forms of CD₂ and CD complexes. The former complexes are responsible for the low temperature peak, and the latter are responsible for the high temperature peak. The ideas were consistent with the theoretical study of Lomidze et al. [27], in which the CD is considered to be in the sp² configuration and the CD₂ is in the sp³ configuration. Details can be found in the review paper [28]. Therefore, we can come to a conclusion with confidence that the appearance of two desorption peaks is induced by the existence of two types of traps.

4 Conclusions

In present work, the structural effects of graphite on the hydrogen retention, re-emission, and thermal desorption are studied using dynamic Monte Carlo method. The simulation results show that almost all the incident hydrogen atoms are retained at substrate temperature below 1000 K, independent of void fraction, and that the retention fraction decreases rapidly when the substrate temperature is over 1000 K. High void fraction is conducive to the hydrogen retention, especially evident at high temperature. In addition, at low temperatures the re-emission of incident hydrogen atoms is mainly molecular hydrogen and at high temperatures is mainly atomic hydrogen. As the void fraction increases, the temperature at which the atomic and molecular hydrogen contribute equally to the release shifts towards higher temperatures. Moreover, the thermal desorption of H₂ depends strongly on the void fraction. Low void fraction tends to cause single desorption peak around 1000 K. As the void fraction increases, another desorption peak appears around 820 K.

Acknowledgments

This work was supported by National Basic Research Program of China under grant No: 2008CB717801, the Fundamental Research Funds for the Central Universities (DUT10ZD111) and the JSPS-CAS Core University program in the field of 'Plasma and Nuclear Fusion'. Authors would like to express their appreciation to Feng Wang for their assistance in computation."

References

- [1] Federici G, Holland D, Janeschitz G, et al. 1997, J. Nucl. Mater., 241-243: 260
- [2] Federici G, Anderl R A, Andrew P, et al. 1999, J. Nucl. Mater., 266-269: 14
- [3] Warriier M, Schneider R, Salonen E, et al. 2004, Contrib. Plasma Phys, 44: 307
- [4] Causey R A. 2002, J. Nucl. Mater., 300: 91
- [5] Haasz A A, Franzen P, Davis J W, et al. 1995, J. Appl. Phys., 77: 66
- [6] Möller W, Scherzer B M U. 1988, J. Appl. Phys., 64: 4860
- [7] Hassanein A, Wiechers B, Konkashbaev I. 1998, J. Nucl. Mater., 258-263: 295
- [8] Salonen E, Nordlund K, Keinonen J, et al. 2001, Phys. Rev. B, 63: 195415
- [9] Ferro Y, Marinelli F, Allouche A. 2003, Chem. Phys. Lett., 368: 609
- [10] Ferro Y, Marinelli F, Allouche A. 2002, J. Chem. Phys., 116: 8124
- [11] Rai A, Schneider R, Warriier M. 2008, J. Nucl. Mater., 374: 304
- [12] Rai A, Warriier M, Schneider R. 2009, Comput. Mater. Sci., 46: 469
- [13] Bortz A B, Kalos M H, Lebowitz J L. 1975, J. Comput. Phys., 17: 10
- [14] Biersack J P, Haggmark L G. 1980, Nucl. Instr. and Meth, 174: 257
- [15] Wilson K L, Hsu W L. 1987, J. Nucl. Mater., 145-147: 121-130
- [16] Causey R A, Baskes M I, Wilson K L. 1986, J. Vac. Sci. Technol. A, 4: 1189
- [17] Federici G, Wu C H. 1992, J. Nucl. Mater., 186: 131-152
- [18] Ashida K, Ichimura K, Matsuyama M, et al. 1984, J. Nucl. Mater., 128-129: 792
- [19] Warriier M, Schneider R, Salonen E, et al. 2007, Nucl. Fusion., 47: 1656
- [20] Kanashenko S L, Gorodetsky A E, Chernikov V N, et al. 1996, J. Nucl. Mater., 233-237: 1207
- [21] Aga R S, Fu C L, Krčmar M, et al. 2007, Phys. Rev. B, 76: 165404
- [22] Franzen P, Vietzke E. 1994, J. Vac. Sci. Technol. A., 12: 820
- [23] Davis J W, Haaze A A. 1994, J. Nucl. Mater., 217: 206
- [24] Suda T, Miyauchi H, Yoshikawa A, et al. 2007, Fusion Eng. Des., 82: 1762

- [25] Tadokoro T, O'hira S, Nishi M, et al. 1998, J. Nucl. Mater., 258-263: 1092
- [26] Atsumi H, Tokura S, Miyake M. 1988, J. Nucl. Mater., 155-157: 241
- [27] Lomidze M A, Gorodetsky A E, Kanashenko S L, et al. 1994, J. Nucl. Mater., 208: 313
- [28] Zakharov A P, Gorodetsky A E, Alimov V Kh, et al. 1997, J. Nucl. Mater., 241-243: 52

Table 1. The attempt frequency r_0 , jump distance L , and activation energy E_d for different jump processes. For the diffusion within the crystallite, low activation energy corresponds to short jump, and high activation energy corresponds to long jump.

Process	$r_0(\text{s}^{-1})$	L (nm)	E_d (eV)	Ref
Diffusing within the crystallites	6.8×10^{12}	0.38	0.015	11, 12
Diffusing on the crystallite surface	2.74×10^{13}	1.0	0.27	11, 12
Going into the bulk	1.0×10^{13}	3.46	0.9	15, 16
Desorption from crystallite surface	1.0×10^{13}	0.3	2.67	17
Detrapping from a trap site	1.0×10^{13}	0.2	1.91	18
Recombination of two trapped H atoms	1.0×10^{13}	0.3	2.7	5, 19
Hydrogen molecule dissociation	1.0×10^{13}	0.4	2.3	20
Hydrogen molecule dissociation	1.0×10^{13}	0.2	4.48	12

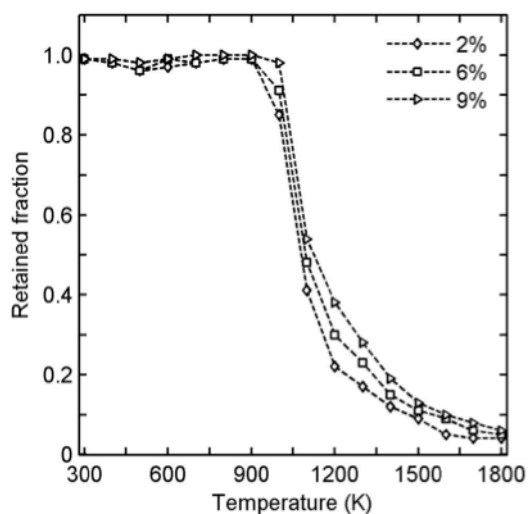


Fig. 1 Retained fraction of hydrogen as a function of temperature for different void fractions at a flux of $3 \times 10^{20} \text{ H/m}^2 \cdot \text{s}^{-1}$. The total of simulation time is 0.01 s.

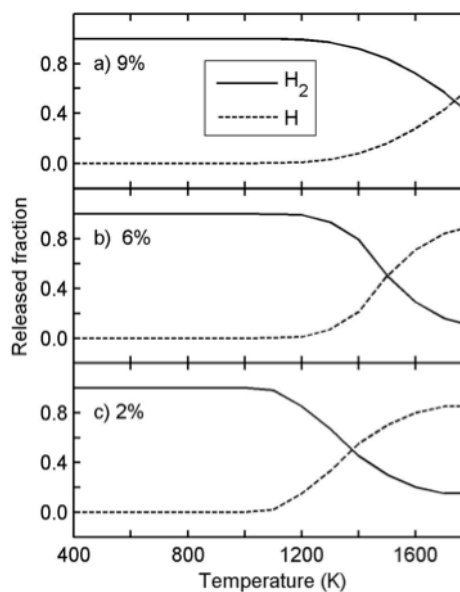


Fig. 2 Released fraction of hydrogen atoms and molecules as a function of temperature for different void fractions at a flux of $3 \times 10^{20} \text{ H/m}^2 \cdot \text{s}^{-1}$. The total of simulation time is 0.01 s.

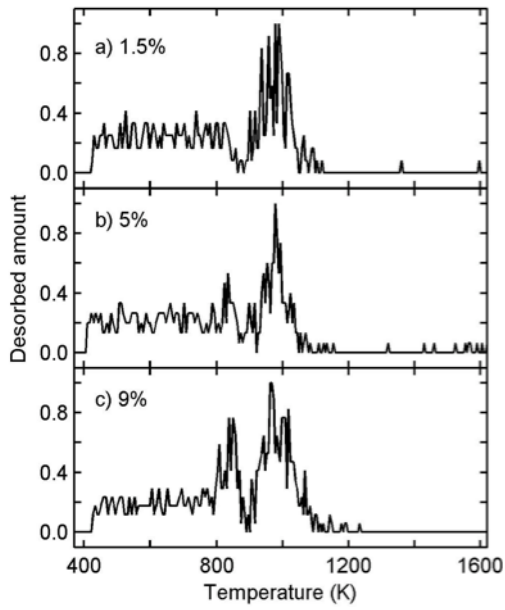


Fig. 3 Desorbed amount of H_2 as a function of substrate temperature with a heating rate of 4 K/s under different void fractions (the initial number of implanted hydrogen atoms is 4000 at room temperature). All the data points are normalized to the maximum of the molecule peak.

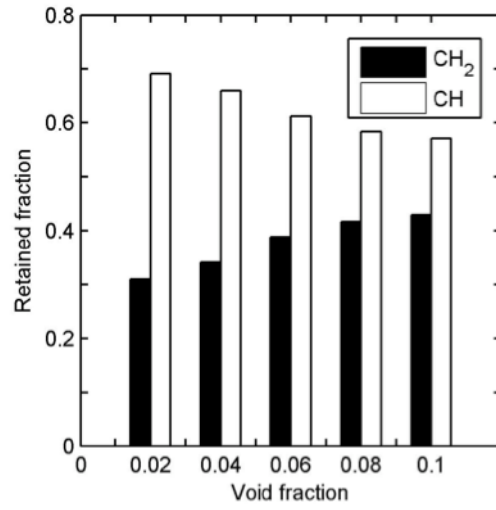


Fig. 4 Retained fraction of CH_2 and CH complexes as a function of void fraction at 400 K (the initial number of implanted hydrogen atoms is 4000 at room temperature, and the heating rate is 4 K/s).

Atomic Modeling of Interactions between Hydrogen and Tungsten

Zhongshi Yang, Qian. Xu, Guang-Hong Lu, Guang-Nan Luo

Institute of Plasma Physics, Chinese Academy of Sciences, P. O. Box 1126, Hefei 230031, China

One important issue concerning the applicability of W for PFM which is exposed to high fluxes of plasma, is the trapping and release of hydrogenic particles that controls the hydrogen isotope retention, particle balance and recycling in fusion devices. The energies of hydrogen particles in divertor region adjacent to the W surface are reduced below 100eV, usually at a magnitude of a few eV. Therefore it is very important to study the interaction between low energy hydrogen and W surface. In this work, an analytical bond-order interatomic potential for modeling nonequilibrium processes in the ternary W–C–H system [1] was adopted in the MD simulations. The purpose of this work is to study the surface effect and the projected range distribution of hydrogen atoms with different incident energy (E_i) on W surface. The point defects such as interstitial hydrogen formation energy and migration energy in W were also investigated.

The initial computational cells with the W (001) plane normal to the incidence direction had variable dimensions according to the incident energies of hydrogen atoms, consisting of 2000~10000 atoms in conventional bcc unit cells in three Cartesian directions with a density of 19.25g/cm³. In order to form a surface, periodic boundary conditions were removed in the z direction and the atoms in the lowest three atomic layers were kept fixed at their original positions all times. Simulating hydrogen atom bombardment was initiated by placing a hydrogen atom at a fixed distance from the surface, z_0 , greater than the potential cutoff radius. Temperature has been controlled using velocity scaling method for the atoms in the three atomic layers both above the fixed layers and at the four side walls. With a series of kinetic energies from 0.5 eV to 50 eV of hydrogen projectiles, we studied the energy dependence of ion reflection and projected range distributions. The final positions of the lattice atoms and H atoms have been recorded and analyzed in order to study the point defects in W bulk lattice.

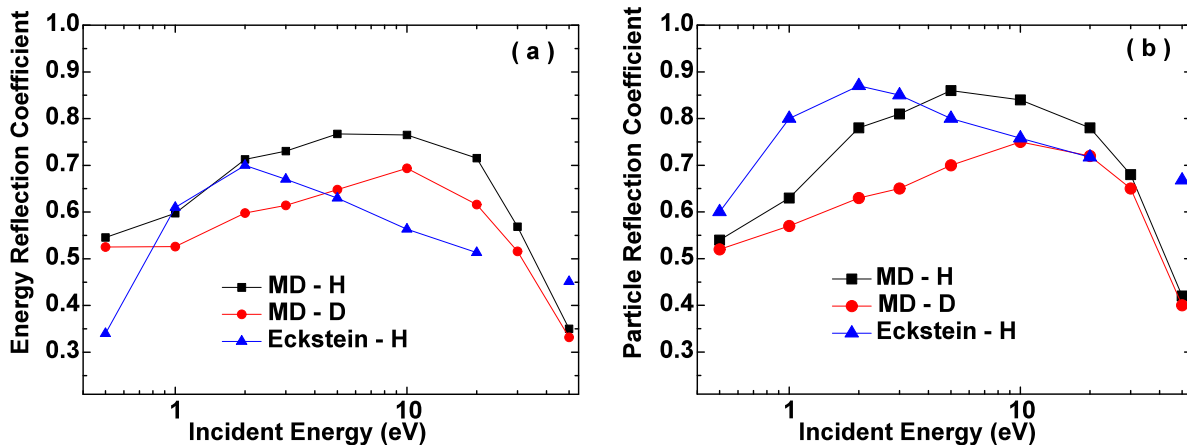


Figure 1. (a) Particle and (b) energy reflection coefficients of normal incident hydrogen atoms (H and D) on bcc W (001) surface as a function of incident energy. Eckstein's results [2, 3] calculated by TRIM.SP are also displayed.

By using MD simulations, the particle reflection coefficients of hydrogen atoms were calculated for normal incidence on W (001) surface as shown in Figure 1(a). At 5 eV incident energy, the reflection coefficient has a largest value of 0.86. When the incident energy is above 5 eV, the reflection coefficient decreases monotonically with increasing incident energy because the energetic projectile has larger probability to be implanted into the W bulk.

Below 5 eV, the reflection coefficient decreases with the decrease in the incident energy and the projectiles have a larger probability to be trapped on or near below the W surface. Another important question is the difference in the reflection for the different hydrogen isotopes. As Figure 1 shows, the difference between H and D in both particle and energy reflections is very small. Also shown in Figure 1(b), the energy reflection upon incident energy has a similar trend to the particle reflection.

Figure 2 shows the average depth (mean range) of the hydrogen atoms implanted into the crystalline W at normal incidence on (001) W surface with different incident energy. In addition to the MD simulations we also have performed BCA calculations using the code

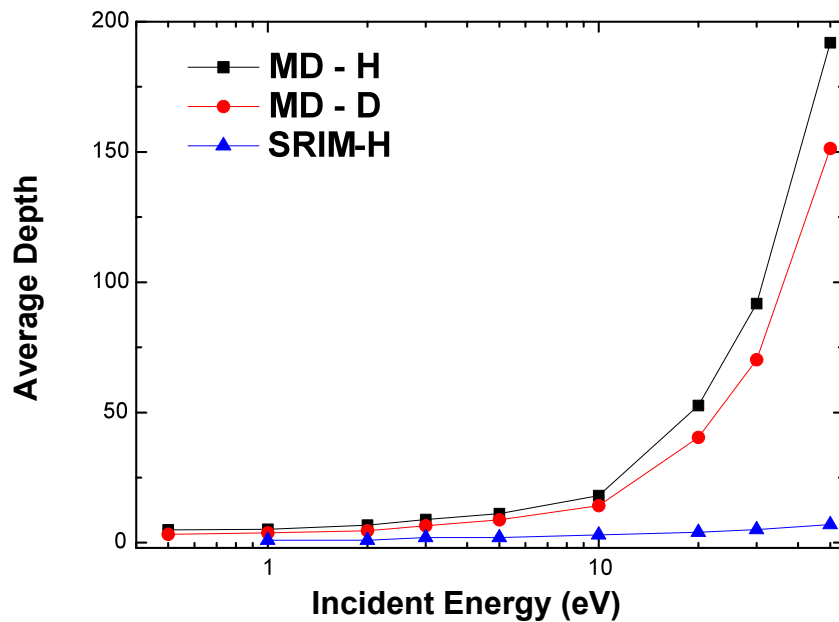


Figure 2. Average depth (mean range) of atomic hydrogen (H and D) implanted in bcc W (001) surface at normal incidence as a function of incident energy. The results calculated by SRIM 2010 code are also shown.

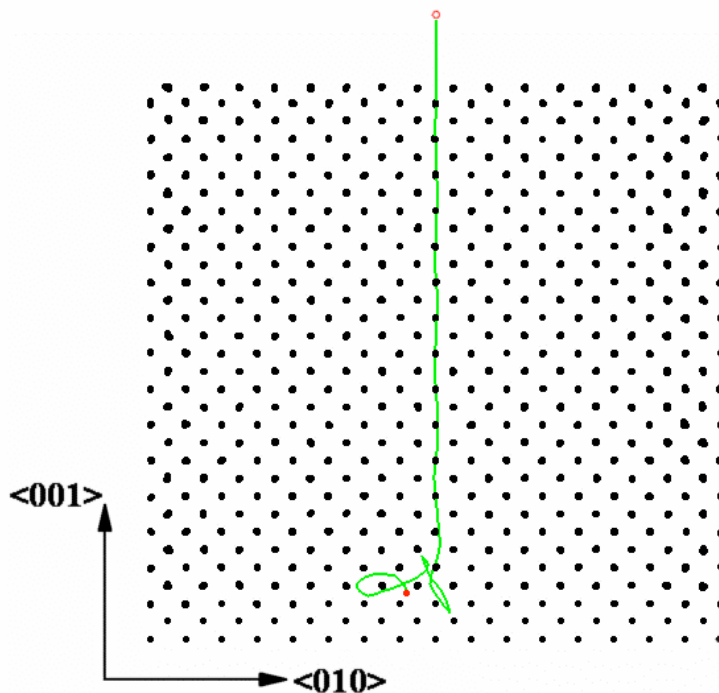


Figure 3. The channeled trajectory of H atom at $E_{in} = 20$ eV in the W bulk.

package SRIM 2010 [4]. The mean projected range represents the most probable location for ion to come to rest. The mean ranges for crystalline W by MD simulations are systematically higher than the results calculated by SRIM 2008. The difference could be most likely attributed to difference between a randomized target structure and a crystalline one as well as many-body nature of BOP in low energy range. In the range of relatively high incident energy, channeling occurs along the $\langle 001 \rangle$ crystallographic axis. To analyze the channeling effect, the normal incident H atoms were initially placed above the bridge site of W atoms on the top layer. Figure 3 shows the trajectory of a H atom at $E_{in} = 20$ eV in the W bulk in the initial stage. It can reach the 14th layer below the surface without significant energy loss. Then through successive collisions with lattice atoms the ion comes to rest in the bulk in the end.

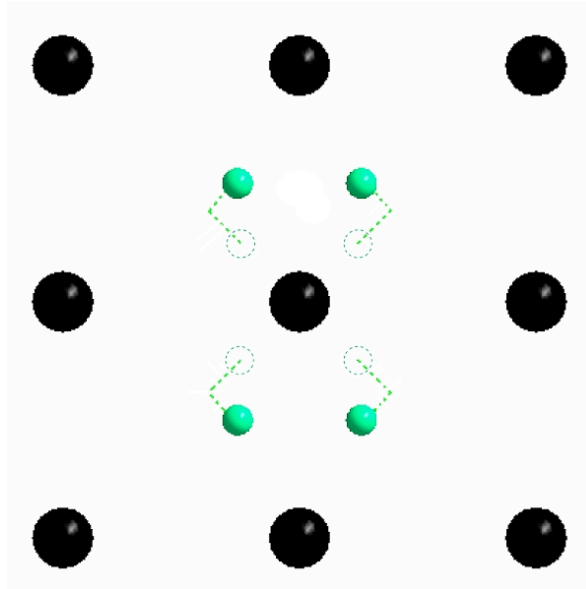


Figure 4. Top view of final configuration of four H atoms which were placed in the vicinity of a W atom after sufficient relaxation.

In this work, the defects of interstitial hydrogen atom in bcc W are investigated using MD calculations. The interstitial H formation energies were calculated as follows:

$$E_{int} = E(NW + H) - NE_{ref}(W) - E_{ref}(H) \quad (1)$$

where $E_{ref}(W)$ is the reference energy of bulk bcc W, $E_{ref}(H)$ is the equilibrium energy of a H atom in the supercell containing only the H atoms. $E(NW+H)$ is the energy of the supercell containing N W atoms and 1 H atom. In bcc W lattice, two kinds of interstitial sites could be occupied, i.e., the octahedral and the tetrahedral sites. Using Eq. (1), we have obtained that the formation energies for the octahedral and the tetrahedral configurations are -4.70 eV and -5.01 eV respectively. Similarly, for D atom in W, the formation energies for the octahedral and the tetrahedral configurations are -4.53 eV and -4.77 eV respectively. These results that the formation energy for a single hydrogen atom in the tetrahedral site is lower than in the octahedral site indicated that the tetrahedral configuration is more stable in agreement with experiments [5-8]. Compared to first-principle (FP) calculations [9], which gave the results for H octahedral and tetrahedral formation energies: -2.07 eV and -2.45 eV, respectively, MD results in this work are higher. However, the energy differences between the two configurations are similar: 0.31 eV (MD) and 0.38 eV (FP). In Figure 4, four H atoms were placed in the vicinity of a W atom. After sufficient relaxation, four H atoms eventually rest at the nearest tetrahedral sites. The trajectories of the four H atoms are also shown in this figure.

The migration energy barrier was obtained by quenched molecular dynamics [10]. For the successive positions along the migration path, the coordinate of the interstitial H atom in the z

direction was kept fixed, while the other two coordinates of the interstitial H atom and all the degrees of freedom of W bulk were let free to relax in its minimum potential energy. The migration energy was deduced as the barrier determined from the potential energy minima at the various positions. The migration energy for the interstitial H atom from a tetrahedral site through the neighboring octahedral site to another tetrahedral site was determined to be 0.31eV. The energy barrier value in MD simulation in this work could be compared to the experimental data of activation energy for H migration in W: 0.39 ± 0.09 eV [11]. After free diffusion in the lattice, the energetic H atom implanted into the W bulk in our irradiation simulation described above reduced its kinetic energy to a value smaller than the migration energy for an interstitial, $E_m \approx 0.30$ eV calculated in the work. Then, the lattice was left free to relax around the H atom, usually trapped in a tetrahedral interstitial site.

Acknowledgements

This work was supported partially by the JSPS-CAS Core-University Program in the field of Plasma and Nuclear Fusion, the National Natural Science Foundation of China under contract Nos. 10905070, 10875148 and 10728510, the Knowledge Innovation Program of the Chinese Academy of Sciences.

References

- [1] N. Juslin, et al., J. Appl. Phys. 98 (2005) 123520.
- [2] W. Eckstain, et al., Appl. Phys. A 38 (1985) 123.
- [3] W. Eckstein, Calculated Sputtering, Reflection and Range Values, IPP 9/132, 2002.
- [4] J.F. Ziegler, SRIM-2010 software package, Available online at: <<http://www.srim.org>>.
- [5] S. T. Picraux and F. L. Vook, J. Nucl. Mater. **53** (1974) 246.
- [6] S. T. Picraux and F. L. Vook, Phys. Rev. Lett. **33** (1974) 1216 .
- [7] E. Ligeon, R. Danielou, J. Fontenille, and R. Eymery, J. Appl. Phys. **59** (1986) 108.
- [8] S. Nagata and K. Takahiro, J. Nucl. Mater. **83–287** (2000) 1038.
- [9] Y.-L Liu et al J. Nucl. Mater. 390-391 (2009) 1032.
- [10] C. H. Bennett, in: Diffusion in Solids, Recent Developments, edited by A. S. Nowick and J. J. Burton, Academic, New York, 1975, pp.73.
- [11] R. Frauenfelder, J. Vac. Sci. Technol. 6 (1969) 388.

Dust Charging and Dynamics in Tokamaks *

Yukihiro Tomita (富田幸博)¹, Gakushi Kawamura (河村学思)¹,
Yudong Pan (潘宇东)², and Longwen Yan (严龙文)²

¹ *National Institute for Fusion Science, Toki 509-5292 Japan*

² *Southwestern Institute of Physics, P.O. Box 432, Chengdu 610041, Sichuan, China*

Abstract

The characteristics of charging of a dust particle and its dynamics in SOL/divertor plasma in tokamaks are studied. As for according to the OML theory, the charging time is so fast (~nanoseconds) compared to the dynamics of the dust particle in SOL/divertor plasma (~milliseconds), which means the equilibrium charge state is enough as the local charge state. It was clarified that the equilibrium charge $Z_{d,eq}$ is determined by the form as $Z_{d,eq} / R_d T_e$, which is a function of the normalized relative speed of plasma ion flow to the velocity of the dust particle and the plasma temperature ratio. After the investigation of the dominant forces on the dust particle, the friction force due to the plasma ion absorption and that due to the plasma ion Coulomb scattering are the same order for the low relative speed. The critical radius of a dust particle, where the gravity is larger than the friction forces due to plasma ions, is obtained.

1. Introduction

In recent years significant interests are increased in dust particles in fusion plasmas, where the dust radii are widely ranged between 10 nm and 100 μm . The components of them were mainly of carbon and constituents of stainless steel, which are used for most plasma-facing materials like divertor plates and vacuum vessels. One of the particular notices in fusion devices is associated with absorption of radioactive tritium [1]. After operation of plasma discharges, the removal of the radioactive dusts is one of key issues from the viewpoint of the safety. Though up to now the mechanisms of the generation and agglomeration of dust particles in fusion plasmas are not clarified, the studies of characteristics of the dust particles are quite important. So far the charging of a dust particle is investigated under the OML model [2,3], which is developed in the field of space plasma. In this study the characteristics of the dust charging according to the OML model are investigated. The dust density ($< 10^4 \text{ m}^{-3}$) in fusion plasmas is so low that the collective phenomena of the dust particles are safely ignored. In this study the characteristics of forces on the dust particle is also investigated.

2. Characteristics of charging of dust particle

The dust particle in relatively low temperature plasmas is negatively charged due to the higher mobility of surrounding plasma electrons compared to plasma ions. The dust charge $q_d (= -Z_d e, Z_d > 0)$ is determined by the plasma current fluxes to the dust particle:

$$\frac{dq_d}{dt} = I_{di} + I_{de}, \quad (1)$$

where I_{di} and I_{de} are the ion and electron absorption current to the dust particle, respectively. Here we neglected the thermionic current, secondary electron emission current and charging current due to impurities. According to the OML theory [2, 3] for the dust with spherical shape, the ion current with the dust radius R_d is obtained with respect to the relative speed of the ion flow velocity \vec{V}_i to the dust velocity \vec{v}_d [4, 5]:

$$I_{di} = \frac{\pi R_d^2 Z_i e n_i v_{th,i}}{2u} \left\{ \frac{2u}{\sqrt{\pi}} e^{-u^2} + \left[1 + 2\left(u^2 + \frac{Z_d Z_i e^2}{4\pi\epsilon_0 R_d T_i}\right) \right] \text{erf}(u) \right\}. \quad (2)$$

Here $u = \left| \vec{V}_i - \vec{v}_d \right| / v_{th,i}$ is the relative speed normalized by the ion thermal speed $v_{th,i} (= \sqrt{2T_i / m_i})$. The quantities n_i , T_i , and Z_i are the density, the temperature and charge state of plasma ions, respectively. On the other hand, since the thermal speed of plasma electrons is much higher than its flow speed, the electron current I_{de} is expressed for the case of Maxwell velocity distribution [4, 5]:

$$I_{de} = -e\pi R_d^2 n_e \sqrt{\frac{8T_e}{\pi m_e}} \exp\left(-\frac{Z_d e^2}{4\pi\epsilon_0 R_d T_e}\right), \quad (3)$$

where n_e and T_e are the electron density and temperature, respectively.

The charging time $\tau_{ch,j}$ ($j = e, i$) of the dust particle, which is defined as the relaxation time from the infinitesimal deviation from the equilibrium dust charge to the equilibrium state, is obtained from Eq. (1) - (3):

$$\frac{1}{\tau_{ch,i}} = \left. \frac{d}{dZ_d} \left(\frac{I_{di}}{e} \right) \right|_{Z_d,eq} = \frac{Z_i^2 e^2 n_i R_d v_{th,i} \text{erf}(u)}{4\epsilon_0 u T_i} : \text{plasma ion}, \quad (4)$$

$$\frac{1}{\tau_{ch,e}} = \left. \frac{d}{dZ_d} \left(\frac{I_{de}}{e} \right) \right|_{Z_d,eq} = \frac{e^2 n_e R_d}{4\epsilon_0 T_e} \sqrt{\frac{8T_e}{\pi m_e}} \exp\left(-\frac{Z_{d,eq} e^2}{4\pi\epsilon_0 R_d T_e}\right) : \text{plasma electron}. \quad (5)$$

Here the quantity $Z_{d,eq}$ is the equilibrium charge state, which is obtained from Eq. (1): $dq_d / dt = I_{di} + I_{de} = 0$. In Fig.1 the charging rates are shown as a function of the normalized relative speed for the case of the dust particle with the typical radius $1 \mu\text{m}$ in the hydrogen plasma of $n_e = 10^{19} \text{ m}^{-3}$, $T_e = T_i = 10 \text{ eV}$, which are the typical plasma parameters in SOL/divertor region in tokamaks. From this result it is clarified that the charging time (\sim few nanoseconds) of the dust around $R_d \sim 1 \mu\text{m}$ in the usual

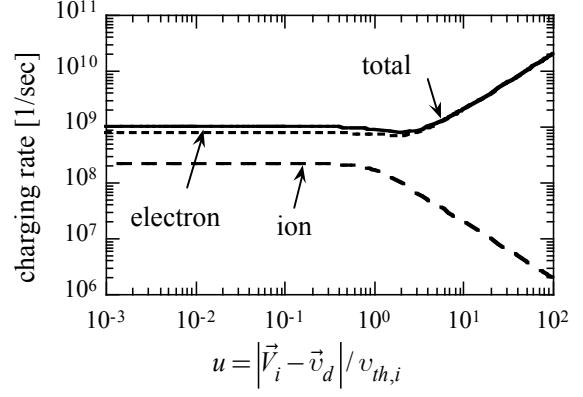


Fig.1 The charging rates of plasma ion (dashed line), plasma electrons (dotted line) and the total one (straight line) as a function of the normalized relative speed. Here the dust particle with the radius $1 \mu\text{m}$ is immersed in the hydrogen plasma of $n_e = 10^{19} \text{ m}^{-3}$, $T_e = T_i = 10 \text{ eV}$.

SOL/Divertor plasma of tokamaks is so fast compared to the dynamics of the dust particle ($>$ few milliseconds). Therefore, in this study the equilibrium charge is applied to the dust charge.

The equilibrium charge $Z_{d,eq}$ of the dust particle is determined by the relation $dq_d / dt = I_{di} + I_{de} = 0$:

$$\frac{1}{2u} \left\{ \frac{2u}{\sqrt{\pi}} e^{-u^2} + \left[1 + 2(u^2 + \frac{Z_i e T_e}{4\pi\epsilon_0 T_i} \xi_{d,eq}) \right] \text{erf}(u) \right\} = \sqrt{\frac{4 m_i T_e}{\pi m_e T_i}} \exp\left(-\frac{e}{4\pi\epsilon_0} \xi_{d,eq}\right). \quad (6)$$

Here the charge neutrality of plasmas, $n_e = Z_i n_i$, is assumed and the quantity $\xi_{d,eq}$ is defined

as $Z_{d,eq} / R_d T_e$, which is the function of the normalized relative speed u and the temperature ratio of plasmas. For hydrogen plasmas, the dependence of the quantity $\xi_{d,eq}$ on the normalized relative speed is shown in Fig.2 for the several temperature ratios, where the dust radius and the electron temperature are denoted with the unit in μm and eV, respectively.

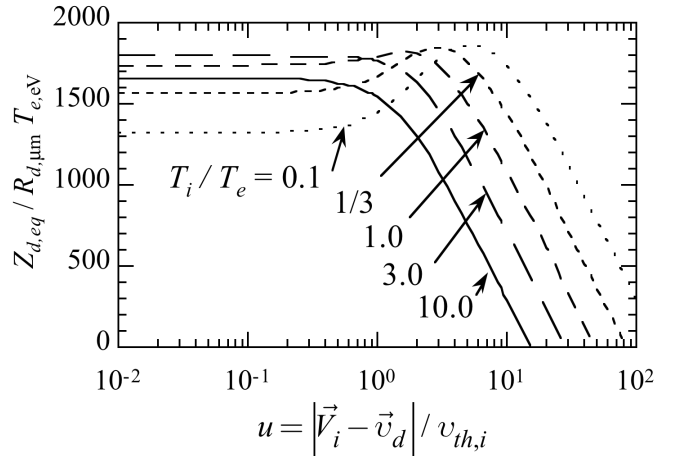


Fig.2 The equilibrium charge as a function of normalized relative speed u for the several plasma temperature ratios, where the dust radius and the electron temperature are denoted with the unit in μm and eV, respectively.

means the ion flux is larger than the electron flux to the dust particle, leads the positive charge state of the dust ($Z_d < 0$).

In the case of the low relative speed, the dependence of the relative speed is weak, where the equilibrium charge state $Z_{d,eq}$ is determined by the temperature ratio.

$$\begin{aligned} & \frac{2}{\sqrt{\pi}} \left(1 + \frac{Z_i e T_e}{4\pi\epsilon_0 T_i} \xi_{d,eq}\right) \\ &= \sqrt{\frac{4 m_i T_e}{\pi m_e T_i}} \exp\left(-\frac{e}{4\pi\epsilon_0} \xi_{d,eq}\right) \quad (7) \end{aligned}$$

In Fig. 3, the equilibrium charge $Z_{d,eq}$ for the case of $u = 0$ is shown. The maximum charge $Z_{d,eq}$ is about 18000 at the medium temperature ratios ($T_i/T_e \sim 3.0$) for the case of $R_d = 1 \mu\text{m}$ and $T_e = 10 \text{ eV}$. On the other hand, the higher the relative speed becomes, the lower the charge state of the dust particle becomes and the higher temperature ratio brings about the lower charge state.

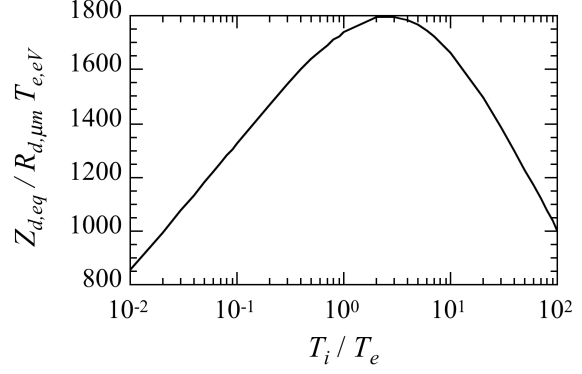


Fig.3 The equilibrium charge state for the case of relative speed $u = 0$ as a function of plasma temperature ratio.

3. Forces on dust

One of the dominant forces is friction force of plasma ions:

$$\vec{F}_{ifr} = \vec{F}_{iab} + \vec{F}_{isc} \quad (8)$$

Here \vec{F}_{iab} is the friction force due to absorption of plasma ions and \vec{F}_{isc} is the force due to Coulomb scattering of plasma ions. They are expressed by the normalized relative speed u :

$$\vec{F}_{iab} = \pi R_d^2 n_i T_i \frac{\vec{V}_i - \vec{v}_d}{|\vec{V}_i - \vec{v}_d|} \eta_{iab}(u, T_i / T_e) \quad \text{and} \quad (9)$$

$$\vec{F}_{isc} = \pi R_d^2 n_i T_i \frac{\vec{V}_i - \vec{v}_d}{|\vec{V}_i - \vec{v}_d|} \eta_{isc}(u, T_i / T_e), \quad (10)$$

Here

$$\eta_{iab}(u, T_i / T_e) \equiv \frac{1}{\sqrt{\pi} u^2} \{u(2u^2 + 1 + 2\chi_i)e^{-u^2} + [4u^4 + 4u^2 - 1 - 2(1 - 2u^2)\chi_i] \frac{\sqrt{\pi}}{2} \text{erf}(u)\}, \quad (11)$$

$$\eta_{isc}(u, T_i / T_e) \equiv 4\chi_i^2 \ln \Lambda \frac{\text{erf}(u) - 2u \exp(-u^2) / \sqrt{\pi}}{2u^2} \quad (12)$$

and

$$\chi_i(u, T_i / T_e) \equiv \frac{Z_i Z_d e^2}{4\pi\epsilon_0 R_d T_i} = \frac{Z_i e}{4\pi\epsilon_0 T_i} \xi_{d,eq} \quad (13)$$

The quantities η_{iab} , η_{isc} and χ_i are the functions of the normalized relative speed u and the temperature ratio. In Fig. 4 the quantities η s are shown as a function of the relative speed u for the case of $T_i / T_e = 0.5$. For the lower relative speed ($u < 1.0$) The difference between the quantities η_{iab} and η_{isc} is small.

These friction forces can be compared to the intrinsic gravity.

$$\begin{aligned} \frac{F_{iab} + F_{isc}}{F_g} &= \frac{3n_i T_i}{4g\rho_d R_d} [\eta_{iab}(u, T_i / T_e) + \eta_{isc}(u, T_i / T_e)] \\ &= 1.23 \times 10^{-17} \frac{n_i T_{i,eV}}{\rho_{d,g/cc} R_{d,\mu m}} [\eta_{iab}(u, T_i / T_e) + \eta_{isc}(u, T_i / T_e)] \end{aligned} \quad (14)$$

For the larger dust particle than the critical radius $R_{d,mm,g}$ gravity is larger than the friction forces:

$$R_{d,\mu m} \geq R_{d,\mu m,g} \equiv 1.23 \times 10^{-17} \frac{n_i T_{i,eV}}{\rho_{d,g/cc}} [\eta_{iab}(u, T_i / T_e) + \eta_{isc}(u, T_i / T_e)] \quad (15)$$

For the case of the carbon dust in the plasma pressure $n_i T_i = 10^{19} \text{ m}^{-3} \text{ eV}$ with $u = 1.0$, the critical radius $R_{d,mm,g}$ is as large as $1.2 \mu\text{m}$.

6. Summary

The characteristics of the dust particle in the plasma were investigated. As for according to the OML theory, the charging time is so fast (\sim nanoseconds) compared to the dynamics of the dust particle in SOL/divertor plasma (\sim milliseconds), which means the equilibrium charge state is enough as the local charge state. It was clarified that the equilibrium charge $Z_{d,eq}$ is determined by the form as $Z_{d,eq} / R_d T_e$, which is a function of the normalized relative speed of plasma ion flow to the velocity of the dust particle and the plasma temperature ratio. In the case of lower relative speed than unity, the equilibrium charge is determined only by the plasma temperature ratio. For the case of $R_d = 1 \mu\text{m}$ and $T_e = 10 \text{ eV}$, the maximum charge $Z_{d,eq}$ is around 18000 at the medium temperature ratios ($T_i / T_e \sim 3.0$). After the investigation of the dominant forces on the dust particle, the friction force due to the plasma ion absorption and that due to the plasma ion Coulomb scattering are the same order for the low relative

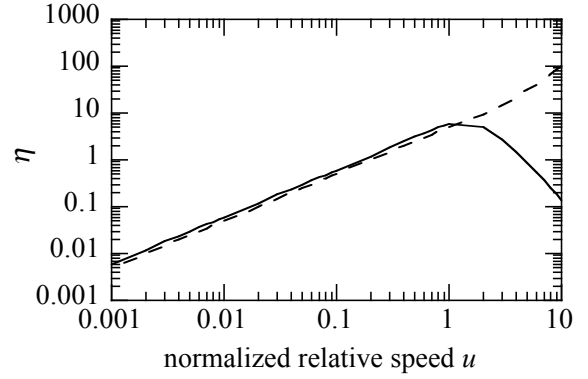


Fig.4 The coefficients h of the friction forces as a function of the normalized relative speed, where $T_i / T_e = 0.5$.

speed. It was found that the larger dust than $1.2\ \mu\text{m}$ falls down by the gravity, which is larger than the friction force due to plasma ions.

These results may be useful to analyze the dust particle in SOL/divertor plasma of fusion devices.

Acknowledgements

This work was partially supported in part by the JSPS-CAS Core-University Program in the field of Plasma and Nuclear Fusion, the Grant-in-Aid for scientific research from Ministry of Education, Science and Culture of Japan (No. 19055005), and the Chinese National Fusion Project for ITER under grant No 2009GB106006.

References

- [1] Winter J., 2004, Plasma Phys. Control. Fusion 46: B583.
- [2] Mott-Smith H and Langmuir I, 1926, Phys. Rev. 28: 727.
- [3] Allen J E, 1992, Physica Scripta 45: 497.
- [4] Pigarov A., Krasheninnikov S., Soboleva T., Rognlien T., 2005, Phys. Plasma, 12: 122508.
- [5] Smirnov R D, Pigarov A Yu, Rosenberg M, et al. 2007, Plasma Phys. Control. Fusion, 49: 347.

Agenda

China- Japan CUP seminar on “Modeling of Theory and Simulation of Fusion Plasmas”

August 30-September 2, 2010, Peking University, Beijing, CHINA

Monday, 30 August 2010

8:30 - 9:00 Registration (also available in the afternoon of 29 Aug)

< Opening > Chair: WANG Xiaogang (Peking Univ.)

9:00 - 9:20 LI Ding (CAS) and KISHIMOTO Yasuyuki (Kyoto Univ.)

‘Opening remarks’

9:20 - 10:00 NAKAJIMA Noriyoshi (NIFS), TOMITA Yukihiro (NIFS),

GAO Zhe (Tsinghua Univ.)

‘Present status and future plans of collaboration researches’

< Turbulence > Chair: LI Ding (CAS)

10:00 - 10:40 KISHIMOTO Yasuyuki (Kyoto Univ.)

‘Profile relaxation and entropy dynamics in turbulent transport’

10:40 - 11:00 Break and Group Photo

11:00 - 11:40 GAO Zhe (Tsinghua Univ.)

‘Analytical theory of the geodesic acoustic mode: plasma shaping effects in small and large orbit drift limit’

11:40 - 12:20 LI Jiquan (Kyoto Univ.)

‘Wave-number spectral characteristics of the multiscale plasma turbulence’

12:20 - 14:00 Lunch

< Turbulence > Chair: Yasuyuki Kishimoto (Kyoto Univ.)

14:00 - 14:40 ZHOU Deng (ASIPP)

‘Zonal flow modes in tokamak plasma with a dominantly poloidal flow’

14:40 - 15:20 ISHIZAWA Akihiro (NIFS)

‘Magnetic reconnection caused by turbulence’

15:20 - 15:40 Break

< Turbulence > Chair: GAO Zhe (Tsinghua Univ.)

15:40 - 16:20 ZHAO Kaijun(SWIP)

‘Experimental study of zonal flow, geodesic acoustic mode and turbulence regulation in Edge Plasmas of the HL-2A’

16:20 - 17:00 KASUYA Naohiro (NIFS)

‘Turbulence Diagnostics on 3-D Fields Obtained by Numerical Simulations in Magnetically Confined Plasmas’

17:00-17:40 CHENG Jun (SWIP)

‘Spatial structure of edge fluctuations on the HL-2A tokamak’

Tuesday, 31 August 2010

< Turbulence and MHD > Chair: FUKUYAMA Atsushi (Kyoto Univ.)

9:00 -9:40 WANG Aike (SWIP)

‘Effects of turbulent dissipation on the formation of transport barrier’

9:40 - 10:20 NAITOU Hiroshi (Yamaguchi Univ.)

‘Global and kinetic MHD simulation by the GpicMHD code’

10:20-11:00 XIAO Weiwen (SWIP)

‘Particle transport in HL-2A tokamak’

11:00 - 11:20 Break

< MHD > Chair: XIANG Nong (ASIPP)

11:20 - 12:00 WANG Xiaogang (Peking Univ.)

‘A model for sawtooth driven neoclassical tearing modes in HL-2A Experiments’

12:00 - 12:40 WANG Zhengxiong (DLUT)

‘Linear growth of collisionless double tearing modes in a cylindrical plasma’

12:40 - 14:00 Lunch

< Peripheral Plasma > Chair: TOMITA Yukihiro (NIFS)

< Special Lecture >

14:00 - 15:00 TAKIZUKA Tomonori (JAEA)

‘Full-particle simulation of a tokamak plasma with open-field SOL-divertor region’

< Transport in SOL/Divertor Plasma >

15:00 - 15:40 KOBAYASHI Masahiro (NIFS)

‘Divertor transport study in the stochastic magnetic boundary of LHD’

15:40 - 16:00 Break

< Transport in SOL/Divertor Plasma > Chair: WANG Aike (SWIP)

16:00 - 16:40 CHEN Yiping (ASIPP)

‘Simulation of SOL-Divertor Plasmas on JT-60U and EAST tokamaks with SOLPS5.0 (B2.5-Eirene) Code’

16:40 - 17:20 KAWAMURA Gakushi (NIFS)

‘Monte Carlo simulation of impurity transport in LHD divertor and model integrations’

Wednesday, 1 September 2010

< MHD > Chair: DENG Zhou (ASIPP)

9:00 - 9:40 NAKAJIMA Noriyoshi (NIFS)

‘MHD equilibrium with a chaotic magnetic field’

9:40 - 10:20 HE Hongda (SWIP)

‘Second stable regime of internal kink modes excited by barely passing energetic ions in tokamak plasmas’

10:20 - 10:40 Break

< MHD and Integrated Modeling > Chair: NAKAJIMA Noriyoshi (NIFS)

10:40 - 11:20 FUKUYAMA Atsushi (Kyoto Univ.)

‘Kinetic integrate modeling of tokamak plasmas by TASK3G’

11:20 - 12:00 TAN Yi (Tsinghua Univ.)

‘Simulation of ECR startup and comparison to experimental observations in SUNIST’

12:00 - 12:30 summary of core plasma

12:30 - 14:00 Lunch

< Impurity Transport near PFW > Chair: TAKIZUKA Tomonori (JAEA)

14:00 - 14:40 DAI Shuyu (DLUT)

‘Simulation of impurity deposition and fuel retention in the gaps between divertor tiles using a hybrid code’

14:40 - 15:20 XU Qian (ASIPP)

‘EDDY code and initial simulation for EAST SiC/C PFMs’

15:20 - 15:40 Break

< Impurity Transport near PFW > Chair: WANG Dezhen (DLUT)

15:40 - 16:30 LIU Shengguang (DLUT)

‘Modeling of hydrogen release and retention in carbon materials’

16:30 - 17:10 YANG Zhongshi (ASIPP)

‘Molecular Dynamics Simulations of Tungsten Plasma Facing Materials’

17:10 - 17:40 TOMITA Yukihiro (NIFS)

‘Dust charging and dynamics in tokamaks’

17:40 - 18:10 summary of peripheral plasma

Thursday, 2 September 2010

9:00 - 11:00 Individual discussions in each category

11:00 - 12:00 Plenary meeting on future J-C collaboration in fields of Theory and
Simulation of Fusion Plasmas
and closing

12:00 - 14:00 Lunch

14:00 - 17:00 Scientific visit to the SUNIST spherical tokamak device and laboratory
at Tsinghua University, and to plasma group at Peking University

List of participants

Name	Affiliation	Email
1 CAI Huishan 蔡 辉山	USTC	hscai@mail.ustc.edu.cn
2 CHEN Yiping 陈 一平	ASIPP	ypchen@ipp.ac.cn
3 CHENG Jun 程 均	SWIP	chengj@swip.ac.cn
4 DAI Shuyu 戴 舒宇	DLUT	
5 DING Rui 丁 锐	ASIPP	rding@ipp.ac.cn
6 FUKUYAMA Atsushi 福山 淳	Kyoto U	fukuyama@nucleng.kyoto-u.ac.jp
7 GAO Zhe 高 喆	Tsinghua U	gaozhe@tsinghua.edu.cn
8 HE Hongda 何 宏达	SWIP	hehd@swip.ac.cn
9 HE Zhixiong 何 志雄	SWIP/Tsinghua U	hezx@swip.ac.cn
10 ISHIZAWA Akihiro 石澤 明宏	NIFS	ishizawa@nifs.ac.jp
11 KASUYA Naohiro 糟谷 直弘	NIFS	kasuya@nifs.ac.jp
12 KAWAMURA Gakushi 河村 学思	NIFS	kawamura.gakushi@nifs.ac.jp
13 KISHIMOTO Yasuaki 岸本 泰明	Kyoto U	kishimoto@energy.kyoto-u.ac.jp
14 KOBAYASHI Masahiro 小林 政弘	NIFS	kobayashi.masahiro@lhd.nifs.ac.jp
15 LI Ding 李 定	CAS	dli@cashq.ac.cn
16 LI Dehui 李 德徽	ASIPP	dhli@ipp.ac.cn
17 LI Jiquan 李 继全	Kyoto U	lijq@energy.kyoto-u.ac.jp
18 LIU Shengguang 刘 升光	DLUT	
19 NAITOU Hiroshi 内藤 裕志	Yamaguchi U	naitou@plasma.eee.yamaguchi-u.ac.jp
20 NAKAJIMA Noriyoshi 中島 徳嘉	NIFS	nakajima@nifs.ac.jp
21 TAKIZUKA Tomonori 滝塚 知典	JAEA	takizuka.tomonori@jaea.go.jp
22 TAN Yi 谭 熠	Tsinghua U	tanyi@sunist.org
23 TOMITA Yukihiro 富田 幸博	NIFS	tomita@nifs.ac.jp
24 WANG Aike 王 爱科	SWIP	akwang@swip.ac.cn
25 WANG Dezhen 王 徳真	DLUT	wangdez@dlut.edu.cn
26 WANG Xiaogang 王 晓钢	PKU	xgwang@pku.edu.cn
27 WANG Zhengxiong 王 正汹	DLUT	zxwang@mail.dlut.edu.cn
28 XIANG Nong 项 农	ASIPP	xiangn@ipp.ac.cn
29 XIAO Chijie 肖 池阶	PKU	cjxiao@pku.edu.cn
30 XIAO Weiwen 肖 维文	SWIP	xiaoww@swip.ac.cn
31 XU Qian 徐 倩	ASIPP	xuq@ipp.ac.cn

32	YANG Zhongshi 杨 钟时	ASIPP	zsyang@ipp.ac.cn
33	ZHAO Kaijun 赵 开君	SWIP	kjzhao@swip.ac.cn
34	ZHOU Deng 周 登	ASIP	dzzhou@ipp.ac.cn